

Three-dimensional Optical Flow Measurements with Short Coherence Holography

Von der Fakultät für Mathematik und Naturwissenschaften
der Carl von Ossietzky Universität Oldenburg
zur Erlangung des Grades eines

Doktors der Naturwissenschaften (Dr. rer. nat.)

angenommene Dissertation von

Sven F. Herrmann

geboren am 15.09.1972 in Bremen.

Gutachter:
Zweitgutachter:
Tag der Disputation:

Prof. Dr. Klaus D. Hinsch
Prof. Dr. Joachim Peinke
13. Juli 2006

Abstract

English Version

Particle holography has proven to be a useful metrological tool for three-dimensional flow velocimetry. After a thorough introduction of the most common technique, called Holographic Particle Image Velocimetry (HPIV), its noise contributions are carefully analysed. In order to provide as many information as possible from a large and densely seeded particle field carried by either an air or water flow, the work presented in this thesis is largely devoted to push barriers of the classical HPIV towards those limits given by the highly resolving recording materials. To this end, a previously introduced short-coherence recording technique (Light-in-Flight Holography or short LiFH) is adapted for the reconstruction of the real particle images, resulting in our technique LiFH-PIV. This technique suppresses the intrinsic out-of-focus noise, while reconstructing only slices of the full three dimensional field. By selecting the slice in focus, the whole field can be scanned successively by means of a CCD or CMOS sensor. For the recording of such large fields of tiny tracer particles on holographic film, ruby lasers have typically been utilised in the past. Reconstructions from such holograms with a continuous wave (cw) source at slightly different wavelength often suffer from aberrations. To overcome this, a specially designed Nd:YAG laser system is applied for the LiFH recording of air flows inside a large industrial wind tunnel. Due to a highly stable cw counterpart of the recording laser, a completely separated and automated reconstruction setup could be developed. With this, the image information from two successively recorded particle fields can be extracted even from those holograms, which are taken close to a noise limit given by the properties of the recording materials. This technique allows to considerably enlarge the measuring fields or to use much smaller particles than commonly needed for good signals. The reconstructed intensity distribution is digitized plane by plane and for the evaluation of these huge data-sets, an intensity-based correlation method is extended to the third dimension. A direct comparison of the classical HPIV and the LiFH-PIV approach reveals the advantages of the latter by evaluating the signal-to-noise ratio in reconstructed and digitised particle images. Future improvements of this technique are under way; these efforts are briefly reported in the extended outlook.

Deutsche Version

Die holographische Aufzeichnung kleinster Streuteilchen hat sich als wertvolle Methode für die Messung drei-dimensionaler Strömungsgeschwindigkeitsfelder herausgestellt. Nach einer ausführlichen Darstellung der am häufigsten verwendeten Methode, der Holographic Particle Image Velocimetry (HPIV), wird detailliert auf deren Rauscheinflüsse eingegangen. Um möglichst viele Informationen von großen und dichten Teilchenfeldern in Luft- oder Wasserströmungen zu erhalten, dienen die dargestellten Forschungsarbeiten einer optimalen Nutzung der hochauflösenden holographischen Aufzeichnungsmaterialien. Zunächst wird eine bereits eingeführte kurzkohärente Aufzeichnungsmethode (Light-in-Flight Holographie oder kurz LiFH) auf die Rekonstruktion reeller holographischer Teilchenbilder angewandt (LiFH-PIV). Diese tomographische Technik erlaubt eine effektive Unterdrückung der Rauschanteile von unscharf abgebildeten Teilchen. Die rekonstruierten Ebenen können dabei kontinuierlich in der Tiefe gewählt werden und erlauben das schrittweise digitalisieren des gesamten Strömungsfeldes mit CCD- oder CMOS-Sensoren. Für die Aufnahme solcher Hologramme sind bislang leistungsstarke gepulste Rubin-Laser zum Einsatz gekommen. Da keine geeignete Lichtquelle im Dauerstrichbetrieb (cw) bei gleicher Wellenlänge existiert, kommt es bei Rekonstruktionen mit angepassten Wellenlängen häufig zu Aberrationen in den Teilchenbildern. Für holographische Aufnahmen an einem großen industriellen Windkanal ist daher ein speziell designtes Nd:YAG Laser-System zum Einsatz gekommen. Passend hierzu konnte ein geeigneter cw-Laser für den Aufbau eines eigenständigen und vollautomatischen Rekonstruktionsaufbaus gewählt werden. Mit diesem können die beiden kurz hintereinander aufgezeichneten Teilchenfelder selbst bei ungünstigen Aufzeichnungsbedingungen durch Ausnutzung der Dynamik von holographischen Aufzeichnungsmaterialien rekonstruiert werden. Diese Technik der "Holographie am Rauschlimit" erlaubt größere als bisher mögliche Messfelder oder die Nutzung kleinerer Streuteilchen. Die rekonstruierten Teilchenbilder werden dann vollautomatisch Ebene für Ebene abgetastet und digitalisiert, bevor die lokale Verschiebung, respektive die Geschwindigkeit, durch eine intensitätsbasierte Korrelationsmethode ermittelt wird. Ein direkter Vergleich der klassischen HPIV mit der LiFH-PIV zeigt die Vorteile der letzteren, rauschunterdrückenden Methode durch Analyse der Signal-Rausch-Verhältnisse einzelner Teilchenbilder. Arbeiten für weitere Verbesserungen der LiFH-PIV Technik sind bereits begonnen worden; diese werden kurz im Ausblick dargestellt.

"A foolish faith in authority
is the worst enemy of truth."

Albert Einstein

Contents

Abstract	V
1 Introduction	1
1.1 Context	1
1.1.1 Flow Visualisation	1
1.1.2 Flow Diagnostics	2
1.1.3 Role of Particle Holography	4
1.1.4 Holographic Particle Image Velocimetry	5
1.2 Main Contributions of this Work	5
1.3 Outline of the Contents	6
2 Holographic Imaging of Particle Distributions	9
2.1 Holography	9
2.1.1 Recording and Reconstruction of a Hologram	9
2.1.2 Recording Geometries	13
2.1.3 Recording Materials	15
2.1.4 Precision Replay of Holograms	19
2.1.4.1 Hologram and Beam Positioning	20
2.1.4.2 Beam Collimation Requirements	21
2.1.4.3 Magnifications in Holographic Replays	23
2.1.4.4 Emulsion Shrinkage	24
2.1.4.5 Phase Errors	25
2.2 Properties of Holographic Particle Images	27
2.2.1 Intensity, Size and Resolution of Ideal Particle Images	27
2.2.2 Aberrations in Particle Images	29
2.3 Light Scattering by Particles	30
2.3.1 Mie-Scattering	31

2.3.2	Influence of Light Scattered by Particles on the Holographic Registration	33
3	Noise Limits for Recording of Particle Fields	37
3.1	Background Noise in Holographic Particle Images	37
3.1.1	Sources of Noise	38
3.2	Signal-to-Noise Ratio in Holographic Images	39
3.2.1	Application to Intrinsic Speckle Noise	39
3.2.2	Application to Emulsion Grain Noise	40
3.2.2.1	Theoretical Determination of the Emulsion Grain Noise Limit	42
3.2.2.2	Experimental Investigations with a Test Object	43
3.2.2.3	The Emulsion Grain Noise Limit in Particle Holography	46
3.2.2.4	Validation of the Results and Conclusions	49
4	Short Coherence Holography	53
4.1	Principle of Light-in-Flight Holography	53
4.1.1	Basic Considerations and Demonstrational Experiment	53
4.1.2	Common Applications of Light-in-Flight Holography	55
4.1.3	Technical Requirements	55
4.1.4	Coherence Theory	56
4.2	Noise Reduction by Short Coherence Recording	60
4.2.1	Backscattering Geometry, Aperture Effect and Coherence Depth	61
4.2.2	Virtual Image Reconstruction	62
4.2.2.1	LiFH for Visualisation Purposes	63
4.2.2.2	Relevance of LiFH for HPIV and First Experiments	64
4.2.2.3	Fast Optical Switching for Cross-correlation Analysis	65
4.2.3	Real Image Reconstruction	67
5	Nd:YAG Laser for Particle Holography	71
5.1	Suitability of Nd:YAG Lasers	71
5.1.1	Green-sensitive Holographic Materials	71
5.1.2	Coherence-Length-Test with Quantel BrilliantB Laser	72
5.1.3	Energy Density Requirements	74
5.2	Pulsed Nd:YAG Laser System for Recording	74

5.2.1	System Design and Properties	74
5.2.1.1	Oscillator Design	75
5.2.1.2	Amplifier Stages	76
5.2.1.3	Second Harmonic Generation by Phase Matching	77
5.2.1.4	Beam Combination Unit	78
5.2.2	Injection Seeding	79
5.2.3	Beam-Pointing Stability and Divergence Control	80
5.2.4	Modes of Operation	81
6	Recording and Scanning Systems	83
6.1	Recording Set-ups in the Laboratory	83
6.1.1	Reference Beam Delivery Unit	84
6.1.2	Recording Set-up with Out-of-plane Illumination and In-plane Reference Beams	85
6.1.3	Recording Set-up with In-plane Illumination and Out-of-plane Reference Beams	87
6.2	Separate Reconstruction Set-up	88
6.2.1	Solid State and Diode Pumped Reconstruction Laser	89
6.2.2	General Scanning Arrangement	90
6.2.3	Technical Implementation	92
6.2.4	Software	94
6.2.5	Scanning Procedure	95
7	Evaluation of Particle Images	97
7.1	Short Review of Evaluation Procedures	97
7.1.1	Stereoscopic Viewing and Phase Conjugate Replay	97
7.1.2	Hybrid HPIV with Orthogonal Views	98
7.1.3	Side-scattering Recording and Center-of-Mass Evaluation	99
7.2	3D Intensity Correlation	100
7.2.1	Motivation	100
7.2.2	Mathematical Formulation	101
7.2.2.1	Subpixel Algorithms	103
7.2.3	Image Data Handling and Correlation Algorithms	105
7.2.3.1	Computing Demands	106
7.2.4	Restrictions when LiFH is used	108

8	Wind-tunnel measurements	111
8.1	Complete recording system at the wind-tunnel	111
8.2	Off-site reconstruction	112
8.3	Results	114
8.4	Discussion of the system and its drawbacks	119
9	Comparison of Imaging Performance	121
9.1	Pre-Knowledge from Theory	121
9.1.1	Average Noise Intensity from Emulsion Grains	121
9.1.2	Deterministic Particle Image Intensity	122
9.1.3	Signal-to-Noise Ratio of Particle Images and its Dependency on Aperture Size	123
9.2	Experimental Realisation of the Comparison-Study	124
9.2.1	Types of Particle Holograms	124
9.2.2	Collection of Aperture-Dependent Data	126
9.3	Evaluation and Results	127
9.3.1	Emulsion Grain Noise	127
9.3.2	Average Total Image Intensity	129
9.3.3	Particle Image Detection	130
9.3.3.1	Visual Inspection and Manual Thresholding	130
9.3.3.2	Histogram-Based Fitting of Probability Density Function for Integrated Speckle	130
9.3.3.3	Intensity-Based Circular Particle Image Finder	131
9.3.3.4	Position-Based Particle Image Finder with Edge De- tection	133
9.3.4	Particle Image Intensity and Resulting SNR from Visual Dis- crimination Method	135
9.3.5	Particle Image Intensity and Resulting SNR from Automated Discrimination Methods	137
9.3.5.1	Disapproved Discrimination Methods	137
9.3.5.2	Approved Position-Based-Particle-Finder Discrimi- nation Method	137
9.3.6	Analysis of Particle-Number-Density Series	139
9.3.6.1	Resulting SNR from the Approved Automated Dis- crimination Method	139
9.3.6.2	Dependency of SNR on the Change of Number Den- sity	140
9.4	Discussion	145

10 Summary, Conclusions and Outlook	147
10.1 Summary of the Contents	147
10.2 Conclusions from the Presented Work	149
10.3 Ongoing Research Work and Outlook	150
A Appendix	155
A.1 Navier-Stokes Equation	155
A.2 Holographic Emulsions	156
A.3 Processing of Holographic Recording Materials	156
A.4 Holographic Imaging Equations	158
A.4.1 Nonparaxial Holographic Imaging Equations	161
A.4.2 Axial Positioning Error of Holographic Particle Images	163
A.5 Mie-Scattering Theory	164
A.6 Line-width, Coherence Time or Length and Spectrum of Radiation	167
A.7 Specifications for Nd:YAG Laser System	168
A.8 Distributed Correlation	171
A.9 Image Enhancements	172
A.9.1 Thresholding and Binarisation	173
A.9.2 Contrast Enhancements	173
A.9.3 Noise Reduction	174
A.10 Determining Dispersed Particle Densities in Water	174
References	179
Acknowledgements	189
Curriculum Vitae	191
Statement	193

1 Introduction

1.1 Context

1.1.1 Flow Visualisation

Fluid motion phenomena and especially those with a high degree of complexity have drawn the attention of mankind ever since they were first observed. Fascinating patterns with a great variety can be observed when tracking such motions using naturally available or artificially added markers mixed into the fluid under inspection. While early visualisations of complex flows often show streamlines in a more intuitive, even artistic and sometimes highly detailed way, today's insight is often guided by a graphical representation of quantitative measures, for example the local velocity or vorticity (see Figure 1.1).

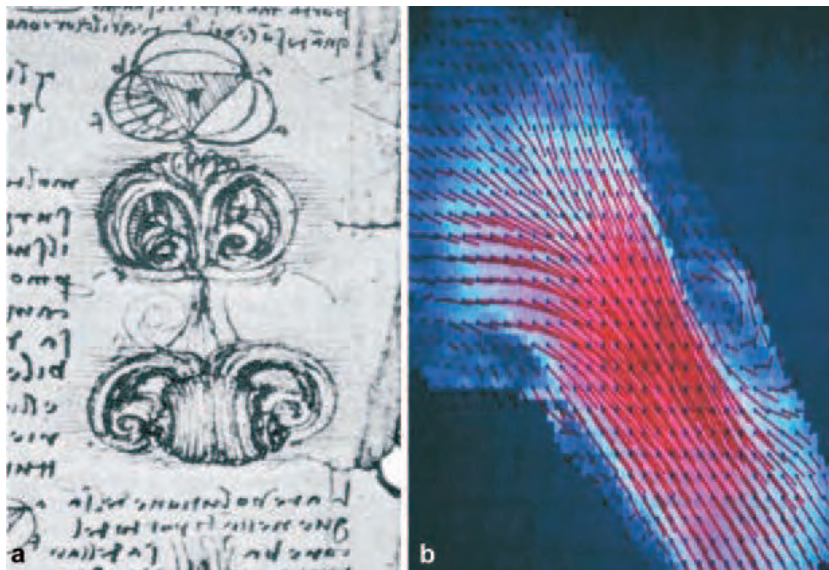


Figure 1.1: (a) Leonardo da Vinci's depiction of aortic valve vortices in the left heart. (b) Velocity vectors from Magnetic Resonance Imaging (MRI) in the left ventricular outflow tract, again showing vortices in the Sinus of Valsalva, after [Gharib et al. \(2002\)](#)

The objective for such visualisations is however, always the same: A deeper understanding of flow phenomena is essential for many scientific fields and helps to gain progress in technology. Thus, the applications of flow visualization and measurement are wide spread and can be found within a wide range of sizes, from micro-scale flows in biological (e.g. blood vessels, heart valves) and technical systems (e.g. micro-channel for mixing and fractioning purposes in chemistry) over macro and laboratory-

scale flows (e.g. convection cells, tab or jet flows, in-cylinder flows with and without combustion) to large-scale (e.g. pipe flows, wind tunnel flows, rivers) and very large-scale flows (e.g. ocean and atmosphere). Nearly all flows have in common a generally three-dimensional nature of the phenomena under investigation, calling for techniques capable to simultaneously record such flows in all dimensions with a high temporal and preferably also with a high spatial resolution. Since nowadays challenging problems in fluid dynamics concern typically non-stationary flows standing out by complex three-dimensional structures, the interest in suitable measurement systems is increasing.

1.1.2 Flow Diagnostics

In the nineteenth century our physical understanding of fluids (i.e. gaseous or liquid media in motion) has been improved with the introduction of the basic equations by Navier and Stokes and a new branch of the classical mechanical science, "fluid mechanics", was born. Typically, one distinguishes between compressible and incompressible fluids - both being described by the Navier-Stokes equation (cf. Appendix A.1) - which has led to some fields of further specialisations. Nowadays from these the most important are aerodynamics and hydrodynamics, respectively. They are the basis for many engineering fields as well as for fundamental research, tackling questions like the unsolved classical problem of turbulence. In either fields, quantitative measurements are used to determine one or more field-quantities given by the terms in the Navier-Stokes-equation. For a complete representation, however, a simultaneous measurement of the pressure, density and velocity field would be required in all three spatial dimensions, a yet unrealistic task (Raffel et al., 1998)!

Generally one can divide measurement techniques for flow diagnostics in intrusive and non-intrusive techniques. Examples for the first category are transducers to sense the pressure (PT) at a selected point in the flow or hot wire anemometry (HWA) to measure one or up to three components of the local flow velocity. As HWA is based on a temperature dependant change in the resistance of a very thin electrical wire, it enables a high temporal but restricted spatial resolution. Most of the "non-intrusive" techniques today are often based on optical principles, employing both white light and monochromatic laser light, but often need artificial markers added to the flow. These can be tracer particles to scatter light or some fluorescent dyes, even molecular tagging is used for these purposes.

While optical pressure measurements in flows, making use of the resulting change in the refractive index (e.g. Schlieren photography for visualisation of shock waves), are yet difficult to manage at low velocities, the measurement of the velocity field itself has undergone a considerable progress in the recent years and is generally termed "optical velocimetry".

Mostly benefiting from the new and rapid developments in laser, computing and digital video technology, fast whole field measurement techniques have been developed, capable to simultaneously measure at spatially separated points. A further classification for optical velocimetry can thus be based on the dimensional size of the data which

is covered by a certain technique (Hinsch, 1995). Beside the three spatial dimensions, commonly abbreviated with the letter D, the temporal dimension (T) and the three components (C) of the velocity vector can be used for this classification. The classical and now widely used method for optical velocity measurements in one plane, particle image velocimetry (PIV), is according to this scheme a 2D2C technique and with repetitive measurements using (high-speed) digital video imaging it gets time-resolved and is thus a t-2D2C technique.

The principle of PIV is explained only briefly here, since a couple of publications have already reviewed this technique in great detail from its development to more advanced systems, which are capable to measure three velocity components in several planes (quasi-3D3C) (Hinsch, 1993; Westerweel, 1993; Grant, 1994; Raffel et al., 1998). To measure the velocity distribution in one plane only a small part of the flow is illuminated by a light-sheet (expansion of a pulsed laser beam by one or more cylindrical lenses, see Figure 1.2).

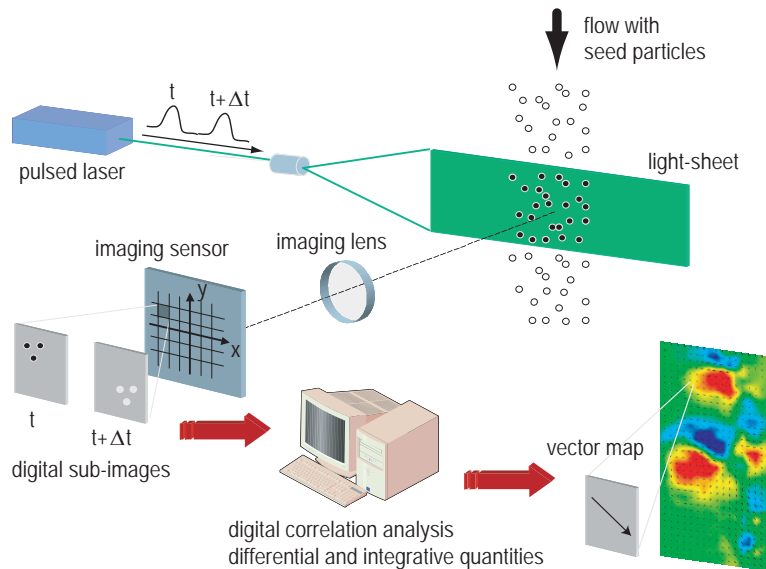


Figure 1.2: Principle of PIV: A light-sheet is formed from two successive laser pulses with a known delay by a set of cylindrical lenses and illuminates the flow seeded with small, mostly neutrally buoyant particles. A selected region from this flow is simultaneously imaged on a digital sensor and the resulting two frames are divided in equally spaced sub-images. Each pair of sub-images permits a single velocity measurement and is evaluated by correlation analysis.

With each laser pulse only tracer particles within this light-sheet are illuminated and their scattered light is imaged on a digital sensor. The recording of an image frame is typically synchronised with a single laser pulse, sometimes also two or more pulses are recorded within one frame. Knowing the temporal pulse separation, one can now measure the displacement of the particle images between the frames or from multiple exposures in one frame and calculate the local velocity. The displacement measurement is conventionally achieved by correlating small sub-images of the recording, which are equally spaced. The result is a regular grid of velocity vectors (vector map), each

presenting the mean velocity in the respective sub-image. Integrating or differentiating this vector map, other quantities like vorticity, rotation and net flow can be calculated.

The cross-correlation between two successive sub-images is preferred in contrast to the auto-correlation signal of a double exposed frame. This suffers from a directional ambiguity of the extracted displacement vector and a restricted dynamic range (i.e. existence of a lower displacement limit). Combining two views of the same light-sheet according to the stereoscopic principle, PIV can be extended to give also the third vector component of the velocity. Although the complexity of such a measurement system is increased, this method is nowadays a widely used and commercially available tool in flow diagnostics.

During the last years PIV has considerably increased its impact on aerodynamic engineering and mainly industrial wind-tunnel tests have benefited from the huge amount of velocity data, which could be obtained by routinely running the different PIV systems in European Co-operations Projects. Two rather big research projects have been consequently devoted to the tasks (Stanislas et al., 2000, 2004), also including research on developments towards volumetric measurements, part of which is also reported in this thesis. The enormous economical importance of wind-tunnel tests prior to the production of airplanes is obvious when the considerable reductions obtained in recent years on fuel-needs and acoustic noise are considered. Other frequent applications for PIV in wind-tunnels are mainly in the automotive industry, while other large scale measurements are also conducted in naval research and household appliances. These, as well as various other applications, have also found their way into a european thematic network on PIV (Kompenhans, 2003), frequently exchanging new developments and contributing to the success of PIV.

1.1.3 Role of Particle Holography

It was realised fairly early that particle holography is the only practical solution to extend optical velocity measurements to the third spatial dimension (Trollinger et al., 1968; Fourney et al., 1969; Trollinger et al., 1968), provided that there is not enough time to allow a scanning method (e.g. in quasi-stationary flows). This is generally the case for complex flows with velocities in the order of some meters per second, which thus require simultaneous measurements. Before holographic velocimetry came into focus the basic research on holographic imaging was carried out on microscopic particles to obtain information about their size, shape and position (Thompson, 1964; Thompson and Ward, 1966). The methodology of these measurements was directly adapted from the first holographic experiments (cf. Section 2.1) and it was found that with small and sparsely distributed objects (particles) the set-up for velocimetry combined simplicity and precision. A single laser beam could be used to illuminate the particles while it also served as the reference beam, which is needed to record the phase information of the light diffracted by the particles. Later on, this recording geometry was termed "in-line holography" in contrast to the off-axis holography using a separated reference beam, which is nowadays the standard method for holographic particle image velocimetry (cf. Section 2.1.2).

1.1.4 Holographic Particle Image Velocimetry

Still considered an advanced technique, Holographic Particle Image Velocimetry (HPIV) has now reached its twelfth anniversary. Barnhart et al. (1994) presented the first practical demonstration of a fully three-dimensional velocity measurement by particle image correlation. During the last decade much effort was taken by only a few groups in the world to develop and demonstrate measurement systems using holographic recordings. Huge storage capacity is needed for the enormous amount of data generated from the light scattered from a densely seeded particle field. Some of the details of these measurement systems are reviewed during the course of this thesis.

More recently a workshop held at the University of Loughborough in England, UK (Coupland, 2003; Herrmann and Hinsch, 2004a) showed the unbroken interest in this field and revealed the status of the current research. There are two major streams which will soon merge when further progress is made in the performance of digital sensors and computing power.

On the one hand, the classical approach using highly resolving photographic emulsions and wet-chemical processing for the development of holograms is still very attractive to further push the limits in size and resolution of the measurement volume. Also more and more knowledge is collected about the complex behaviour of light fields diffracted from densely-seeded volumetric particle fields. This helps to increase the accuracy of the measurement process by refining the evaluation techniques for holographic images. On the other hand, a fully digitized recording and reconstruction process is considered to be necessary for the breakthrough of HPIV to become a generally accepted and widely used technique for three-dimensional velocity measurements. Thus, many researchers are concerned with the development of numerical algorithms to determine the intensity distribution in one plane of the recorded volume from its digital hologram. This method however, is presently limited by the size and the resolution of the available imaging sensors which only permit the recording of a few thousand particles within a substantially smaller volume than with current photosensitive recording media.

1.2 Main Contributions of this Work

In order to provide as many information as possible from a large and densely seeded particle field carried by either an air or water flow, the work presented in this thesis is largely devoted to push barriers of the classical HPIV towards those limits given by the highly resolving recording materials. To this end, a previously introduced short-coherence recording technique (Light-in-Flight Holography, or short LiFH) is adapted for the reconstruction of the real particle images. This technique suppresses the intrinsic out-of-focus noise, while reconstructing only slices of the full three dimensional field. By selecting the slice in focus, the whole field can be scanned successively by means of a CCD or CMOS sensor. For the recording of such large fields of tiny tracer particles on holographic film, ruby lasers have typically been utilised in the past. Reconstructions from such holograms with a continuous wave (cw) source at slightly dif-

ferent wavelength often suffer from aberrations. To overcome this, a specially designed Nd:YAG laser system is applied for the LiFH recording of air flows inside a large wind tunnel. Due to a highly stable cw counterpart of the recording laser, a completely separated and automated reconstruction setup could be developed. With this, the image information from two successively recorded particle fields can be extracted. The reconstructed intensity distribution is digitized plane by plane and for the evaluation of the intensity images, the correlation method described in Section 1.1.2 is extended to the third dimension. A direct comparison of the classical HPIV and the LiFH-PIV approach reveals the advantages of the latter by evaluating the signal-to-noise ratio in reconstructed particle images.

1.3 Outline of the Contents

The Sections above introduce the context and the aim of this work, which review that Holographic Particle Image Velocimetry (HPIV) is identified as the only practical technique to obtain a full three-dimensional representation of velocities with high resolution from large and deep flow fields. Several improvements to this technique are subject of this thesis, wherein noise suppression and the gain in image quality play a key role.

After reviewing the basic properties of holography and discussing typical recording geometries and materials as well as the needs for a precise reconstruction, Chapter 2 focuses on the image properties of small tracer particles. Since they carry the whole information on velocities in HPIV and mainly determine the resulting holographic image quality, knowledge of their scattering behaviour helps to interpret the reconstructed particle images.

When dense particle fields are recorded, the intermodulation or out-of-focus noise (which is inherent to the holographic method) severely affects the quality of the particle images. Chapter 3 addresses this well-known topic but also shows that another source of noise, the emulsion grain noise has an impact on the image quality. After defining a signal-to-noise ratio for reconstructed particle images, a theory based on the properties of the recording materials and speckle is reviewed and extended, as well as experimentally tested and proven.

Chapter 4 introduces Light-in-flight Holography (LiFH) and discusses its requirements, before showing an adaption of the method for noise suppression in holographic particle image velocimetry. Some results obtained with the virtual image reconstruction using LiFH are reviewed to mark the state-of-the-art at the beginning of the work for this thesis. Finally, the real image reconstruction is used to demonstrate the gain in particle image quality obtained by LiFH.

To overcome the disadvantages in particle holography, when using a ruby laser for the recording, a dedicated Nd:YAG laser system was developed. Chapter 5 describes the details of the double-cavity laser system and focuses on the effort undertaken to combine the two beams with crossed polarisations. The new laser system permits comparative studies in HPIV research work by allowing for either long or short coherence pulsed radiation.

Based on the aforementioned laser system, a recording set-up with different reference beam options is developed in Chapter 6. The set-up is build in a lab with a small test wind-tunnel, but can also be adapted for an application inside a large wind-tunnel. Reconstruction and scanning of the real image is done completely separated from the recording set-up, an automated system for this task ist presented.

Chapter 7 first reviews three basically different methods to extract the velocity information from reconstructed holographic particle images. These methods are closely related to the set-ups used by different research groups, which therefore are dicussed together with the evaluation methods. For the experiments described in this thesis, an extension of the intensity correlation to three dimensions is used to evaluate the scanned and digitised real particle images. This evaluation method is introduced mathematically and realised in implementations differing in the consumption of computing power.

A first application of the developed LiFH-PIV method at a large industrial wind tunnel is described in Chapter 8, revealing its ability to record particle images with sufficient signal-to-noise ratio even through densely seeded air (fog or turbid media like) inside and surrounding the open two meter wide and one meter deep test section.

The gain in the signal-to-noise ratio of reconstructed particle images due to the LiFH method is analysed in detail in Chapter 9 by comparing long and short coherence recordings. Basic experiments are conducted with model particle fields and controlled particle densities in a water flows. Reconstructed and digitised images from varying aperture sizes are then subjected to different methods and algorithms to obtain a measure of the signal-to-noise ratio for either a single particle or the whole image.

Finally, Chapter 10 summarises and concludes the presented work. In an extended outlook a revised set-up, subject of ongoing research work, is briefly introduced by reporting about its advantages.

2 Holographic Imaging of three-dimensional Particle Distributions

As stated already in Section 1.1.3 holography is considered the only practical but yet not fully exploited technique to extend particle velocimetry for non-stationary flows to the third dimension. In this chapter the requirements to successfully record and analyse spatial particle distributions are explained. Beginning with the holographic principle and some basic considerations for high quality recordings in Section 2.1.1, the recording schemes and materials for particle holography are mentioned in the Sections 2.1.2 and 2.1.3, respectively, the requirements for precise reconstructions are discussed in Section 2.1.4. The last two Sections are devoted to a deeper understanding of the final measurement data, namely the reconstructed and digitised particle images. The ideal particle image properties and the influence of the holographic process are introduced in Section 2.2 before the influence of light scattering by small tracer particles is discussed in Section 2.3.1. The latter is yet not fully understood, which is due to the complex nature of the coherent superposition of light scattered by many particles and the holographic imaging process involved, this problematic is discussed in more detail in Chapter 3.

2.1 Holography

To obtain a three-dimensional image of an object the whole information contained in a diffracted light field, namely the spatial distribution of amplitudes and phases needs to be recorded. A principle to accomplish this was first presented by Gabor (1948), who described a method based on the interference of two wavefronts to obtain a replica of the original object wave. Initially intended for use in electron microscopy, by this time he was only able to demonstrate this principle with visible light. It took about another 14 years, before this method came into focus for practical use, however, it was mainly applied for the recording of visible light distributions. Right after invention of the laser first experiments (Leith and Upatnieks, 1962) have demonstrated the principle of reconstructed wavefronts and the term holography (from the greek words $\sigma\lambda\omicron\varsigma$ for whole and $\gamma\rho\alpha\varphi\iota\alpha$ for image) was found to describe this principle most suitably.

2.1.1 Recording and Reconstruction of a Hologram

Consider the situation in Figure 2.1 where coherent light scattered by tiny particles forms a resulting wavefront O and interferes with a (planar) reference wave R . If we denote O_i the individual scattering wavefronts, each given with amplitude and phase,

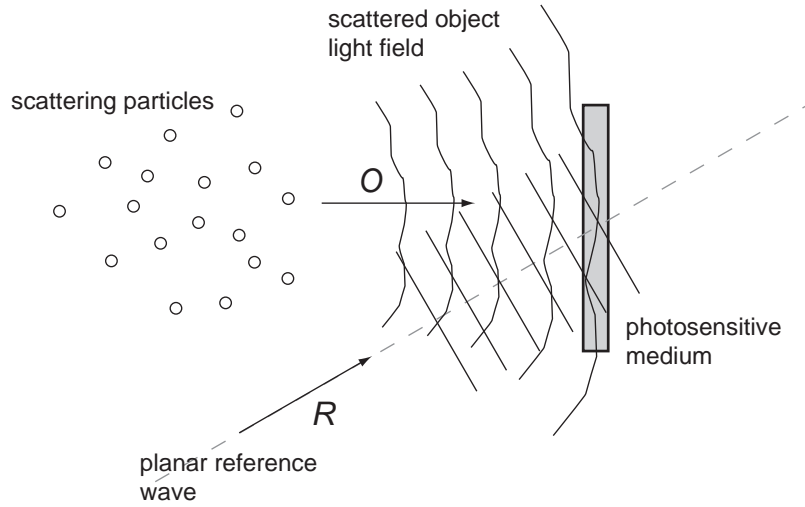


Figure 2.1: The forming of a hologram is achieved by superimposing two light fields incident on a photosensitive medium. Most likely the reference wave R is a planar wave which interferes with a more complicated object light field O , in the case of particles typically represented as the sum of the individually scattered light fields.

the object wave can be written as the sum over all particles $O = \sum O_i$ and the resulting intensity distribution in the plane of the recording medium is given by:

$$I_T = |R + O|^2 = |R|^2 + RO^* + R^*O + |O|^2, \quad (2.1)$$

where $|R|^2$ and $|O|^2$ denote the reference and object wave intensity, respectively. The resulting interference pattern is exposed onto the photosensitive emulsion, usually coated on either a triacetat (TAC) film carrier or a glass plate. After a wet chemical processing (development and fixation) the emulsion is cleaned from remaining chemicals and dried to yield the hologram. The recorded pattern now represents a permanent absorption grating of sufficiently high frequencies to diffract light at a wavelength similar or equal to the recording wavelength. Provided that a proper total exposure $E = \tau I_T$ is achieved by either adjusting the reference beam intensity $|R|^2$ or the exposure time τ a linear relation between E and the amplitude transmittance $t = t_0 - t_E = t_0 - kI_T$ can be assumed. Taking into account only the terms including the exposure-dependent transmittance t_E the following product describes the light diffracted by the grating when the hologram is illuminated with the reference wave R :

$$I_R = tR = k|R|^2R + kRRO^* + kR^*RO + k|O|^2R, \quad (2.2)$$

where k is a constant and all terms linked to the transmittance t_0 of the unexposed plate have been neglected, since they show up only by absorption.

In (2.2) the third term on the right side is of primary interest here, it represents a replica proportional to the object wave O scaled by the reference wave intensity $|R|^2 = R^*R$ and can be observed through the hologram as the so-called virtual image (cf. Figure 2.2). Provided a perfect match of the reference wave is obtained (cf. condition for

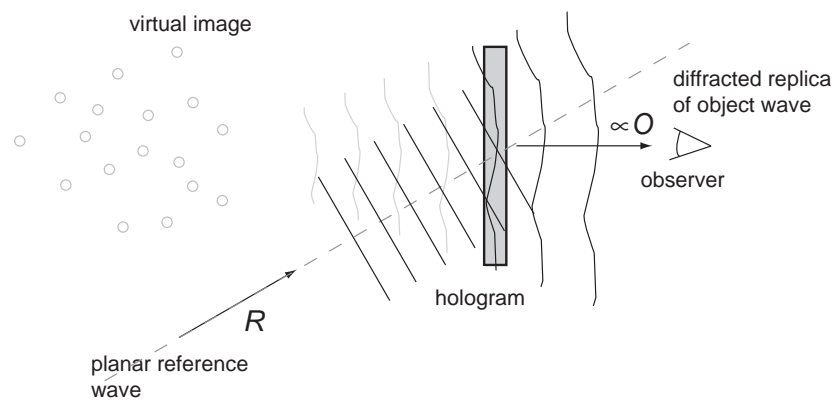


Figure 2.2: After development and fixation of the photographic emulsion the recorded intensity distribution serves as an absorption grating which diffracts light incident onto the hologram. When the original reference wave R is used to illuminate the repositioned hologram the diffracted light field resembles the original object wavefront. An observer - or a camera with a lens - behind the hologram can view a non-real, the so-called virtual image.

precision replay of holograms in Section 2.1.4) only the brightness of the image is subject to alterations and a truly three-dimensional image is generated, which could for instance be imaged by a CCD camera with a mounted lens to view the object space through the hologram.

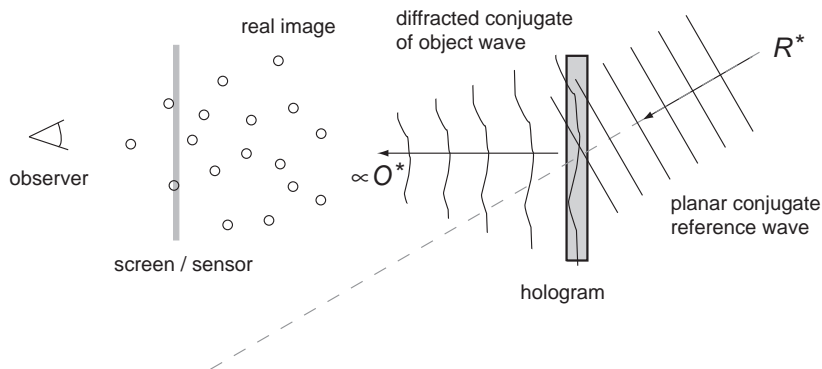


Figure 2.3: If the hologram is illuminated by a wave conjugate R^* of the initial reference wave the light diffracted by the grating produces a wave conjugate O^* of the object light field. Thus an intensity distribution in the object space can be observed which forms the so-called real image.

Considering small particles for metrology purposes the so-called "real image" has always been of special interest, since the positions, sizes as well as shapes of tiny reconstructed images could be directly imaged onto a screen or sensor (photographic film or CCD target). Such a real image is obtained when the hologram is illuminated with the wave conjugate R^* of the initial reference wave (cf. Figure 2.3). A wave is conjugate to another when in any plane its complex amplitude is a complex conjugate of the other and all its rays are reversed in direction with respect to the other's (Collier et al., 1971).

Thus all waves are travelling in the opposite direction and the diffracted light is then expressed by:

$$I_{R^*} = tR^* = k|R|^2R^* + kRR^*O^* + kR^*R^*O + k|O|^2R^*, \quad (2.3)$$

again omitting the terms describing the transmittance of the unexposed plate. In (2.3) the second term on the right represents now the object information as a proportional wave conjugate, scaled only in brightness by the reference beam intensity $|R|^2 = R^*R$. As long as the object is opaque and still in place, the light field is at any point a replica of the initial complex amplitude distribution in space (provided that scattered light can be neglected), except for the now inverted sign denominating the direction of the light wave. In the case of a planar reference wave incident horizontally, the appropriate wave conjugate can be obtained from the original reference wave when the hologram is flipped over in its vertical axis, which however, also turns around the object space to a position opposite to that of the object itself.

To successfully record a hologram the existence of a high contrast interference pattern is of primary concern. Its modulation depth or contrast is quantitatively measured by the fringe visibility V_f :

$$V_f = \frac{I_{max} - I_{min}}{I_{max} + I_{min}}, \quad (2.4)$$

where I_{max} and I_{min} denote the maximum and minimum intensities of the interference fringes obtained from the superposition of reference and object wavefront. In the representation of scalar waves their complex amplitudes are given as $\mathbf{R} = R \exp(i\varphi_R)$ and $\mathbf{O} = O \exp(i\varphi_O)$, respectively, and the resulting intensity I can be written as:

$$I = |R|^2 + |O|^2 + 2R \cdot O \cos(\varphi_O - \varphi_R). \quad (2.5)$$

Taking into account the polarisation and the coherence of the interfering beams it can be shown (Collier et al., 1971) that the fringe visibility depends on the beam ratio $r_b = (r/o)^2$, the angle Ω between the directions of the polarisation and the degree of temporal coherence $|\mu_T(\Delta t)|$, when spatial coherence is guaranteed over the entire beam profile used to illuminate the holographic material. It thus follows:

$$V_f = \frac{2|\mu_T(\Delta t)|\sqrt{r_b} \cos \Omega}{r_b + 1}. \quad (2.6)$$

From this formulation it is clear that the fringe visibility V_f has a maximum value of unity when $|\mu_T(\Delta t)|$, r_b and $\cos \Omega$ are each unity. Thus the beam-lengths of the reference and object beams are usually adjusted to be nearly identical, in order to maintain a difference in the travelling time δt between both beams small enough to fulfil the condition

$$|\mu_T(\Delta t)| > |\mu_T(t_H)| = 1/\sqrt{(2)} \approx 0.71. \quad (2.7)$$

The coherence time t_H depends on the longitudinal mode structure of the laser and is infinite for a single-frequency operation of a continuous laser or equals the pulse length when using pulsed lasers. Details on the degree of coherence for typical lasers used in particle holography are given in Section 4.1.3 and a discussion on beam-path conditions with respect to the coherence time t_H is given in Section 4.1.4. Furthermore both beams should be s-polarised with respect to the plane of incidence on the holographic material. In this way, any angular separation of the beams (refer to Figure 2.5) becomes possible without loss of fringe visibility. The beam ratio r_b can be adjusted to yield a value of unity, but generally $r_b > 1$ is chosen to maintain linearity in the recording, which in turn is a prerequisite for a high diffraction efficiency, i.e. bright reconstructed images (cf. Section 2.1.3).

2.1.2 Recording Geometries

In the first days of Holographic Velocimetry (HV) the predominant recording scheme for particle displacement measurements was the in-line holography due to its simplicity and the fundamental knowledge about properties of the method from earlier particle analysis experiments (Meng and Hussain, 1991). Figure 2.4 shows an in-line setup, in which the reference beam is also used to illuminate the particles and interference takes place between the scattered and transmitted light fields. Although such a setup has the advantage of considerably stronger signals from the particles (cf. forward scattering in Section 2.3.1) this geometry is only suitable for the recording of sparsely seeded particle fields, which in turn restricts the spatial resolution drastically. An increased background noise visible as a strong granular modulation (speckle pattern) is due to the overlapping real and virtual image, as well as the additional superposition of the reference beam (dc component) (Meng et al., 1993). At higher particle concentrations the detection of particle images is prevented, since the bright images tend to hide in the strong speckle noise which consists of a few very bright spots, too. Contrary to a planar (2D) technique called Laser Speckle Velocimetry (LSV), the information contained in the speckle pattern cannot be used to decode the displacement from an in-line HV setup. LSV uses speckle information from a single, well defined object plane (light-sheet illumination like in PIV) to evaluate the displacement between two successive recordings, whereas in HV the speckle information represents generally an integrated quantity over the entire depth of the illuminated field.

Another more promising and now widely used recording geometry is the off-axis configuration, where the directions of incidence of the reference and object light form an angle. This leads to higher spatial frequencies of the interference pattern to be recorded and thus puts higher demands on the resolving power of the recording material (refer to Section 2.1.3). A great advantage is the separation of the reference beam and the reconstructed image (Leith and Upatnieks, 1962), greatly relaxing the problem of speckle noise. Furthermore, an additional reference beam can be used to record a second hologram on the same area of the photosensitive emulsion. Using either beam for the reconstruction the holographic images can be reconstructed separately and thus a displacement measurement from two successively recorded particle distributions becomes feasible (Meng and Hussain, 1993; Adrian et al., 1993; Cha et al., 1993).

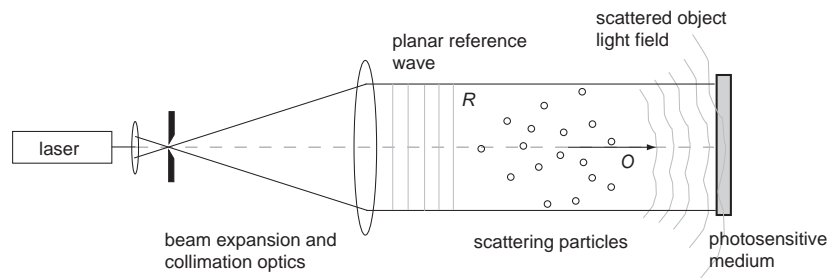


Figure 2.4: Setup to record an in-line hologram of sparsely seeded flow volume. The reference beam (plane wave) serves also for the illumination of the tracer particles. Scattered light interferes with the directly transmitted light and forms the hologram on a photosensitive medium.

Figure 2.5 shows a basic configuration for such a double-exposure recording. Due to the angle-selective diffraction process the recorded images can be reconstructed separately by illuminating the two superimposed holograms with either reference beam. Another degree of freedom is obtained by the scattering behaviour of small particles (cf. Section 2.3.1), which permits to illuminate the particles from nearly any direction as long as a sufficient exposure is achieved and the illuminating beam does not hit the photosensitive medium directly. All these advantages, however, require an increased complexity of the recording and reconstruction system.

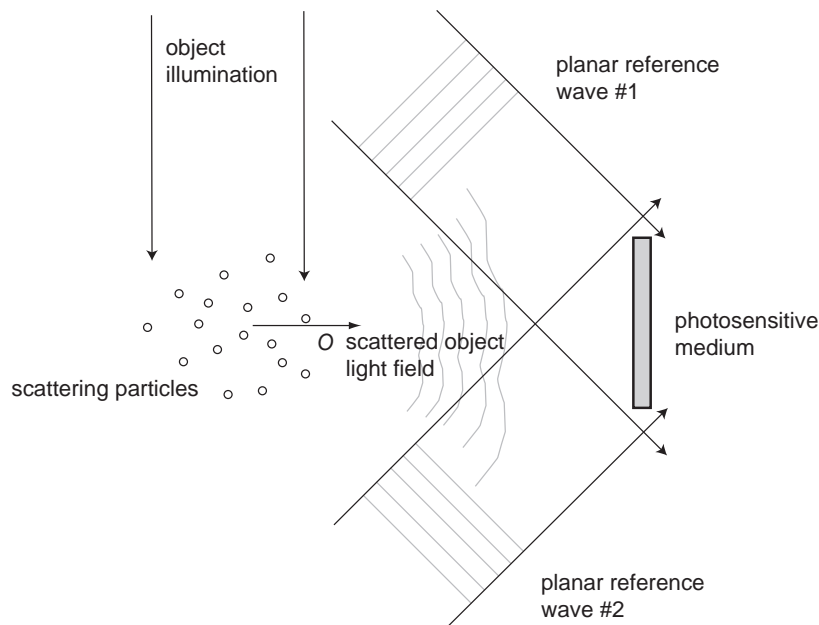


Figure 2.5: Setup to record two superimposed off-axis holograms on a single holographic plate.

2.1.3 Recording Materials

Although there is a great variety of recording materials available for holography, only a few are frequently used for particle diagnostics. Among the most important deciding factors for or against a specific material are the sensitivity (often called photographic speed) and the resolution, as well as the spectral response, the recording linearity, the diffraction efficiency and the handling (ease-of-use) of the material.

Silver-halide emulsions spin-coated on glass substrates or triacetat carriers have been the first materials used for holography already by Gabor (1949, 1971). Their sensitivity is rather high as these materials were initially developed for photographic purposes. Today, special holographic emulsions are available, which have been tailored to meet the requirements for (pulsed) laser light illumination. These also offer a significantly increased resolution, but with a loss of sensitivity compared to ordinary photographic emulsions. A major disadvantage are the still cumbersome wet-chemical processing steps for their development and fixation. Nevertheless, silver-halide emulsions are the most common recording materials for many applications of holography and so they are for particle field holography. Consequently, the majority of knowledge about the recording process has been gathered using these emulsions.

Before some alternative materials are discussed the basic properties of silver-halide emulsions are introduced. Thick recording media, such as photorefractive crystals, are beyond the scope of this thesis and the following theoretical description is limited to thin holographic materials only, which are used to record so-called "plane holograms". Furthermore the discussion is also restricted to transmission holograms of the absorption type unless otherwise stated. These holograms act like a diffraction grating with a varying amplitude transmittance as shown above in Figures 2.2 and 2.3.

The resolution of a holographic emulsion (see Appendix A.2 for information on the materials used for the present studies) is usually given in cycles or lines per millimetre and is sometimes also called resolving power. The resolution necessary for a successful recording is given by the smallest fringe spacing d in the hologram plane, defined as the corresponding spatial frequency:

$$\nu_0 = 1/d. \quad (2.8)$$

Taking into account the largest angle 2Θ separating the reference beam and the object beam at the holographic plate, the fringe spacing d can be calculated from Bragg's law (i.e. interference of two plane waves):

$$d = \frac{\lambda}{2 \sin \Theta}, \quad (2.9)$$

where λ is the recording wavelength. The fringe pattern is exposed into silver-halide compounds which are dispersed as extremely fine grains in gelatine. Additional sensitising agents determine the wavelength at which the material has its maximum sensitivity. During the development process the exposed grains are converted to metallic silver (see Appendix A.3 for a detailed description of the process) and thus absorb light and reduce the transmittance $t_A = t \exp(i\phi)$ locally.

According to Collier et al. (1971) the intensity of the reconstructed wave at the hologram is:

$$I_V = \frac{1}{4} \left[r \frac{dt_A}{dE} E_0 V \right]^2, \quad (2.10)$$

where the total exposure $E = E_0 + E_1(x, y)$ is split into an unmodulated part (index 0) and a modulated part depending on position on the holographic plate (index 1). Since $I_V \propto V^2$ and $V \propto |\mu_T(\Delta T)|$ (refer to Equations (2.6) and (2.7)) the choice of $|\mu_T(t_H)| = 1/\sqrt{2}$ ensures that the intensity I_V remains within 50 % of the value it would have for perfect coherence.

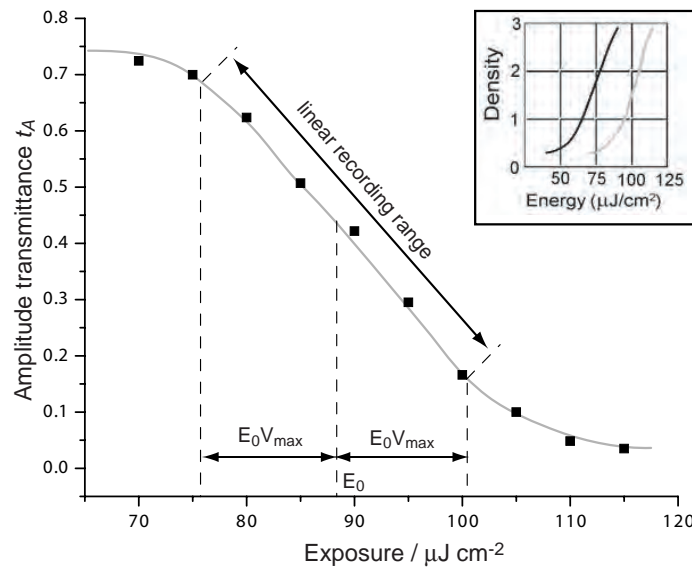


Figure 2.6: Amplitude transmittance t_A versus exposure E (t_A - E curve) derived from manufacturers brochure for Slavich PFG-01 emulsion, the inset shows the original information (Slavich, 2001).

A linear wavefront recording is obtained when $dt_A/dE = \text{const}$. For an absorption type hologram the alteration of the phase should be $d\phi/dE = 0$ and thus

$$\frac{dt_A}{dE} = \frac{dt}{dE} \exp(i\phi). \quad (2.11)$$

The region where $dt/dE = \text{const}$ can be found for a given holographic material experimentally by measuring the intensity transmittance t_I as a function of the exposure and plotting $t_A = \sqrt{t_I}$ over E . For many photographic and holographic films the so-called Hurter-Drieffield (H&D) curve, relating the optical density $D = -\log_{10} t_I$ to the exposure E , is given by the manufacturer. Figure 2.6 shows an example of a t_A - E curve derived from an H&D curve of the Slavich PFG-01 emulsion.

A given t_A - E curve (derived or experimentally obtained) allows an estimate of the maximum fringe pattern contrast V_{\max} which can be obtained within a linear recording

at an optimum average exposure E_0 . The corresponding exposure range is then given by:

$$E_0(1 - V_{\max}) < E < E_0(1 + V_{\max}). \quad (2.12)$$

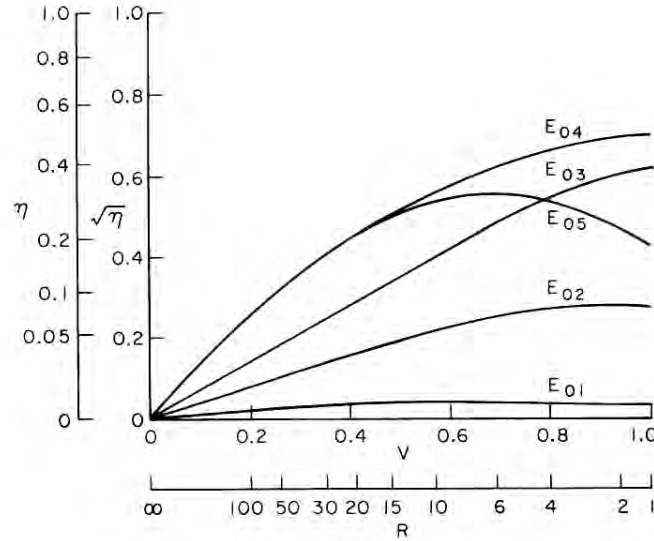


Figure 2.7: Square root of diffraction efficiency $\sqrt{\eta}$ versus fringe pattern contrast V (linear scales) for a real recording material at increasing mean exposures E_{0n} , after (Collier et al., 1971). For comparison the non-linear scales of η and the beam ratio (here $R = r_b$) are given.

More informative, but experimentally not easy to obtain, is the material's diffraction efficiency $\eta = I_V/r^2$, namely the fraction of light diffracted by a given grating (fringe pattern) with contrast V recorded in a range of feasible mean exposures E_0 . For this, numerous holograms from two plane waves with a fixed inter-beam angle 2Θ need to be recorded with a varying beam ratio r_b and mean exposure E_0 . During reconstruction the fraction of light I_V in the object replica beam needs to be measured for all holograms, which of course need to be processed with a comparable chemical treatment (constant temperature and original developer). A typical result for a real recording material is shown in Figure 2.7, where the square root of the efficiency $\sqrt{\eta}$ is plotted versus the fringe pattern contrast V .

Although this result is obtained from phase type holograms (for HPIV typically absorption type holograms are preferred), Figure 2.7 can be used to discuss some properties of real recording media. A representation like this allows (a) to choose a good linear recording range (straight-line portions of $\sqrt{\eta} - V$ curves) by adjusting the mean exposure E_0 of the recording for a given beam ratio r_b , (b) to express the maximum achievable diffraction efficiency, (c) to choose the best compromise between linearity and diffraction efficiency and (d) to give a measure of the material's sensitivity S

(relative figure-of-merit) by computing:

$$S = \frac{\sqrt{\eta}}{VE_0}, \quad (2.13)$$

as the largest of the slopes of the straight-line portions in Figure 2.7 (i.e. first half of the curves for E_{04} and E_{05}). It should be noted, however, that the theoretical limit for the best diffraction efficiency from plane absorption holograms is only 6.25%. The low diffraction efficiency for absorption type transmission holograms is due to the fact that only $1/4$ of the incident light amplitude is diffracted into the $+1$ or the -1 diffraction order, resulting in $1/4^2 = 1/16 = 0.0625$ for the intensity. For real recording materials η is typically 4% at the best, since the above value assumes linearity over the entire exposure range.

Under aspects of diffraction efficiency, phase type holograms should be preferred for particle holography. But, the production of phase type holograms requires a significantly higher exposure to reach average optical densities of $D = 2$ and thus the working point is shifted close to a non-linear region of the recording. Another and more severe disadvantage of phase type holograms is a deterioration of the microscopic image due to a shrinkage of the emulsion from the bleaching procedure. Chemical bleaching is a process where developed silver grains are interchanged with transparent silver salt, exhibiting a refractive index greater than the surrounding gelatine (cf. Appendix A.3).

The silver-halide dispersed in gelatine has a finite grain size of some ten to several hundred nanometre. In absorption type holograms the exposed grains turn into silver during development and get considerably larger. Thus, they become a significant source of noise due to light scattered into the direction of the holographic image during reconstruction (see also Section 3.1.1). Nevertheless, absorption type holograms recorded on silver-halide are a good solution for HPIV, where a precision replay down to microscopic scales is needed. Furthermore, they can be stored after proper processing steps for a very long time without suffering from alterations of the emulsion (e.g. hydration).

Also other recording materials have been considered for use in HPIV experiments. Closely related to silver-halide films, at least concerning the need for wet-chemical processing steps, are dichromated gelatine films. The recording process is also known as hardening or tanning caused by the gelatin molecules which tend to cross link when exposed to ultraviolet or blue light. The processing involves a dehydration step of the gelatine, causing it to shrink after it was first swollen when washing out the dichromat with water. The shrinkage can cause crests which is one of the major disadvantages. Furthermore holograms recorded on dichromated gelatin are naturally phase type holograms with the above mentioned drawbacks affecting the microscopic-scale image and the emulsions itself do not remain stable for a longer period unless covered and prevented from absorption of water. But they provide optical properties close to the ideal behaviour of holograms with little light absorption and very low scattering and offer diffraction efficiencies close to the theoretical limit of 100%.

Holographers have tested many alternative materials to avoid the time delay and effort in processing standard photographic film, all of which still show at least major dis-

advantages in resolution, sensitivity or handling. Among those promising more ease during the processing are photoconductor-thermoplastics, other photochromic materials and photopolymers. The thermoplastic materials are usually falling short on resolution and photochromic materials are generally less sensitive. Photopolymers might be a good alternative but those materials, which perform well, are restricted in their commercial availability since they are also used for security holograms on credit cards and banknotes.

More recently a genetically modified version of the photochromic protein bacteriorhodopsin (BR) has been introduced to HPIV measurements (Barnhart et al., 2002, 2004; Chan et al., 2004). It offers perfect resolution and sufficient optical sensitivity to object light. Furthermore, also polarisation dependent recordings can be made. The disadvantages are a considerable loss in overall sensitivity compared to silver-halide emulsions and a limited storage time of the hologram in the range of minutes to some hours depending on the ambient temperature. The first can be compensated for by less attenuated reference beams (using pulsed lasers, typically the reflection from a glass-plate is sufficient to expose the holographic materials). The later is a serious problem when the reconstructed particle image field is scanned in the intensity domain for later correlation analysis (i.e. time consuming scanning of the real image). Instead one can imagine sampling the frequency domain behind a lens positioned at given points in space. An alternative proposed by the authors might be the scanning of the recorded interference pattern for a digital processing of the holographic information. This task would require enormous computer power as long as the full resolution (comparable to silver-halide emulsions) is used. Even today's largest imaging sensors used for digital holography would fall short compared to size and resolution achievable with a scanned BR hologram, consequently an optical magnification to match the recorded fringe pattern to typical pixel-sizes and a precision scanning stage is required to sample the whole hologram. Assuming a tenth of the fringe spacing according to (2.9) for a typical positioning accuracy of the needed translation stages, this would be already some ten nanometres.

Fully digital holography does not use any recording material but an imaging sensor (CCD or CMOS). Currently, their limited resolution permits only measurements with particle-concentrations considerably lower than those used for typical HPIV experiments and makes inline setups favourable to keep the fringe spacing high. Nevertheless, many impressive results have been achieved and numerous researchers are actively working to enhance its usability and a transition towards fully digital HPIV is expected in the next years (Meng et al., 2004).

2.1.4 Precision Replay of Holograms

Holographic velocimetry requires the precise determination of a displacement between two images of a single particle or a group of tracer particles within a volume filled with many other particles and at various locations (as many as possible) within this volume. Such a displacement is generally extracted from a double or two single exposures by reconstructing the image from the corresponding hologram and measuring the distance

between particle clusters in chosen sub-areas or single particles in either image. Errors in such a measurement can arise from a variety of sources. Some of them are also affecting the appearance of the particle image itself (i.e. aberrations and influence of background noise) and are often inherent to the holographic imaging process. These will be treated in Sections 2.2.2, 2.3.2 and 3.1, while errors due to the digitisation and the evaluation procedure are addressed in Chapter 7. Among the error-sources directly related to the optical replay of holograms the most important are:

- a. misaligned holograms during reconstruction (e.g. translation and rotations)
- b. misaligned reference beams (including imperfect collimation)
- c. changes in the recording medium (e.g. emulsion shrinkage and distortion)
- d. different wavelengths between recording and reconstruction
- e. refraction at interfaces between glass, air and water
- f. changes in the laser beams (e.g. phase variations across the profile of pulsed lasers or their pointing stability)

The above mentioned error-sources are picked up again in the following Sections, which are reviewing those parts of literature treating the relevant aspects to maintain a good holographic replay.

2.1.4.1 Hologram and Beam Positioning

After repositioning the developed hologram, any deviation with respect to the reference beam used for the recording will cause a deviation of the image itself. Typically, HPIV only needs relative displacement measurements. Pure translations of the hologram are thus considered as non-critical deviations, not only for double exposures but also for two single exposures as long as both holograms are translated by the same amount (i.e. recorded on a single medium). They only cause the image to translate by the same amount. Rotations, however, which are always present in practice when a hologram is replaced, are more severe and should thus be minimised. A detailed theoretical and experimental investigation by Sholes and Farrell (2000) shows that in general the repositioning, even with specialised plate holders, does not allow to reproduce the angle simultaneously for both of two plane wave reference beams within the required precision. For a typical HPIV dual-beam geometry, an object-to-hologram distance of $z_0 = 250$ mm and a minimal accepted displacement error of $1 \mu\text{m}$ the required beam-pointing accuracy of $2 \mu\text{rad}$ is unattainable in view of the repeated laboratory results of typically 1 mrad. This illustrates the need for manual corrections before the read-out process, which is typically achieved with calibration procedures like the recording of a reference hologram.

A point worthwhile to mention is the shot-to-shot repeatability of laser beam characteristics when (high energy) pulsed lasers are used. Typically, these lasers exhibit

a noticeable jitter in the beam direction, commonly addressed as the beam-pointing stability. Furthermore the divergence of the laser beam is influenced by the active medium, which is thermally in a non-equilibrium state with rapid changes of its birefringence. These effects are discussed in detail in Section 5.2.3. For the replay of holograms, however, one should keep in mind that even with a calibration-hologram the final displacement-measurements may differ significantly from hologram to hologram. The positioning error caused by the beam-pointing depends on the actual geometry, the laser type and energy, as well as on the optics used to form the reference beam. It is thus not easily determined, unless a calibration for every recorded hologram is realized. For this an interferometric approach is proposed. Along with the particle images a static spherical wavefront, serving as an artificial marker is recorded twice. By simultaneously reconstructing both spherical wavefronts their resulting interference can be observed by an imaging sensor and the type, orientation and spacing of the fringes indicate the relative displacement between the two holographic images (in the meantime, first investigations to incorporate such an interferometric calibration have been conducted (Hülsmann, 2005)).

2.1.4.2 Beam Collimation Requirements

The phase-conjugate beam for the reconstruction of the real image from a transmission hologram is conveniently achieved by using the same planar wave as for the recording, and by rotating the hologram over its vertical axis as illustrated in Figure 2.8. Only in this case there is no need to produce a divergent reconstructing beam corresponding to the convergent recording wave (or vice versa) with a wavefront radius r_w of to the same absolute value $|r_w|$. Doing so would require large aperture optics to minimise aberrations from lenses and a method to adjust the optics with a very high precision. A perfectly planar wave, on the other hand, is never achieved in practice, but tools are available to guide the experimenter in adjusting collimation optics of the required accuracy.

With the aid of a shearing interferometer (Murty, 1964; Rimmer, 1974; Mantravadi, 1992) the wavefront curvature close to the collimated case can be analysed and any divergence or convergence can be found from the orientation of a fringe pattern. Such an interferometer basically consists of a wedged, uncoated optical flat, introduced at 45° with respect to the beam under investigation (Figure 2.9). The reflections from the front and rear side of the flat are sheared according to the thickness of the flat and are slightly tilted due to its wedge angle Θ , producing a fringe pattern which is viewed on a screen. By adjusting the curvature of the wavefront the fringe pattern can be orientated parallel to the given cursor, which corresponds to the case of best collimation ($\alpha = 0$). In this case the biggest fringe spacing d_{\max} can be determined from the wavelength λ and the refractive index n_g of the flat:

$$d_{\max} = \frac{\lambda}{2n_g\Theta}. \quad (2.14)$$

As long as the wavefront radius is large compared to the plate thickness, small angle

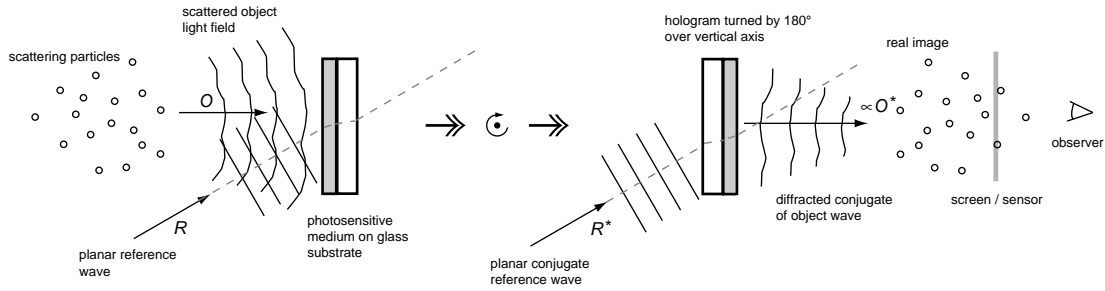


Figure 2.8: During recording a planar reference wave R is used. After development the hologram is replaced, flipped over its vertical axis and the planar wave now serves as the phase-conjugate R^* of the reference wave.

approximations can be used and the wavefront radius R_w can be calculated from data simply determined on the screen:

$$R_w = \frac{S d}{\lambda \sin \alpha}, \quad (2.15)$$

where S is the shear, α the orientation of the fringes with respect to the cursor and d the fringe spacing perpendicular to the direction of separation (Figure 2.9). The divergence $d_b = D/R_w$ of the beam is obtained from the effective aperture D and the calculated radius.

The sensitivity of a given collimation tester to a fringe rotation depends on the effective aperture and defines the best collimation resolution, typically given in terms of a remaining divergence in radians, which can be achieved. The corresponding wavefront radius $R_{\text{lim}} \leq R_w$ can be used to estimate a maximum axial positioning error δz of a holographic particle image. According to Sholes and Farrell (2000) this error is given by:

$$\delta z \approx \pm \frac{4z_O}{R_{\text{lim}}}, \quad (2.16)$$

where z_O is the axial distance between the hologram and the particle position (see also Appendix A.4).

With the aid of a collimation tester aberrations in the beam can also be detected. They are present whenever the fringes are no longer straight but show curved forms or if their spacing is not uniform across the observation field. The influence of beam aberrations to particle images is discussed in Section 2.2.2.

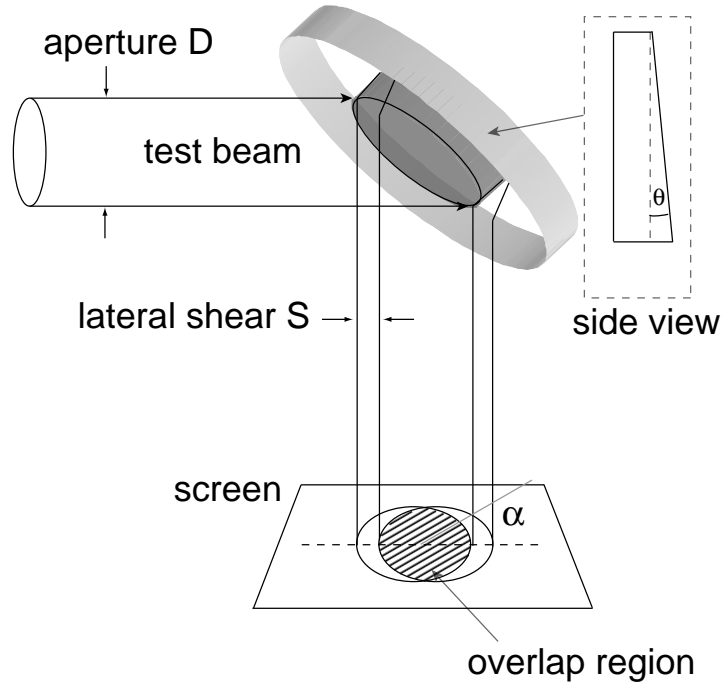


Figure 2.9: Principle sketch of a lateral shearing interferometer used to determine the test beams wavefront curvature from the measurement of the fringe rotation and spacing.

2.1.4.3 Magnifications in Holographic Replays

As we have seen in Sections 2.1.4.1 and 2.1.4.2 a precise beam alignment with as large as possible a wavefront radius is important for a high precision reconstruction. Also the wavelength plays a dominant role; when it is changed between recording and reconstruction the holographic image is irregularly magnified. From a geometrical analysis of point-source holograms, three imaging equations can be obtained from first-order approximations for the phase terms (Meier, 1965; Collier et al., 1971; Groh, 1973). In common coordinates with z parallel to the systems optical axis, the reconstructed image point (index i) is related to a given point source of the reference beam (index r), the source of the reconstructing beam (index g) and the subject position (index s) during recording (see also Appendix A.4). Along with these relations one can define expressions for lateral and angular magnifications, taking also into account the aspect of scaling the hologram (e.g. the recorded structure) by a factor m :

$$M_{\text{lat}} = \frac{dx_i}{dx_s} = \frac{dy_i}{dy_s} = m \left(1 \pm \frac{m^2 z_s}{\mu z_g} - \frac{z_s}{z_r} \right)^{-1} \quad (2.17)$$

and

$$M_{\text{lat}} = \frac{d(x_i/z_i)}{d(x_s/z_s)} = \pm \frac{\mu}{m}, \quad (2.18)$$

with $\mu = \lambda_g/\lambda_r$ being the ratio of the wavelength used for the reconstruction and for the recording, respectively. Calculating the longitudinal magnification:

$$M_{\text{long}} = \frac{dz_i}{dz_s} = -\frac{1}{\mu} \frac{m^2}{\{1 - z_s [(m^2/\mu z_g) + (1/z_r)]\}^2} = -\frac{1}{\mu} M_{\text{lat}}^2 \quad (2.19)$$

shows that (2.19) differs from the magnification in conventional imaging by the factor $1/\mu$, which was already shown by Gabor (1949). A magnification of the image can be obtained also by changing the curvature of the recording and reconstructing reference wavefront when $\mu = m = 1$, however, this cannot be employed without producing aberrations, which are described by the difference to the third- and fifth-order terms in the expansions series of the relative phase. An aberration-free magnification is obtained for plane reference waves when the condition $\mu = m$ holds and the reconstructing wave is incident at the same angle with the optical axis as the recording reference wave: $\Theta_g = \Theta_r$. Note, that by magnifying the hologram itself there is no longer a lensless imaging method and thus it is likely to introduce aberrations from the additional lens. The lateral magnification resulting from $\mu \neq 1$ can be compensated in the case of planar reference waves by modifying Θ_g accordingly (Champagne, 1967), however, the longitudinal imaging scaling according to μ still remains.

In practice, changes of the wavelength between recording and replay have to be considered for example when the pulsed recording light source has no counterpart as a continuous emission light source as it is the case for the ruby-laser. Konrath et al. (2002) have used the formulation after Champagne (1967) to predict the temperature stabilisation requirements of a laser diode used for a replay near the wavelength $\lambda = 694.3$ nm of the ruby laser to meet a tolerable shift of Θ_g .

When replaying holograms in air (refraction index n_a) recorded from objects initially immersed in water (n_w) the refraction caused by the air/water interface causes a shift of the focal plane towards the boundary and for objects far from the optical axis not only longitudinal compression according to $n_a/n_w \approx 3/4$ occurs but they are affected by aberrations, mainly astigmatism and field curvature. Upon changing the replay-wavelength these aberrations can be minimised at least for a given hologram-to-object distance (Kilpatrick and Watson, 1994; Hobson and Watson, 1999).

2.1.4.4 Emulsion Shrinkage

Emulsion effects are treated extensively in Barnhart et al. (1994) with the result that a finite image displacement of the order of some micrometers can be caused from emulsion shrinkage, when using an off-axis geometry and absorption type transmission holograms. In this case, using the proper chemical processing, the shrinkage is believed to change the emulsion thickness by less than 0.5 %. As long as both particle images are locally displaced by approximately the same amount a relative displacement measurement is not influenced. But this only holds true, if the particles or their intermediate images are placed close to the holographic plate and the effective aperture size is determined by their dominating scattering lobes (cf. Section 2.3.2). In all other cases an influence of the emulsion shrinkage on the measurement result could

be accounted for, this is still an open issue of HPIV. Furthermore, the position of a measurement within the recorded volume is also slightly changed due to the emulsion shrinkage. But compared to a typical interrogation-cell size of some hundred micrometers this effect can be neglected.

2.1.4.5 Phase Errors

Holography codes the phase of the subject light in an interference pattern. Upon reconstruction with an exact phase-conjugate beam the relative phase of this subject light remains unchanged at each position in the object space. But any phase deviation in the reconstructing wave illuminating the hologram leads to a deviation of the phase in the reconstructed beam. Contributions from different areas of the hologram do not overlap with the right phase in object space. In the worst case of a $\lambda/2$ -shift this partially could delete information by destructive interference as well as add spurious information by constructive interference.

When using separated setups with different lasers for recording and reconstruction, an influence of phase deviations on images of tiny objects such as the tracer particles is expected, but not yet studied in detail. Especially, when high energy laser pulses are used for the recording the typical beam profiles do not show the gaussian-shaped intensity distribution of a TEM₀₀ mode. To add to the complication, with changing distance from the laser output there are rapidly changing intensity profiles of these lasers as a consequence of numerous transversal modes emerging from the resonator (cf. Section 5.2.1). As the example of the beam profile of our pulsed Nd:YAG laser in Figure 2.10 shows, such distributions are non homogeneous, nor continuous or smooth. The accompanying phase map could be obtained by wavefront sensitive measurements, e.g. with a Hartmann-Shack sensor and a comparison with the phase map from the light source illuminating the hologram for reconstruction would permit a prediction of erroneous signals. Absorption type holograms recorded with a high-energy pulsed laser typically show an overall intensity variation across the area illuminated by the reference beam. When reconstructing with a homogeneous intensity distribution, several parts of the recorded hologram do not contribute with the same amount than during recording.

If the optical path length of a signal beam changes during the exposure of a hologram (e.g. due to motion of the holographic plate or the tracer particles) this may prevent successful recording. Analogous to the mechanical stability required for a long time exposure one can define a required "stability" of fast moving objects to be recorded with laser pulses. Though, even pulsed lasers used for velocimetry emit pulses of a few nanoseconds duration, the velocity limit is in the region of a few meters per second only, for distinct geometries. Typically, such a stability-condition is expressed as an allowable difference in the optical path length of well below half a wavelength. According to Vikram (1972) then the following condition holds:

$$|f(t)| \ll \frac{\lambda}{2|G|}, \quad (2.20)$$

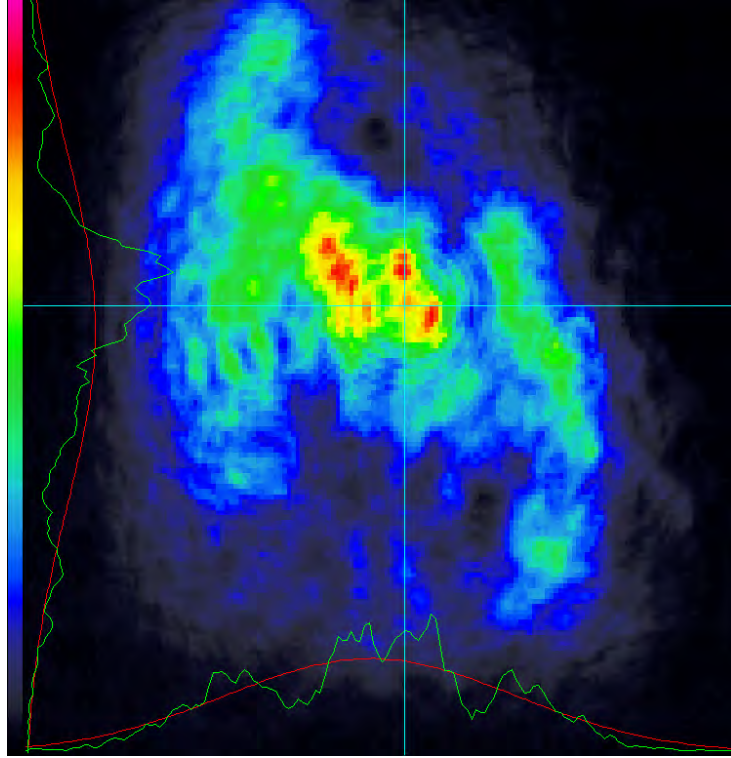


Figure 2.10: Beam profile of pulsed Nd:YAG laser with 1.3 J per pulse at 10 Hz repetition rate and $\lambda = 532$ nm

where $|f(t)|$ is the magnitude of displacement of the object from its original position. The function $f(t)$ has to be chosen according to the worst possible case of the flow studied by holographic methods. In the case of constant velocity (typically assumed for HPIV as shown next) it follows $f(t) = vt$. The geometrical factor:

$$G = (\hat{\mathbf{n}}_r + \hat{\mathbf{n}}_s) \cdot \hat{\mathbf{n}}_m = \cos \alpha + \cos \beta, \quad (2.21)$$

is given by the emitter (laser) and observer (hologram) position, as well as the direction of movement (Figure 2.11) and takes values between 0 and 2.

For holographic recording of particles with pulsed lasers the object travel time t can be replaced by the pulse duration τ . According to Konrath et al. (2002) the ratio λ/τ can be considered as a system parameter describing the light source. It mainly determines the velocity limit for a given recording geometry by multiplying with $1/\{n|G|\} = \{n | [(1 - \cos \beta) \cos \alpha] - [\sin \beta \sin \alpha] \}^{-1}$:

$$|v| \leq \frac{1}{n} \frac{\lambda}{\tau} \frac{1}{|G|}, \quad (2.22)$$

where $n > 2$ defines the tolerable reduction of the fringe-contrast in the recording plane. Typically in HPIV, $n = 4$ is sufficient to determine positions and displacements

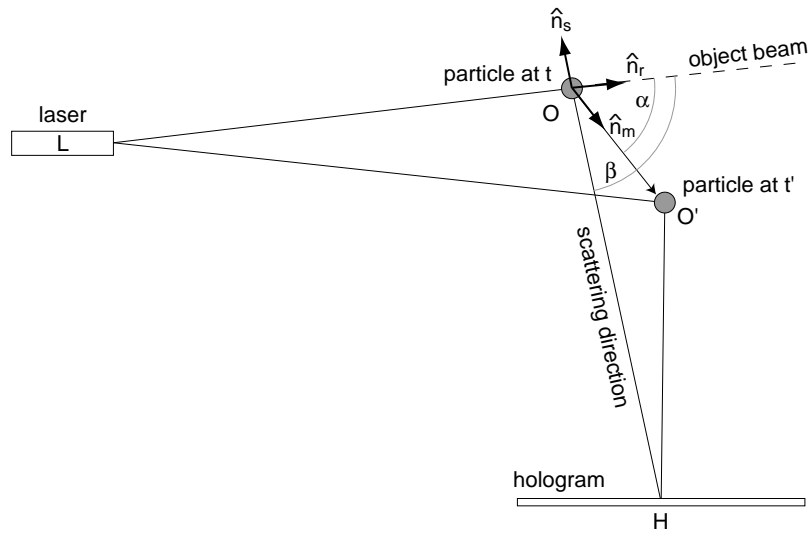


Figure 2.11: The maximum allowable velocity for a particle mainly depends on the recording geometry, the path difference of the light incident on the hologram over the positions O and O' , respectively, and should be well below half a wavelength.

of particles. For a typical Nd:YAG laser ($\lambda/\tau = 532 \text{ nm}/5 \text{ ns} = 106 \text{ ms}^{-1}$) the lower velocity limit is then $v = 13.25 \text{ ms}^{-1}$ for a backscattering geometry.

2.2 Properties of Holographic Particle Images

The final measurement data, namely the digitised planes from the reconstruction of a holographic recording of a dense cloud of particles, can be thought of as a coherent superposition of deteriorated particle images (signal) with an underlying speckle pattern (noise) sampled at distinct positions. In this Section the primary contributions to the signal are discussed. Beginning with a representation of noise-less ideal particle images, their spatial extent is described, which also defines a theoretical achievable imaging resolution. Deviations in the beam geometry during the reconstruction process can cause significant aberrations in particle images and thus also have an influence on their size and appearance. The origin of these aberrations is discussed in the following.

2.2.1 Intensity, Size and Resolution of Ideal Particle Images

Since holographic particle images are often treated in a first approximation as spherical waves converging from the hologram aperture towards the initial particle position, a formulation analogous to a single-lens imaging system can be used to discuss their properties. In this case the limiting aperture $D = 2R$ of the imaging system, in many cases simply the area of the hologram contributing to the reconstruction, defines the resolution of the holographic replay.

Given the amplitude A of the incident wave, it follows according to (Born and Wolf, 1980) for the intensity I_0 at the geometrical focus or the initial position of the particle, respectively:

$$I_0 = \left(\frac{\pi R^2 |A|}{\lambda z^2} \right)^2, \quad (2.23)$$

where R is the circular aperture radius on the hologram, z the distance between the particle image and the hologram and $\tan \Omega = R/z$ the half angular aperture.

Assuming particles much smaller than the diameter of a diffraction limited spot allows to approximate the resulting particle image diameter from the intensity distribution of the diffraction limited spot around the geometrical focal point. The well known equations of this problem have already been derived by Debye (1909a) on the basis of calculations by Lommel (1885). In a plane parallel to the aperture the spot size d_s is determined by the first dark ring of the resulting Airy-function, which is defined by the first zero of the Bessel function of the first kind. The particle image diameter d_i is then (Born and Wolf, 1980):

$$d_i \approx d_s = 2.44 \frac{z\lambda}{R} \approx \frac{\lambda}{\Omega}, \quad (2.24)$$

For large particle diameter d_p the resulting lateral image diameter is obtained by:

$$d_i = \sqrt{d_p^2 + d_s^2}. \quad (2.25)$$

Similarly, the resolution along the depth axis perpendicular to the hologram plane is also determined by the limiting aperture D . The intensity distribution of a diffraction limited spot along this axis is described by a sinc-function $(\sin x/x)^2$, having its first zero at $\Delta z = \pm 2\lambda(z/R)^2$. In a first approximation this value can be used to describe the spatial extent of a particle image along the depth axis.

If, following the Rayleigh criterion, a loss of about 20 % in intensity compared to that in the focal point is taken as the boundary, Δz reduces to $\approx \pm \frac{1}{2}\lambda(z/R)^2$ (Born and Wolf, 1980). This provides a reasonable definition of the depth-of-focus (DOF) or d_f , which is twice this number:

$$d_f \approx \frac{\lambda z^2}{R^2} = \frac{\lambda}{\Omega^2}. \quad (2.26)$$

Care should be taken with other definitions of DOF in papers dealing with particle imaging as already mentioned by Royer (1997). For example, when the total loss in intensity is used as a focusing criterion the particle size is often used in the formulas defining the DOF (Forbes and Kuehn, 1990), which leads especially for large particles to a much larger DOF than observed in experiments.

When coherent light is used for imaging it typically forms a speckle pattern, which deteriorates the individual particle images. As the size of the speckle is given also

by (2.24) (Goodman, 1984) the resolution of the image is reduced by a factor of at least 2. Experiments on the resolving power however, suggest a factor of 2.5 to give a reasonable fit to the observed contrast necessary to distinguish small objects from the background (Austin, 1984). Further discussion of this noise contribution can be found in Chapter 3.

2.2.2 Aberrations in Particle Images

Provided that no wavelength change between recording and reconstruction is introduced and that emulsion shrinkage can be neglected, the primary source of image aberrations are misalignments of the reference beam illuminating the hologram during reconstruction. This includes angular mismatch, collimation mismatch and, more complicated, beam aberrations due to imperfect optical elements like lenses and mirrors. Based on the theory by Champagne (1967) the aberrations of particle images for off-axis holography have been investigated by Chan et al. (2000), showing that the significant aberration due to misalignments is astigmatism. This is consistent with observations already reported by Austin (1984), who determined astigmatic image shifts depending on a given rotation of the hologram about its vertical axis and validated the results with a simple ray tracing model.

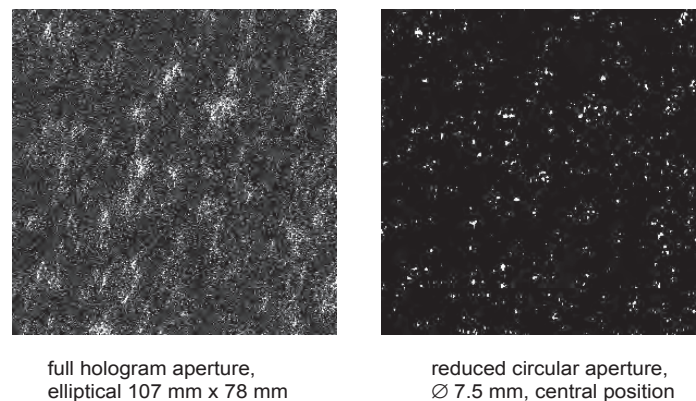


Figure 2.12: Example of aberrated real particle images (left) and reduction of aberrations due to limited aperture reconstruction (right), field of view $2.9 \times 2.9 \text{ mm}^2$.

A collimation mismatch resulting in a slight curvature of the reference wavefront can severely distort the particle images, when for the reconstruction of the real image the hologram is flipped by 180° over its vertical axis and the effects of deviation from a collimated wave is doubled. Care should thus be taken to minimise the collimation mismatch, for example by using a shear-plate collimation tester (cf. Section 2.1.4.2). If a non-collimated reference beam is incident normal to the hologram the deviation in the angle of incidence is zero only in the hologram center and increases towards the edges of the hologram. A typical image obtained with a significant collimation mismatch from a hologram of a model particle field recorded in side-scattering mode is shown in Figure 2.12. The aberrations can be reduced by reducing the aperture. Obviously, in

this case the particle images vary significantly in shape, size and position when they are reconstructed from different locations on the hologram (Poppen, 2003).

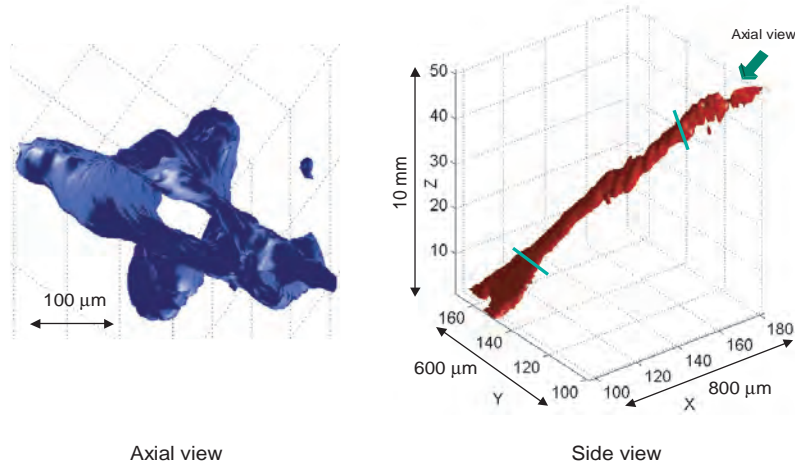


Figure 2.13: Example of an astigmatic aberration of a particle image obtained from a depth scan with a magnifying imaging sensor. The shape represents the iso-surface of a threshold intensity value.

A collimation mismatch causes aberrations in the particle image also in depth direction. Figure 2.13 shows details of a particle image shape obtained by a depth scan with a CCD camera carrying a microscopic lens. The particle image shape is obtained by drawing an iso-surface at positions in space obeying a threshold intensity value. Astigmatism is nicely observed in this case, evident from the two "focal points" in different depth regions and the crossed shape of the defocusing regions.

2.3 Light Scattering by Particles

Particle holography records light scattered towards the holographic plate by small tracer particles. Scattering of electro-magnetic radiation depends on the particle size, the wavelength, the state of polarization and the illumination direction, as well as on the index of refraction of the particle and the surrounding medium. These parameters have a direct influence on the holographic registration. Commonly, the size parameter a is used to describe the scattering characteristics independently of the actual size of the particle or the wavelength:

$$a = k_m r = \frac{2\pi}{\lambda_m} r, \quad (2.27)$$

where r is the radius of the particle and k_m denotes the wave-number in a virtual medium with a relative index of refraction given by $m = n_{\text{particle}}/n_{\text{medium}}$.

For HPIV, typical tracer particle sizes (diameter) range from $0.5 \mu\text{m}$ in air flows and up to $100 \mu\text{m}$ in water flows, resulting in size parameters of $a \approx 3 \dots 1180$ for a wavelength of $\lambda = 532 \text{ nm}$. The normalised cross-section Q of light scattered by particles

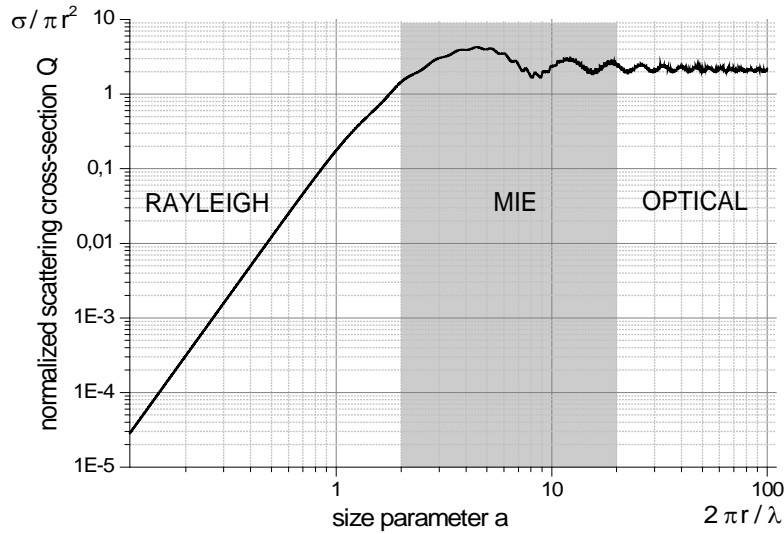


Figure 2.14: Normalised total scattering cross-section (or scattering efficiency) Q versus the size parameter $a = 2\pi r/\lambda_m$, calculated with Matlab Mie functions by Barnett (1996). The Mie scattering regime, where interference of light diffracted and refracted by the particle produces complex scattering characteristics, is shaded.

versus their size parameter a is plotted in Figure 2.14 for a relative index of refraction of $m = 1.4527$. The steep slope for $a \leq 1$ is described by Rayleigh scattering, a theory valid for particles sufficiently smaller than the wavelength and less important for HPIV applications. When the particle size is of the order of a wavelength Mie-scattering is predominant, where interference between diffracted and refracted light results in a more complex scattering behaviour.

The total scattering cross-section in the optical regime is mainly determined by the particle size. Scattering beyond $a > 10$ causes $Q = \sigma/\pi r^2$ to converge towards a value greater than two, although geometrical optics suggests a total cross-section of πr^2 and thus $Q = 1$. This phenomenon is called the "extinction paradox" and is discussed in detail by van de Hulst (1981) and Bohren and Huffman (1998).

2.3.1 Mie-Scattering

For the design of an HPIV measurement system it is useful to know the angular dependency of the scattering characteristic of the particles, which can be obtained from Mie's theory (Mie, 1908). Mie scattering theory is a rigorous solution on the basis of the electromagnetic theory (Maxwell's equations) for the diffraction of a plane monochromatic wave by a homogeneous sphere of any diameter and of any composition situated in a homogeneous medium (Born and Wolf, 1980). The theory is valid only for far-field conditions (Fraunhofer regime), where the particle-to-hologram distance z_H is large as

compared to the particle diameter d_p :

$$z_H \gg \frac{\pi d_p^2}{4\lambda}. \quad (2.28)$$

Other formulations of the same problem have been found by Lorenz (1898) and Debye (1909b). Near-field formulations, needed for a description of particle-particle interactions, have been treated extensively in the last two decades (Gouesbet and Grehan, 1999) and are commonly derived from generalised Lorenz-Mie theories (GLMT). For HPIV however, condition (2.28) generally holds and particle-particle interactions can be neglected even for the highest seeding concentrations.

In Figure 2.15 the geometry for scattered light recording on a hologram is depicted, together with an example of a scattered intensity distribution $I(\theta, \phi)$ obtained with parameters typical for HPIV. The coordinate system is chosen relative to the holographic plate. Incident (E_i) and scattered (E_{sca}) amplitudes are given relative to the scattering plane, defined by the positions of the light source, the scatterer and the hologram. The scattered intensity has a radially symmetric distribution over the elevation angle ϕ .

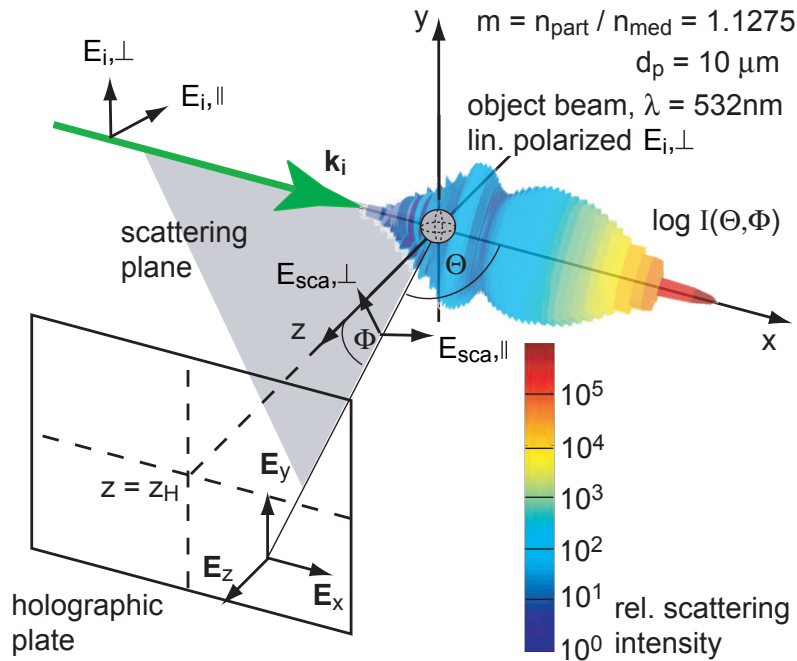


Figure 2.15: Geometry for scattered light recording, incident and scattered amplitudes are given with respect to the scattering plane, defined by the positions of the light source, the scatterer and the hologram. The amplitude distribution in the plane of the hologram can be obtained by an appropriate coordinate transformation. The light scattering strongly depends on the angle θ and is radially symmetric over the angle ϕ . The colours represent the scattered intensity on a logarithmic scale from a $10 \mu\text{m}$ particle with $m = 1.1275$ (e.g. melamin resin in perspex) at a wavelength of $\lambda = 532 \text{ nm}$.

The computation of Mie scattering diagrams, as shown in Figure 2.15 in three di-

mensions, is conveniently achieved by computer algorithms (Bohren and Huffman, 1983; Barnett, 1996). In the example of Figure 2.16 the scattered-intensity functions $I_{\perp} = |S_1(\theta)|^2$ for polarisations perpendicular and $I_{\parallel} = |S_2(\theta)|^2$ parallel to the scattering plane are given as a function of the scattering angle θ . Details about the calculation of the elements $S_1(\theta)$ and $S_2(\theta)$ of the Jones scattering matrix and the computation of complex amplitudes of the scattered wave-front can be found in appendix A.5. Light is incident from left, producing significantly stronger scattering in forward ($\theta = 0^\circ$) than in backward direction. The dominant scattering lobes are essentially determining the effective illumination of the hologram by a particle. From Figure 2.16 this is evident for the perpendicular polarisation case in rearward direction or for large particle diameters in sideward scattering, as well as in forward direction for both polarisation cases.

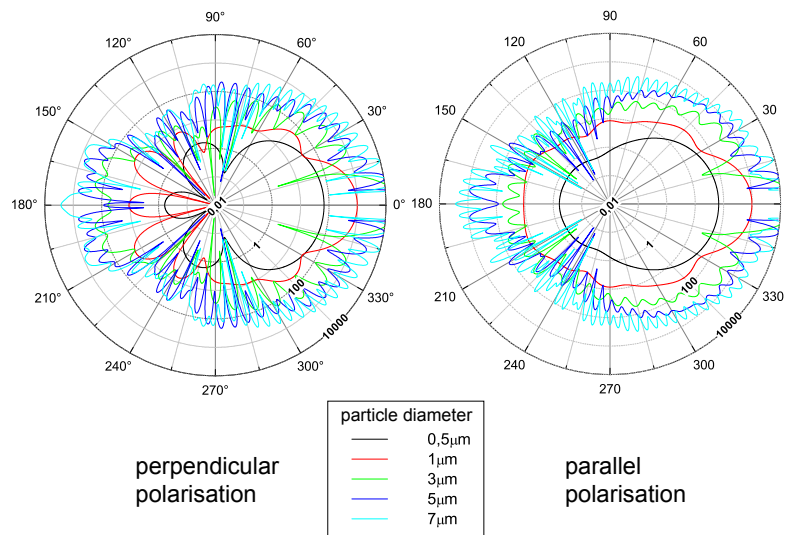


Figure 2.16: Mie-scattering diagrams for polarisations perpendicular and parallel to the scattering plane for various diameters of particles with $m = 1.4527$ (e.g. DEHS in air) at a wavelength of $\lambda = 532$ nm

2.3.2 Influence of Light Scattered by Particles on the Holographic Registration

From the light scattered by each particle in nearly all directions only a small part, depending on the position and size of the hologram, is finally recorded (limited spatial band width). When particles are recorded in forward scattering mode (in-line setup) the strongest signals can be achieved for the exposure. However, this usually goes on cost of the effective aperture, which is often significantly reduced due to the scattering-lobes (e.g. to $\pm 15^\circ$ for I_{\perp} and a particle diameter of $3 \mu\text{m}$). A limited aperture results in limited resolution (cf. Sections 2.2.1) and in difficulties to find the focal plane of the particle, hence it is a source of error in the evaluation of particle images (Belz and Shofner, 1990).

Side scattering generally allows a much larger effective aperture and has been used to facilitate recent HPIV measurements (Lozano et al., 1999; Pu and Meng, 2000a). Nevertheless, an aperture limited recording of the scattered field and its replay in absence of the scatterer causes considerable errors due to aberrations intrinsic to this holographic imaging process.

A detailed study by Pu and Meng (2003) pays attention to the complex particle image shapes obtained even from an ideal holographic replay and identifies the intrinsic aberrations and their influence on the measurement process. To this end, the authors used Mie scattering algorithms to find the complex amplitude distribution in the plane of the hologram (cf. Figure 2.15) and applied a Fresnel transformation for digital reconstruction, a method well known from digital holography (Schnars and Jüptner, 1994, 2002). They found that, depending on the mean angle θ_m under which the light scattered by a single particle is recorded on the ideally modelled hologram, the aberrations have a strong impact on the particle image shape, cause shifts of the intensity maximum along axial or transverse directions and produce multiple competing foci. While for $\theta_m \leq 15^\circ$ spherical aberration dominates and large axial shifts are observed, coma and astigmatism are the main source of errors in the regime $30^\circ \leq \theta_m \leq 150^\circ$, producing highly complex particle images. Further increases of θ_m produce again higher influence of spherical aberration. Conclusions about the image quality are drawn by a comparison of the principal image (i.e. in the plane where the particle was located) and the brightest spot image (i.e. in the focal plane). For very small particles the scattered wave is almost an undisturbed spherical wave and both images agree well. As the particle size increases, the phase deviation becomes more and more severe and the intrinsic aberrations result in appreciable shifts of the particle image.

The above mentioned algorithms have been used to validate our own findings. Firstly the effect of an increasing particle size was analysed for a side-scattering arrangement ($\theta_m = 90^\circ$), as it was used in the experiments described in Section 2.2.2. Here a model particle field with melamin particles embedded in perspex was recorded on a hologram, which has been taken using a long coherence continuous wave Nd:YAG laser (see Section 6.2.1 for details). The particles inside the perspex had a mean size of $9.86 \mu\text{m}$.

Figure 2.17 shows the simulation result for scattering at particles of four different sizes. The intensity distribution in the $24 \times 24 \mu\text{m}^2$ view of the reconstructed particle image is scaled non-linearly to show the next order diffraction rings and their deformation, respectively. Furthermore the distribution of the electromagnetic field in the plane is given separately for each component. Clearly the fluctuating distribution along the x-axis can be made responsible for the aberration effect, which increases with increasing particle size. Judging from Figure 2.17 for a particle size of $d_p = 10 \mu\text{m}$ we expect a similar behaviour in our experiment with the model particle field. Indeed some non-symmetrical particle images are found (Poppen, 2003), the clear two competing foci, however, could not be observed. This might be due to the resolution of only $9 \mu\text{m}$ in the experimental images, whereas in the simulated images a resolution of $\lambda/4 = 0.13 \mu\text{m}$ is obtained.

The effects of aberrations can be quantified according to Pu and Meng (2003) by the

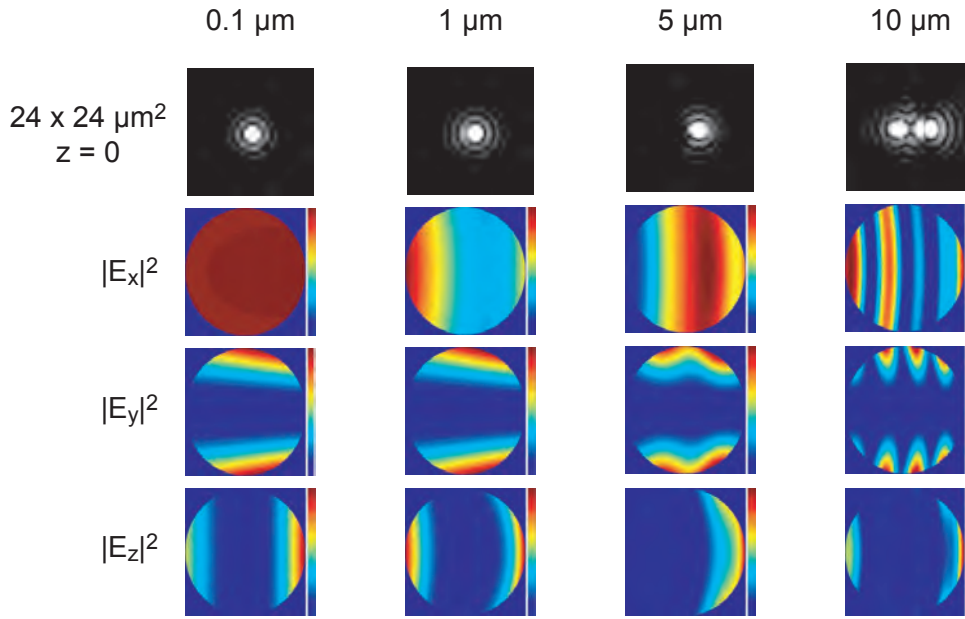


Figure 2.17: Simulated holographic images from melamin particles embedded in perspex with a rescaled, non-linear intensity distribution to visualise the considerably darker diffraction rings next to the main particle image. The hologram aperture with a diameter of 10 cm was located centered to the 90° -scattering direction. Shown are the digitally reconstructed holographic images (field of view $24 \times 24 \mu\text{m}^2$) of four particles with different sizes, thus exhibiting different Mie-characteristics. The components of the scattered electromagnetic field in the plane of the hologram are shown as an artificial intensity $|E_{x,y,z}|^2$ scaled, however, to make use of the full colour range.

introduction of a quantity called "image integrity" γ , which is the ratio of the actual focal intensity (I_f) to the diffraction-limited image intensity (I_0):

$$\gamma = I_f/I_0. \quad (2.29)$$

Figure 2.18 shows image integrity γ as a function of the size parameter a for various scattering angles θ . As long as sufficiently small particles are imaged, their volume fractions in air are negligible. In this case the amplitude distribution is not strongly influenced by the absence of the particle during the reconstruction and the corresponding holographic particle image still appears like a focal spot. For large size parameters however, a further source of errors in HPIV is predicted by these simulations. The reconstructed wave converging to the initial position of the particle propagates further, even behind the initial surface of the particle, forms a focal spot, diverges again and contributes to the coherent background noise perturbing other particle images. A decreased image integrity γ indicates that the reconstructed particle image is likely to show a focal spot which is considerably displaced with respect to the initial particle position. An effect, which does not severely affects the relative displacement measurements of two closely located images from the same particle. Competing foci however are ought to be avoided, since they could have a significant influence on the evaluation methods (see Chapter 7 for details).

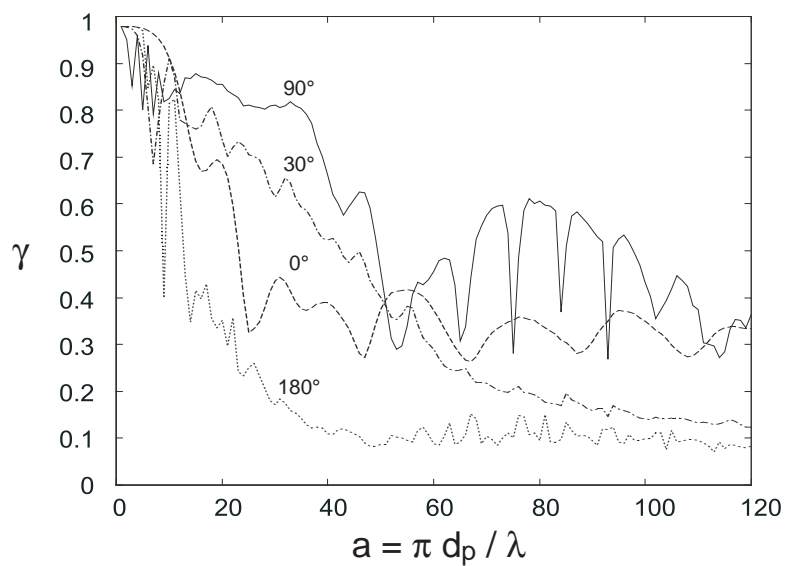


Figure 2.18: Image integrity γ of a single numerically reconstructed particle image versus its size parameter a for different scattering angles θ_m , relative index of refraction $m = 1.15$ and angular aperture $\Omega = 30^\circ$, after (Pu and Meng, 2003).

3 Noise Limits for Successful Recording of Particle Fields

The particle images, the properties of which have been discussed in Chapter 2, are considered as the signal in holographic particle image velocimetry (HPIV). They are used to determine the local displacements between two successive images. Any further intensity variation in the background of these particle images is considered as noise. Even more drastically than in conventional PIV, the noise in holographic particle images can render a measurement impossible, especially when deep and densely seeded volumes are imaged. Details about the background-noise in particle images are addressed in Section 3.1 introducing into the main concern of this thesis: noise suppression by short-coherence recording of holograms or Light-in-Flight Holography (LiFH), respectively and the implementation of this method for HPIV (further detailed in Chapter 4).

Defining a signal-to-noise ratio (SNR) which is directly measurable from holographic particle images is not a trivial task, as will be clear from the discussion in Chapter 9. Nevertheless, the literature provides a feasible definition of a SNR (reviewed in Section 3.2) which can guide the experimenter in designing an HPIV system. As already mentioned in Section 2.1.3, a further source of noise is light scattered by grains embedded in the emulsion of the recording material. This noise only gets predominant when the holographic image is of weak intensity. Because in particle holography the available amount of laser energy limits the size of the region under investigation, a detailed study of the limits set out by the emulsion noise is presented in Section 3.2.2. This leads to a novel mode of HPIV allowing to observe a larger field and which we termed "Particle Holography at the Noise Limit" (Herrmann and Hinsch, 2001).

3.1 Background Noise in Holographic Particle Images

Noise in holographic images is generally observed as a granular structure of strong fluctuating intensities, the so-called "laser speckles". These are a consequence of the coherent superposition of light with random phases. Contrary to speckle metrology techniques, like speckle velocimetry (Dudderar and Simpkins, 1982) or ESPI (Andrés et al., 1999; Arroyo et al., 2000), the speckles in holographic particle images cannot be used to extract information about the differences between the first and second exposure. Whereas in in-line holography the speckle noise is mainly due to the overlapping of the real and virtual image with the illuminating wave, in off-axis holography the speckles are mainly the result of the self-interference among different phasors forming the holographic image itself. The resulting noise has thus been termed "intermodulation" or "intrinsic" speckle noise, because it is inherent to the holographic imaging process.

In any observation plane (plane receiving light from the hologram), speckles from the out-of-focus images are present that add coherently to any signal, that are the in-focus particle images. Figure 3.1 shows the impact of a few out-of-focus images on several in-focus particle images. Two clearly distinctive cases are marked with arrows. Near the upper and lower image border however, overlapping with in- and out-of-focus occurs and a clear separation is no longer visible. Since speckles are the result of a random process, the intensity distribution in particle images is also exposed to random fluctuations, strongly degrading the image quality.

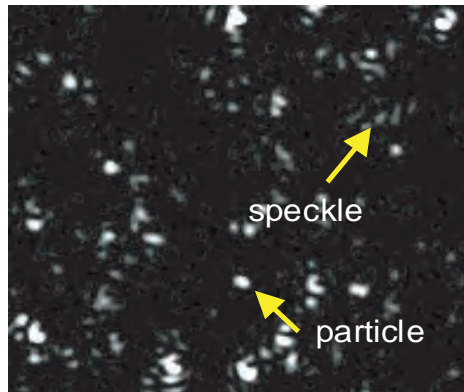


Figure 3.1: Focused particle images with superimposed speckle noise from out-of-focus particle images: a clear separation of signal and noise is not always visible.

3.1.1 Sources of Noise

Disturbing light from reflections (e.g. interfaces glass-air or glass-water) which reaches the holographic plate is also recorded in the holographic image, and should thus be minimised by a good control of the experiment. Nevertheless, many measurements require to obtain the flow field close to an object, which interacts with the fluid flow. In such cases the illumination needs to be tailored to mainly hit the seed particles rather than the object. The object is preferably painted mat black or covered with a special fluorescent dye to absorb as much of the coherent light as possible.

Also during reconstruction, reflections and scattered light can add artificial intensity to the particle image under inspection. Thus it should be ensured that only light illuminating the hologram contributes to the image. In that case only two predominant sources of noise need to be considered at the position of the imaging sensor, which is used to digitise the holographic particle images:

- a. Intrinsic speckle noise due to overlapping in- and out-of-focus particle images forms a speckle pattern. The number of independent phasors relevant for this speckle noise increases proportional to the number density of the particles imaged.
- b. Light scattered by the developed emulsion-grains of the recording material forms a speckle pattern which coherently adds to the reconstructed image.

The second source of noise can be neglected, if the intensity of the light scattered by the particles compared to that of the reference beam yields a good fringe pattern contrast V of the hologram. In that case the diffraction efficiency is high enough to reconstruct high intensity particle images much brighter than the scattered light from the emulsion grains. Intentionally violating this condition results in an increased speckle intensity, which superimposes to the particle images. But it also provides a way to record particle images with less energy and allows for larger illuminating cross-sections and thus larger measurement volumes (cf. Section 3.2.2) unless the signal-to-noise ratio is sufficient to distinguish the particle images from the background.

3.2 Signal-to-Noise Ratio in Holographic Images

The interference between the signal image and the speckle noise needs to be taken into account when defining a SNR in the reconstructed holographic image. Goodman (1967) has devised a formulation for SNR from two models describing the holographic emulsion, wherein the grains act as scatterers forming the noisy speckle pattern.

Consider a well defined image intensity I_0 above a background given by the speckle pattern originating from the independently scattering emulsion grains. The SNR is reasonably defined as the ratio of I_0 and the standard deviation of the total image intensity σ_N for the same point. When modelling each image point as the coherent superposition of the deterministic image amplitude with randomly phased complex amplitudes (zero-mean and gaussian distributed variables) the SNR is found to be a monotonically increasing function of $I_0/\langle I_N \rangle$, where $\langle I_N \rangle$ represents the spatially averaged noise intensity:

$$\frac{I_0}{\sigma_N} = \frac{I_0 / \langle I_N \rangle}{\sqrt{1 + 2I_0 / \langle I_N \rangle}}. \quad (3.1)$$

From this definition of SNR in holographic images two limiting cases of interest can be derived:

$$\frac{I_0}{\sigma_N} = \begin{cases} I_0 / \langle I_N \rangle & \text{if } I_0 / \langle I_N \rangle \ll 1 \\ \sqrt{I_0 / 2 \langle I_N \rangle} & \text{if } I_0 / \langle I_N \rangle \gg 1. \end{cases} \quad (3.2)$$

The first case describes an image where the deterministic portion of the intensity is much weaker than the noise amplitude, which is the sole source of randomness and hence $\sigma_N = \langle I_N \rangle$. The latter case is dominated by the interference of a weak noise amplitude with the stronger image amplitude and σ_N depends on the strength of the deterministic portion of the intensity.

3.2.1 Application to Intrinsic Speckle Noise

Most likely the second case derived above can be applied to HPIV, where particle images should be bright spots over noise. Using first-order statistics the speckle noise

$\langle I_N \rangle$ originating from the self-interference among the particle images can be related to more practical parameters of an HPIV system, namely the wavelength λ used for recording and reconstruction, the number density n_s of particles, the illuminated particle field depth L and the angular aperture 2Ω . Pu et al. (2002) have derived the following prescription:

$$\frac{I_0}{\langle I_N \rangle} = \frac{\pi \tan^2 \Omega}{\lambda^2 n_s L}, \quad (3.3)$$

where the reconstructed particle image has an intensity I_0 modelled as a diffraction limited spot at the geometrical focus (cf. Equation (2.23)). A further refinement (Pu and Meng, 2004) takes into account the image integrity $\gamma \leq 1$ due to Mie scattering, which was already introduced in Section 2.3.2, and the ratio of the pixel to the speckle size $\mathcal{M} \geq 1$ when the imaging sensor does not fully resolve the speckle pattern (Goodman, 1984):

$$\frac{I_0}{\langle I_N \rangle} = \frac{\pi \gamma \tan^2 \Omega}{\mathcal{M} \lambda^2 n_s L}. \quad (3.4)$$

To achieve a minimal SNR of say 5, the value according to (3.4) must be $I_0/\langle I_N \rangle = 2(I_0/\sigma_N)^2 = 50$. The connection between SNR, Ω and n_s is plotted in Figure 3.2 for $\lambda = 532$ nm, $L = 40$ mm, $\gamma = 0.5$, $\mathcal{M} = 3$ and either $n_s \approx 20$ mm⁻³ (black lines) or $\Omega = 8.5^\circ$ (gray lines). Marked with circles is SNR = 5 considered as a lower boundary for a good HPIV recording. The dashed lines represent (3.3) without the correction for aberrations and sensor resolution ($\gamma = \mathcal{M} = 1$).

The following Chapters examine a short-coherence hologram recording method, the so-called Light-in-Flight Holography (LiFH), to considerably reduce the intrinsic speckle noise due simultaneously reconstructed out-of-focus particle images. As we will see in Chapter 9 the above prediction does not fit to the situation in our experiments, where a reduced aperture is used to select the region in depth reconstructed by LiFH. Furthermore, also those holograms recorded with long coherence do not show a significant increase in SNR when increasing the aperture.

3.2.2 Application to Emulsion Grain Noise

Similar to the intrinsic speckle noise approach, the definition of SNR according to (3.1) can also be applied to the noise originating from the emulsion grains. Developed silver-halide film consists of an emulsion layer made from gelatine with embedded silver grains. Here, the typical grain size is some ten to several hundred nanometres. Light used for the reconstruction is not only diffracted by the recorded pattern, but is also scattered by these grains in the direction of the holographic image. The scattered light forms also a speckle field, which is superimposed onto the holographic image. Typically, this speckle intensity is considerably lower than the image intensity. However, with tiny objects which scatter only sparsely or holograms with a very low diffraction

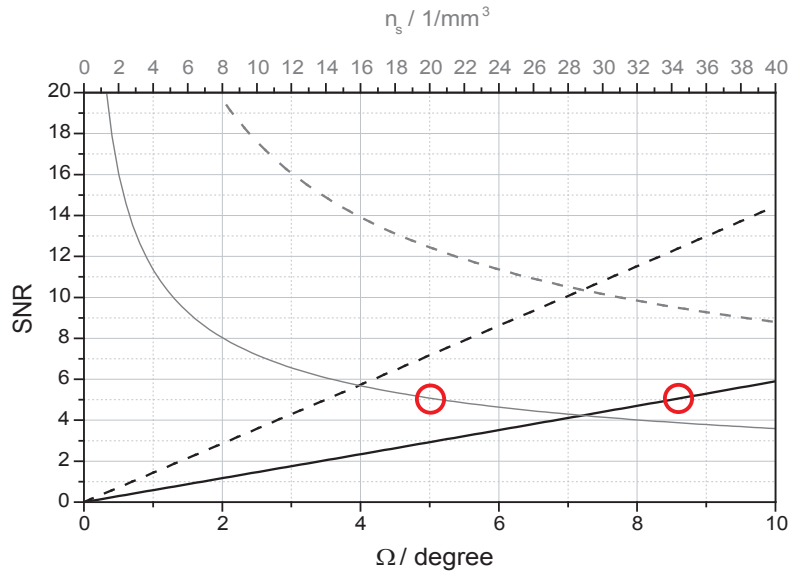


Figure 3.2: SNR of holographic particle images versus half aperture Ω and seeding density n_s for the HPIV system according to Pu and Meng (2004).

efficiency, the speckle intensity can be of the same order of magnitude and could even completely mask the image.

In HPIV, where tiny tracer particles are used to probe air flows, it is thus a common approach to achieve the maximum diffraction efficiency from a recorded hologram with the available amount of light scattered by the tracer particles. On silver-halide film this requires typically an object-to-reference intensity ratio of $r_b = 0.25$, which however, is often difficult to achieve with the weak object light in HPIV when large volumes have to be illuminated. At the expense of the reconstructed image intensity, this ratio can be decreased by several orders of magnitude depending on the type of object and the scattering behaviour of the granular structures in the film emulsion. Now, with less object light needed for recording, larger measuring volumes become feasible for a variety of new applications. However, during reconstruction a long time exposure may become necessary for the evaluation of particle images.

A theoretical approach to estimating the smallest detectable signal, linked to the SNR according to (3.1), from parameters of holographic emulsions is presented in Section 3.2.2.1. In Section 3.2.2.2 a general experiment is described which has been carried out to find the noise limit for proper registration of objects at different spatial resolutions. In a second step (Section 3.2.2.3) a similar analysis is done for a model particle field. Finally, Section 3.2.2.4 combines the above theory with a measure, which is accessible from two reconstructed but slightly shifted particle images, as they are used in HPIV to

determine the local velocity. It is shown that this approach provides a good prediction of tendencies observed in the model particle field experiment.

3.2.2.1 Theoretical Determination of the Emulsion Grain Noise Limit

Although initially calculated for Fourier transform holograms by Friesem et al. (1967), the smallest detectable signal, derived from properties of the holographic emulsion, can also be approximated for Fresnel holograms (Kozma, 1968), the lens less hologram recording method frequently used in HPIV. The signal is again assumed to be a point-like source of light with the deterministic intensity I_0 . The noise $\langle I_N \rangle$ due to the emulsion grains is a weak speckle pattern with random fluctuations in intensity. Now, as long as the reference intensity is chosen to operate in a linear recording range, the ratio of signal to average film-grain noise is proportional to the object-to-reference beam intensity ratio $r_b = (|O| / |R|)^2 \leq 0.25$:

$$\frac{I_0}{\langle I_N \rangle} = \frac{K^2 \eta^2 A_t}{\Phi(\nu)} \cdot r_b, \quad (3.5)$$

where K is a factor determined by the primary spatial-frequency ν_0 and depends on the modulation transfer function of the holographic film, η is the slope of the normalised¹ t_A - E curve (see also Section 2.1.3), A_t is the area of the hologram and $\Phi(\nu)$ is the Wiener or transmittance spectrum of the film-grain noise.

An increasing area A_t results in brighter spot images, but also increases the intensity of the background noise. The quantity $\Phi(\nu)$ is defined as the power of light scattered into a certain spatial frequency divided by the power incident on the hologram and has been measured for a holographic emulsion widely used in the scientific community several years ago, the so-called Kodak 649F spectroscopic plates. For an amplitude transmittance of $t_A = 0.529$, the measured data can be approximated by the expression (Burckhardt, 1966):

$$\Phi(\nu) = [\exp(-0.00248\nu)] \cdot 10^{-8}. \quad (3.6)$$

In the present situation $\Phi(\nu)$ is evaluated for the primary spatial frequency ν_0 , which is given by the angle between the object and reference beams according to (2.8) and (2.9).

A good agreement between this theory and an experiment was obtained by Meng and Hussain (1995), who have used a pinhole as a point-like object. Using a beam ratio of as low as $r_b = 10^{-8}$ it was still possible to distinguish the reconstructed single point from the background. Substituting typical values for the Kodak 649F plates in (3.5) as follows: $\nu = 300$ lp/mm, $\Phi(\nu) = 0.48 \times 10^{-8}$, $K = 0.95$, $\eta = 0.56$ and $A_t = 100$ mm² and assuming an SNR of 5 the corresponding theoretical minimum beam ratio would be $r_b = 0.84 \times 10^{-8}$.

¹The curve is normalised in such a way that a unit exposure, which in this case should be achieved by the reference beam, produces a transmittance which is centered on the linear portion of the t_A - E curve.

When the object is made up of N resolved, uniformly distributed and equally bright points, each with intensity $|O'|^2$, and assuming that the total exposure of the holographic material is the same, the proper beam ratio is:

$$r_{b,N} = \frac{|O|_{\Sigma}^2}{|R|^2}, \text{ with } |O|_{\Sigma}^2 = N \cdot |O'|^2. \quad (3.7)$$

Now, replacing the single point scattered intensity $|O|^2$, which solely exposed the holographic film in the first case, with the intensity scattered by each individual particle $|O'|^2 = |O|_{\Sigma}^2 / N$ equation (3.5) yields:

$$\frac{I_0}{\langle I_N \rangle} = \frac{K^2 \eta^2 A_t}{\Phi(\nu) N} \cdot \frac{|O|_{\Sigma}^2}{|R|^2}. \quad (3.8)$$

Thus a beam ratio $r_{b,N}$ reduced by the factor $1/N$ with respect to r_b needs to be accepted to achieve the same minimal SNR, determined by $\left(\frac{I_0}{\langle I_N \rangle}\right)_{\min}$ according to (3.2) for each of the resolved N objects:

$$r_{b,N} = \frac{N \Phi(\nu) \left(\frac{I_0}{\langle I_N \rangle}\right)_{\min}}{K^2 \eta^2 A_t}. \quad (3.9)$$

As we will see later, the comfortable margin of eight orders of magnitude is considerably reduced when many tracer particle have to be considered, but still an increase of the measurement volume with respect to the case of best diffraction efficiency is feasible.

3.2.2.2 Experimental Investigations with a Test Object

Using the real-image reconstruction provides a way to digitise the reconstructed intensity distribution on a bare CCD sensor (or record it on photographic paper or film) for later evaluation. This can be done for the reconstructed volume slice by slice, a principle often used in HPIV setups.

By using a continuous-wave laser for reconstruction this method is not bound to fixed exposure times and hence a longer exposure time can be used to "collect" light even from a weakly diffracting hologram. The main limiting condition in such a time-averaging reconstruction process is the amount of scattered light from the emulsion grains and any diffuse external light reaching the medium. If this amount (noise) is of the order of the diffracted light (signal) objects may vanish in a noisy background. The noise limit applicable to a common amplitude hologram is the subject of this study, intended to find the lower boundary on object light needed to successfully record holograms.

A first investigation of the noise limit was carried out with a test pattern known as "resolution chart" (USAF-1951 negative) providing a variety of spatial frequencies.

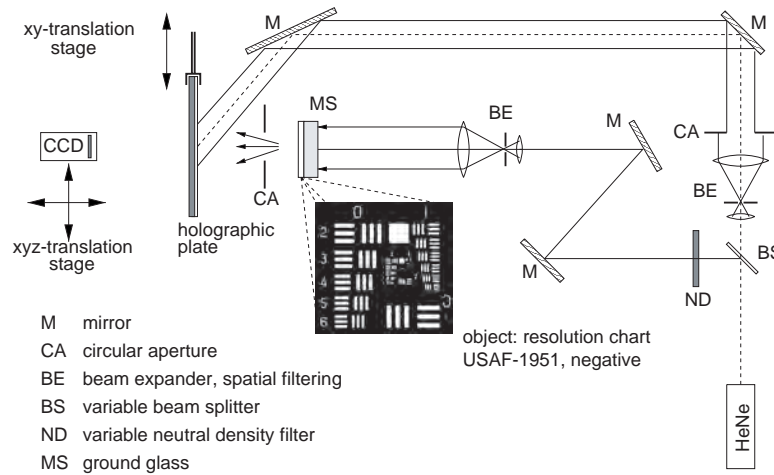


Figure 3.3: Setup to record holograms of test pattern with controlled object-to-reference intensity ratio, up to nine holograms could be recorded on one plate, the reconstruction of the virtual image is done in the same setup, a bare CCD sensor is used to digitise the image.

An off-axis setup (Figure 3.3) was used with a reference beam incident at 45° on the holographic plate to record and to reconstruct the test pattern. A ground glass directly adjacent to the glass substrate of the object produces light scattered towards the holographic plate from which only a small fraction was selected by a circular aperture to illuminate a limited part of the plate. The reference beam was also illuminating this part, producing elliptical holograms with axes of 33 mm and 25 mm, from which up to nine could be stored on one $4" \times 5"$ plate. It was thus possible to eliminate fluctuations, usually originating from the wet chemical processing within a series of holograms, by developing all at once.

By introducing neutral density filters in the object beam the amount of object light was reduced for each hologram step by step. The total exposure of the holographic film was initially set by adjusting the beam splitter to provide an object-to-reference beam ratio of $r_b = 0.25$ and choosing the exposure time to operate in the middle of the linear recording range. For each hologram the total exposure was kept constant to obtain a constant optical density throughout the experiment by modifying the exposure time according to the neutral density filter used.

After developing, the plate was turned by 180° to reconstruct the real image using the same setup. This image was then digitised by a bare CCD sensor capable of long time exposure. The average grey level within a bright spot of the test pattern was kept constant using an adapted exposure time for the CCD. The effect of reduced r_b can be seen in Figure 3.4. The superimposed speckle pattern becomes clearly visible when $r_b > 10^{-4}$.

To study quantitatively the effect of reduced r_b the reconstructed image visibility V_i was calculated for each hologram and for four spatial frequencies using image pro-

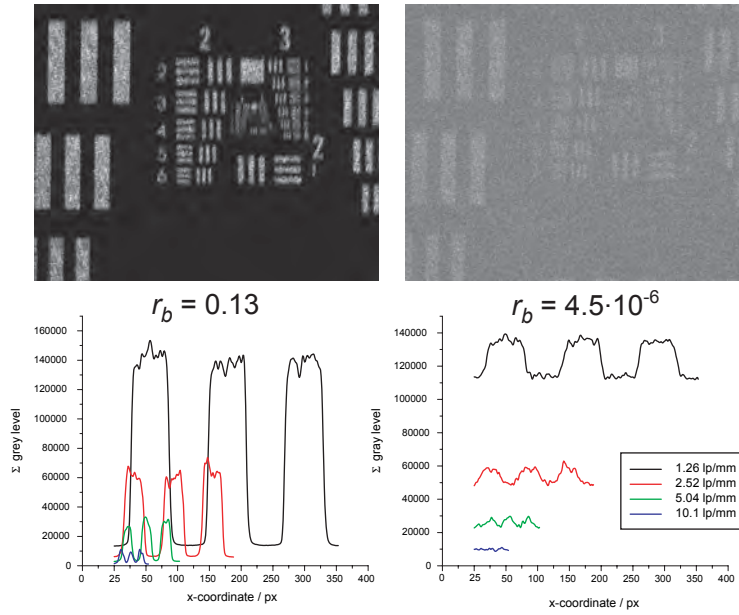


Figure 3.4: Example reconstructions of the test pattern for two different ratios of the object-to-reference intensity r_b (top) and corresponding line-averaged profiles used to calculate the reconstructed image visibility (bottom).

cessing scripts under MATLAB. In a first step, all chosen vertical structures (we used the element number 3 of the groups 0 to 3) were averaged column-wise to obtain a line-profile for the corresponding spatial frequency as depicted in Figure 3.4. In a second step these profiles have been correlated with an ideal rectangular function of the same spatial frequency. The resulting shift Δx is then used to identify the sections of the upper and lower level (Figure 3.5). Finally, the values within each section are averaged to obtain G_{\max} (upper level) and G_{\min} (lower level) values from which the image visibility V_i is calculated according to:

$$V_i = \frac{G_{\max} - G_{\min}}{G_{\max} + G_{\min}}. \quad (3.10)$$

As a criterion for the acceptance of values of V_i , the standard deviations σ_1 and σ_2 within both ranges are used to discard questionable results (refer to Figure 3.5). Values for the image visibility V_i which comply with the following rule have been discarded:

$$G_{\max} - G_{\min} < \sigma_1 + \sigma_2, \quad (3.11)$$

since these are related to cases in which the vertical structures are no more clearly visible in front of the background.

Plotting the calculated visibility versus the ratio r_b of object-to-reference intensity (Figure 3.6) shows distinct curves. It is found that noise does not spoil the image quality for a range of approximately three orders of magnitude of r_b . A further decrease of r_b causes a rapidly decreasing visibility. The remaining fluctuations of V_i can

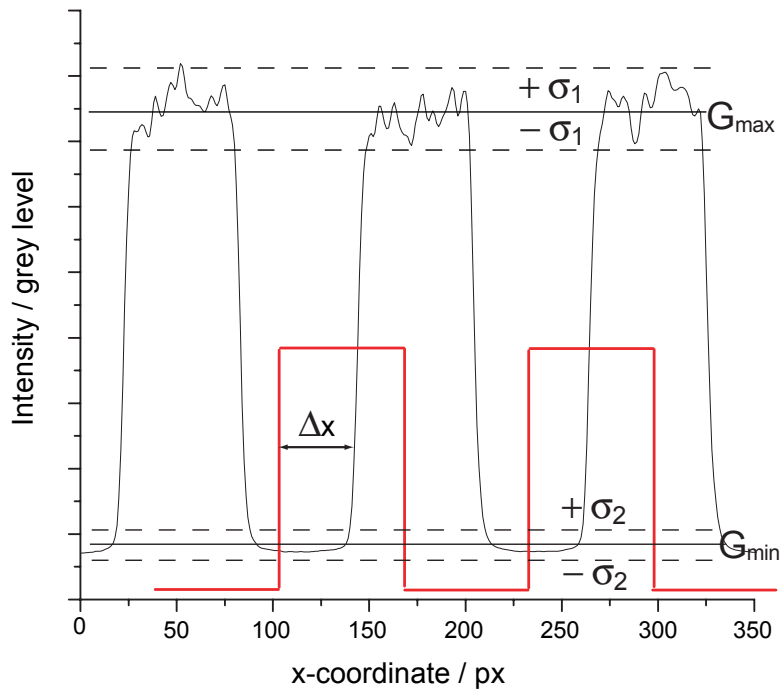


Figure 3.5: Values within the profile are assigned to be either a max-value or a min-value by a correlation procedure determining the relative shift Δx with respect to an ideal rectangular function. Values from both sections are averaged for the calculation of the image visibility V_i . A criterion to discard questionable values is formulated on the basis of the standard deviation of those values.

be attributed to the reproducibility of the wet chemical developing process. At certain values of r_b (marked with dashed lines) two holograms from different plates have been investigated, showing variations in their image visibility of up to 20 %, especially at lower values for r_b .

3.2.2.3 The Emulsion Grain Noise Limit in Particle Holography

As already mentioned in the introduction of this Chapter, the noise limit at which holographic particles images can be reconstructed plays an important role when large volumes need to be investigated. In particle holography the sizes of the structures (tracer particles) are in general somewhat smaller as those structures observed in the experiment of Section 3.2.2.2. Furthermore their shapes are no more regular, as we have seen in Section 2.3.1 and their number density is considerably higher. It is therefore expected that the reconstructed particle images vanish much earlier in a noisy background when r_b is decreased, a behaviour which is also predicted by (3.9).

A HPIV model experiment with a particle-laden block of perspex (PMMA) was carried out to find the noise limit which prevents an evaluation by correlation techniques. For this purpose the setup was modified to provide a thick light sheet (3 mm) normal to the viewing direction and a translation stage to introduce a known displacement of the particle block (Figure 3.7).

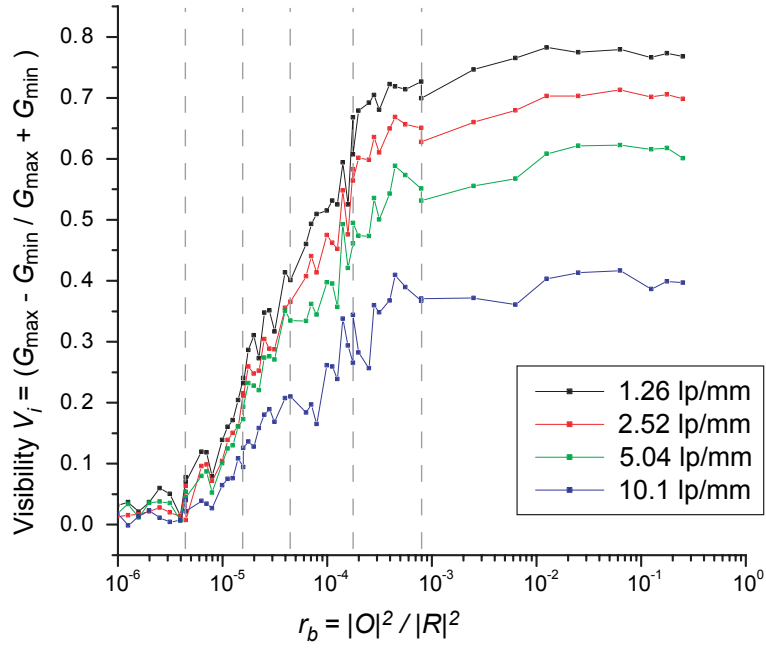


Figure 3.6: Image visibility V_i of the test pattern versus object-to-reference beam ratio r_b for four different spatial frequencies.

For each beam ratio r_b two holograms were recorded using a double exposure and displacing the block in between. The reconstructed images ($1280 \text{ px} \times 1024 \text{ px}$), digitised at the middle of the light sheet, have then been evaluated using an autocorrelation algorithm giving more than 1000 individual interrogation areas of $128 \text{ px} \times 128 \text{ px}$. From each correlation function the corresponding SNR (here the height of signal peak R_d over the height of largest noise peak R_n) was used to characterise the image quality. According to Keane and Adrian (1990) we call this ratio the "peak detectability":

$$D_p = \frac{R_d}{R_n}. \quad (3.12)$$

This criterion is related to the success of an evaluation of the local displacement from both recordings. Since in this case a quality criterion different from the previously used SNR has been applied, we will establish a relation between both in Section 3.2.2.4.

Samples of reconstructed images for different values of r_b are shown in Figure 3.8, each giving a magnified view of one interrogation area. Even though the particle density is lower than recommended for an optimum detectability, it becomes clear from inspecting the images that particle pairs tend to hide in a speckle pattern when r_b is decreased. Since the speckle size is similar to the size of the particle images the detectability becomes more and more independent of the number of particle pairs per interrogation area for decreasing r_b (i.e. brighter speckles). This is due to the self correlation of the speckle field which produces numerous peaks R_n similar in size to R_d .

An estimate of the noise limit for this type of particle holography is obtained by plotting the detectability D_p versus the object-to-reference intensity ratio r_b as shown in

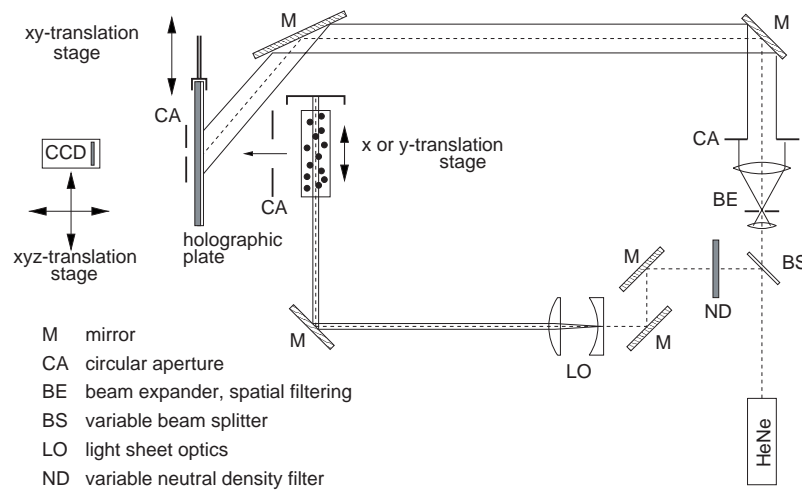


Figure 3.7: Modified setup to provide for double exposed images for different values of the object-to-reference beam intensity ratio r_b . The particle block is illuminated with a thick light sheet normal to the viewing direction and translated between exposures to simulate HPIV recordings.

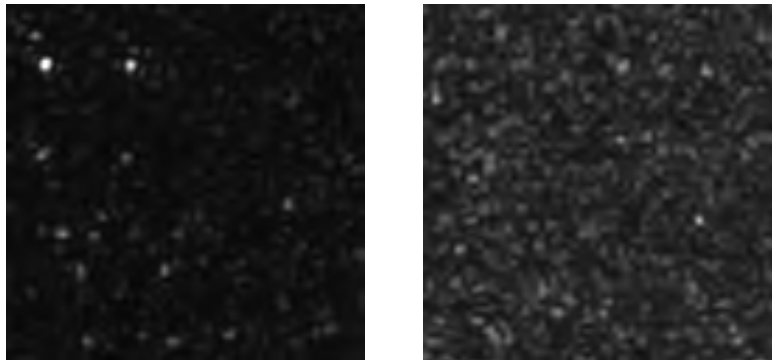


Figure 3.8: Magnification of single interrogation areas ($128 \text{ px} \times 128 \text{ px}$) from experiment with a model particle block at $r_b = 3.1 \times 10^{-2}$ (left) and $r_b = 1.5 \times 10^{-4}$ (right).

Figure 3.9. In this plot, each point is an average value of the detectability of all interrogation areas in one image related to a double exposure hologram recorded at the given beam ratio r_b . The influence of variations of particle density and brightness is thus minimised. However, it can be found from Figure 3.9 that reproducibility is a crucial point in this experiment. Holograms recorded at the same beam ratio r_b sometimes show a significant difference in their values D_p . Two results (shown as open circles) have even been discarded for the following analysis. Thus, only tendencies can be extracted from the experimental data. The acceptable noise limit for the evaluation of a local displacement by autocorrelation in two dimensions is given according to (Keane and Adrian, 1990) at a minimum detectability of $D_p = 1.5$ and thus corresponds to a beam ratio of $r_b \approx 10^{-3}$ for the present situation.

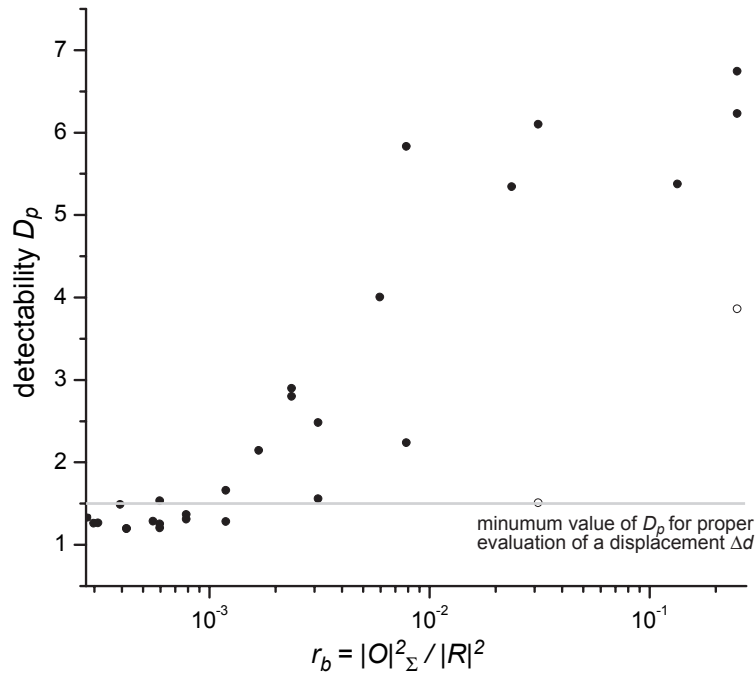


Figure 3.9: Experimental data on the influence of a decreasing object-to-reference intensity ratio r_b during the recording of a double-exposed particle hologram. The detectability D_p , a measure to detect a displacement of particles introduced between the two exposures, is shown versus r_b . A reasonable limit for successful evaluation of the displacement is according to Keane and Adrian (1990) at $D_p = 1.5$

3.2.2.4 Validation of the Results and Conclusions

The SNR of the particle images under investigation, or their ratio of particle image to background intensity, respectively, is closely related to the detectability obtained in the correlation scheme to evaluate displacements. To show this a Monte-Carlo simulation was used exploring the influence of speckle size and SNR on the detectability. Figure 3.10 shows an example of a modelled particle image with gaussian intensity distribution, from which always two with known but constant horizontal displacement have been placed randomly over a simulated speckle pattern (1280 px \times 1024 px). The particle image intensity was always set to a grey value of 250 and the mean background intensity to a value determined by $I_0 / \langle I_N \rangle$. Furthermore, the speckle size was varied over a large range to check their influence. Mostly, the particle images in HPIV are diffraction limited in size and thus should have a similar size. A further example of a single interrogation area shows the overlapped image. From the resulting curves it can be seen that smaller speckle sizes permit slightly lower intensity ratios to reach a certain detectability, while around $I_0 / \langle I_N \rangle = 100$ an influence of the speckle field can be no longer observed. Shown with dashed lines is a good contrast case with SNR = 5, corresponding to $I_0 / \langle I_N \rangle = 50$ according to (3.2).

To check our experimental data, the properties of the holographic material (refer also to Figure 2.6), as well as the number of particles and the proper spatial frequency,

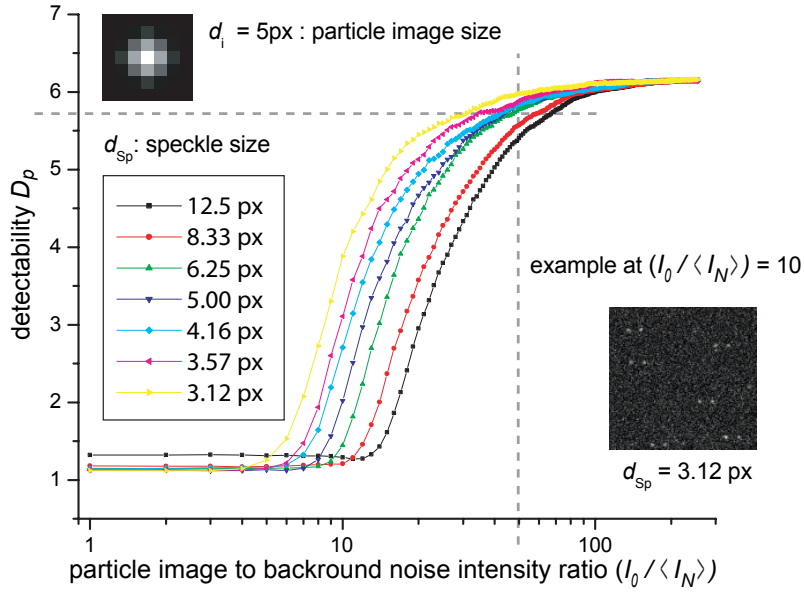


Figure 3.10: Monte-Carlo simulation to describe the influence of speckle size and SNR in particle images on the detectability using auto correlation algorithms.

corresponding to our experiment are introduced in (3.9). It has to be mentioned that the value for the Wiener spectrum $\Phi(\nu)$ can be only a rough estimation based on the known function for the Kodak 694F plates, since this function has yet not been measured for the Slavich PFG-01 plates. With $\Phi(\nu) = 1 \times 10^{-8}$, $K = 0.87$, $\eta = 0.526$, $A_t = 20 \text{ mm}^2$ and $N = 3.3 \times 10^4$ the beam intensity ratio r_b can be calculated for each ratio $I_0 / \langle I_N \rangle$ given for a known detectability D_p according to the simulation as shown in Figure 3.10. The resulting plot of detectability D_p versus r_b is shown in Figure 3.11 together with the experimentally obtained data. It is seen, that the simulation results slightly underestimate the limiting beam intensity ratio of the experiment (the difference is probably due to the approximated value $\Phi(\nu)$) but indeed show a similar behaviour.

From a practical point of view two boundaries can be defined from the results of the present study. Since a more pronounced speckle background than in PIV is present in HPIV, the detectability threshold defining an acceptable noise limit is set to $D_p = 2$, the lower boundary for the beam intensity ratio is thus $r_b = 2 \times 10^{-3}$. The upper boundary is reasonably given by the afore mentioned, but arbitrarily assumed $\text{SNR} = 5$ (cf. Section 3.2.1), which corresponds to a beam intensity ratio of $r_b = 2 \times 10^{-2}$. Presuming that only small fractions of light are scattered by the particles contained in an illuminated volume (i.e. the energy density of the illuminating beam stays constant along the depth direction), the cross section of the illumination can thus be increased by a factor of $k_i = 0.25/0.02 \dots 0.002 = 12.5 \dots 125$. Typical HPIV experiments with present length scales in the order of 100 mm could thus be extended by $\sqrt{k_i}$ to dimensions of 350 ... 1120 mm! But care should be taken, that with larger cross-sections typically also the distance between the measurement volume and the hologram increases and

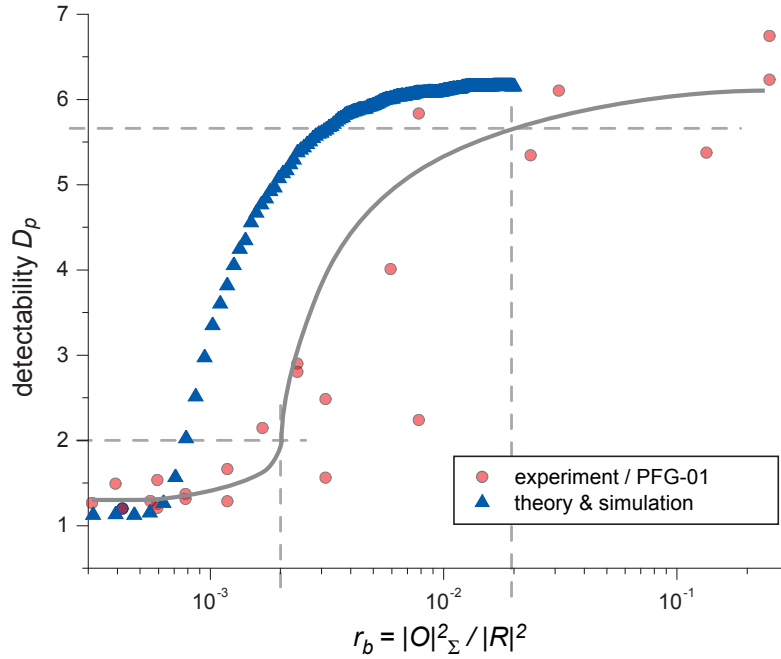


Figure 3.11: Theoretical behaviour of detectability D_p versus beam intensity ratio r_b for Slavich PFG-01 plates. The experimental data obtained with these plates is shown for the purpose of comparison.

thus more particles contribute by adding intrinsic speckle noise. Even though the depth of the light sheet is considerably larger than the depth-of-focus (according to (2.26): $d_f \approx 41 \mu\text{m}$) of the corresponding holograms, the latter source of noise has not been considered in the present study.

As a conclusion, present restrictions in the size of the volume under investigation can be relaxed by taking advantage of the high dynamic range of common holographic materials. A method has been proposed using a time-integrating reconstruction to cope with lower than required object light still producing bright enough holographic images. This principle can be used to compensate for the loss in diffraction efficiency. Limits of this technique are given by disturbing background light, mainly scattered from the silver grains in the developed holographic emulsion. It has been shown that considerable reductions of object light are tolerable, still enabling the reconstruction of object images. General experiments on test targets gave a first idea about the limits of this technique. For particle holography these limits are strongly related to the number of particles, as also shown in a theoretical approach. Nevertheless, for common HPIV setups a considerable gain in the dimensions of the measuring volume is expected. Thus, applications in larger flow facilities become feasible as we will show in Chapter 8.

4 Short Coherence Holography for Background Noise Reduction

The chosen method for the reduction of background noise in holographic particle images is a short coherence recording of holograms, the so-called Light-in-Flight Holography (LiFH). Section 4.1 describes this method in its initial context and discusses applications and requirements. The application of LiFH to HPIV, forming our method of LiFH-PIV, is introduced in Section 4.2. Previous achievements using the virtual image reconstruction are reviewed, before the real image reconstruction, which is generally favoured for HPIV, is demonstrated with this method.

4.1 Principle of Light-in-Flight Holography

4.1.1 Basic Considerations and Demonstrational Experiment

The idea of frameless motion pictures from holograms of ultrafast phenomena was first mentioned by Abramson (1972) before its realisation was published in great detail and after extensive development during the 70's with many holographic experiments by the same author (Abramson, 1983). This publication was driven by a great response from the scientific community to a short demonstration published earlier (Abramson, 1978). The light-in-flight technique is based on holographic recording with short-coherence laser light (see Section 4.1.4) or, alternatively, with short laser pulses. Both realisations are equivalent, due to the fact that only a coherent superposition of light forms the interference pattern recorded by the holographic plate.

In the case of short laser pulses (picosecond pulses have been used for the experiments reported in the literature given above), the length of a wave train is typically a few tenths of a millimetre. It follows, that the path difference between reference and object light must be in the same order of magnitude to record any information holographically. If short coherence light sources are used, the path difference must be in the order of the corresponding coherence length l_c . Light with path differences larger than this value lacks a constant phase relation and thus does not contribute to the recorded information. Provided that the interaction length, wherein the interference pattern is formed, is sufficiently small, the information can be distributed on the hologram along the path of a grazing incident reference beam.

A basic experiment to demonstrate LiFH is shown in Figure 4.1 (Abramson, 1983). A light source L with short coherence length l_c grazingly illuminates a ruler. At position E part of the light is directed to another mirror D to be obliquely incident on the holographic plate H. Along the holographic plate, this reference beam travels with an increasing path length, which must be compensated by a corresponding path length of

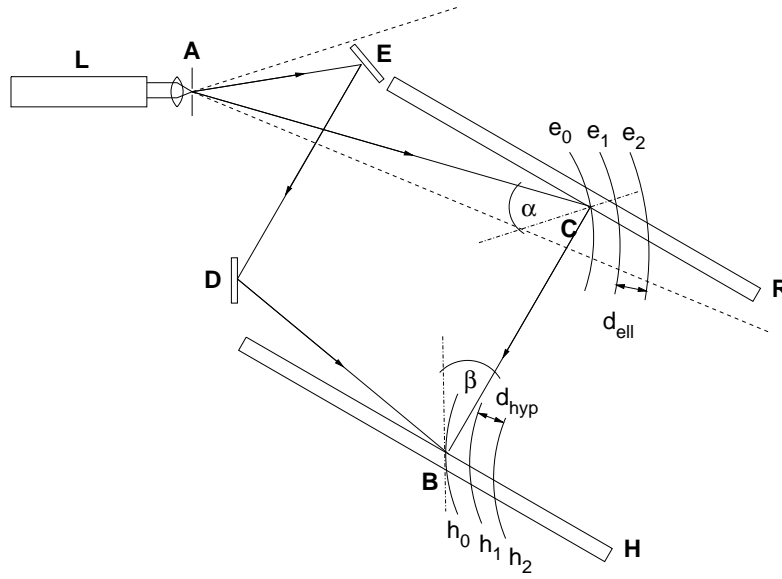


Figure 4.1: Principle experiment to demonstrate Light-in-Flight holography (LiFH) after Abramson (1983). A: point source of light, B: observing point on hologram, C: from point B reconstructed point on the ruler, D and E: mirrors, H: holographic plate, R: ruler, e_i : ellipsoids, h_i : hyperboloids

the object light, travelling along the ruler. The difference between both path lengths must not exceed the coherence length l_c . If such a hologram is reconstructed, different parts of the ruler can be seen when viewed through the corresponding sections on the hologram. Point B for instance is connected to the point C on the ruler. Positions of equal path length corresponding to a given point on the holographic plate (say B), are distributed on an ellipsoid (e_0) in space having its focal points at the point source A and the given point (here again B). The other way round, positions of the same path length for a given point on the ruler (say C) are located on a hyperboloid (h_0) with focal points A and C' as the mirror image of C across the point A. Taking into account that deviations between the corresponding path lengths smaller than the coherence length l_c lead to an interference, all path lengths must comply to the relationship:

$$|ACB - AEDB| \leq l_c. \quad (4.1)$$

The distances d_{ell} and d_{hyp} in Figure 4.1 represent the thickness of a shell either viewed through an observation point or corresponding to a reconstructed point and are defined by the above condition for changing either B or C. This depth depends on the coherence length l_c of the light source and for the special case $\alpha \approx \beta$ it follows: $d_{\text{ell}} \approx d_{\text{hyp}} \approx l_c$.

In LiFH, space and time are equivalent apart from the constant c , the velocity of light. Assembling frames reconstructed from equally spaced observation points leads to a motion picture with incredibly high frame rates. Abramson (1983) has demonstrated

this ability with impressive results from light passing through a thick lens, showing refraction and delay of the light wave by the glass.

4.1.2 Common Applications of Light-in-Flight Holography

During the 80's a whole series on applications of Light-in-Flight Holography was published by Nils H. Abramson et al. Not all of them aimed to study temporal dynamics in interferometry, reflection, refraction and diffraction, but imaging of ultrahigh-speed phenomena still remains one of the major fields of LiFH (Abramson, 1984a). Also optical relativistic effects and their compensation have been treated (Abramson, 1984b, 1985), as well as light passing through optical fibres (Abramson, 1987). Further extensions of the method have been proposed and tested (Abramson et al., 1989; Pettersson et al., 1989) and 3D shaping with micrometer resolution was demonstrated with a single shot of a short-pulsed laser offering sufficient energy, which just had become available at that time (Abramson and Spears, 1989). The analogy to the radar principle has led to the term Optical Coherence Radar (OCR) or OC Tomography (OCT). Another closely related technique is the White-Light-Interferometry (WLI). All of them are nowadays widely used techniques in many applications, as they can also be applied in non-imaging mode based on the interference of single laser beams. A similar method is used in an autocorrelator device to measure the pulse length of ultrashort laser pulses, its basics, however dates back to the time before Light-in-Flight (Staselko et al., 1969).

4.1.3 Technical Requirements

To record holograms with the LiFH method the light source has to be pulsed with a sufficiently short pulse length (typically a few picoseconds) or must have a sufficiently short coherence length (a few millimeter down to a few micrometer) depending on the desired resolution. Pulsed lasers used for LiFH are typically operated with mode-locking, i.e. the phases of the amplified resonator modes are coupled to each other and only a single pulse is existent in the resonator. The pulse length τ can then be obtained from the number of modes N oscillating in a resonator of length L (Kneubühl and Sigrist, 1995):

$$\tau = \frac{2\pi L}{cN}. \quad (4.2)$$

Since for most applications, lasers are required which exhibit a long coherence length, light sources suited for LiFH are often not available. But a few modifications can render a long coherence laser usable for LiFH. Removing a mode selecting (tilted) etalon for example was already used by Abramson (1978) to shorten the coherence length of an ordinary argon-ion laser. Another method, but with comparatively higher effort, would be to increase the resonator length of an existent laser design to increase the number of amplified modes.

For the studies presented in this thesis, lasers with a short coherence length l_c have been used, which were available with sufficiently high pulse energies to illuminate small tracer particles. These lasers are Q-switched solid state lasers: a ruby laser emitting at $\lambda = 694$ nm and a Nd:YAG laser with frequency conversion to obtain $\lambda = 532$ nm with pulse lengths of $\tau \approx 20$ ns and $\tau = 7$ ns and a coherence lengths of $l_c = 10$ mm or $l_c = 7$ mm, respectively.

4.1.4 Coherence Theory

The coherence length l_c of a light source determines the resolution of the Light-in-Flight method. In the following, a short review of the coherence theory is given to introduce the term coherence length, followed by a discussion on the properties of lasers which influence the coherence length.

Optical coherence is generally defined by the correlation properties between quantities of an optical field, where the usual interference is the simplest phenomenon revealing correlations between light waves (Lauterborn et al., 1995). A general description of coherence is given by the so-called complex degree of mutual coherence (also called spatiotemporal coherence) defined at a point P and dependent on the source points \mathbf{r}_1 and \mathbf{r}_2 according to Figure 4.2:

$$\gamma_{12}(\tau) = \frac{\Gamma_{12}(\tau)}{\sqrt{\Gamma_{11}(0)\Gamma_{22}(0)}}, \quad (4.3)$$

with $\Gamma_{12}(\tau) = \langle E(r_1, t + \tau) E^*(r_2, t) \rangle$ the complex mutual coherence function and $\Gamma_{11}(0), \Gamma_{22}(0)$ the intensity at \mathbf{r}_1 and \mathbf{r}_2 , respectively (Zernike, 1938).

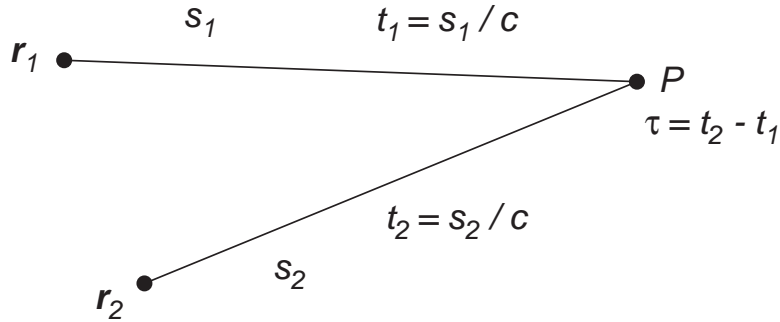


Figure 4.2: Notation used in the derivation of the mutual coherence

The contrast V of the resulting interference fringes can be determined as follows:

$$V = \frac{I_{max} - I_{min}}{I_{max} + I_{min}} = 2 \frac{\sqrt{\Gamma_{11}(0)\Gamma_{22}(0)}}{\Gamma_{11}(0) + \Gamma_{22}(0)} |\gamma_{12}(\tau)|, \quad (4.4)$$

or in the case of interfering waves with equal intensity: $V = |\gamma_{12}(\tau)|$.

The mutual coherence has two limiting cases, temporal and spatial coherence, from which the first is directly related to LiFH. The special case of self coherence, the superposition of two time-shifted light waves from the same source, is described by the complex self coherence function:

$$\Gamma(\tau) = \langle E^*(t)E(t + \tau) \rangle = \lim_{T \rightarrow \infty} \frac{1}{T} \int_{-T/2}^{+T/2} E^*(t)E(t + \tau) dt \quad (4.5)$$

and is thus the autocorrelation function of the complex light wave $E(t)$. When normalised with $\Gamma(0) = I = |E(0)|^2$ the complex degree of self coherence is obtained:

$$\gamma(\tau) = \frac{\Gamma(\tau)}{\Gamma(0)} \leq 1. \quad (4.6)$$

For monochromatic light $\gamma(\tau) = \exp(-i\omega\tau)$ shows the remains of a harmonic wave and $V(\tau) = |\gamma(\tau)| = 1$. Such light is then called completely coherent and has by definition an unlimited coherence length $l_c = \infty$. This limiting case can only be realized approximately, for instance, with a stabilised single-mode laser. Any natural or artificial light source exhibits a decreasing contrast function, which is often also monotonously decreasing. This decay is characterised by the coherence time τ_c , defined as the time shift when the contrast function has decayed to the value $1/e \approx 0.368$. The coherence length l_c is then readily defined as:

$$l_c = \tau_c \cdot c. \quad (4.7)$$

When lasers are used as the light source, the contrast function often shows a periodic dependence on τ due to many frequencies arising in a resonator. By letting $E(t)$ be the sum of many harmonic waves of different frequency:

$$E(t) = \sum_{m=1}^M E_m \exp(-i\omega_m t), \quad (4.8)$$

with (4.5), the self coherence function is then:

$$\Gamma(\tau) = \sum_{m=1}^M |E_m|^2 \exp(-i\omega_m \tau). \quad (4.9)$$

When the limit to arbitrarily densely spaced harmonic waves is calculated with:

$$E(t) = \int_{m=1}^M E(\nu) \exp(-i2\pi\nu t) d\nu, \quad (4.10)$$

it follows again from (4.5):

$$\begin{aligned}\Gamma(\tau) &= \int_0^{\infty} |E(\nu)|^2 \exp(-i2\pi\nu\tau) d\nu \\ &= W(\nu) \exp(-i2\pi\nu\tau) d\nu.\end{aligned}\tag{4.11}$$

From (4.11) it can be seen that the self coherence function is the fourier transform of the power spectrum $W(\nu) = |E(\nu)|^2$ of the complex light field and thus the result is the optical equivalent of the Wiener-Khintchine-Theorem (Wiener, 1930; Khintchine, 1934).

Assuming that the power spectrum $W(\nu)$ has a gaussian shape it can be shown (see Appendix A.6) that the coherence length l_c is inversely related to the line width $\Delta\nu$ of the corresponding radiation:

$$l_c \approx \frac{c}{\Delta\nu}.\tag{4.12}$$

Assuming a lorentzian shape, the coherence length l_c is further reduced by the factor $1/2\pi$ (Kneubühl and Sigrist, 1995).

The resulting line-width $\Delta\nu_L$ of light amplified by stimulated emission of radiation (LASER) depends on a variety of factors, including properties of the active material and the type of the optical resonator. In many cases the spectral cleanliness or simply the final linewidth of the radiation output can be found from the manuals of the laser manufacturer, thus only a short review of the influencing factors is given here.

The line-width $\Delta\nu_D$ of radiation from an active material is never a sharp line solely determined by the energy difference between excited and (meta-) stable states, but is broadened by a variety of mechanisms, depending on the type of laser (Koechner, 1999). One distinguishes between homogeneously (same effect on all atoms) and inhomogeneously (effect on individual atoms by displacing their center frequency) broadening mechanisms. Among the first type there is lifetime broadening due to spontaneous emission or fluorescence, which is referred to as the natural line-width $\Delta\nu_N$ of radiation. Furthermore, there is collision broadening especially in gas lasers at higher pressures, dipolar broadening from interactions between the magnetic or electric dipolar fields of neighbouring atoms and thermal broadening due to lattice vibrations in solid state materials. The inhomogeneous broadening can be due to Doppler shifts of randomly moving gas atoms and is hence a common mechanism in gas lasers. Another mechanism of this type is broadening due to crystal inhomogeneities, like crystalline defects. Depending on the predominate mechanism, the shape of the corresponding radiation spectrum is either more gaussian (inhomogeneous effects dominate) or more lorentzian (homogeneous effects dominate) and the broadened line-width is referred to as $\Delta\nu_D$, indicating that the Doppler broadening is the main mechanism in many lasers.

When the laser is operated without mode selection techniques (e.g. tilted etalons, dye absorber) many modes start to oscillate and the resulting line-width $\Delta\nu_L$ strongly de-

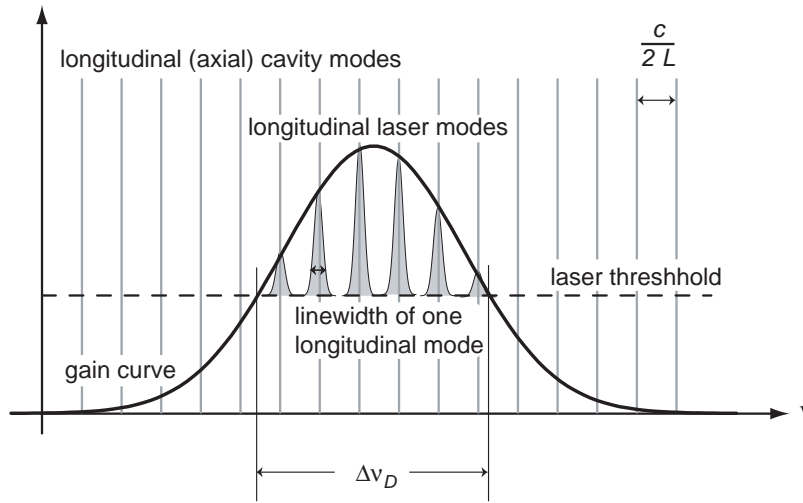


Figure 4.3: The number of oscillating axial modes in a laser cavity is determined by the gain threshold, the distance $c/2L$ of the passive cavity modes and the line-width of the active medium radiation $\Delta\nu_D$.

depends on the type of the resonator (cavity). Figure 4.3 illustrates the situation schematically. The number N of oscillating axial modes (Eigen-frequencies of the laser resonator) is mainly determined by:

$$N = 2 \Delta\nu_D \cdot \frac{L}{c}, \quad (4.13)$$

with L the length and $c/2L$ the distance between single modes of the optical resonator (Weber and Herziger, 1972). According to Booth et al. (1970), the contrast and thus the self coherence function (Figure 4.4) can also be obtained from the number N of amplified modes in a resonator of length L from:

$$|\gamma(\tau)| = \left| \frac{\sin\left(\frac{N\pi c\tau}{2L}\right)}{N \sin\left(\frac{\pi c\tau}{2L}\right)} \right|. \quad (4.14)$$

Whenever the coherence length l_c in the sense defined above is not meaningful, i.e. $\gamma(\tau)$ is a rapidly oscillating function, the location of the first root or the first minimum can be taken as a measure of the coherence time τ_c .

Further conclusions about a Nd:YAG laser suited for LiFH and ordinary holography, as well as details about its coherence length are given in Section 5.2.2.

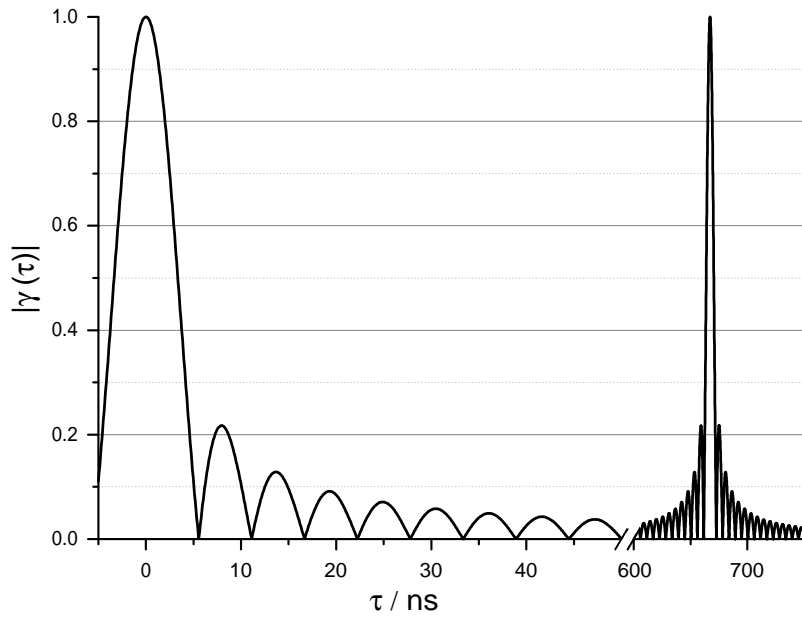


Figure 4.4: Approximation of self coherence function $|\gamma(\tau)|$ for resonator length $L = 1$ m and $N = 120$ amplified modes.

4.2 Noise Reduction by Short Coherence Recording in Particle Holography

As already mentioned in Chapter 3, holographic particle images especially from densely seeded and deep volumes, suffer from inherent background noise due to coherent superposition of the in-focus particle images (signal) with the out-of-focus images (noise) of particles further away from the observation plane. Masking the noise contribution is thus highly desirable to obtain high quality particle images throughout a deep volume. First approaches to relax the noise problem in HPIV used a multi-light-sheet configuration made up from a folded beam path illuminating the particles (Hinsch et al., 1990, 1993). A short coherence length and several reference beams, each adapted in their path length to those light scattered from particles of the corresponding light sheet, had to be adjusted. Thus, the setup was highly complex and limited to a few parallel measurement planes.

Section 4.2.1 discusses how the LiFH method, introduced above in Section 4.1, can be utilised for an adaptive masking covering the whole recorded volume. The virtual image reconstruction in LiFH can be used for visualization purposes, revealing detailed insight in flow structures as described Section 4.2.2, but also the first applications of LiFH to HPIV used this image. Finally, Section 4.2.3 demonstrates the gain in particle image quality, when using LiFH and the real image reconstruction.

4.2.1 Backscattering Geometry, Aperture Effect and Coherence Depth

With careful construction of a LiFH experiment similar to those of Figure 4.1, it is possible to obtain reconstructed shells nearly parallel to the holographic plate. For this, two conditions have to be met. Firstly, the beam-splitting element dividing object and reference beam with a cross-section of some centimeters (compare to point A in Figure 4.1) needs to be far away from the combining point (compare to point B) on the holographic plate. This ensures a small curvature of the reconstructed ellipsoids. Secondly, the beam illuminating the object should ideally travel on the line connecting holographic plate and object. In this way, the optical path difference is identical for left and right hand areas of the object at the same depth position but maximised for depth positions in front or to the rear of the object area. A beam splitter in front of the holographic plate would allow to illuminate the particles in such a way and simultaneously observe the back-scattered light. But, since the beam splitter needs to be large enough to make use of the full aperture, the more practical solution to meet the second condition is to slightly incline the illumination and observation direction by an angle φ as shown in Figure 4.5.

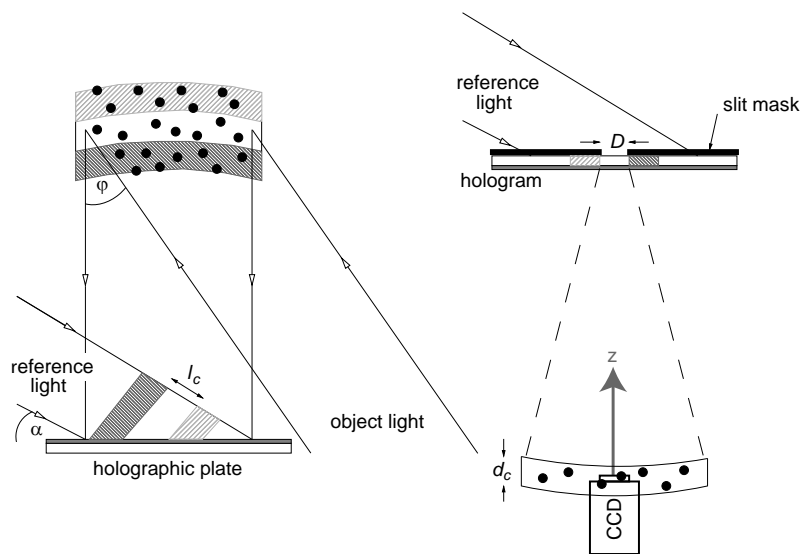


Figure 4.5: A schematic diagram of the set-up for recording light-in-flight holograms of particle fields and reconstructing real particle images. The finite coherence length l_c restricts holographic recording to a field limited in depth. Its location depends on the position of the aperture on the hologram.

Observing light scattered from particles in a nearly backward direction has two advantages over other HPIV realizations: the intensity of scattered light is usually much higher than in a side-scattering configurations and additionally the angular characteristic ensures recording on the entire holographic plate (cf. Section 2.3.1), which is usually not the case for systems employing near forward scattering to utilize the higher intensity scattering lobes.

The scattered light is superimposed on the holographic plate with a collimated reference wave, which is obliquely incident. In the case depicted in Figure 4.5 the reference wave has travelled a longer path at the right of the plate than at the left. Similarly, the light from the far-off particles has travelled further than light from those nearby. Recording of the desired depth range is achieved by adjusting the reference path length to be nearly identical to the path of light travelling from the middle of the particle field at the middle of the holographic plate. Due to the limited coherence length l_c a successful holographic recording at a given position on the holographic plate is obtained only with light from a confined area in depth.

To separate different regions in depth, the reconstruction of a LiF hologram needs to be done through a limited aperture which can be moved along the hologram. This method can be used either for the reconstruction of the virtual image, which is observed directly through the aperture or (as depicted in Figure 4.5) for the real image. In the latter case, the observer or imaging sensor has to be positioned within the reconstructed shell and traversed accordingly when the aperture is moved. Further details of the real image evaluation are given in Section 6.2.3.

The aperture on the hologram is a key-element of the Light-in-Flight technique, its influence is twofold and contrary in terms of image quality. On the one hand this aperture determines the depth resolution of the holographic image (cf. Section 2.2) and should thus be maximised. On the other hand it confines the extent of the reconstructed shell and should thus be as small as possible to achieve a good suppression of background noise.

The latter effect, a consequence of the Light-in-Flight recording, can be thought off as a convolution of the coherence depth for an imaginary point-like hologram with the dimension of the aperture along the reference beam direction. The precise value of this coherence depth d_c thus depends on the shape of the aperture, the angle φ between the illumination and viewing directions and the angle of incidence α of the reference wave. A limited-area aperture on the hologram (let it have the size D along the hologram direction) will reconstruct only images within a shell of depth:

$$d_c = \frac{l_c + D \cos \alpha}{1 + \cos \varphi} \approx \frac{D + l_c}{2}, \quad (4.15)$$

where the approximation only holds for our typical situation of a grazing incident reference wave and almost backscatter viewing.

4.2.2 Virtual Image Reconstruction

This section reviews briefly the achievements obtained with LiFH and virtual particle image reconstruction using a modified ruby laser (JK Laser System 2000, $\lambda = 694$ nm). With all its intracavity etalons removed, this ruby laser provided a coherence length of $l_c \approx 1$ cm. In double-pulse configuration the system delivered pulses of up to 5 J energy with a duration of typically $\tau = 20 - 30$ ns.

4.2.2.1 LiFH for Visualisation Purposes

For visualisation purposes the virtual image of a LiF hologram is ideal. It can be easily viewed by eye or camera, when simultaneously moving the aperture and the observer along the hologram as shown in Figure 4.6 for a CCD camera. In that way a large number of sheet-like extractions can be obtained from a single hologram. Each position of the camera, closely placed behind the hologram defines a limited aperture due to the f-number setting of the camera, which can be reduced by an external aperture (e.g. slit or circular mask). A linear relationship between hologram position and depth ensures that the corresponding plane in focus can be shifted equally spaced at their mid-depth position. The planes in focus, however, are not parallel but slightly tilted, which must be taken into account when assembling a full-field view from the digitised planes.

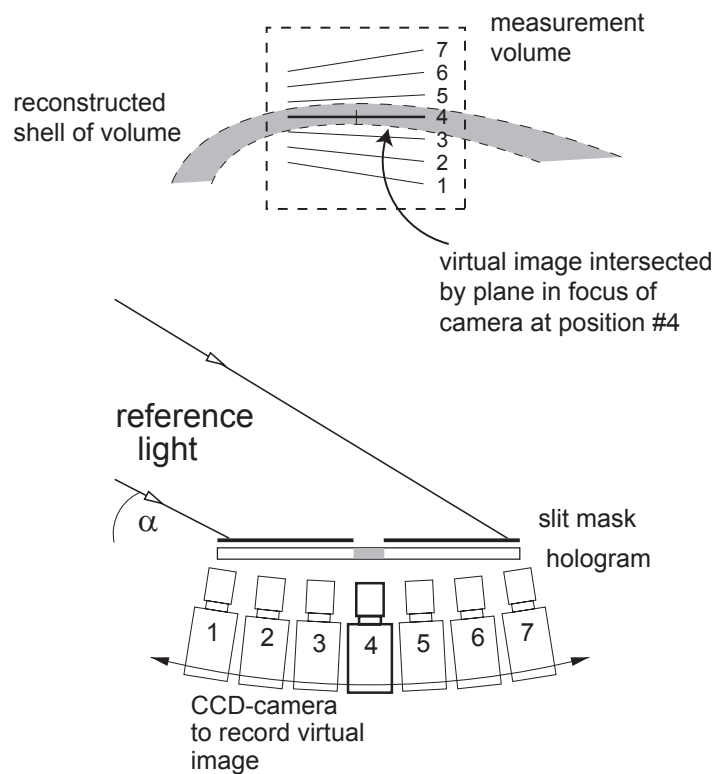


Figure 4.6: Sheet-like extraction of virtual LiFH image, the sensor and aperture position defines the depth of the reconstructed shell (gray shaded area) in which the plane of focus is centered. By moving the aperture the shell moves in depth accordingly.

The ability of the method to view images through a disturbing background has been successfully demonstrated in the study of a nozzle flow (Herrmann et al., 2000). Only the air flow from the nozzle ($v = 2$ m/s at the outlet) was seeded to ensure conditions suitable for visualisation. Figure 4.7 a) shows details of the measurement volume and its location with respect to the nozzle's center axis. Results from the virtual image are presented in the form of a series of selected cuts normal to the viewing direction through the volume, which were all evaluated from a single holographic record (Figure 4.7 b)-g)). Under ordinary conditions, a photographic account of the irregularly seeded

flow would produce just a single bright cloud due to the superposition of all the many particles within the deeply illuminated cross-section of the jet. Here, however, it is obvious that structural information that is equivalent to data usually obtained from a single light sheet can be gathered for each of the sampled shells in depth. Roughly speaking, the light-scattering fog in front and behind the chosen sheet does not impair the viewing.

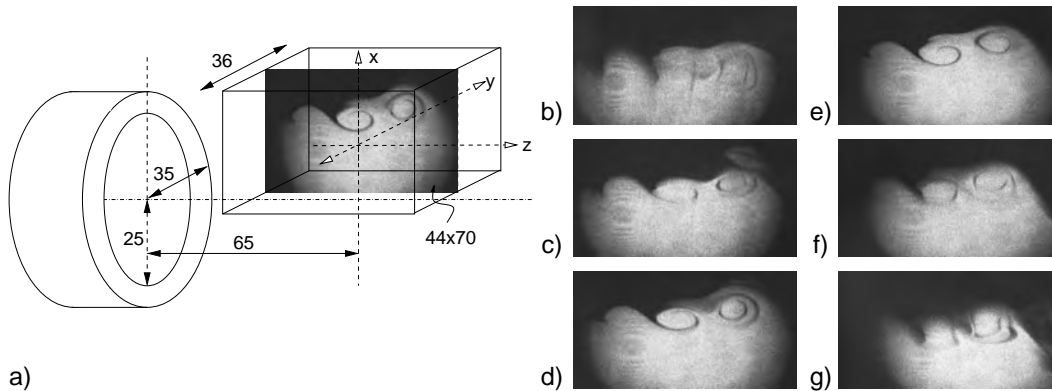


Figure 4.7: a) Nozzle outlet and location of measurement volume. b) - g) Reconstruction of selected sheets of particle distribution for flow visualisation of nozzle flow. The field of observation is $44 \times 70 \text{ mm}^2$ and the selected image planes are equally separated over 35 mm in depth.

Figure 4.7 illustrates quite clearly the plane-wise sampling of the three-dimensional vortex structure in the boundary layer between the jet and the surrounding (unseeded) air. It can be seen that the ring-vortex is cut at significantly lower positions by the front and rear planes than by the mid plane. The field depth, sampled by a total of 21 image planes is 46 mm and the cross-sectional area covers $44 \times 70 \text{ mm}^2$. The lower field boundary coincides with the nozzle axis.

4.2.2.2 Relevance of LiFH for HPIV and First Experiments

As shown in the example above, the Light-in-Flight method combines tomographic imaging with holography. The information is still a three-dimensional intensity distribution, which however, can be selectively replayed at certain depth positions and moved continuously through the volume. Thus LiFH is also suited for precise 3D position and shape measurements.

The advantage of LiFH for HPIV has been illustrated by a study examining the influence of the imaged particle-field depth on the success rate of correlation results (i.e. percentage of valid velocity vectors), both numerically and experimentally (Hinrichs et al., 1998). Depending on the correlation scheme (auto- or cross-correlation) used for the evaluation of either a doubly exposed or two single exposed holographic images, the success rate drops down with increasing field depth at rates of 2.9%/mm and 0.9%/mm, respectively. The evaluation by cross-correlation however, is more tolerant

to noise and enables success rates of nearly 100 % at a field depth of about 3 mm and rates still above 90 % until a depth of about 14 mm is reached. With an effective field depth of some 7 millimetres (refer to Equation (4.15)), the Light-in-Flight approach for HPIV thus permits successful measurements over total field depths which are considerably larger than those used in the simulation. Consequently, LiFH has been applied to HPIV measurements in flow-studies, first using the virtual image and is presently incorporated in more advanced set-ups scanning the real image (cf. Chapter 6).

The first application of LiFH for particle imaging (Hinrichs et al., 1997) was demonstrated in a single-exposure record with 5 μm particles in a water tank. The total depth of field illuminated by the object beam was 200 mm. By using a slit mask, 10 mm wide, the reconstructed images from different aperture positions have been correlated to determine the similarity between the images. In this way a measure for the coherence depth d_c was obtained.

Hinrichs et al. (1998) then applied the LiFH method successfully in a study of irregular vortex shedding behind a cylinder in a wind tunnel by using water-glycerine particles of a few μm in diameter. The evaluation of the double-exposure Light-in-Flight holograms was carried out by auto-correlation analysis which basically restricted the dynamic range of the system and requires a minimum particle displacement to ensure correct measurements (Keane and Adrian, 1990).

4.2.2.3 Fast Optical Switching for Cross-correlation Analysis

Cross-correlation analysis of two single exposed particle images allows for a much better dynamic range and is more tolerable to background noise (Keane and Adrian, 1991, 1992). To enable an evaluation in HPIV by cross-correlation, it is necessary to record two holograms in succession which can be reconstructed separately. The holograms can be separated either spatially (e.g. on different areas of the same plate or on different plates) or, in the case of superimposed recordings on one plate, by using reference waves incident at different angles. The latter (often referred to as angular multiplexing) is widely used in HPIV measurement systems and has also been applied in the system described by Herrmann et al. (2002).

In LiFH however, there occurs a special problem, because the angle of the obliquely incident reference beam determines which region in depth of the virtual image is visible from a certain location on the hologram. Each slit aperture normal to the plane of incidence reproduces a sheet in depth. Furthermore, to avoid misalignments between the images from first and second recording, it is necessary to reconstruct the same depth region for both holographic images without changing the position of the CCD camera, i.e. through the same aperture. As a consequence, the propagation direction of the reference waves had to be chosen in such a way that they are incident on the plate with the same azimuthal angle, but differ in the vertical angle - in the present case by about 10° . Cross-talk between the images is thus prevented sufficiently. Such an arrangement is depicted in Figure 4.8. The concept of a common aperture to reconstruct from both holograms is also used in our present set-up as described in the Sections 6.1.3 and 8.2.

Since for the recording of the holograms a double-pulse ruby laser has been used, the pulses had to be separated by a fast optical switch. The separation for the two reference beams was produced by a Pockels cell followed by a polarising beamsplitter. The electro-optic effect is used to rotate the polarisation of the second laser pulse by 90° . Consequently, the first pulse is reflected while the second is transmitted at the beam-splitter. To maintain good interference on the holographic plate with the object light the polarisation of the second pulse is turned back by a half-wave-plate.

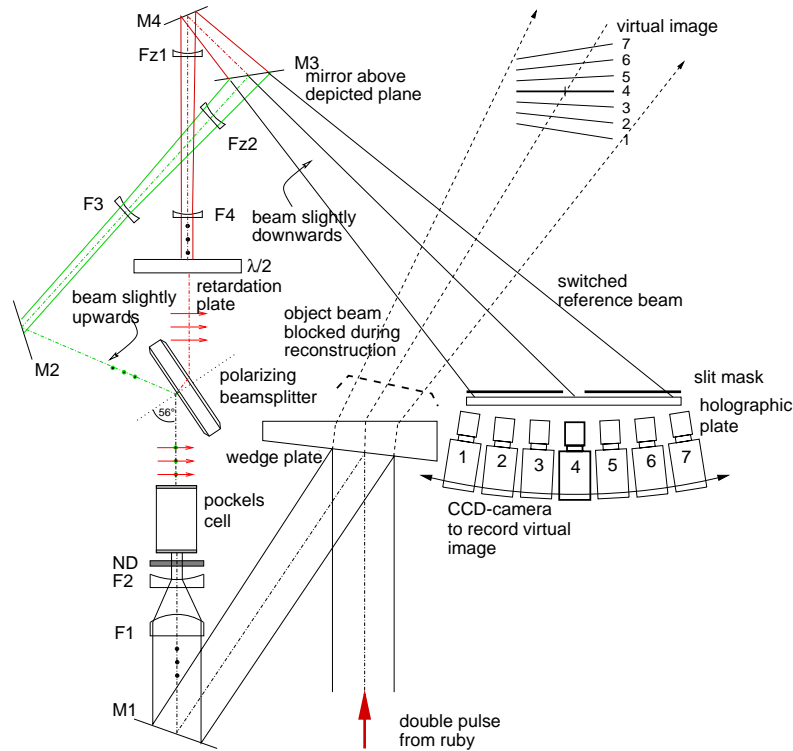


Figure 4.8: Light-in-flight setup for recording with polarisation-switched reference beams offering different angles of incidence. The reference beam expanded by lens F3 projects out of the paper plane to fall onto the holographic plate from above. Sheet-wise reconstruction is done with the same setup after blocking the object beam and using the reference beams one after the other. In-focus planes in the virtual image correspond to the horizontal positions of the CCD camera.

During reconstruction, a slit mask (or simply the limiting aperture of the imaging system) is used to select the aperture in both holograms which reconstructs the same region in depth. Results have been obtained from a free jet in air during measurements in the region of transition to turbulence (Geiger et al., 2000). Up to 21 planes were obtained from which the inner 18 were used to evaluate 64.800 velocity vectors. It was found that the validity rate is as good as 97%. As an example, a single plane of velocity vectors without filtering or interpolation is shown in Figure 4.9.

It has been shown that cross-correlation analysis of noise-reduced holographic particle image fields from a ruby laser yields high quality measurements of even non-stationary and turbulent flows. The maximum flow velocity, however, is restricted by

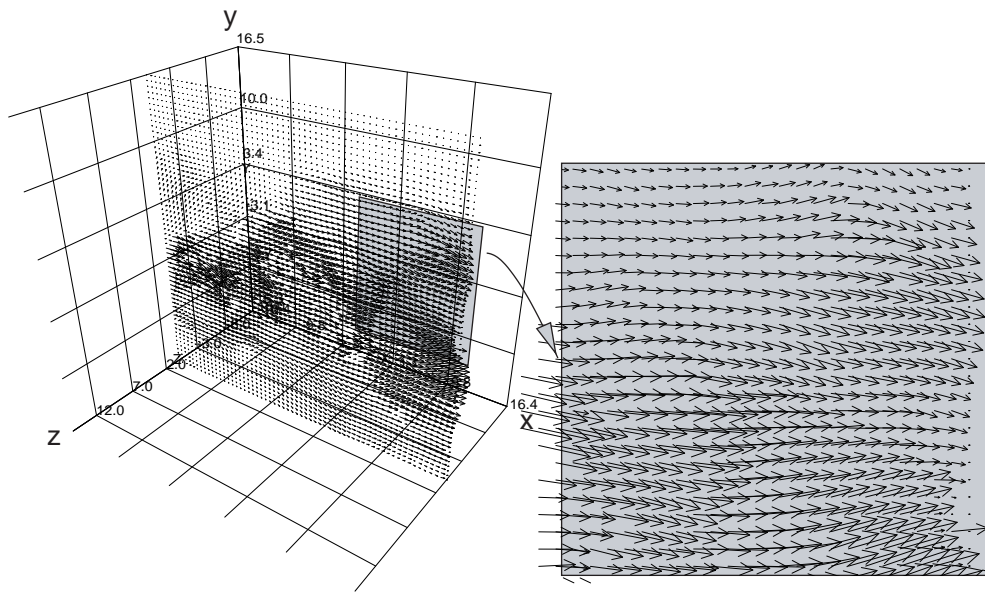


Figure 4.9: Example of a LiFH-PIV measurement from digitised virtual image reconstruction of particles carried by a free air jet. Under observation was the transition to turbulence and only one sample plane from the measurement is shown. The whole volume as indicated by the grid was sampled with a total of 21 such planes (Geiger et al., 2000).

the minimum pulse delay of the ruby laser (typically $\Delta t = 50$ ms), and a cumbersome alignment procedure of the imaging system for the virtual image readout is needed. Furthermore, only two components of each velocity vector are obtained, even though holography is capable of recording the full three-dimensional information with high spatial resolution. Interrogation of the virtual image requires a minimum working distance of the camera, which is slightly larger than the distance between holographic plate and flow (usually several ten centimetres). Thus, the imaging used in this experiment does not make use of the full resolution determined by the hologram aperture.

4.2.3 Real Image Reconstruction

The reconstruction of virtual particle images, as used in the experiment described in Section 4.2.2.3, implies limitations in the resolution with which a particle field can be digitised. This is due to the large distance between the particle field and the imaging lens caused by the necessity to view through the hologram. Furthermore, the allocation of spatial positions inside the particle field requires a complicated calibration procedure and calculations for every single combination of camera and aperture position. Finally, the resulting vector field consists of only two velocity components and needs to be remapped by interpolation onto a regular grid to be viewed in three dimensions. To overcome these obstacles towards a fully three-dimensional measurement the evaluation of the real image has been favoured by many researchers (Barnhart et al., 1994;

Lozano et al., 1999; Pu and Meng, 2000a; Zhang et al., 1997) but not yet implemented in combination with LiFH. Most important, this approach is generally suited to make use of the full resolution determined by the reconstructing aperture and allows a much simpler access to the spatial position inside the particle field by logging the actual image sensor position.

The arrangement depicted in Figure 4.5 was used to demonstrate the gain in image quality for the recording of small particles within a wind-tunnel flow. For details about the setup and the flow-configuration the reader is referred to Chapter 8 and the paper by Herrmann and Hinsch (2004b). Here, only a qualitative overview of the results shall be given, the more detailed examination of which is discussed in Chapter 9 and in a paper by Hinsch and Herrmann (2004).

For a direct comparison of the light-in-flight technique with ordinary holography, a pulsed Nd:YAG laser system able to switch between long and short coherence mode via an injection seeder (cf. Chapter 5) was used to record a set of particle holograms. The particles - DEHS (di-2-ethylhexyl-sebacate) of about $1 \mu\text{m}$ diameter, typical number density of some 20 mm^{-3} - have been illuminated from a direction about $\varphi = 30^\circ$ off the viewing axis to the center of the hologram. The reference wave was incident at about 70° to the normal of the plate ($\alpha = 20^\circ$). Reconstruction of the real image was obtained with a continuous wave (cw) Nd:YAG laser, emitting at the same wavelength ($\lambda = 532 \text{ nm}$).

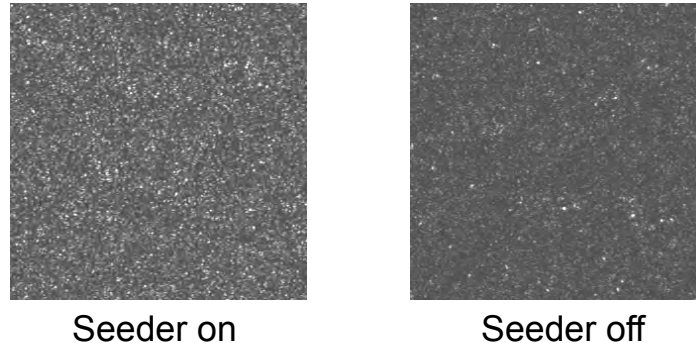


Figure 4.10: Comparison of reconstructed images at zero path length difference for an ordinary long-coherence hologram (left) and a light-in-flight hologram (right). Aperture 15 mm in either case. Field of view $300 \text{ px} \times 300 \text{ px}$ ($2 \times 2 \text{ mm}^2$)

Figure 4.10 shows a direct comparison of reconstructions with and without LiFH or with the injection seeder turned off (right) and on (left), respectively. The aperture ($D = 15 \text{ mm}$ in either case) was placed in the center of the hologram, and the sensor at the position of zero path length difference $\Delta s = 0$ midwise in depth direction z of the reconstructed shell. For purposes of a better comparison, the presentation of the low-coherence picture was enhanced in brightness by a factor of 3 to equalise the brightness of particle images in the other picture. It is clearly seen that the long-coherence image is affected far more by noise originating from the out-of-focus particle images that superimpose on a speckle background.

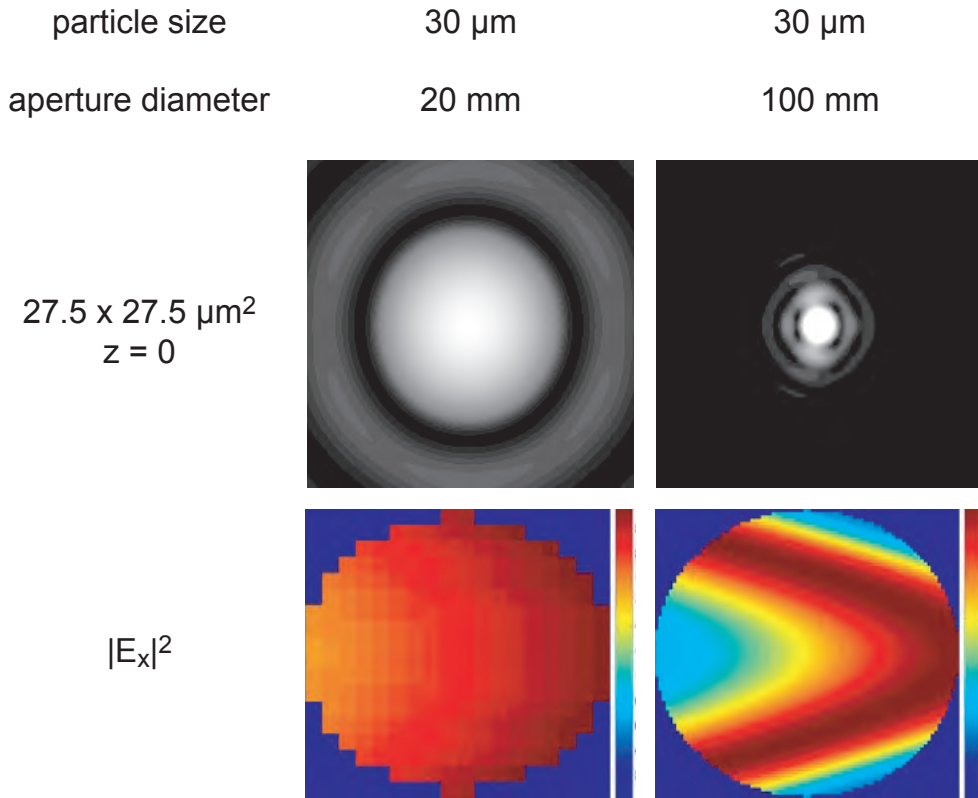


Figure 4.11: Simulation result of a digitally reconstructed particle image from differently sized apertures. In the hologram plane at a distance of 300 mm from the particle, the scattered light field at $\theta_m = 90^\circ$ of a DEHS particle in air with relative index of refraction $m = 1.45$ and size $d_p = 30 \mu\text{m}$ is recorded. The distribution of the x -component of the light field is shown in the hologram plane for the two circular apertures, 20 and 100 mm in diameter.

The situation in Figure 4.10 was compared to the corresponding simulation results using the Mie-scattering and digital-reconstruction algorithm from Section 2.3.2. For the above mentioned DEHS particles with relative index of refraction $m = 1.45$ the scattering recorded under $\theta_m = 180^\circ - \varphi = 150^\circ$ did not produce any noticeable aberration in the particle images, but small vertical shifts of less than $1 \mu\text{m}$. Most remarkably, the situation for increasing particle or aperture sizes does not get as bad as for the $\theta_m = 90^\circ$ case (Figure 4.11). Thus, the LiFH constellation utilising near-backward scattering can be used for almost any size of particles without suffering from strong aberrations if a good collimation of the reference and reconstructing beams is achieved.

To investigate the extension in depth of the reconstructed field the sensor was moved along the depth coordinate z , while the aperture with diameter $D = 20 \text{ mm}$ was kept fixed at the center position. In Figure 4.12, results for five positions of the sensor are shown with their respective path length differences Δs . It is seen that the central location produces a high-quality image with many clearly distinguishable particle images while the image intensity has decreased slightly at positions where $\Delta s = \pm 4.22 \text{ mm}$. When the path length difference with respect to the center is raised further, the particle images loose brightness until most of them vanish in the background. At positions

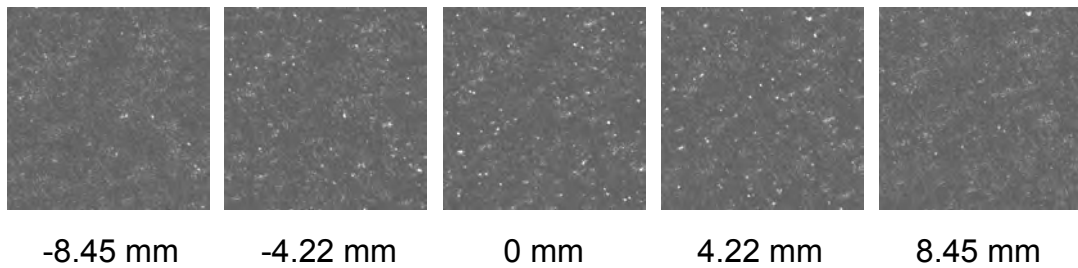


Figure 4.12: Real-image holographic particle records obtained on a CCD sensor from a light-in-flight hologram of a wind-tunnel flow. While the reconstructing aperture of 20 mm diameter was kept fixed on the hologram, the pictures were obtained at different depth positions of the sensor. The position of the centre image corresponded to zero path length difference Δ_s between object and reference light. Indicated are the values Δ_s for the different images. Field of view $300 \text{ px} \times 300 \text{ px}$ ($2 \times 2 \text{ mm}^2$).

according to $\Delta_s \approx \pm 8 \text{ mm}$, hardly any particle images are left. Keeping in mind that the difference in depth coordinates z is approximately half the path length difference, the results are in good agreement with the predictions of 4.15. The gradual drop in the particle image brightness is a consequence of the self coherence function (Figure 4.4). For zero path length, difference maximal coherence is obtained, resulting in a maximal modulation recorded by the hologram. Since the recorded modulation depth determines the diffraction efficiency (cf. Section 2.1.3), particles recorded with non-zero path length differences appear to be weaker.

5 State-of-the-art Nd:YAG Laser System for Particle Holography

An instantaneous and high-resolution volumetric flow velocity measurement requires two successive recordings of light scattered from millions of tiny tracer particles on a holographic recording material. Furthermore, the reconstruction and evaluation of these two images has to be done with a precision in the sub-micrometre range over the whole field, which is commonly achieved by the reconstruction of real holographic images (see Section 6.2).

These requirements put high technical demands on the light sources which are used for such measurements. For the recording a high-energy pulsed laser with a smooth beam profile is desirable to illuminate the flow region with a large but homogeneous cross-section while the holographic material still receives enough light scattered from every single particle. Furthermore, such a light source should allow a short-coherence operation suited for LiFH flow recordings to incorporate an efficient noise reduction.

Consequently, the suitability of a Nd:YAG laser (the most common pulsed solid-state laser) as a new recording light source was explored (see Section 5.1). After an extensive and detailed survey among four different laser manufacturers a laser system was selected, which had to be especially designed to fulfil the above mentioned requirements. Details of this system are given in Section 5.2.

5.1 Suitability of Nd:YAG Lasers

The suitability of Nd:YAG lasers for the pulsed recording of particle holograms was explored under three points of view: the pulse energy needed for a proper exposure of green-sensitive holographic materials (Section 5.1.1), the coherence properties of a pulsed laser under inspection (Section 5.1.2) and a test of the energy density required for single pulse recording of nearly backscattering tracer particles in air (Section 5.1.3).

5.1.1 Green-sensitive Holographic Materials

The pulse-energy requirements have been determined with exposure-tests of two commercially available recording materials sensitised in the green spectral range (details on the materials are reported in Appendix A.2). A pulsed Nd:YAG laser (Coherent, Model "infinity") operated in TEM₀₀ and single pulse mode ($\tau = 3.5$ ns) was used to expose these materials with a widely spread and rather homogeneous cross section of a beam incident normal to the plates. The pulse energy was monitored from reflected signals, firstly with a power-meter capable of single-pulse measurements (Coherent, Model Powermate M) and secondly, with a power-meter giving the mean power at

10 Hz repetition rate immediately before and after the exposure. Unfortunately, the single-pulse measurement results had to be discarded due to a failure of the measuring instrument, resulting in a relatively large measurement error of the effective exposure. After a standard development procedure suited for the material, the obtained optical density was determined by means of an absorption measurement conducted with parallel laser light on a circular area of the material with 10 mm diameter.

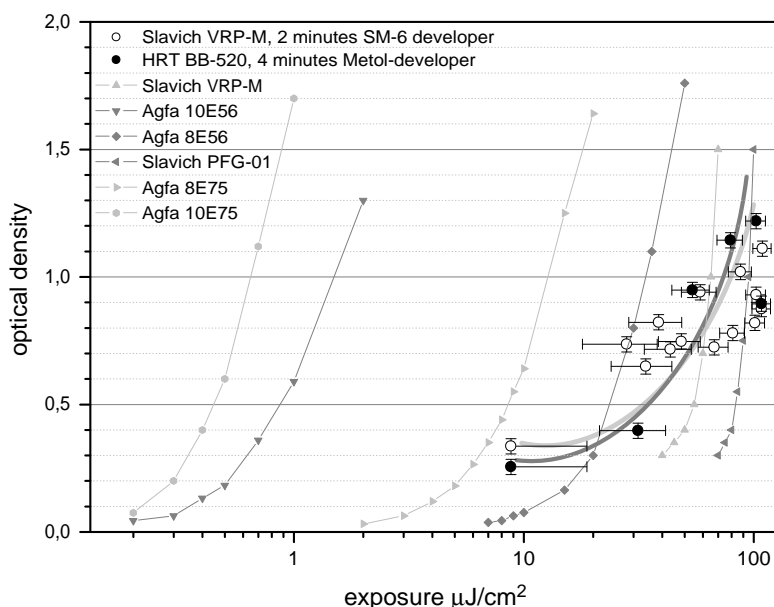


Figure 5.1: Results of the measurement of characteristic curves for two green-sensitive holographic materials exposed with short pulses from a Nd:YAG laser

The results of these measurements are shown in Figure 5.1 together with characteristic curves from the available brochures given by the manufacturers of the corresponding holographic films. Due to the large errors from pulse-to-pulse variations and the measurement of the mean power only, tendencies could be validated, but the characteristic curve of the two materials was not well reproduced. Compared to the known characteristics of various holographic films, the exposures with short pulses on the two tested materials exhibit a considerably shallower course of the characteristic curve. It could be found, however, that for recordings on both materials the exposure should be roughly four times higher than commonly used for the Agfa 8E75 material in the experiments described in Section 4.2.2. Compared with the ruby laser it is obvious that the power or pulse energy requirements do not decrease, but increase drastically when holographic imaging of tiny tracer particles with a wavelength of $\lambda = 532$ nm is envisaged.

5.1.2 Coherence-Length-Test with Quantel BrilliantB Laser

An available pulsed laser system for PIV measurements (Quantel, Model BrilliantB Twins) was used for the first holographic explorations with pulsed LiFH at a wavelength of $\lambda = 532$ nm. For this purpose, an existing arrangement of beam guiding

optics was used to operate in a 2 m wide and 1 m deep test section in the acoustic wind tunnel at the University of Oldenburg from the control room next door. The demonstrational LiFH setup according to Figure 4.1 was slightly modified: A collimated laser beam (3.5 cm in diameter) entering the test section was first split by a glass wedge plate to obtain the reference beam from a reflection, before it illuminated a ruler, tilted by 25° with respect to the beam. The hologram was recorded on HRT BB-520 holographic plates (now manufactured by Coulorholographic Ltd., refer to Appendix A.2) with a single pulse of approximately 275 mJ and a length of $\tau = 5$ ns. About 4 % of the energy was reflected into the reference beam, resulting in an exposure of roughly $78 \mu\text{J}/\text{cm}^2$.

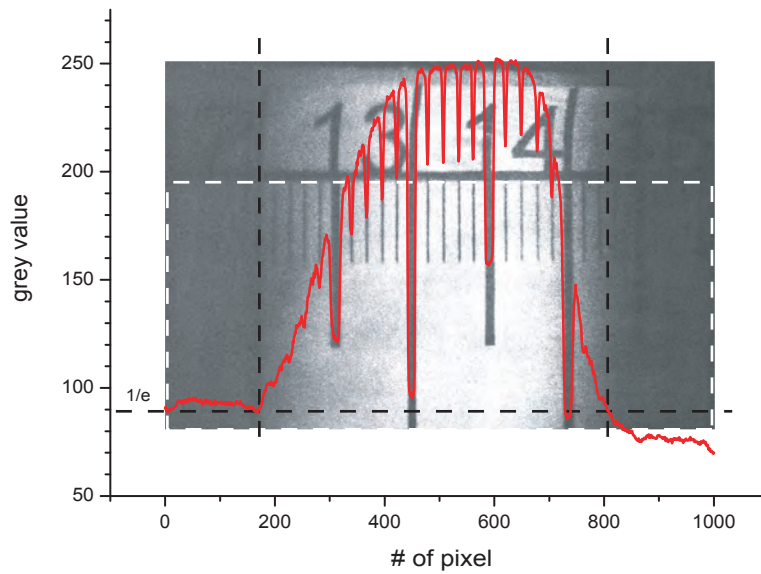


Figure 5.2: Reconstruction of ruler recorded with LiFH and a single pulse of Quantels BrilliantB Nd:YAG laser. The coherence function folded with the influence of a finite reconstruction aperture is seen as a projection onto the ruler, the illuminated depth d_c can be measured directly from the image.

After a 4-minute development in the suggested Metol-developer, the optical density was $D = 0.4 - 0.5$, compared with Figure 5.1 i.e. only half the value expected. Nevertheless, the reconstructed image was brilliant and with low noise due to scattered light, which is probably due to the clear appearance of the plate at unexposed areas (unlike other materials!). Figure 5.2 shows a digitised portion of the virtual image, viewed by a CCD camera without saturating the bright pixel. Overlaid in red is the horizontal profile as obtained from vertically averaging the data from the rectangle indicated by the white dashed lines. The black dashed lines illustrate the points of loss in intensity to $1/e$ of the highest value and can be considered as the boundary of the coherence function projected onto the ruler. Totally darkness is not achieved due to the integrative effect of the finite aperture and remaining noise contribution from light scattered at the hologram. With an angle $\varphi = 25^\circ$ between illumination and observation direction the coherence depth d_c is 14.5 mm. The reference beam was incident on the holographic plate at $\alpha = 25^\circ$. Assuming an effective aperture of $D = 20$ mm the coherence length according to (4.15) of the BrilliantB laser is $l_c = 9.5$ mm. This

value does not agree very well with those predicted by (4.12) from the bandwidth $\Delta\nu = 1.5 \text{ cm}^{-1} \cdot c = 4.5 \times 10^{10} \text{ Hz}$ given in the manual by the manufacturer of the laser ($l_c = 6.7 \text{ mm}$).

5.1.3 Energy Density Requirements

The energy density required in the object beam for successfully recording small tracer particles (4:1 glycerine-water mixture) in air was estimated using the same setup as in Section 5.1.2. First of all, double pulsed LiF holograms have been recorded with the collimated object beam, resulting in non visible particle images during the reconstruction with either reference beam. To increase the energy density, the object beam was then focused by a singlet lens ($f = 200 \text{ mm}$). Only a few single particle images near the focus could be found in the reconstructed virtual image. The corresponding energy density at this region was well above 1 J/cm^2 per pulse. This experiment was repeated with two Quantel BrilliantB Twin systems at the German Aerospace Centre (DLR) in Göttingen. All the four lasers were fired simultaneously to illuminate DEHS particles in air with a cross section of roughly 5 cm^2 . Due to different polarisations two holograms have been recorded effectively at the same time. Nevertheless, reconstructions of particle images were possible. An estimate of the energy density for every single hologram is approximately 120 mJ/cm^2 . Though these numbers are not very reliable it was clear from these experiments that pulse energies of more than 1 J have to be envisaged for a new Nd:YAG laser system.

5.2 Pulsed Nd:YAG Laser System for Recording

Based on the above empirical values and the needs for high precision holographic imaging, the specifications of a laser system for LiFH-PIV have been formulated (see Appendix A.7). It was obvious that commercially available laser systems could not meet all specifications, thus a specially designed double-resonator system was built according to our demands by Spectra-Physics. Based on the Quanta-Ray PRO-Series the most powerful model, the PRO-350 was selected and modified accordingly. Emphasis was put more on the similarity of the beam parameters between both single laser heads and a smooth beam behind each crystal for the frequency conversion, than on using the highest energy-output possible from each resonator. Moderate losses in pulse energy have thus been accepted to obtain a better and stable beam combination.

5.2.1 System Design and Properties

A detailed overview of the new laser system is given in Figure 5.3. Both laser heads and the beam combination unit are covered separately by either the standard laser head case or a customised box (gray lines) and have been placed on a common optical table, which can be moved on special high-load removable air-tires. The external and also mobile power and control units are connected by extra long (5 meter) umbilicals to the

laser heads, which can be removed for transportation. Thus, maximum flexibility for the use at various wind tunnels is maintained simultaneously with an optimum stability of the system when it is operated.

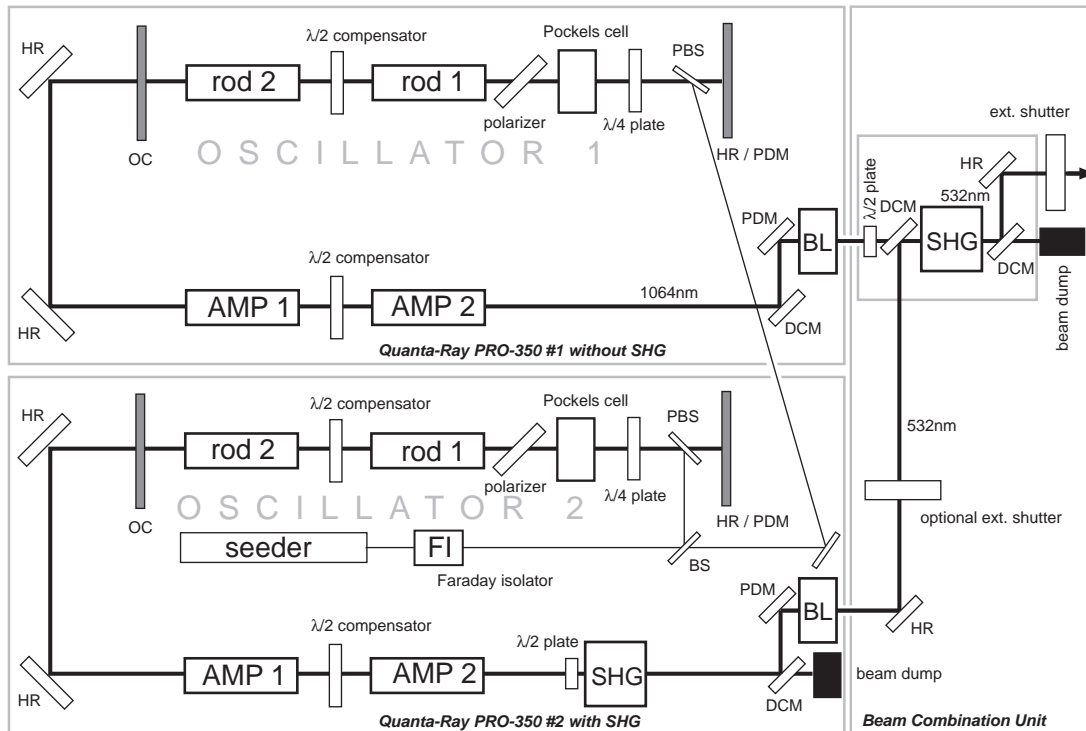


Figure 5.3: Sketch of the Nd:YAG laser system consisting of two modified Quanta-Ray PRO-350 laser heads with a common seeding device and an external beam combination unit. See text for details on the single parts of the system.

The optical configuration of the system has been designed to enable a variety of output modes, as described in Section 5.2.4. For comparison tests between short and long coherence hologram recording and mutual interference between both pulsed laser beams, a common injection seeder serves as a master laser operating in a single longitudinal mode (SLM) when turned "on" (Section 5.2.2). In the turned "off" mode the system delivers multimode radiation suitable for LiFH. Beam properties are controlled with feedback systems to obtain optimum stability with almost no changes in the divergence throughout the lifetime of the pumping flashlamps (Section 5.2.3).

5.2.1.1 Oscillator Design

For a good balance between beam quality and efficient extraction of energy in the Nd:YAG rod, an unstable resonator design was chosen in which the illuminated volume is much larger than in stable resonator designs. The output coupler (OC) is a specially coated mirror with a gaussian-like distribution of reflectivity over its cross-section to

obtain a near flat-top profile, the so-called super-gaussian profile. Its characteristic is to fill the aperture created by the rod diameter more uniformly to extract more energy and with a smooth but fast drop towards zero intensity at the edges. Furthermore, the OC design is selected to minimise effects of thermal lensing in the rod by appropriate variation of the reflectivity and by adding a negative lens at the output. The rear mirror is a highly reflecting mirror mounted on a kinematic and piezo driven mount (see Section 5.2.2 for further details). A pockels cell in combination with a polariser enables Q-switching according to the on-switching principle for the build-up of short laser pulses.

A unique feature of the Spectra-Physics system is the patented birefringence compensation by a dual rod design. Birefringence in the rods is a thermally induced effect manifested by a temperature gradient resulting from a hot centre and a cooler outer surface. Tension from and compression towards the centre gives rise to a refractive index gradient along the rod cross-section. In cylindrical coordinates the difference in refractive index change is given by:

$$\Delta n_r - \Delta n_t = (C_r - C_t)P_a r^2, \quad (5.1)$$

where Δn_r and Δn_t are the radial and tangential refractive index change, C_r and C_t material dependent constants and P_a the total power absorbed by the rod. The birefringence causes the beam to depolarise because a phase difference between the radial and the tangential vector of the light's electrical field is introduced when it passes through the rod. Such a depolarisation causes losses at the polariser used to Q-switch the cavity, it degrades beam quality and results in lower conversion efficiencies in crystals used for harmonic generation.

In a dual rod design, the light enters a 90° polarisation rotator ($\lambda/2$ wave plate) swapping the out-of-phase radial and tangential components before entering the second rod. The phase retardation that was introduced by the first rod can now be compensated for by the second rod. Light leaving the second rod is again linearly polarised but rotated by 90° . The rods for the laser system have been specially selected to fulfil the high requirements on the two nearly identical beam profiles.

The pump chambers where each of the rods is placed next to a flashlamp are elliptical in shape providing a good beam quality and almost no hot spots in the profile by illuminating the entire rod surface. In contrast to the closed coupled pump chambers in other Nd:YAG lasers, this design is usually less efficient (Koechner, 1999). A diffuse reflecting gold surface, however, increases the pump chambers reflectivity and therefore also its efficiency and eliminates the need for glass claddings which often crack at higher thermal loads. The flashlamps can be changed without opening the pump chambers, reducing chances of misalignment and contamination of the Nd:YAG rod surfaces.

5.2.1.2 Amplifier Stages

The beam path behind the oscillator is folded by two high-reflecting mirrors to guide the laser pulses through two amplifier stages. Each amplifier stage consists of a pump

chamber with one flashlamp and a Nd:YAG rod in a design similar to those used in the oscillator. The rod diameter, however, is now larger to obtain sufficient gain in the amplification process. Both amplifiers represent again, a dual-rod design with a $\lambda/2$ compensator in between to further preserve the beam quality. All optical paths, inside the oscillator as well as outside towards the second-harmonic generators (SHG), are sealed with a tube system. Firstly, this increases laser safety when the system is operated without covers for alignment procedures, secondly, this prevents damages on the coated optical elements due to dust burned by the high energy pulses (up to 3 J per pulse at $\lambda = 1,064$ nm). The sealed cavity is purged with dry nitrogen at a slightly higher than the environmental pressure to keep it clean from dust outside of this cavity.

5.2.1.3 Second Harmonic Generation by Phase Matching

To convert the fundamental Nd:YAG line at $\lambda = 1,064$ nm to its second harmonic at $\lambda = 532$ nm a KD*P (KD_2PO_4 , a potassium dideuterium phosphate) crystal is used, which offers the natural birefringence needed for phase matching. Incoming and generated light have to have a defined phase relation along their path of interaction to substantially generate sum or difference frequencies.

Harmonic generation is an elastic and thus optical-energy-conserving process first observed by Bass et al. (1962). It is usually described as a special case of the general three wave parametric interaction. This case is the non-linear interaction between two waves with common frequency ω_1 . In the generation of the second harmonic wave two processes are involved (Koechner, 1999). Firstly, the interaction of the two waves produces a polarisation wave at the second harmonic $2\omega_1$ with a phase velocity and wavelength in the medium determined by the index of refraction n_1 for the fundamental wave. The second step is a transfer of energy from the polarisation wave to an electromagnetic wave at the doubled frequency. Their phase velocity and wavelength are now determined by n_2 , the index of refraction for the doubled frequency.

For efficient energy transfer it is necessary that the waves remain in phase. The dispersion effects can be reduced or even cancelled by the birefringence of the KD*P crystal when the beam polarisation and direction of the propagation is appropriately chosen. Depending on the application, the type of the phase matching process is selected to yield either high conversion efficiency or the scrambled polarisation of the input wave. For the application in a high power laser where only the green line is used, type-II phase matching is ideal to get almost half the energy coupled into the second harmonic, while the residual radiation at the fundamental line is dumped anyway. In the type-II process the polarisation vectors of the incident beam need to be orthogonal, which is accomplished by rotating the linear polarisation of a single beam with a $\lambda/2$ wave plate incident at 45° with respect to the crystals x-axis (see Figure 5.4). The output wave is then again linearly polarised and is separated from the residual 1,064 nm line by a dichroic mirror (DCM).

In this laser system the KD*P crystal is mounted in a special housing which can be rotated about the beam propagation axis. In this way the output beam can be chosen to be horizontally or vertically linearly polarised. The optimum phase-matching position

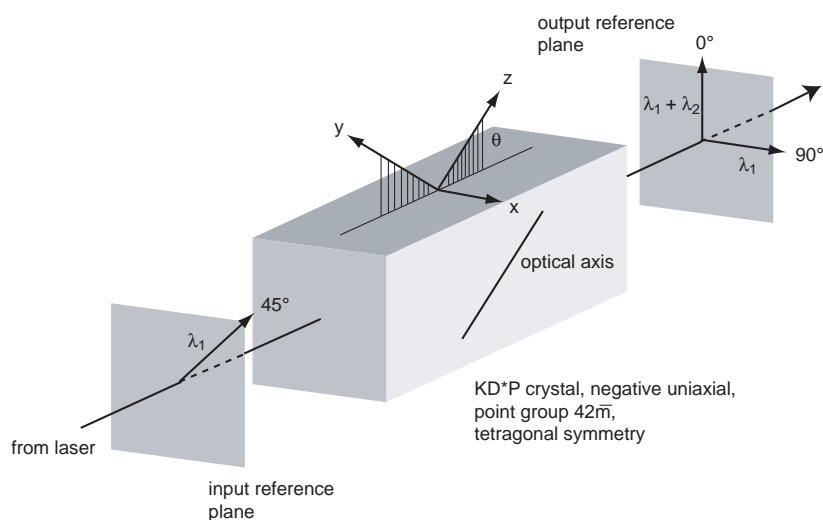


Figure 5.4: Optical configuration of a KD*P crystal to obtain the second harmonic (532 nm) with a type-II phase matching process.

of the crystal is fine-tuned by slightly rotating the crystal about its x-axis with a high angular resolution (80 threads per inch acting on a lever-like translation arm). The optimum and stable crystal temperature is obtained by simultaneously heating and water cooling. The beam path inside the housing is purged by dry nitrogen to be kept clean.

5.2.1.4 Beam Combination Unit

To minimise the number of high power guiding-optics for the beam illuminating the tracer particles it is useful to combine both laser beams before they are directed through the recording setup. Another advantage of this method comes from the effort to align a LiFH setup, where the reference beam path-length needs to be identical to those of the object beam. Having the latter already combined, only the one path-length for the object beam needs to be adapted. One of several possible realisations of such a beam combination is shown in Figure 5.3. The beams are overlapped at different wavelengths at the position of the first dichroic mirror (DCM) in the beam combination unit. Both beams enter the following second harmonic generator (SHG), where only the 1,064 nm line of the first laser interacts with the crystal. It is important, that the $\lambda/2$ wave plate for this wavelength is introduced before both beams are combined, since it also has an effect on the 532 nm line of the second laser. After separating the residual radiation, the overlapped beams are directed through a shutter to select individual pulses from the 10 Hz repetition. A second and optional shutter is introduced in the beam path of the second laser to allow for much longer pulse separations than 1/10 s.

Adjustments of the beam combination are a very critical point. The two beams leaving the second harmonic generator should be crossed-polarised to obtain a high conversion rate and thus high output power. This can be utilised for the necessary reference beam separation as demonstrated in the setup shown in Figure 4.8 and in the experiment

described in Chapter 8.

The beam combination unit is designed to allow also for separated beams. For this, another high-reflecting mirror (HR) can be introduced behind the optional shutter in the 532 nm beam to direct it through a second port of the unit's cover.

5.2.2 Injection Seeding

The process of achieving SLM operation by injecting radiation from a narrow band laser into the pulsed cavity during the time where the Q-switch is activated is commonly referred to as "injection seeding" (Park et al., 1980; Rahn, 1985). To obtain an injection seeded operation, the seed laser emission has to be several orders of magnitude larger than the spontaneous emission of the pulsed cavity. In that way only one narrow mode of the host or slave laser (Q-switched Nd:YAG cavity) which overlaps with the seeder frequency can develop (see Figure 5.5). The pulse developing from this signal saturates the gain medium and extracts energy at the given frequency before any other pulse develops from the spontaneous emission during the Q-switch time.

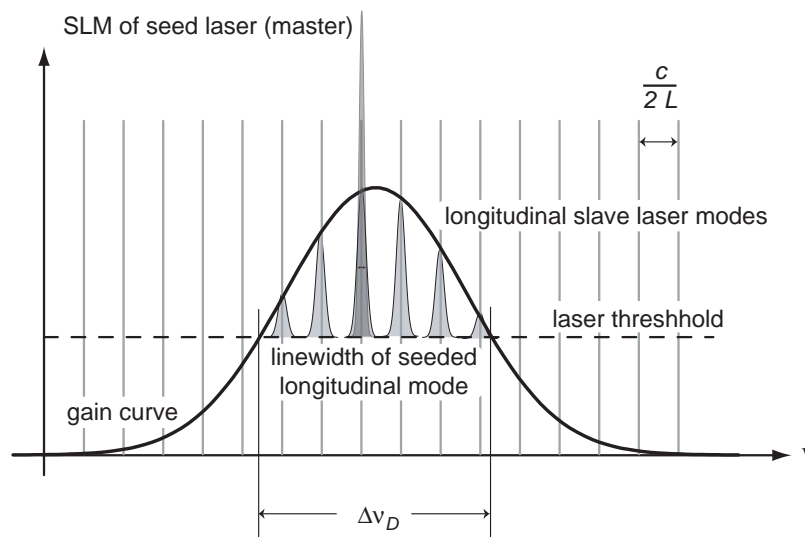


Figure 5.5: The injection seeding process allows only one narrow mode to develop in the pulsed Nd:YAG laser which is given by the seeder frequency. The seed laser emission from the master cavity is considerably larger than the spontaneous laser emission in the slave cavity.

To maintain optimum overlap between the SLM seed laser and a single slave laser mode, the resonator length of the pulsed laser is adjusted by a control system using a piezo driven mirror (HR / PDM) as the rear cavity mirror. The most efficient seed operation is obtained by monitoring the Q-switch pulse build-up time, which is significantly reduced in the correctly seeded mode and locked at a minimum value from the loop. The pulse build-up time is determined by the number of round trips in the resonator required for circulating photons to extract enough energy and to reach the

saturation fluency level. Due to the significantly larger emission this process is faster than from spontaneously emitted photons.

The injected radiation is strong enough to cause spatial hole burning in the Nd:YAG rod caused by two counter-propagating waves of similar intensity and identical polarisation. Their interference produces a standing wave pattern causing nodal points in the gain medium. Spatial hole burning is observed in seeded cavities mostly from a post lasing effect, following the main Q-switch pulse. To circumvent this problem, the Nd:YAG rods are surrounded with a pair of $\lambda/4$ wave plates (not shown in Figure 5.3), yielding counter-rotating, circularly-polarised light inside the gain medium.

A common injection seeder with 3.5 mW output power is used in the laser system to seed both Nd:YAG lasers. Therefore its beam is split by a beam splitter (BS) and directed into the corresponding cavities. The seed laser is a monolithic, single-frequency Nd:YVO₄ laser with an output wavelength of 1,064 nm, the same wavelength as the Nd:YAG laser. Optical pumping of this laser is achieved by a laser diode that is set slightly off-axis to prevent feedback. Its output wavelength is temperature sensitive and controlled electronically, the same as with the Nd:YVO₄ laser. These two control loops allow to scan the output wavelength to further optimise the frequency overlap between master and slave laser (active stabilisation). The SLM mode is conveniently achieved in these laser types due to short resonators (only a few mm long), avoiding spatial hole burning due to the ring configuration and a small gain volume producing a stable TEM₀₀ mode. The seed beam is directed through a Faraday isolator (FI) and introduced in the resonator cavity through reflection off the polarising beam splitter (PBS). Their combination provides isolation between the master laser and the slave laser, both to protect the master laser from possible damage and to prevent destabilisation from feedback into the master oscillator (Koechner, 1999).

When the seeder is turned "on" the line-width of the 1,064 nm radiation is narrowed to a value of approximately $\Delta\nu = 0.003 \text{ cm}^{-1} \cdot c = 10 \text{ kHz}$, resulting in a theoretical coherence length according to (4.12) at this wavelength of $l_c \approx 3.3 \text{ m}$. In practice the coherence length is limited by the pulse duration of 7 ns and thus reaches roughly 2 m. When the laser is operated unseeded, a line-width of approximately $\Delta\nu = 1 \text{ cm}^{-1} \cdot c = 30 \text{ GHz}$ results from mode beating under a gain curve for Nd:YAG of 4 cm^{-1} or 120 GHz at FWHM. The coherence length reduces to only 1 cm at 1,064 nm and half this value at 532 nm. Given a resonator length of 60 cm, the frequency spacing is 250 MHz and the number of modes according to (4.13) $N = 120$.

5.2.3 Beam-Pointing Stability and Divergence Control

The system beam parameters are controlled to yield a stable operation of the two lasers. For this purpose the so-called "BeamLok" Digital Controllers are attached directly to the power supplies instead of using the analog remote controller. These controllers receive various signals from the laser heads and control the laser start-up as well as its operation and shut-down processes. Two main features of these controllers are the active stabilisation of the beam-pointing and the control of the flashlamp voltage to maintain a stable beam divergence.

The beam-pointing stability is a critical parameter in pulsed high-power and especially flashlamp pumped laser systems. Due to varying thermal loads in the Nd:YAG rods and other components of the laser, the beam shows a significant angular drift from pulse to pulse which is of particular concern in applications such as laser-based metrology and laser-based material processing. The beam pointing stability of a laser system and how fluctuations are actively compensated, is often the main factor that limits the achievable precision for a given application. In HPIV, the exact pointing of the reference beam is influenced by this drift, resulting in a displacement error in the final measurement data which has to be corrected. This for example can be achieved by recording calibration information on any particle hologram to fit the different images later on.

The pointing stability is typically determined from the displacement of the beam position at the focal plane of a suitable lens system ([International Organization for Standardization, 1999](#)). The beam displacement is measured with a position sensitive detector. The angular drift is obtained by dividing the displacement by the appropriate focal length. Depending on how such a measurement is implemented, this technique can detect angular drifts ranging from milliradians to less than 1 microradian ([Gray et al., 2001](#)).

In the Spectra-Physics Quanta-Ray Pro-350 system described above, each laser shows a long term pointing drift (over 8 hours, $\pm 3^\circ\text{C}$) of $< 50 \mu\text{rad}$ without and $< 25 \mu\text{rad}$ with the BeamLok Control turned on. Obviously these values are doubled when the combined beams from both lasers are considered. This considerable increase of the pointing stability is achieved by loop-back reading the displacement signal from the four-quadrant diode located in the BeamLok optical head (BL in [Figure 5.3](#)) and correcting the piezo driven mirror (PDM) accordingly. The shot-to-shot stability is typically a factor of two smaller than the long term drift.

The beam divergence is known to be a monotonous function of the lifetime of the flashlamps, given as the number of total shots. Due to ageing, the effective pump power decreases, which can be compensated by increasing the lamp voltage. This procedure is used in the controller boxes to adjust the voltage on the flashlamps according to their age, thus yielding a stable divergence with a maximal increase of only a factor of two over their entire lifetime. A stable divergence, is the key element for obtaining planar reference wave fronts from the repeatedly pulsed laser. Thus, the alignment of the reference beams needs to be checked only once in a couple of weeks (depending on the usage of the laser system and assuming a mean lifetime of the flashlamps of four to six months).

Finally, the control boxes allow us to monitor almost every system parameter on the units display and it can be connected to a PC via a GPIB (IEEE 488.2) interface for a complete control via software.

5.2.4 Modes of Operation

The laser system is designed for a flexible usage in laboratory and wind-tunnel environments and also allows for more advanced multi-pulse setups. The beam combination

unit can be equipped with an optional mirror to direct the laser pulses from the second laser through an extra output port, passing over the combination at the dichroic mirror (DCM). The polarisation of this beam needs to remain vertical, to prevent a possible damage of the four-quadrant-diode from horizontally polarised reflections in the BeamLok unit (BL). For the first laser, however, the external SHG housing can be rotated to obtain either horizontal or vertical polarisation. Depending on the housing position this allows parallel and crossed polarisation states of the two beams.

For a more flexible laser control during adjustments of the optical setup, the so-called remote boxes can be attached to the power units instead of the digital controllers described above. These allow start-up, operation at various power levels and shut-down of the system, but with no active control of the beam pointing and divergence. For fine tuning of a holographic setup, requiring plane waves and adjustments of spatial filters, the control over the remote boxes cannot be recommended. A considerable angular drift as well as changes in the divergence have been observed when changing between both controller types.

More advanced applications using four laser pulses (e.g. for the determination of the local acceleration from two successive velocity measurements) can be build using the double pulse option of each laser. For this, modifications inside each laser head are required. Additionally, high-voltage pulse generators (so-called Marx banks) need to be attached to the pockels cell with special cables, which prevent the back-propagating high-voltage pulses inside the cable due to the diodes. The temporal pulse separation can be varied from 20 to 200 μs , resulting in differing pulse energies. These assume roughly half the energy of a single pulse when an optimum separation time of approximately 65 μs is chosen.

6 Recording and Scanning Systems for Real Holographic Images

Section 6.1 describes two optical layouts for the recording of holographic images by utilizing the pulsed Nd:YAG laser system introduced in Chapter 5. Both set-ups allow to record two successive holograms, either of ordinary or LiF type, from particles inside an air or water flow. After development, these holograms can be reconstructed to view the real images in a separated and highly flexible set-up using two planar conjugate waves from a continuous-wave Nd:YAG laser. Section 6.2 discusses a scanning system for holographic particle images. Motorised translation stages allow to easily map digitised images from a CCD array to a regular grid with cartesian coordinates and enable an automated, computer controlled readout of both, the ordinary and the LiF holograms.

6.1 Recording Set-ups in the Laboratory

Two basic optical layouts for holographic flow measurements, both allowing ordinary and LiF hologram recordings, have been tested in a laboratory equipped with a small test wind-tunnel. Flows in small water tanks and model particle fields (perspex block with embedded particles) have been analysed using the same set-ups by introducing them into the test section of the wind-tunnel. Attention was paid to the extendability of both set-ups for their use also at larger wind tunnel facilities and to their suitability for the more harsh industrial environments encountered there. To this end, the complexity of the beam delivery had to be decreased to a minimum, by simultaneously allowing for a highly flexible geometrical layout of the reference beams to adapt to various wind-tunnel facilities.

Both set-ups are using the combined and cross-polarised beams emitted by the pulsed laser system presented in Chapter 5 and a flexible Reference Beam Delivery Unit (RBDU) described in the following Section 6.1.1. The basic difference between both set-ups is given by the propagation direction of the reference beams. Thus, the set-ups are best classified by a common plane incorporating the object (center point of the flow measurement volume) and the holographic plate (center point), as well as either the final propagation-direction of the two reference beams (Figure 6.1 left) or that of the beam illuminating the flow volume (Figure 6.1 right). The angle α determines the volume depth, which can be recorded in the LiF hologram (cf. Section 4.2.1). The consequences of the different propagation directions are further discussed in the Sections 6.1.2 and 6.1.3.

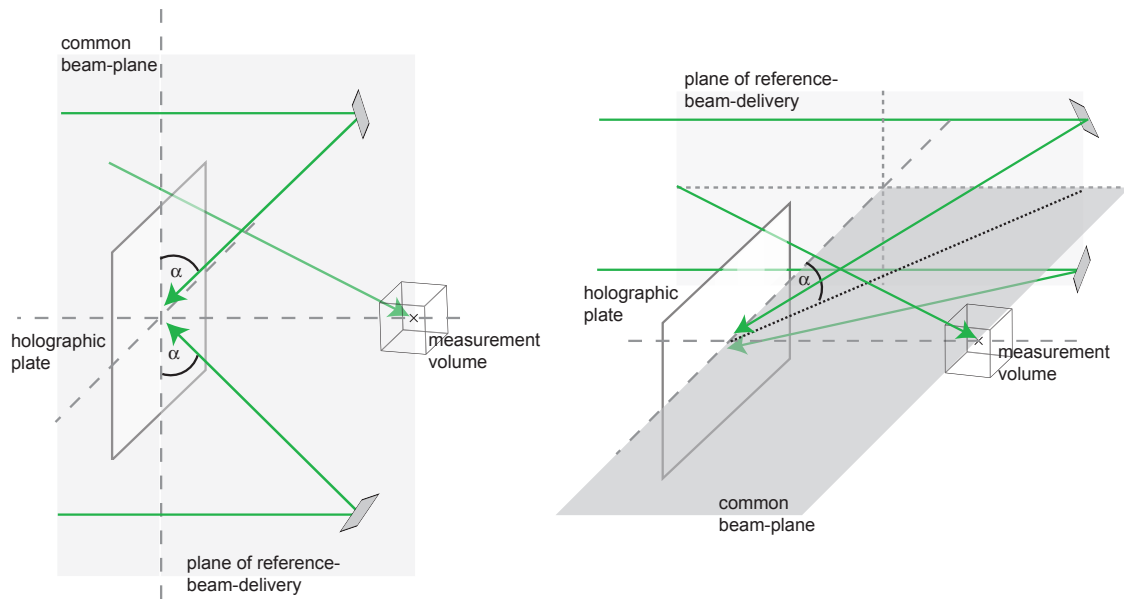


Figure 6.1: Classification of the two set-ups by a common beam plane: The center point of the measurement volume, the center point of the holographic plate and the two reference beams, incident from top and bottom, define a vertical common beam-plane in the first case (left). In the second case a horizontal common beam plane is defined by the same points and the beam illuminating the flow volume (right). For later reference the plane of the reference-beam-delivery unit is also given in the two figures.

6.1.1 Reference Beam Delivery Unit

In a dual reference beam LiFH set-up, the path-lengths of both reference beams have to be nearly identical to record exactly the same region in depth in both holograms. This requirement led to the design of a flexible Reference Beam Delivery Unit (RBDU) as shown in Figures 6.2 and 6.3.

All components of the RBDU are mounted on a variable rail system, in which the distances in vertical and horizontal direction can be tailored to meet the geometry of the flow facility. The reference signals are obtained from the reflection at a wedge plate, as shown in the overview of the whole set-ups in the next Sections. They are first collimated by a telescope built from two lenses, then this beam, about 6 – 8 mm in cross-section now, is steered according to its polarisation into the upper or lower arm by a polarising beam splitter (this corresponds to the first or the second pulse from the laser system or vice versa). Thus angular multiplexing of the two holographic recordings is achieved regardless of the pulse delay time.

Fine adjustment of the path-length in each arm can be done with an optional arrangement of two mirrors and a prism mounted on a small manual translation stage. The beam expansion to illuminate the entire holographic plate is obtained either by a single concave lens or by a spatial frequency filter, made up of a convex singlet lens and a pinhole. A large singlet (convex lens) is used to collimate the beam at a cross-section of roughly 250 mm, before a large planar mirror on an adjustable mount (for

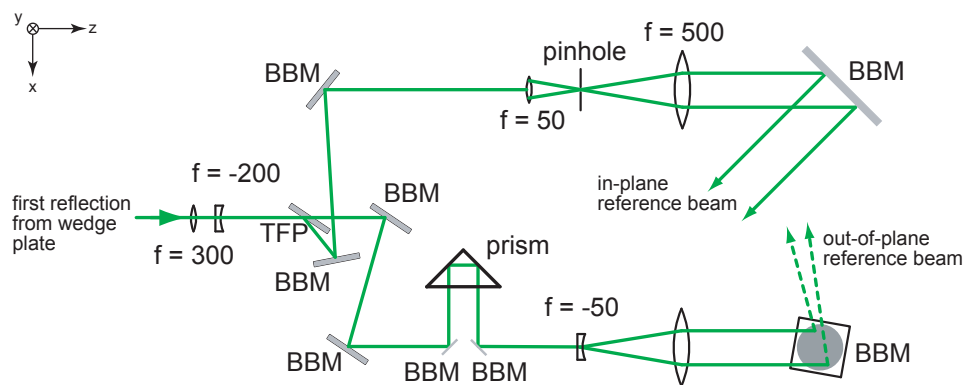


Figure 6.2: Principal sketch of the RBDU for two reference beams, used to multiplex the holographic recordings by separation at a polarising thin-film beam-splitter (TFP). The whole arrangement is placed vertically and the object beam (not shown) propagates perpendicular to this plane of depiction. Typically, the beam delivery unit is used with an identical upper and lower part, the sketch however shows possible variations. Upper part: no fine-tuning of path-length, beam expansion by a lens plus spatial filter and in-plane propagation of the reference beam, lower part: fine-tuning possibility, beam expansion by concave lens and out-of-plane propagation of the reference beam.

rotation and tilt) guides the collimated reference beam towards the holographic plate. The collimation of both reference beams is adjusted under control of a lateral shearing interferogram (cf. Section 2.1.4.2), which however requires to operate the laser system in long coherence mode. Assuming the initial beam divergence at the laser output as constant, when switching between long and short coherence mode, allows to obtain a similar collimation

Both LiFH recording set-ups, presented in the following two Sections, use basically the same vertical arrangement (RBDU) for the delivery of the two reference beams, as already indicated in Figure 6.1 with the terminus "plane of reference-beam-delivery".

6.1.2 Recording Set-up with Out-of-plane Illumination and In-plane Reference Beams

Figure 6.4 shows the set-up corresponding to the first case, where the reference beams are in a common plane with the center point of the flow volume. After passing the beam combination unit of the laser system (see Section 5.2.1.4) the beams are steered upwards by two high-reflecting mirrors to match the height of the measurement section. The first reflection of a glass wedge plate (about 10 %) is used to obtain the reference signals and the directly transmitted beam illuminates the flow field. To maintain similar lengths of the object- and reference beam paths for LiF recording, the path of the illuminating beam has to be folded by various high-reflecting mirrors.

The main intention for this recording geometry was to enable a stable and robust reconstruction set-up, in which beams only propagate in one horizontal plane (shown later in Section 6.2.2). The symmetrical design of the recording set-up is in favour of a



Figure 6.3: Photograph of the RBDU equipped with optional tools for fine-adjustment of the reference beams path-lengths and beam expansion with spatial frequency filter (beam propagation artificially added for clarity).

much larger aperture in the direction perpendicular to the reference beam propagation, thus the reconstructing aperture can be a slit. Equally oriented for the reconstruction of both recordings, this aperture can be moved along the line given by the projection of the common plane onto the holographic plate (see inlet of Figure 6.4). Thus, the horizontal extension of the aperture utilizes the full width of the holographic plate, increasing the numerical aperture (NA) of the recording system. The full length of the plate however, is used to map a flow volume with sufficient depth by simultaneously allowing for a narrow slit aperture, resulting in efficient noise suppression by LiFH.

Shown as gray overlay are all optical components which are not placed in the plane of depiction. Details of the reference beam delivery have been described in Section 6.1.1 and are indicated by the dashed line in Figure 6.4. A major drawback of this set-up is the fact, that generally the same depth of a measurement volume is mapped to different positions on the holographic plate when LiFH recording with a short coherence length is used. Depending on the evaluation method this can cause problems to match particle image pairs. Consider the reconstructed particle image as a long and thin ellipsoid in space with its major axis pointing towards the reconstructing aperture. Now, when reconstructing from different locations on the holographic plate, the reconstructed images have differently oriented major axes and an evaluation by correlation fails (further discussion is given in Section 7.2.4).

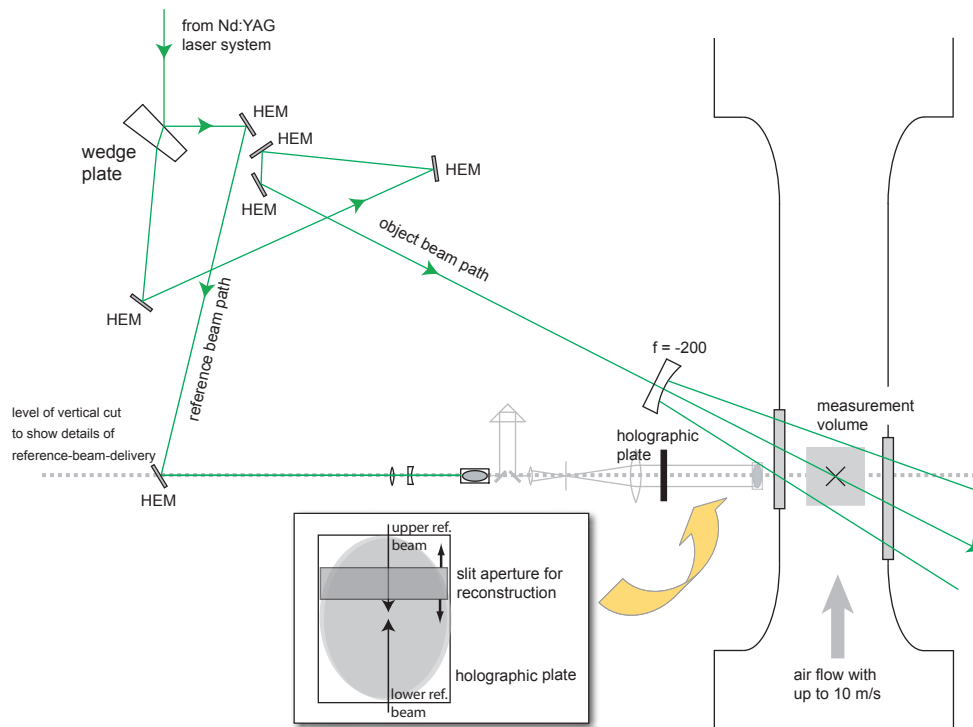


Figure 6.4: Recording set-up with in-plane reference beams. The illuminated areas on the holographic plate have an almost perfect overlap, a slit aperture can be used for the reconstruction. A single depth position is mapped symmetrically to either side of the holographic plate, depending on whether the according reference beam is incident from left or right. Only for the mid-depth position do both regions on the holographic plate overlap.

6.1.3 Recording Set-up with In-plane Illumination and Out-of-plane Reference Beams

To overcome the problems of particle image matching, a set-up with out-of-plane reference beams was realised (see Figure 6.5). Again, the laser beams are steered upwards to match the height of the measurement section and the first reflection of a glass wedge plate is used to obtain reference signals. Despite an additional collimation lens and a differently folded beam path, the object illumination has not been changed.

For the reference beams, exactly the same delivery unit as for the set-up in Figure 6.4 was used (again indicated by the dashed line in Figure 6.5), only the final propagation direction of the reference beams towards the holographic plate was modified. Both beams are now incident from the rear side, one slightly from above, the other slightly from below the depicted plane. The beams are grazing incident as defined by their common horizontal angle α in Figure 6.1. However, their azimuthal angle differs by some 20° to multiplex both the two recordings.

Such an arrangement allows to reconstruct the same region in depth from both the superimposed holograms through the same circular aperture on the hologram. For this, the reconstructing aperture has to be moved along the line bisecting the projections

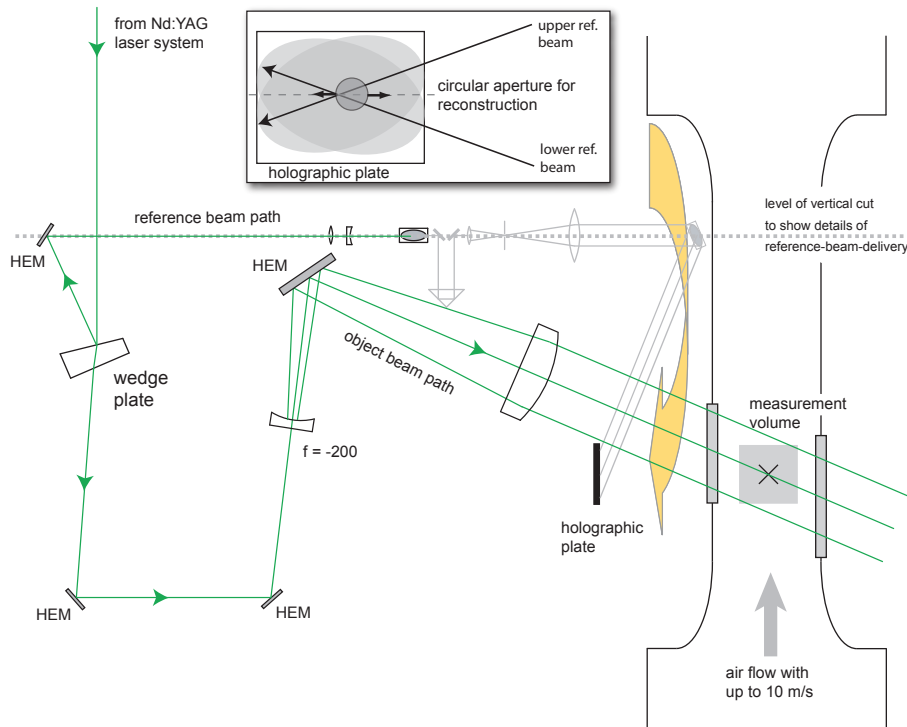


Figure 6.5: Recording set-up with out-of-plane reference beams only differing by their azimuthal angle of incidence. As a consequence, the overlap of the illuminated areas is decreased, but a small circular aperture can maintain the reconstruction of approximately the same depth from the same aperture position for both reference beams.

of the planes of incidence of both the reference waves onto the hologram (see inlet of Figure 6.5) when scanning the depth. In the present case this results in a horizontal scan of the aperture through the centre of the hologram.

6.2 Separate Reconstruction Set-up

The reconstructed real images need to be distortion-free and stable for a long period to be scanned by an imaging sensor. Thus, beside high quality beam-guiding optics and motorised translation stages the light source used for the reconstruction is a key element of the measurement system. It should emit a stable laser beam at exactly the same wavelength as used for the recording. Since the ruby laser used in previous experiments can be operated only in single or double pulse mode with a low repetition rate, a continuous-wave (cw) laser at $\lambda = 694 \text{ nm}$ would be required for the scanning. There is, however, no such counterpart to the ruby laser and the only solution would be to fine-tune a laser diode (Konrath et al., 2002), which calls for an extremely stable temperature control. More easily, in the LiFH experiment with the pulsed Nd:YAG laser presented in Chapter 5 there exists a cw counterpart at $\lambda = 532 \text{ nm}$.

A suitable cw Nd:YAG laser for the scanning is shortly presented in Section 6.2.1 of this Chapter. In Section 6.2.2 a simple arrangement to scan holographic particle

images from both, a normal hologram or a LiF hologram is described. The following Section 6.2.3 deals with the technical implementation of such a scanning system, used throughout the studies presented in this thesis. A scanning procedure described in Section 6.2.5 has been especially developed to obtain reliable data from real particle images much larger in cross-section than the imaging sensor itself.

6.2.1 Solid State and Diode Pumped Reconstruction Laser

The real image of a particle hologram is preferably reconstructed by a cw-laser to prevent the necessity to synchronise the digitising imaging sensor with a pulsed laser source. Furthermore, high energy is generally not needed for the reconstruction, and pulsed lasers even in fast repetitive mode have usually higher operating costs and a less stable beam-pointing due to non-equilibrium thermal loads during their operation (see also Section 5.2.3). Finally, our method "Holography at the Noise Limit" can be easily realised by just increasing the exposure time of the digitising sensor.

For the reconstruction of LiFH holograms with their typically small aperture size, and hence low reconstructed image intensity, a medium power continuous-wave Nd:YAG laser was selected which can easily saturate the available imaging sensors when reconstructing a hologram. A good compromise between reliability, stability and price is obtained from diode pumped Nd:YAG lasers in an ultra-compact and robust design. A OEM module, model Compass 315M-150 from Coherent (Deutschland) GmbH, was selected to build a separate reconstruction set-up. With an optical power of 150 mW in TEM₀₀ and SLM mode this laser provides a good basis for this task.

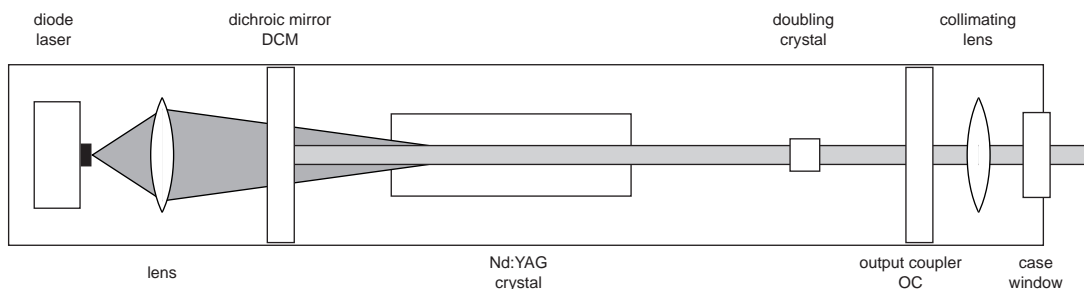


Figure 6.6: Sketch of diode end-pumped Nd:YAG laser used for the reconstruction of holograms in the separate reconstruction set-up.

The optical layout of the Compass 315M is shown in Figure 6.6. The emission characteristic of the diode laser ($\lambda = 815$ nm) permits effective pumping in an end-pump configuration. Therefore the divergent and astigmatic output beam of the diode laser is imaged into the laser rod by a lens through the dichroic mirror (DCM). The DCM and the output coupler (OC) are forming the Nd:YAG laser resonator. Inside this resonator, a frequency doubling crystal is placed which generates light of 532 nm wavelength through a non-linear process (see Section 5.2.1.3) when a sufficiently high internal

power is achieved. The resonator mirrors are highly reflective only for the fundamental 1064 nm wavelength and the OC is transparent for the green light. For optimum stability the pumping laser diode is thermally stabilised by a thermoelectric element which provides either cooling or heating as needed. In addition, the excess heat from the base plate of the laser has to be removed via a suitable heat sink.

6.2.2 General Scanning Arrangement

For an accurate reconstruction of both holographic images, and - most important - their relative position, it is necessary to precisely rebuild the reference beam geometry of a given recording set-up, inversely propagating however, to yield the conjugate beams (see also Section 2.1.4). For the discussion of the automated scanning procedure, a typical scanning arrangement is shown here only in its more simpler, horizontal form (Figure 6.7), which matches the recording set-up of Section 6.1.2. However, the geometrical layout of the beam delivery towards the hologram can be far more complex than depicted in Figure 6.7. Especially when LiFH with correlation analysis is applied, the reconstruction set-up needs to be extended also to the third dimension to match the recording set-up of Section 6.1.3. Such an extension for the purpose of reconstructing holograms recorded at a large wind tunnel is described in Section 8.2.

To obtain two plane reconstructing waves, the laser beam is split by a beam splitter (BS). Then, every beam is expanded by a microscopic objective (MO), spatially filtered by a pinhole (P) and collimated by an achromatic lens. Although, only a single wavelength is used, these high quality lenses have been selected due to their low astigmatic failure. The collimation has been checked again using a shear-plate interferometer (cf. Section 2.1.4.2). Figure 6.8 shows a typical fringe pattern obtained from the reference beams in our reconstruction set-up, here the beam was purposely adjusted slightly out of collimation to demonstrate the method. From the measures available in the figure and the smallest detectable deviation from the collimated case given by the manufacturer of the shear plate one can calculate the wavefront radius R_w as a worst-case boundary using (2.15). Given a distance $z_0 = 30$ cm between the hologram and a reconstructed particle image, the remaining axial positioning error of the particle image according to (2.16) can reach $\delta_z \approx \pm 0.15 \mu\text{m}$, resulting in twice this number for the maximum error of a displacement measurement from two separately reconstructed particle images.

Each beam is then directed by a highly planar ($< \lambda/20$) mirror to illuminate the hologram. Fine tuning of the direction of incidence can be obtained with a house-made kinematic mirror mount. Roll, pitch and yaw of the plate holding the mirror are introduced by two micro-screws located above a ball bearing fixation. Since it is more or less impossible to simply copy the angular beam geometry of a recording set-up by statically setting a mirror position, the possibility to fine-tune the conjugate beam pointing to a high precision is mandatory.

To calibrate the reconstruction set-up, an additional hologram of a static object, ideally with tiny markers less than a camera pixel in size, needs to be taken with the recording set-up. During reconstruction, these two real images can be shifted to perfectly over-

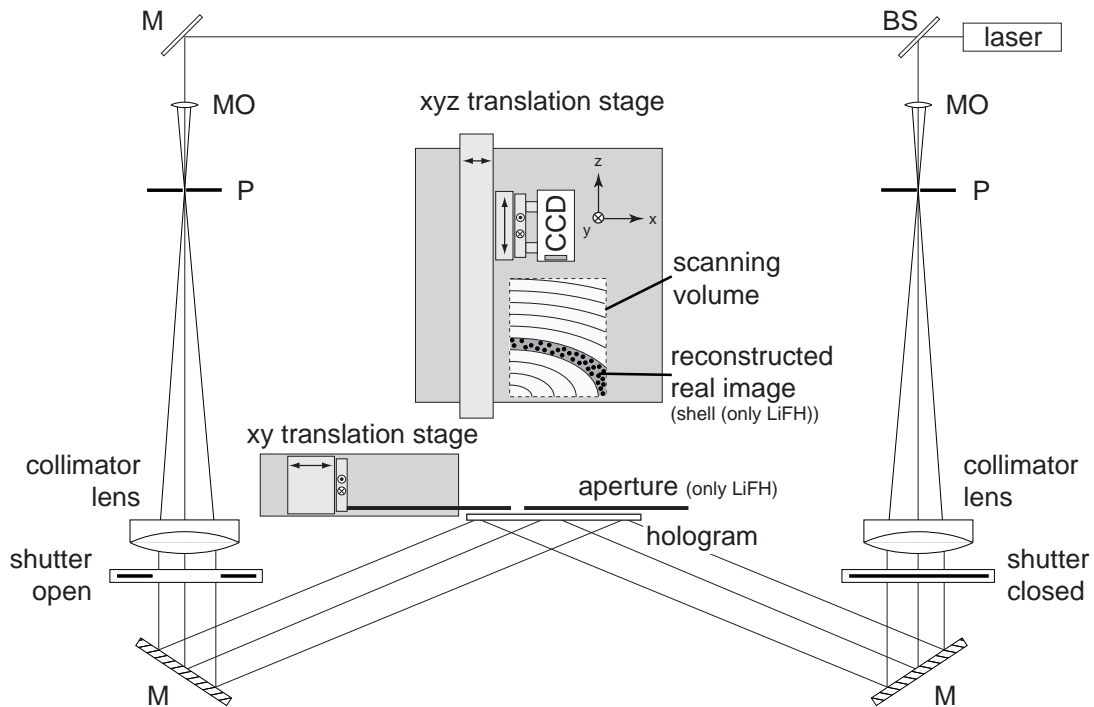


Figure 6.7: General arrangement to scan two successively recorded holographic particle images by a CCD array for a computer-aided evaluation of digitised image planes. The xy translation stage is used to select the depth of the reconstructed real image shell from LiF holograms according to the actual position of the CCD array. Two shutters are used alternately to reconstruct either the first or second image, which are digitised separately by the CCD.

lap. Alternatively, random but static markers can be used and the calibration is done with respect to the displacement between the two images obtained from a correlation procedure similar to those used for planar PIV and adjusting the mirrors accordingly. If the flow around an object is studied, which is also recorded on the hologram, the calibration information might be already contained in the flow hologram unless the object itself has moved between the two exposures.

Each beam reconstructs one of the two recorded holographic images. These real images are then scanned by a bare CCD sensor mounted on a xyz translation stage controlled by a PC. In order to select the first or second holographic recording, two electro-mechanical shutters are used alternately to block either beam. In the case of a LiF hologram, the reconstructed shell is selected by an aperture mounted behind the hologram. This aperture is moved by a second translation stage parallel to the hologram plane and according to the actual position of the CCD array. In the case of a normal hologram this aperture is not needed or fully opened to reconstruct the particle images in the whole scanning volume.

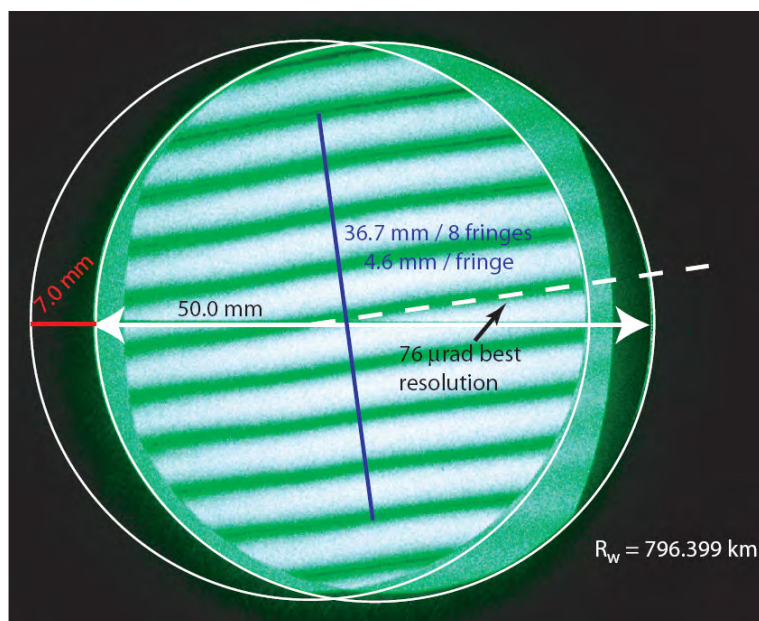


Figure 6.8: Checking the reference beam collimation in the reconstruction set-up using a shear-plate interferometer. The uncertainty in the orientation of the fringes parallel to the cursor (hidden by the white arrows) defines the deviation from a perfectly plane wave by calculating the worst-case wave front radius R_w .

6.2.3 Technical Implementation

The reconstruction set-up is designed to fulfil three major needs, which are commonly arising from HPIV experiments. Firstly, recorded holograms often have to be inspected manually, prior to a full scan. This is done to obtain optimum reconstruction parameters, like image brightness, exposure time of the CCD array and aperture positions for LiFH, but also to check for unwanted reflections or larger defects in the holographic image. Secondly, the scanning procedure should be automated, with no need for any manual intervention, to run autonomously even over a period of several days. And thirdly, a possibility to also record holograms with the cw laser in the reconstruction set-up is a plus, e.g. for experiments comparing the achievable image quality from model particle fields, recorded either with the pulsed or the cw light source.

For recordings with the cw laser, the optical set-up shown in Figure 6.7 has been extended with an additional time controlled shutter and a variable beam splitter right behind the laser. The reflection from this beam splitter can be used as an object beam, further guided and manipulated by lenses and mirrors according to the experiment's need. To meet the two first requirements mentioned above, the whole arrangement is controlled by a single PC, equipped with an additional COM port extension card and a Matrox Genesis frame grabber with a digital I/O interface. Connected to the latter, is the CCD array (Hamamatsu) via its control box, which also sets image size, pixel binning and exposure times by serial line commands issued from the PC over one of its six available COM ports. Two COM ports are used for the communication with the two control boxes steering the translation stages, another for switching the shutters by producing logical TTL signals on a Hewlett Packard function generator. The remaining

Axis	Mean and standard deviation of half step motion				Repositioning error after calibration at origin	
	ρx	σ	μm	σ	ρx	μm
x	1.03	0.23	9.27	2.07	< 2.5	< 22.5
y	0.54	0.14	4.86	1.26	< 0.5	< 4.5
z	1.08	0.26	9.72	2.34	< 0.5	< 4.5

Table 6.1: Measured precision of xyz translation stage which is used to scan the real particle images.

COM port (one serial mouse is used) can be used in future to control the laser output via an optional digital laser control box. In that way, the laser could be switched ON and OFF remotely and the power could be adjusted during a scan.

The translation stages ("Isel-x/y/z-Anlage" and "Isel-x/y-Anlage" from Isert-Electronic GmbH, Germany) are driven by stepper motors in half step mode. At maximum, a translation of 250 mm, 100 mm and 400 mm in x,y and z direction, respectively can be obtained with the stage moving the CCD array. The second stage allows to move the aperture along the dimensions of a typical holographic plate, 4 in \times 5 in or 102 mm \times 127 mm in size. According to the manufacturer, the precision of these stages is $< 10 \mu m$. To obtain reliable data on the achievable resolution, the step size and the repositioning precision of each axis, the absolute movement was measured by correlating images of a fixed Gaussian-shaped light spot (a few pixel in diameter) from a CCD array, which was mounted parallel to the moving direction of the axis. Since mechanical hysteresis effects arising from driving the threaded spindle many times back and forth are considerably affecting the precision, these have been prevented by starting each run from the same initial position. The starting side was always at the axis origin, at which the stage position is automatically calibrated by touching a micro switch when moving back. The stage moved to the following positions in step-wise increasing order. Each axis was measured ten times with ten steps after acquiring the initial image, resulting in a total of 110 images. Table 6.1 shows the mean step size for each axis and their standard deviation, as well as the repositioning error for a repeated run to the initial position after calibrating the stage position at its origin.

The x-axis was found to be less precise due to a pollution with grease at the threaded spindle and bushing. Furthermore, a non-strain-free assembly of the stages base plate was found to be another reason for a decrease of the precision. After cleaning and reassembling this axis showed a precision similar to that of the z-axis. The influence of the translation stage precision on the scanning procedure and its measurements errors is discussed in Section 6.2.5. For the positioning of apertures by the xy translation stage a similar precision is assumed, which is entirely suited for LiFH.

6.2.4 Software

To provide a comfortable and easy control of the translation stages, the CCD array and the two shutters for switching the holographic recording, a software written in Visual C++ was developed. It offers a graphical user interface (GUI) for on-line control of the set-up (see Figure 6.9) and allows a visual inspection of the reconstructed holographic image by manually moving the CCD array. The camera module can be switched ON/OFF and its exposure time, gain and offset can also be controlled. A live image is shown on a separate monitor, directly attached to the frame grabber card. When reconstructing a LiF-hologram the aperture can also be moved manually.

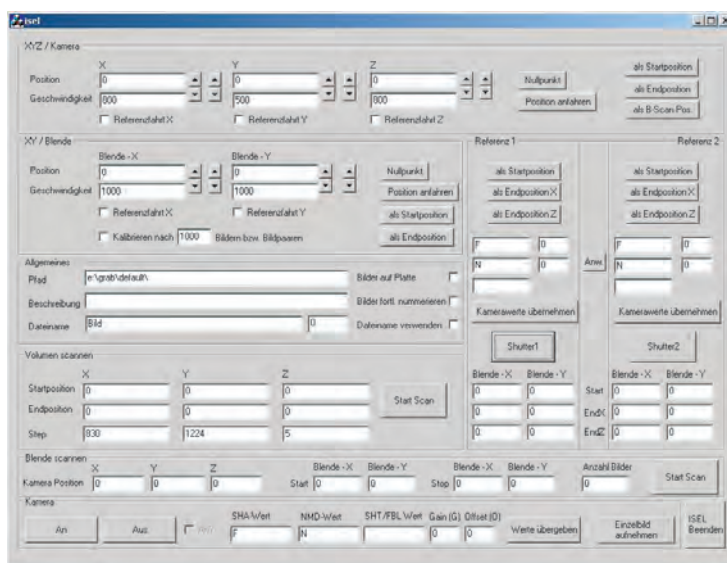


Figure 6.9: Graphical user interface of the software for steering and controlling the reconstruction set-up and the scanning of real images from particle holograms.

The software's GUI expects as an input the file system path, where grabbed image data has to be stored. Single images or automatically numbered sequences can then be grabbed for referencing and documenting a given holographic reconstruction. These single image grabs are saved with a filename consisting of an user-given base name and an optional extension with an increasing image number. A major part of this software is devoted to two automatic scanning procedures. Beside a more experimental procedure to study effects related to LiFH, the main procedure is the one for scanning a selected volume from two successively recorded holographic images. This procedure is discussed in detail in Section 6.2.5. By convention, the filenames during an automatic scan are referencing to the co-ordinates of the active translation stage (either the CCD array or the aperture) and the number of the reference beam used for the reconstruction. Thus, a clear relationship to the position and the holographic image is kept for an automated analysis of the image data. For each started scan the software creates a description file, holding all data necessary to identify the extent of the measurement volume and the scanning resolution. Furthermore, it holds a short description of the measurement, the place where the image data is stored and two camera-dependent pa-

rameters, together with the transversal step size describing the resulting overlap of the images.

The software allows the inspection of the two reconstructed images alternately by blocking either reference beam and moving the CCD array accordingly. In that way the spatial extent of the measurement volume can be determined precisely. Edge and corner positions in a holographic image can be found empirically and the corresponding co-ordinates of the translation stages can be copied to yield the start and end values for an automatic scan. In the case of an LiF hologram, the exact position of the aperture corresponding to a given position of the CCD array has to be found empirically, too. This can be done by manually controlling the xy translation stage and observing the image quality at a fixed CCD position (best focus and brightness of particle images). In case of edge or corner positions in the holographic image, the aperture position can also be copied, to be used as start or end values for an automatic scan.

6.2.5 Scanning Procedure

The scanning of the two successive holographic images can be optimised under two points of view. Firstly, scanning speed and secondly, scanning precision. Since the final measurement data are small local displacements between two holographic images, accuracy in the positioning of the CCD chip is a crucial point. Typical displacements, which can be detected from digitised images are in the range of 1/10 to 1/100 of a pixel. Comparing this with the precision of the translation stage (see Table 6.1) it becomes clear, that any movement between the digitisation of two successive images has a major impact on the measurement accuracy. Thus optical switching of the two holographic images at every CCD position is favoured, instead of scanning each holographic image separately, which would result in a much higher overall scanning speed. The position of the holographic images with respect to each other is also kept stable by use of a thermally-stabilized cw Nd:YAG laser for the reconstruction (cf. Section 6.2.1).

Figure 6.10 illustrates the concept of a procedure to scan images considerably larger in cross-section than the dimension of the CCD array. After calibrating all three axes at their origin, the stage is moving to the initial position of the scan. At this position two digital images are grabbed successively, each exposed by one of the two holographic images, which are reconstructed each by opening the respective shutter (see Figure 6.7). Then, the translation stage is moved along a direction normal to the CCD array (along the depth direction z of the holographic image), to maintain a stable relationship between neighboured pixels of a grabbed frame in either plane. In this way only the distance between two depth-wise separated images is affected by the precision of the translation stage. After scanning the full depth the sensor is moved back to the foremost point and translated in x -direction. An overlap of about 130 pixel ensures that a randomly placed local sub-area, typically between 16×16 and 128×128 pixel in size, fits entirely in a single grabbed image. This prevents from patching up a larger area digital image from the many grabbed frames in one plane. Again, the scan is continued depth-wise, as it is also done in the following for all positions along the x -

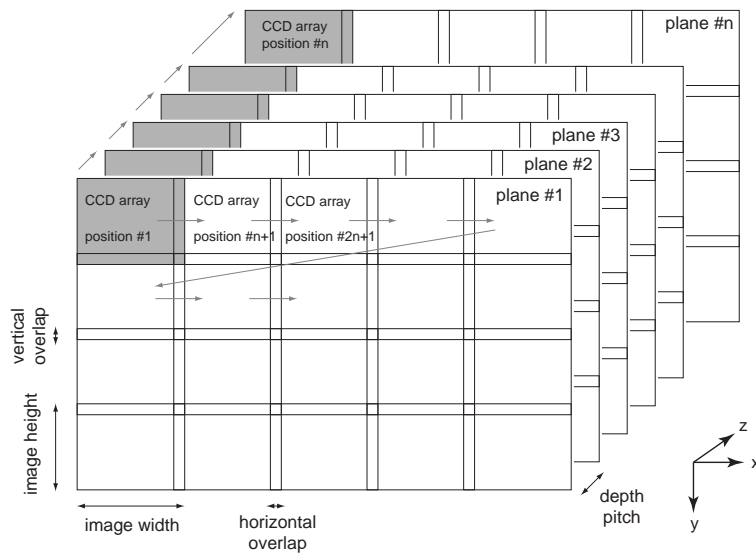


Figure 6.10: Operational sequences of the real image scan to digitise the two holographic particle images.

direction. After completion of a full row, the x -axis is driven to its initial and the y -axis to its next position simultaneously. After completion of all rows the axes are moved back to their origin. Re-calibration of a single axis during the scan is commonly not needed, but should be used whenever one of the axes has been travelled for more than a hundred times back and forth.

7 Evaluation Procedures of Real Holographic Particle Images

Different evaluation methods of digitised particle images are reviewed in Section 7.1, before an extension of the classical PIV evaluation - the three-dimensional intensity correlation - is presented as the method-of-choice for LiFH-PIV in Section 7.2.

7.1 Short Review of Evaluation Procedures

Once the holographic particle images have been scanned, the most complex part on the way to a full 3D velocity information is reached: the evaluation of the particle images to extract their displacement. This task has been tackled in various ways and was reported extensively in literature. Here only a short review of the most elaborated methods shall be given, keeping in mind that each method is also an expression of the individual optical layout of the given HPIV system and can not necessarily be adapted to other systems. However, this review expresses the effort undertaken by researchers to analyse the huge amounts of images extracted from the mass-storage device hologram.

7.1.1 Stereoscopic Viewing and Phase Conjugate Replay

Barnhart et al. (1994) presented a holographic camera system capable of recording two separate views of the flow. Both views were recorded twice on a single holographic plate, separated in time by angular multiplexing the reference beam. The recording of the two views required additional guiding optics for the scattered object light. In order to reconstruct the particle images without severe aberrations, a phase conjugate reconstruction was necessary requiring to replace not only the hologram but also the guiding optics (Barnhart et al., 1993). During the reconstruction one of the views was blocked. Switching the reference beam allowed to scan the volume and to acquire two images for cross-correlation analysis at each position. In a second run, the scan was repeated with the second view opened. The digitised particle images have then been analysed, plane by plane and for each view separately by two-dimensional cross-correlation with advanced windowing techniques to increase resolution and correlation peak finding ability (Adrian et al., 1993). By combining the data from the two views according to the stereoscopic PIV principle (Arroyo and Greated, 1991; Prasad and Adrian, 1993) the third velocity component could be extracted.

The system was designed to measure a $100 \text{ mm} \times 100 \text{ mm} \times 100 \text{ mm}$ volume at 1 mm resolution, requiring 2×10^6 two-dimensional cross-correlations, two for each resolution cell. At the time of the publication a self-constructed parallel processor com-

puter system was used and the acquired digital images have been subdivided into eight arrays, each passed to a single processor. With a Fast Fourier Transform (FFT) algorithm a rate of 100 vectors per second could be reached. To investigate a turbulent air flow through a circular pipe, $0.5 - 1 \mu\text{m}$ oil droplets have been used in a concentration of ~ 10 particles/ mm^3 . With an interrogation window overlap of 50% a total of $57 \times 57 \times 138 = 448,362$ vectors has been obtained within a $24,5 \times 24,5 \times 60 \text{ mm}^3$ measurement volume. The size of the particle images was $15 - 30 \mu\text{m}$ in transversal direction depending on the particle size, but also with the position of the image with respect to the reconstructing aperture. The later is a consequence of the orientation of the CCD sensor, intersecting the particle images with a varying angle when moving through the holographic image. Thus, the transversal displacement results obtained from the cross-correlation analysis had to be corrected according to the local intersection angle. In longitudinal direction the image sizes are found to be in the range of $100 - 700 \mu\text{m}$, again depending on the particle size.

7.1.2 Hybrid HPIV with Orthogonal Views

A combination of in-line and off-axis recording geometry was used by Zhang et al. (1997) to measure a turbulent water-flow in a square duct. A unique feature was the utilization of the strong near-forward scattered light, while blocking the direct illumination light by an optical high-pass filter. The scattered light could thus be recorded with an off-axis reference beam. Due to the relay lenses needed to filter the scattered light, a stereoscopic viewing of the particle images was impossible. Instead, the system incorporated two orthogonal views, recorded on two separated holographic plates. While for the recording a double-pulsed ruby laser (at a relatively low energy of 25 mJ) was used, the reconstruction was done with a 5 mW helium-neon laser. Image distortions according to (2.1.4.3) have been prevented by adjusting the reference beam angle accordingly and the remaining axial shrinkage has been countered for in the data analysis.

The two holographic particle images were scanned separately, each with 97 slices, 0.466 mm apart. Each slice was assembled from 270 single frames (containing 640×480 pixels) patched together. Analysis was done with auto-correlation and window-sizes of 192×192 pixel, overlapping 50%. The 3D velocity field was obtained by combining the two data sets, where the redundant component was further used for precision matching both sets. From the water-flow seeded with $15 \mu\text{m}$ polystyrene particles at a concentration of $1 - 8$ particles/ mm^3 , a total of $97 \times 97 \times 87 = 818,583$ vectors has been obtained within a $46.60 \times 46.60 \times 42.25 \text{ mm}^3$ measurement volume.

Drawbacks of the hybrid HPIV system are the complexity of the setup, including the need of at least four windows for optical access to a flow chamber or tunnel and a low-pass filtering effect on the calculated velocities. The later is due to the large depth-of-focus d_f from utilizing the near-forward scattering regime (with typically narrow scattering lobes decreasing the effective aperture, cf. Section 2.3.1) such that d_f is comparable to roughly twice the image plane separation. A more recent approach of the same research group aims to overcome these limitations (Sheng et al., 2003). The two

views are recorded simultaneously on a single holographic plate, one as the "original" image of each particle, the other as the "mirror" image. The later has been obtained by introducing a mirror at 45° , which either reflects the light scattered by each particle or reflects the light illuminating each particle. Using this system, measuring the particle locations was only possible with a remaining uncertainty of $7\ \mu\text{m}$, thus calculating the 3D velocity field by a 3D direct correlation as intended has failed. Instead, the previously described procedure (Zhang et al., 1997; Tao, 2000; Roth and Katz, 2001) was modified. Before calculating the auto-correlation the images are pre-processed to trim the elongated particle images. Together with a sophisticated calibration procedure to find precisely the mirror plane and matching the two views, the spatial resolution of the measurements could be increased to $110 \times 77 \times 250\ \mu\text{m}^3$ (a total of $96 \times 110 \times 61 = 644,160$ vectors within a $10.56 \times 8.47 \times 15.25\ \text{mm}^3$ volume). For this, a water flow was seeded with $20\ \mu\text{m}$ particles at a number density of roughly $200\ \text{particles}/\text{mm}^3$.

7.1.3 Side-scattering Recording and Center-of-Mass Evaluation

The currently most actively reported research work on classical HPIV is based on the so-called Gemini HPIV system (Pu and Meng, 2000a; Pu et al., 2000; Pu, 2002; Pu and Meng, 2003, 2004; Meng et al., 2004), claiming for the first time also semi-time-resolved, full-field 3D3C measurements by means of recording a phase-locked tab flow at eight distinct snapshots (Pu, 2002). Its basic configuration and the fast Concise Cross-Correlation (CCC) algorithm are patented world-wide (Pu and Meng, 2000b).

The system utilizes a 90° side-scattering recording to yield a high effective numerical aperture by shortening the recording distance to a minimum. Recording and reconstruction are done with the same pulsed laser source (frequency doubled Nd:YAG twin-laser system, $400\ \text{mJ}/\text{pulse}$, $10\ \text{Hz}$ repetition rate) using the same reference beam optics. These two separate reference beams are expanded by commercial high quality beam-expander. The two plane waves (roughly $7.6\ \text{cm}$ in diameter) are incident under $\pm 45^\circ$ on the holographic plate, to allow angular multiplexing and single exposure recording per reference beam. A major drawback of the side-scattering configuration is the weak scattering from particles about three orders of magnitude less in intensity than light scattered in forward direction (cf. Section 2.3.1).

The two real images of either hologram are reconstructed alternately, each at $10\ \text{Hz}$ repetition rate. A CCD sensor synchronised with the laser source and mounted on a 3D traversing system is used to capture images at a rate of roughly 2 frames per second (fps), or one image pair from the first and second recording, respectively. However, the reconstruction with the same pulsed laser source than used for the recording implies that phase changes in the beam profile (cf. Section 2.1.4.5), which occur from one digitised plane to the next, can enter in the primary measurement data, the intensity distribution. The particle images are magnified by a microscopic objective with low magnification ($\times 2 - \times 4$) mounted to the CCD camera head. A trade-off between processing speed (large area images) and accuracy (reduced depth-of-focus due to magnification) has to be found.

The huge amount of raw image data is first compressed into a list of particle cen-

troid locations. This task involves a thresholding procedure to separate particle image pixels from background pixels, clustering by searching the neighbourhood of the high-intensity pixels and computing the geometric centroid of each cluster by an intensity-weighted-mean procedure (see also Section 7.2.2.1). The two sets of locations are then cross-correlated and optionally a particle-pairing based on the evaluated displacement is carried out to obtain for each identified particle-pair one displacement vector (CCC algorithm). Finally, the irregularly placed vectors are rearranged on a regular grid by interpolation.

The air-flow inside and around an acoustically induced vortex-ring, seeded with $5\ \mu\text{m}$ water droplets at a concentration of $30\ \text{particles}/\text{mm}^3$ has been measured with the Gemini HPIV system. A total of $50 \times 40 \times 50 = 12,500$ interrogation cells (ICs), each consisting of 20 image planes with $1\ \text{k} \times 1\ \text{k}$ resolution and $2 \times 2 \times 2\ \text{mm}^3$ in size, has been analysed. In a $25 \times 20 \times 25\ \text{mm}^3$ measurement volume a total of 6,000 vectors has been obtained by the correlation-only procedure, which could be increased by a factor of 15 to a total of 92,000 vectors after particle pairing by the CCC algorithm was used. Thus, in average only every sixteenth particle image has been paired successfully. Quite impressive for the time of the experiment (1997) is the processing time of only 50 hours with raw image data amounting to 250 GB.

From a tab-flow in water seeded with $9\ \mu\text{m}$ hollow glass beads a total of roughly 80,000 vectors has been obtained after particle pairing ($11 \times 14 \times 64 = 9,856$ ICs) within a $44 \times 56 \times 32\ \text{mm}^3$ measurement volume. After Gaussian-interpolation on a regular grid with 0.6 mm pitch the number of vectors was further increased to 400,000.

7.2 A Straight-Forward Approach: 3D Intensity Correlation

Two-dimensional intensity correlation is widely used in many fields of optical metrology and builds the basis for the evaluation of particle images in PIV. Moreover, the mathematical formulation can be easily extended to the three-dimensional case, which makes the method a potential candidate for the direct evaluation of volumetric particle image samples, like those obtained from scanning holographic particle images. This section discusses the basics of a three-dimensional intensity correlation and describes the developments to implement the method for the evaluation of full-field 3D3C-displacements from holographic particle images.

7.2.1 Motivation

During the last decade many algorithms based on the 2D intensity correlation have been developed to extract displacements from particle images, which are captured during a pulsed illumination from a sheet-like laser beam (see also Section 1.1.2). The two successively recorded digital images are subdivided in equally spaced interrogation areas (IA), each from the first frame to be correlated with the corresponding area

from the second frame. The methods to measure the displacement are based on finding a peak-position with sub-pixel accuracy in the correlation function, which is related to the mean particle image displacement between the two exposures. This is done by searching for the largest peak of the correlation function and fitting various functions or using estimators derived from optimal fit functions. Most of the estimators can readily be used also for the third dimension, as they are mainly operating in one dimension (see Section 7.2.2.1). More advanced estimators would need own developments, to be used in full 3D space.

Generally, the accuracy of directly computed correlations (using Direct Fourier Transforms (DFT)) is comparable to those obtained by Fast Fourier Transform (FFT) algorithms (Foucaut et al., 2004). The FFT method is however, considerably faster unless no a-priori knowledge about the approximate peak location can be applied, which in turn allows to decrease the number of computations for the DFT considerably and hence increases the computing speed to be faster than FFT on the full field (Roth and Katz, 2001). The high demands on computing power have been the main reason in the past for not extending the correlation based methods to 3D. Nowadays high-end PCs offer a working memory large enough to hold the data during the processing of reasonably large samples (e.g. 2×128^3 px) and the processors are fast enough to decrease the overall computing time to hours instead of days, making the evaluation of fully volumetric data affordable. In the following Sections the basics and the implementation of a FFT-based algorithm is described.

Due to the assumption that the image sample is repeated infinitely (which is to make up for the computation over a finite and discrete domain instead of following the mathematical definition of the Fourier transform as an integral over an infinite domain) some unwanted side-effects arise from computing the FFTs to get the correlation signal. These have been treated theoretically for the 2D case (Keane and Adrian, 1992; Westerweel, 1997; Raffel et al., 1998) and the recommendations for optimum use with particle images also apply to 3D.

More recent PIV algorithms aim to overcome remaining problems related to the correlation analysis, such as in-plane loss of pairs, velocity gradient compensation and correlation peak locking (Keane et al., 1995; Lecordier et al., 1999; Scarano and Riethmuller, 2000; Nogueira et al., 2001; Scarano, 2002; Gui and Wereley, 2002; Nogueira et al., 2004). Although they are generally more demanding by means of computing power (interpolation, deformation and iterative steps are involved), they clearly demonstrate that accuracy and resolution in PIV measurements can be significantly increased. In this sense, it can be assumed that in future also 3D algorithms can be enhanced by these advanced techniques.

7.2.2 Mathematical Formulation

The cross-correlation function of two functions $f(t)$ and $g(t)$ is defined by:

$$C(f, g) = \overline{f}(-t) \odot g(t), \quad (7.1)$$

where \odot denotes convolution and $\bar{f}(-t)$ is the complex conjugate of $f(-t)$. With the definition of the convolution it can be shown that (7.1) is equivalent to:

$$C(f, g) = \int_{-\infty}^{\infty} \bar{f}(\tau)g(t + \tau)d\tau. \quad (7.2)$$

Similar to the derivation of the Wiener-Khinchin theorem the cross-correlation theorem

$$C(f, g) = \mathcal{F}^{-1} [\bar{F}(\nu)G(\nu)] \quad (7.3)$$

can be obtained from the definition of the Fourier transform plugged into the definition of the cross-correlation. Here, the inverse Fourier transform is denoted by \mathcal{F}^{-1} and the upper-case functions are the Fourier-transforms of \bar{f} and g . By letting $F = G$, i.e. computing the auto-correlation, it can be seen that the Wiener-Khinchin theorem is a special case of the cross-correlation theorem.

Since ordinary digitised particle images represent discrete samples of the intensity distribution in two dimensions, the cross-correlation-function has been rewritten into a 2D-discrete form (Willert and Gharib, 1991; Westerweel, 1993). Stacks of digitised particle images can be viewed as a 3D intensity distribution and thus a 3D-discrete form is needed. Giving (7.2) explicitly in three spatial dimensions and with continuous intensity distributions I_1 and I_2 , for the first and second exposure respectively, yields:

$$C(x_0, y_0, z_0) = \iiint_{-\infty}^{\infty} I_1(x, y, z)I_2(x + x_0, y + y_0, z + z_0) dx dy dz. \quad (7.4)$$

With the discretization of the form $x = j\Delta x + x_0$, $y = k\Delta y + y_0$, $z = l\Delta z + z_0$ it then follows for the discrete cross-correlation function in three dimensions:

$$R_{II}(j_0, k_0, l_0) = \sum_{j=-J/2}^{J/2} \sum_{k=-K/2}^{K/2} \sum_{l=-L/2}^{L/2} I_1(j, k, l)I_2(j + j_0, k + k_0, l + l_0). \quad (7.5)$$

As seen in (7.3) the computation of the cross-correlation can be obtained by three Fourier-transforms, one of which is an inverse transform. The discrete Direct Fourier-transform (DFT) in three dimensions over a square volume of $N^3 = J \times K \times L$ pixel is given by:

$$DFT(\nu_x, \nu_y, \nu_z) = \frac{1}{N^3} \sum_{j=1}^N \sum_{k=1}^N \sum_{l=1}^N I(j, k, l) \exp \left[-\frac{2\pi i}{N} (j\nu_x + k\nu_y + l\nu_z) \right]. \quad (7.6)$$

The complexity \mathcal{O} for the calculation of Fourier-transforms can be decreased significantly by implementing the Fast-Fourier-Transform (FFT) algorithm after Cooley

Dimensions	DFT	FFT
1	$\mathcal{O}(N^2)$	$\mathcal{O}(N \log N)$
2	$\mathcal{O}(N^4)$	$\mathcal{O}(N^2 \log N)$
3	$\mathcal{O}(N^8)$	$\mathcal{O}(N^3 \log N)$

Table 7.1: The numerical complexity \mathcal{O} for the calculation of the Fourier-transform in one to three dimensions for the Direct Fourier-Transform (DFT) and the Fast-Fourier-Transform (FFT).

and Tukey (1965)¹, which results in a considerable gain of processing-speed for 3D-Transformations (see Table 7.1). Furthermore, the 3D-FFT can be computed by consecutive 1D FFTs along the respective rows, columns and depth-wise columns, which allows an optimisation of the algorithms used.

7.2.2.1 Subpixel Algorithms

Obtaining the position of the correlation peak with sub-pixel accuracy from the cross-correlation function is not at all straight forward. Many researchers have adopted methods which are suited for a variety of particle image types. Centroiding, namely the ratio between the first and zeroth order moments, works quite good for large particle images, where the correlation peak is spread over many pixels. Fairly well focused and resolved particle images, however, are typically only 2 to 3 pixels in diameter and have an intensity distribution which is well approximated with a Gaussian curve. As a consequence, the correlation peak is also a Gaussian curve distributed over 2-3 pixels. To obtain sub-pixel information from these, the so-called three-point estimators are well suited. Depending on particle image size and shape, as well as on the noise level, different estimators are suited and can be chosen by setting options for the evaluation (for example for those based on fitting a parabola or a Gaussian function to the correlation peak).

In a first step, the standard sub-pixel estimators have been extended to the third dimension, neglecting the fact, that the holographically reconstructed particle images are considerably larger in axial direction than in transversal direction (see also Section 2.2.1). A summary of the estimators for the 3D case is given in Table 7.2. The maximum correlation value $R_{(i,j,k)} = R_{II}$ determines the approximate position of the correlation peak and from the adjoining correlation values the sub-pixel information is extracted according to the estimators given in the table.

¹The algorithm, including its recursive application, was already known around 1805 to Carl Friedrich Gauss, who used it to interpolate the trajectories of the asteroids Pallas and Juno, but his work was not widely recognized and has been published only posthumously in neo-Latin (Gauss, 1866)

Fitting function	Estimator
<p>Peak centroid</p> $C_0 = \frac{M_1}{M_0} = \frac{\int xI(x)dx}{\int I(x)dx}$	$x_0 = \frac{(j-1)R_{(j-1,k,l)} + jR_{(j,k,l)} + (j+1)R_{(j+1,k,l)}}{R_{(j-1,k,l)} + R_{(j,k,l)} + R_{(j+1,k,l)}}$ $y_0 = \frac{(k-1)R_{(j,k-1,l)} + kR_{(j,k,l)} + (k+1)R_{(j,k+1,l)}}{R_{(j,k-1,l)} + R_{(j,k,l)} + R_{(j,k+1,l)}}$ $z_0 = \frac{(l-1)R_{(j,k,l-1)} + lR_{(j,k,l)} + (l+1)R_{(j,k,l+1)}}{R_{(j,k,l-1)} + R_{(j,k,l)} + R_{(j,k,l+1)}}$
<p>Parabolic peak fit</p> $f(x) = Ax^2 + Bx + C$	$x_0 = j + \frac{R_{(j-1,k,l)} - R_{(j+1,k,l)}}{2R_{(j-1,k,l)} - 4R_{(j,k,l)} + 2R_{(j+1,k,l)}}$ $y_0 = k + \frac{R_{(j,k-1,l)} - R_{(j,k+1,l)}}{2R_{(j,k-1,l)} - 4R_{(j,k,l)} + 2R_{(j,k+1,l)}}$ $z_0 = l + \frac{R_{(j,k,l-1)} - R_{(j,k,l+1)}}{2R_{(j,k,l-1)} - 4R_{(j,k,l)} + 2R_{(j,k,l+1)}}$
<p>Gaussian peak fit</p> $f(x) = C \exp \left[\frac{-(x_0-x)^2}{k} \right]$	$x_0 = j + \frac{\ln R_{(j-1,k,l)} - \ln R_{(j+1,k,l)}}{2 \ln R_{(j-1,k,l)} - 4 \ln R_{(j,k,l)} + 2 \ln R_{(j+1,k,l)}}$ $y_0 = k + \frac{\ln R_{(j,k-1,l)} - \ln R_{(j,k+1,l)}}{2 \ln R_{(j,k-1,l)} - 4 \ln R_{(j,k,l)} + 2 \ln R_{(j,k+1,l)}}$ $z_0 = l + \frac{\ln R_{(j,k,l-1)} - \ln R_{(j,k,l+1)}}{2 \ln R_{(j,k,l-1)} - 4 \ln R_{(j,k,l)} + 2 \ln R_{(j,k,l+1)}}$

Table 7.2: An overview of three-point estimators used to obtain the displacement with sub-pixel accuracy (adopted from Raffel et al. (1998)).

In a second step, the elongated particle images have been taken into account by modifying the three-point estimators to work not only on directly neighboring pixels. Instead, the estimators are now accepting a value given in pixel, which increases the sampling interval related to the actual particle image size d_f in axial direction. Thus, the formerly adjoining values are replaced by:

$$R_{(j,k,l\pm 1)} \rightarrow R_{(j,k,l\pm d_f/2)}. \quad (7.7)$$

No precautions were made to separate between background and correlation peak before calculating the sub-pixel values, since thresholding is a difficult task in highly noisy images (see also Section 9.3.3). It is believed, but not yet proven, that the estimators often fail when the shape of the reconstructed particle images in the ICs shows complex boundaries and the noise level is rather high. These effects are in accordance with literature and in a future version of the estimators for (LiF-)HPIV. Especially the centroiding should be extended to work on either only pixels in between $\pm d_f/2$ (as done by Pu and Meng (2000a) for directly finding the centroid of a particle image) resulting in a rectangular-shaped sub-space or on an ellipsoidal sub-space from which the volumetric center-of-mass can be extracted directly.

7.2.3 Image Data Handling and Correlation Algorithms

The algorithms used here for the evaluation of the digitised particle images have been continuously developed throughout the course of various experiments and yet they are still being improved, especially under aspects of processing speed and accuracy. All algorithms have been written as Matlab scripts, allowing fast coding and testing, as well as cross-platform implementations. The development so far can roughly be divided into two stages.

The first stage is a very simple implementation for extracting the desired image data and calculating the three-dimensional cross-correlation for a given sub-volume, commonly called interrogation cell (IC). First a regular grid covering the whole measurement volume is defined, corresponding to the size of the ICs and their overlap. This grid represents the spatial resolution of the measurement and is then processed point by point. At each grid point only one pair of ICs is extracted from the image data stored on the hard-disc. The corresponding image data is found from the parameters saved in the measurement description file (cf. Section 6.2.4). Only those ICs fitting entirely in the overlap-region of two transversely neighbouring images are always extracted from the second image. This ensures that a positioning error of the translation stage does not enter into the displacement result, since the correlation procedure supposes that the image pixels in a sub-volume are identically spaced over the whole IC (see also Section 6.2.5).

Due to the huge amount of memory allocated during the computation of the correlation, only a single IC pair can be stored in the memory of the computer (512 MB ram). Thus, each saved image file is opened separately and the image area corresponding to the point on the evaluation grid is extracted. This small area (usually 64^2 or 128^2 pixel)

is then stored as one plane into one of two three-dimensional matrices. These matrices, forming the ICs of the first and second exposure, are then correlated according to (7.6). From the resulting correlation matrix the position of the peak is determined with sub-pixel-accuracy (see Section 7.2.2.1) indicating the mean displacement of the particle ensemble covered by this IC. In this first stage, the sub-pixel-routines have been only a simple extension to the 3D case and did not take into account the considerably longer particle images in axial direction. It was found, that the parabolic and the gaussian peak fit were extremely sensitive to noise and due to the over sampling they did not produce very accurate results. Hence, in this stage the evaluation was preferably done with the peak centroid algorithm. Since the whole procedure has to be repeated for every point on the grid, each image file is opened multiple times when neighboured ICs are processed, resulting in a low overall processing speed.

The development for the second stage aimed to increase the processing speed by combining two approaches. Firstly, the number of ICs extracted from a series of digitised planes located in depth-wise succession has been increased to avoid unnecessary reloading of image data. Unfortunately, writing all ICs to the hard-disk and reloading them again for the computation of the correlation matrix did not speed up the evaluation significantly. After some optimisation of the code (alternately processing of only a part of the image data and extracting the corresponding ICs, followed by calculation of the cross-correlation functions and sub-pixel peak finding) a major decrease of the mean computation time per vector could be achieved (see Section 7.2.3.1). Secondly, distributed computation over several computers was used, resulting in a further decrease of computation time. This parallel processing has been implemented on a heterogeneous network using mDICE (Pfarthofer et al., 2003). The server extracts a larger number of IC-pairs (typically 252 at 64^3 and 63 at 128^3 IC size) from the stored image data, splits up these tasks according to the available number of clients in his domain of the local area network (LAN) and starts to distribute the so called jobs (see Appendix A.8).

Discrete window offset to reduce the measurement noise, as proposed by Keane and Adrian (1992) and analyzed in detail by Westerweel et al. (1997), has not yet been implemented into our 3D-algorithms due to an even larger memory consumption during the calculation. It is obvious, that further improvements, analogous to the development of 2D-PIV algorithms, are suited to significantly increase the accuracy of 3D particle image correlation results.

7.2.3.1 Computing Demands

The first implementation of the 3D intensity correlation, as used in most experiments described in this thesis, has high demands on computing performance. Both, permanent storage capacity as well as memory needs during computation of the vector field are still very high. Nevertheless, it is nowadays feasible to carry out this kind of particle image evaluation within reasonable times. During the course of the experiments the computer power has increased by a factor of 8 according to Moore's law. The following analysis is based on a state-of-the-art PC from the year 2002. Shown in Figure 7.1 is the mean computation time per vector depending on the size of the interrogation

cell (IC) and obtained from correlating 100 ICs each. This gives a good estimate for determining the total time for the evaluation of a complete measurement volume.

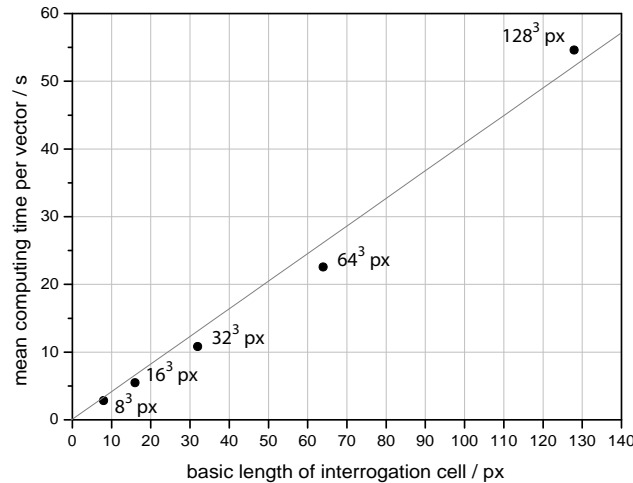


Figure 7.1: Mean computation time per vector versus size of IC on a Pentium P4 processor with 2.0 GHz clock frequency and fast IDE hard disk drive.

As an example, some 6.800 vectors can be evaluated from 64^3 px-size ICs per day on the given machine. To compare this with the performance of other computers, the evaluation of 100 ICs, each 64^3 px in size, was repeated on other machines available at the time of the experiments. The results are shown in Figure 7.2.

Practically, most of the full-field evaluations at that time have been done on two or three machines simultaneously and the whole vector field was rearranged after computation from the different sub-volumes. It turned out, that this approach is not well suited under a Windows-based computing environment, since copying of thousands of image files via network to another machine is very time consuming. Only with FTP a reliable and stable file exchange could be realized. Using simple network connections, e.g. mapped drives of remote computers, did not perform very well (see also last bar in Figure 7.2). Furthermore, the connection was generally not stable enough over evaluation periods of some days.

The second stage of the software development took into account the actual demands on computing power. Consequently, distributed or parallel computing was considered. Figure 7.3 demonstrates the decrease of the overall evaluation time obtained with an improved evaluation method (cf. Appendix A.8). In this case, the computation for a whole volume was split in 540 tasks, each covering 252 interrogation cells, from which always 18 have been transmitted as one job to a single client. The mean computation time per task was under the given conditions (depending on the actual load of the network and clients) 206.5 seconds, split up into roughly 45 seconds for the data preparation and 161.5 seconds for correlation and peak-finding. Thus, in less than 31 hours a total of 136,050 vectors was evaluated, resulting in 0.82 seconds per vector. Details about the evaluation process, which is still being continuously improved, are given in Appendix A.8.

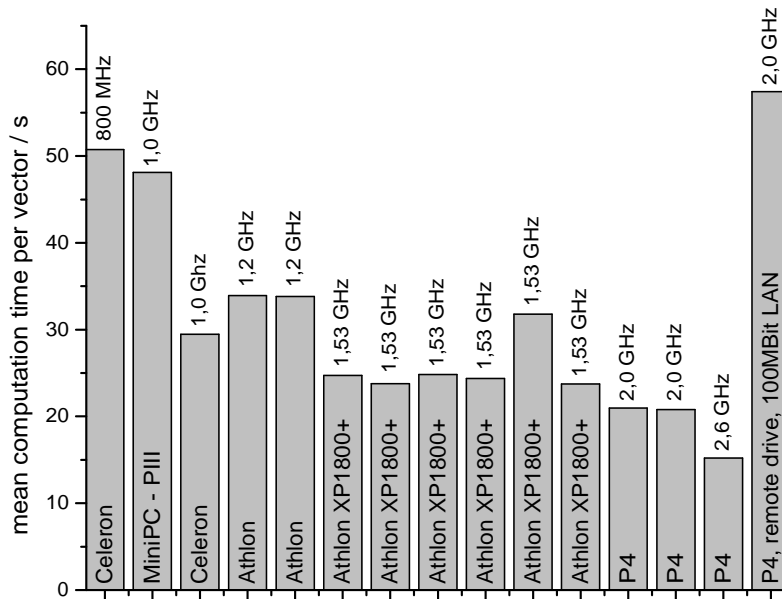


Figure 7.2: Mean computation time per vector from an 64^3 px-size IC on various PCs.

7.2.4 Restrictions when LiFH is used

It was observed that the 3D intensity correlation completely fails when the set-up according to Figure 6.4 with in-plane reference beams is used. The reason becomes clear by visualizing the 3D intensity distribution in a selected interrogation cell from the rear of the measurement volume. Figure 7.4 shows the isosurface plots of the intensity distribution at an appropriate threshold value.

The two reconstructed images, which are supposed to be correlated, differ significantly in their orientation. This is clearly a consequence of the LiFH method with in-plane reference beams. Particle images in the same depth-position are reconstructed from different aperture positions for the two reference beams. This results in different axial directions of the particle images. For a successful three-dimensional correlation however, the particle images in space have to be as identical as possible, which is only guaranteed when the reconstruction is done from the same aperture position.

Furthermore, the particle images appear slightly curved, a consequence of the simultaneously moving aperture when the CCD sensor is moved through the particle images (see also Section 6.2.2). Thus, for every digitised plane along the depth axis (Z -axis) the direction of the light - coming from the hologram aperture and being incident on the CCD sensor - is slightly different. As a rough estimate, the aperture in this experiment was moved for about 10 mm to cover the depth ($128 \times 50 \mu\text{m} = 6.4 \text{ mm}$) of the larger interrogation cell. This corresponds to a noticeable change in the reconstruction angle of about 1.9° at a distance of 30 cm between the hologram and the CCD sensor.

It follows that in order to use 3D intensity correlation together with LiFH recording, only the Setup according to Figure 6.1.3) with in-plane illumination and out-of-plane reference beams is suited. This however, comes with a reduced overall aperture size

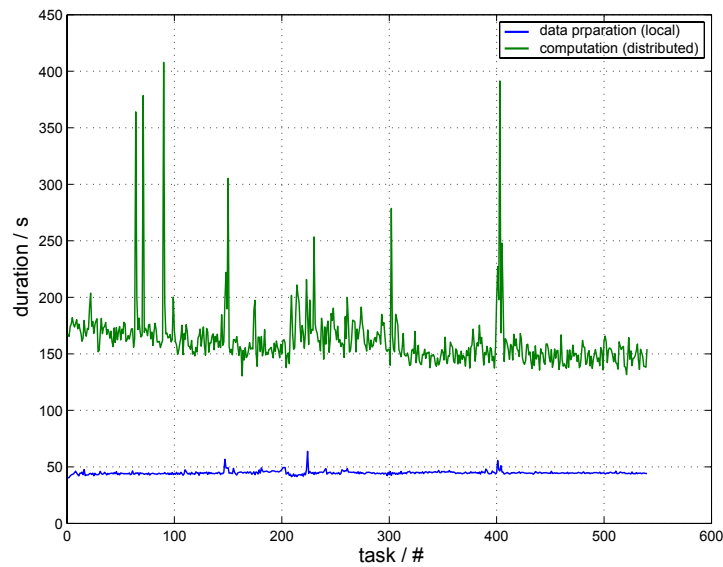


Figure 7.3: Evaluation performance of distributed computation using 7 PCs processing 540 tasks with 252 interrogation cells each. A total of 136,050 vectors from 64^3 px-size ICs was calculated in less than 31 hours. The duration for data preparation on a single machine stays almost constant (blue line), whereas the duration for the evaluation strongly depends on the load of the network and the clients.

(circular aperture instead of slit aperture) which in turn results in a larger DOF of the reconstructed particle images. Whether this drawback can be compensated by the evaluation method, especially compared to the other methods reviewed in Section 7.1, has not been studied yet.

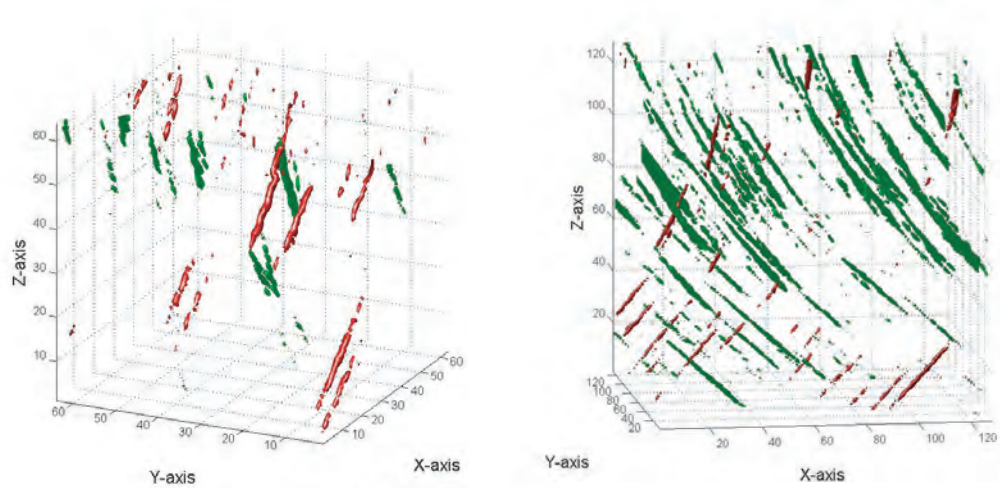


Figure 7.4: Differing Particle Image Orientation in a selected interrogation cell (IC) of size 64^3 pixel (left) and 128^3 pixel (right) for the two reference beams. Shown in green is the isosurface plot of the image intensity above a given threshold as reconstructed from the first illumination, in red from the second illumination. The plot is scaled pixel-wise and does not represent the real aspect ratio of the IC.

8 Wind-tunnel measurements with LiFH

This Chapter describes a study, in which the LiFH-technique was applied for the first time at a large industrial wind-tunnel using a double cavity pulsed Nd:YAG laser ($\lambda = 532$ nm). The utilised laser system is nearly identical to that presented in Section 5.2 but did not have a BeamLok control. The separate reconstruction set-up, presented in Section 6.2, was used at the laboratory in Oldenburg. Using our method "Holography at the Noise Limit", an intensity-integrated reconstruction of the weak particle images from two superimposed Light-in-Flight holograms of a globally seeded wind tunnel flow was realised.

8.1 Complete recording system at the wind-tunnel

In Figure 8.1 the optical set-up at the wind tunnel is shown true to scale. The open test section is about two meters wide and one meter deep. In the flow, a generic airfoil produced two counter-rotating tip-vortices. The reference signal is produced by the first reflection from a glass wedge plate that is split into two polarization dependent reference beams by a polarizing beam splitter (TFP).

A detailed side view showing both arms above and beneath the tunnel outlet is given in Figure 8.2. On each a prism was mounted on a mechanical translation stage to control the path length of each reference beam. Since the coherence length l_c of the unseeded laser is some 7 mm, the path lengths need to be identical within 1 mm compared to the path length of the object beam. This travels over three bending mirrors (HEM) before it is expanded by a set of two anti-reflection coated lenses to illuminate a small part of the wake flow behind the profile. The position of the centre of the measurement volume is located at a distance of some 35 cm from the holographic plate, which was placed exactly at the flow boundary. This is far enough to avoid vibrations affecting the stability of the measurement system but close enough to ensure high signals from the scattering particles. The delivery of the reference beams was realized with the vertical arrangement introduced in Section 6.1.1 in order to maintain the same azimuthal angle α of incidence onto the holographic plate, while the two recordings are distinguished by their elevation angles $\pm\beta$.

Perfect collimation of the reference beams was again controlled by a shearing interferometer (cf. Section 2.1.4.2). The beam profiles of the two laser heads showed intensity variations typical of a multi-mode laser which are changing with increasing distance from the laser-head aperture. Since a low pulse energy in the reference beams is already sufficient for a proper plate exposure, pinholes could be introduced without damage to improve the beam profile. A couple of holograms have been recorded under different

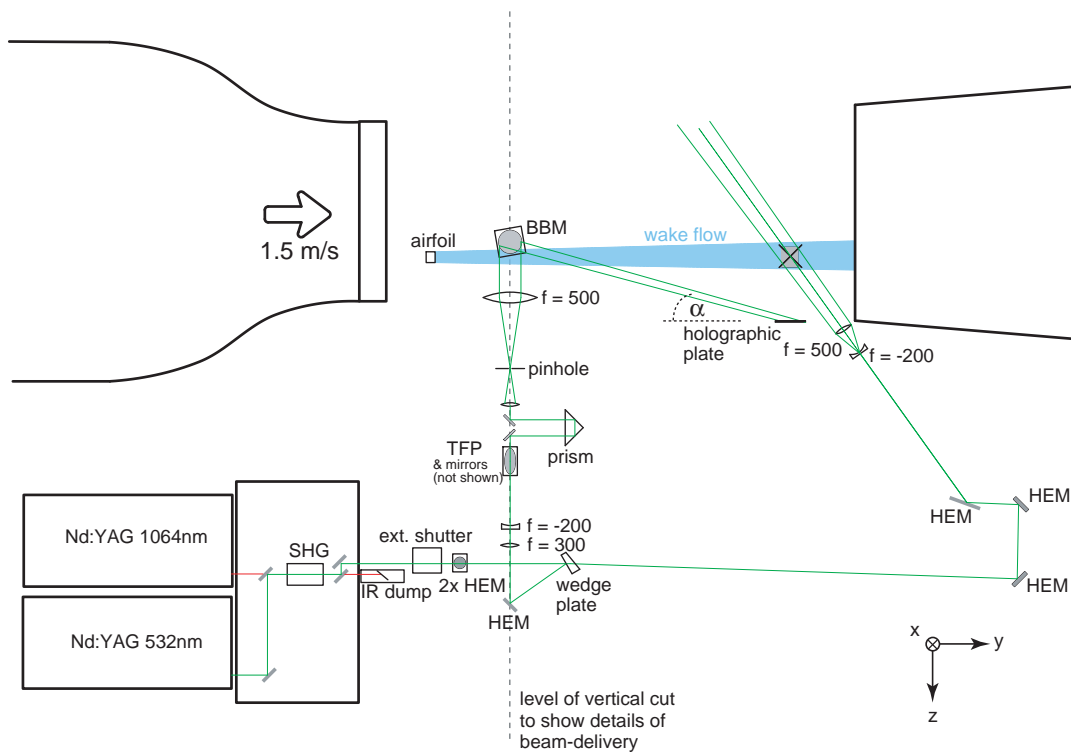


Figure 8.1: Set-up for recording LiFH-PIV holograms at the 1m wind tunnel at the German aerospace agency (DLR) in Göttingen, showing the beam paths from the laser heads through the combining optics and shutter, two mirrors (HEM) for adaptation of the beam height to fit the measurement area and the optics for holography as explained in the text. For the out-of-plane propagation as indicated by the dashed line and details of the reference beams see Figure 8.2.

conditions regarding type and size of particles as well as density, all having in common a very low amount of object light as compared to the reference light intensities. The mean flow of about 1.5 m/s produced rather stable vortices, but with fluctuating positions. Since there was no control to trigger the events, it turned out to be difficult to catch single vortices by the holographic method.

8.2 Off-site reconstruction

The automatic read-out set-up presented in Section 6.2 was used in a modified form to reconstruct the particle image fields from the wind-tunnel-flow holograms. Except the hologram and the translation stages shown in Figure 6.7, the whole part for the beam handling was placed again horizontally on the optical table. Together with the two final mirrors, which are now used to direct each reference beam upwards (out of the depicted plane) to illuminate the holographic plate, this arrangement forms the lower part of the scanning system. The upper part is shown schematically on the left of

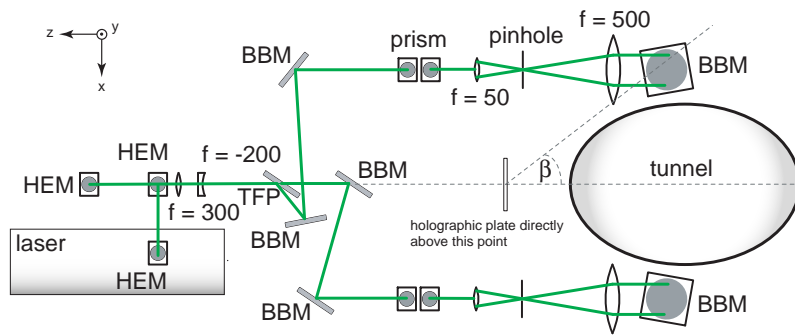


Figure 8.2: Side view of the reference beams with spatial filters (pinhole) for a more uniform illumination of the holographic plate. Given in grey are the outlet of the wind tunnel and the cover box of the combining optics. The thin-film polarizer (TFP) directs each pulse according to its polarization into one of the optical arms, guided by specially coated broad-band-mirrors (BBM). The beam is then directed out of the projected plane towards the holographic plate.

Figure 8.3. This scanning unit comprises the holographic plate and the two translation stages carrying the aperture and the CCD sensor.

The relative positions of the hologram and the mirrors are precisely scaled down from the arrangement at the wind tunnel to produce the same angles of incidence as before. For the sake of convenience, the complete arrangement has been turned by 90° with respect to the original recording orientation and the illumination of the plate (Figure 8.3, right) is now from below. Thus, angle β is now the originally vertical component of the angle of incidence, while the originally azimuthal component α determines the out-of-plane propagation direction.

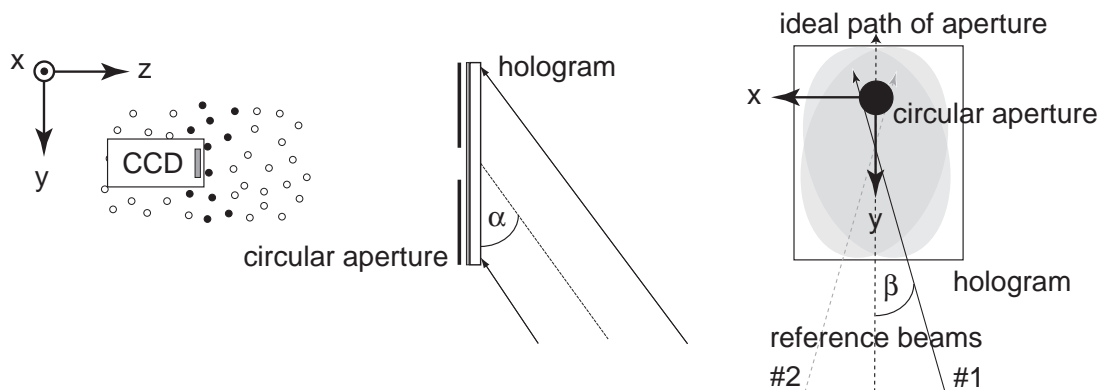


Figure 8.3: Upper part of the reconstruction setup used for the evaluation of the holograms from the wind tunnel experiments, showing the scanning unit (left) and the beam propagation towards the holograms (right). A moving aperture is used to select the corresponding depth according to the position of the sensor, while the beams are switched to reconstruct either particle field.

It was stated in Section 6.1.3 that the alignment has been made such that a single

aperture position allows the reconstruction of the same depth slice for both reference beams. Unfortunately, this scheme could not be fully realized in the present investigation. It was found that quite often the quality of the holographic images from the same aperture differed considerably. This occurred because the obliquely oriented elliptical fields of illumination did not evenly expose the complete holographic plate. The observed cross-sectional inhomogeneities are probably due to a not perfectly matched combination of lenses and pinholes used for expansion of the reference beams (in the laboratory a better adjustment of the expansion has been obtain later on). As a consequence, the aperture positions were corrected for better image quality, guided by an empirically established relation between aperture position and location of the reconstructed volume. Mainly, however, the apertures were each moved along the track set by the respective planes of incidence. A degradation of the correlation performance due to slightly dissimilar particle images was accepted, since the effect was by far not that critical as described in Section 7.2.4 for the completely opposing aperture positions.

Due to the large cross-section (≈ 40 mm in diameter) of the illuminated volume, the amount of scattered light was low, resulting in holograms with low diffraction efficiencies η . The method described in Section 3.2.2.3 uses a long-time exposure of the CCD sensor to compensate for these low diffraction efficiencies. We used this procedure for all evaluations of the flow holograms from the wind tunnel experiments, since exposure times usually used in CCD sensors (typically $\tau = 100$ ms) turned out to be insufficient for proper image quality. By carefully minimizing all scattered light reaching the sensor from directions other than the hologram it was indeed possible to extract long-exposure (up to $\tau = 2$ s) particle images with a good signal-to-noise ratio. Scanning times, of course, have been increased drastically, yet it becomes possible to record volumes of sufficiently large cross-sectional sizes from a globally seeded wind tunnel flow.

8.3 Results

All holograms recorded at the wind tunnel have been examined in a first step as to their particle image quality and density. In an intermediate check during the measurement-campaign it turned out, that appropriate particle image densities are only obtained by very long operating times of the seeding-generator (four Laskin nozzles in a common base). To obtain a sufficient number of larger particles the generator was operated for up to one hour with lower pressure settings that achieve a broader particle size distribution than commonly used in wind tunnel measurements. According to previous measurements of size distributions using a similar pressure and also DEHS as liquid, about 50 % of the particles were smaller than $1 \mu\text{m}$ and only 7.5 % reached sizes larger than $3 \mu\text{m}$.

With a cross-sectional dimension of the object light beam of about 40 mm the scattered light intensities have thus been rather low. Judging from the type of reconstructed images we assume that only larger particles (i.e. $d_p > 1 \mu\text{m}$) contribute to the signals obtained from long-exposure reconstructions. Unfortunately, in most cases the particle

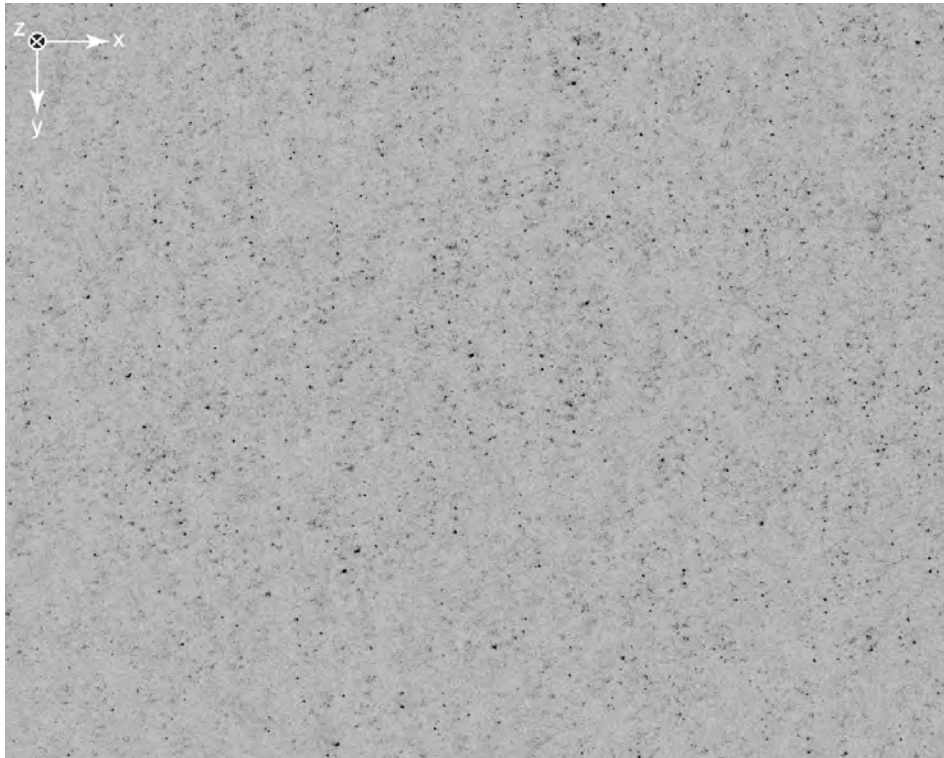


Figure 8.4: Artificially assembled double-exposure by superposition of two intensity-inverted digital images ($1280 \text{ px} \times 1024 \text{ px}$). These are obtained from two successively reconstructed corresponding holographic real images of a wind tunnel flow using either reference beam and an exposure time of 0.5 seconds. The field of view corresponds to $8.6 \times 6.9 \text{ mm}^2$ and the xy -plane shown is located at $z = 14.1 \text{ mm}$ in the measurement volume.

image densities have still been too low to allow for a proper correlation analysis on the images obtained. For the best hologram, however, the particle number density is high enough to evaluate the complete set of images by three-dimensional cross-correlations on 128^3 px -sub-volumes (cf. Section 7.2). A volume of $24.0 \times 18.8 \times 29.1 \text{ mm}^3$ was scanned within 35 hours of operation time of the read-out-unit, the bottleneck still being the slow translation stage moving the circular aperture over the hologram between exposures. The result are 5,409 image pairs, each 2.5 MB in size in total more than 13 GB of image data.

A sample plane from the reconstructed image is shown in Figure 8.4 as an artificially assembled double-exposure by superposition of the images reconstructed by both the reference beams. The double structure in the particle image distribution is quite obvious. The xy -plane corresponds to a depth coordinate of $z = 14.1 \text{ mm}$ (cf. Figure 8.7) and shows displacements mainly in the y -direction, i.e. the direction of the mean wind-tunnel flow. Due to the out-of-plane motion, however, not every particle image shows a twin partner. Despite the maximum depth resolution ($9.8 \mu\text{m}$) of the translation stage, adjacent image planes have been acquired with a separation of $49 \mu\text{m}$ to facilitate the

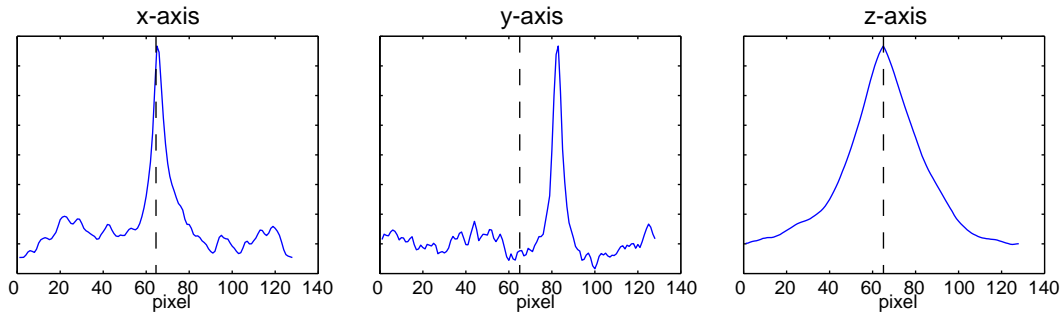


Figure 8.5: Example profiles through the maximum value of a three-dimensional matrix of the correlation function, the IC size is $128 \times 128 \times 128 \text{ px}^3$ and corresponds to a size of the interrogation cell of $857 \times 857 \times 6272 \mu\text{m}^3$, since the pixel-pitch in z-direction is $49 \mu\text{m}$ and in x- and y-direction given by the pixel size of the CCD array ($6.7 \mu\text{m}$).

use of sub-pixel algorithms and to prevent from over-sampling the elongated particle images, a consequence of the small aperture used to determine the depth position of the reconstructed shell within the measurement volume. Thus, the resulting interrogation volumes are $857 \times 857 \times 6272 \mu\text{m}^3$ in size.

As also can be seen from Figure 8.4 the noise level is still very low, allowing for a much higher number density of particles. Yet, their number was sufficient for a correlation analysis. Assuming a DOF (see Equation (2.26)) of about 0.65 mm the analysis of these images yields a density of about $14 \text{ particles per mm}^3$. This allows a comparison with the situation described by Equation (3.4). Taking for L the coherence depth of about 14 mm and introducing the proper experimental data (angular aperture $\Omega = 1/35$, $\text{SNR} = 5$, $\lambda = 532 \text{ nm}$ and best case values $\mathcal{M}, \gamma = 1$) we obtain a number density of $n_s = 13 \text{ per mm}^3$ at a given SNR of 5. Note, that the physical depth of the total illuminated volume was about 60 mm which would result in a much higher noise level under standard HPIV conditions, allowing for only $n_s = 3 \text{ per mm}^3$! As we will see in Section 9.3, it is not straight forward to obtain the SNR from such experimental images. Nevertheless, we can predict from Figure 8.4 that a considerably higher number density would be feasible for LiFH-PIV and Figure 3.2 suggests $n_s = 45 \text{ per mm}^3$ if an SNR of 3 can be accepted.

In Figure 8.5 three cuts through the maximum value of the correlation function are shown. Along the x- and y-direction the width of this function is similar to those known from two-dimensional PIV, while along the z-direction a much broader peak is observed. The width of the peak at a loss of 20 % in intensity is in good agreement with the depth-of-focus according to (2.26), which predicts $d_f \approx 0.65 \text{ mm} = 13.3 \text{ px}$, proving that the depth resolution of the measurement is mainly restricted by the small aperture. The y-cut shows a displacement of some 18 px, in the x- or z-directions displacement is about 1 px only.

As mentioned before, the moving vortices behind the generic air-foil provided an unfavourable flow configuration. A single snap-shot hologram of a small region is unlikely to reveal characteristic parts of a single vortex. Therefore, it is not astonish-

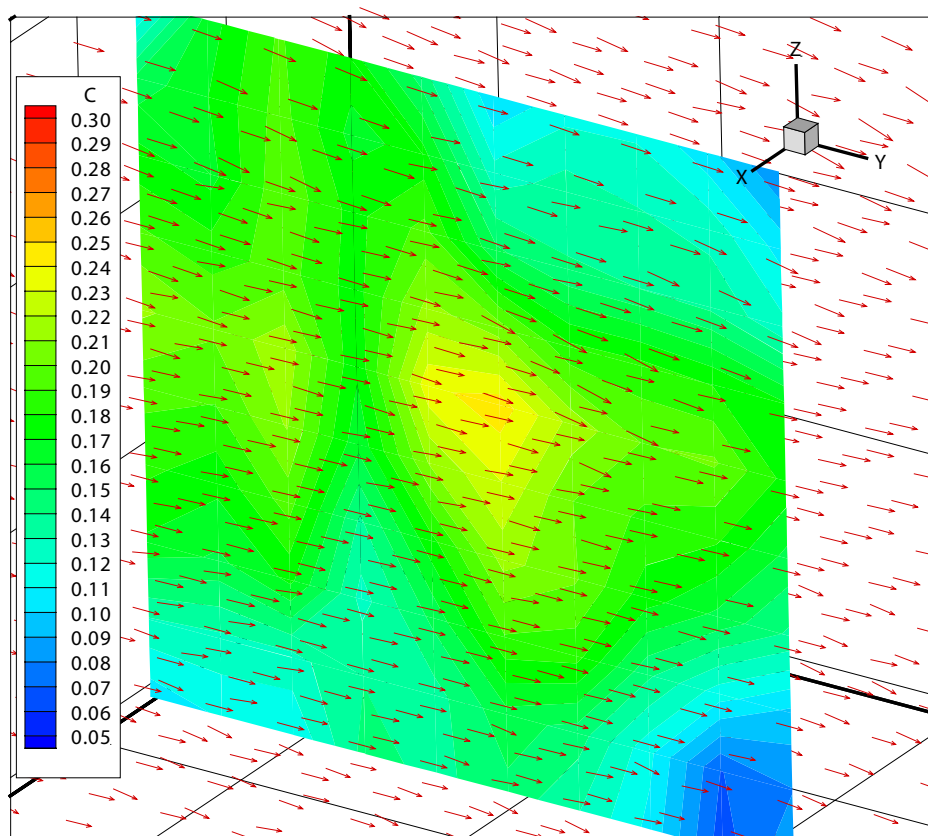


Figure 8.6: Detailed view, from inner part of the evaluated volume, showing the three-dimensional velocity distribution and the maximum value of the normalised correlation function (C) in one slice as a measure for the reliability of the velocity value.

ing that the hologram yields mainly the mean velocity of the wind-tunnel flow. A detailed view of the velocities in the interior of the flow field obtained from a three-dimensional correlation is shown in Figure 8.6, the corresponding maximum values of the normalised correlation function are given as a contour plot in one plane. For this evaluation an interrogation cell (IC) size of 128^3 px and an overlap of 75 % was used, resulting in a total number of vectors of 124, 800 within the reconstructed volume.

Figure 8.7 shows the complete correlation result of an evaluation with 50 % overlap of the 128^3 px ICs in each direction. A total of only 16, 640 vectors have thus been obtained, from which the mean velocity has been calculated to $[\bar{u}, \bar{v}, \bar{w}] = [0.01, 1.30, -0.28] \text{ms}^{-1}$. This is a reasonable result compared to 1.5ms^{-1} for the pure wind-tunnel flow as determined from the rotation rate of the driving rotor. In this representation the mean velocity has been subtracted and the plane-like distribution of vectors is clearly visible, which is a result of the densely-spaced grid points along the x - and y -direction and the much wider spacing (approx. $\times 7.3$) along the z -direction. Besides some spurious vectors due to poor image quality in the lower part, a net flow perpendicular to the mean flow is thus observed in the lower and upper regions (corre-

sponding to the front and the rear of the flow volume, respectively, which is marked with a cross in Figure 8.1) producing the arrows that project out of the planes. The quality of the correlation is still impeded because of the non-ideal matching of the aperture that produced dissimilar particle images. However, future improvements in the properties of the reference beams, especially towards a more homogeneous beam profile, should help overcome this problem.

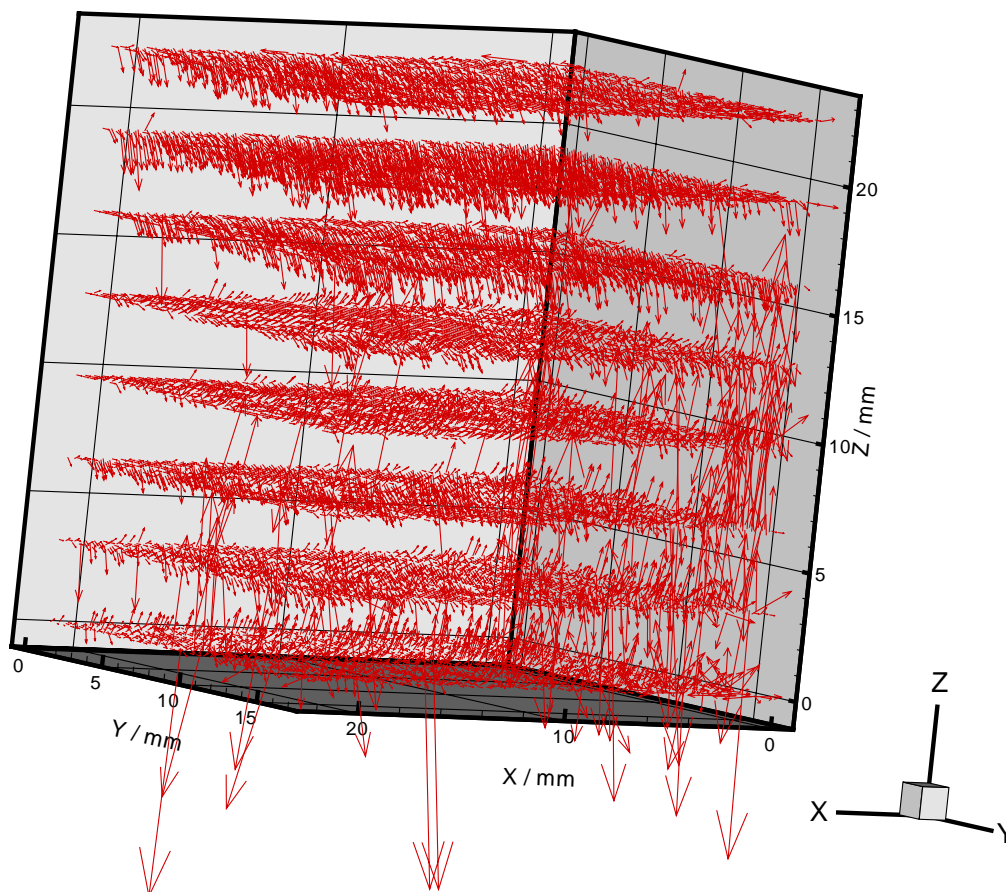


Figure 8.7: Evaluated wind tunnel flow, 16,640 vectors have been obtained by three-dimensional grey-value correlation. The plane-like distribution of the vectors is a result of a relatively large separation between adjacent digitised image slices, from which 128 enter in each correlation.

Even if these results do not furnish important flow data, it was shown that particle images of a quality sufficient for further processing could be extracted, yet with still too low a particle image number density. Judging from Figure 8.4 it becomes clear, that some correlations were based on only a single particle image pair and some could have been calculated from ICs without any in-focus particle image. A maximum depth (Z-axis) of 47 mm has been covered from other holograms, which however, could not be evaluated due to even lower particle number densities. The useable cross-section

of the measurement volume extended to $30 \times 30 \text{ mm}^2$ providing particles of sufficient brightness even at its border.

8.4 Discussion of the system and its drawbacks

It has been demonstrated that LiFH-PIV, which facilitates effective background noise reduction by use of a short coherence light source for the recording, is capable of mapping the three-dimensional flow field from a small section in a globally seeded large wind tunnel flow. The utilization of a separate reconstruction set-up using a continuous wave laser effectively reduces the necessary operating time of the wind tunnel and allows for simultaneous evaluation when recording the next LiF holograms. Furthermore, low intensity particle images have been analysed by an integrating reconstruction method, thus reducing the effective energy density of the pulsed illumination light needed for the recording and allowing for considerably larger cross-sections of the measurement volume.

The restricted depth resolution, one of the drawbacks of this LiFH-PIV realisation, however, needs to be addressed in further experiments. Reconstructions with larger effective apertures are feasible without impairing the principle of limited depth reconstruction (see Section 6.1.2) but call for a different evaluation scheme. Together with this study, however, for the first time a three-dimensional grey value correlation of sub-volumes to analyse an extended volume mapped by particle holography has been reported (Herrmann and Hinsch, 2004a). This approach, yet very time consuming and with high demands on computer power, is favourable when advanced evaluation algorithms are envisaged, most of which can be adapted without loss of generality from the two-dimensional case.

For further wind tunnel measurements the production of seeding particles needs to be optimised in terms of size distribution and number density. For this purpose, investigations have been made to understand the physical processes of particle generation (Kähler et al., 2002) and the influence of particle parameters on the holographic imaging process (Pu et al., 2002). Increasing seeding densities allows for smaller IC's, with 64 px (cf. Section 10.3) or even 32 px side-length. Also non cubic IC's in the pixel-domain are feasible to account for the smaller sampling intervals in depth-direction.

9 Comparison of Imaging Performance

A comparison of an LiFH- and other HPIV systems based on their imaging performance is not straight forward. The set-ups for particle holography, which are presented in literature, are usually optimized under different aspects, like particle scattering efficiency or high numerical aperture. Thus, a direct comparison can only be established by operating the same laser in either long-coherence or short-coherence mode and recording and reconstructing particle images with exactly the same set-up.

While in Section 4.2.3 only a qualitative overview of the differences between ordinary and LiF holography was given, in this Chapter a more profound discussion, based on theoretical (Section 9.1) and experimental (Section 9.2) checks, shall underline the advantage of LiFH when imaging deep particle fields. The complexity and difficulties in extracting robust and reliable information on the SNR of reconstructed particle images is considered and the direct results of this study are given in Section 9.3. In Section 9.4 these results are discussed and suggestions for a further elaboration of the comparison between LiFH- and ordinary HPIV are given.

9.1 Pre-Knowledge from Theory of Holographic Image Intensity

In HPIV, imaging performance is mainly determined by how good a particle image can be distinguished from a noisy background. Unfortunately, in many cases such a particle image (signal) can not be clearly separated from the background (noise). A detailed study of the influence of noise on particle images thus needs a comparison with theoretical predictions to better understand the noise contribution. A suitable model describing the holographic image intensity in presence of coherently added noise was already introduced in Section 3.2. A closer look to the different contributions reveals characteristic dependencies on a crucial parameter in HPIV, the hologram aperture.

9.1.1 Average Noise Intensity from Emulsion Grains

The theory for this type of noise is well established and various models have been applied for different purposes. Emulsion noise results from a random superposition of many coherent contributions scattered by photographic grains and thus follows speckle characteristics. This is independent of the type of model used. Goodman (1967), for example, elaborates a checkerboard and an overlapping circular-grain model. In either case, the average noise intensity $\langle I_N(\alpha, \beta) \rangle$ in the image plane increases in propor-

tion to the reconstructing aperture in the hologram plane $A_t(x, y)$ (see Appendix A in (Goodman, 1967)):

$$\langle I_N(\alpha, \beta) \rangle = \frac{I_p A_t}{\lambda_2^2 d_i^2} \iint_{-\infty}^{+\infty} \phi_{\tau'\tau'}(\Delta x, \Delta y) d\Delta x d\Delta y, \quad (9.1)$$

where $\phi_{\tau'\tau'}(\Delta x, \Delta y)$ is the autocorrelation function of the random transmittance $\tau'(x, y)$ of the developed photographic emulsion and I_p is the intensity of the reference beam with wavelength λ_2 incident on the hologram during reconstruction. The integration enters from evaluating the Huygens-Fresnel principle under par-axial conditions, where the difference between two arbitrary points, one in the image and the other in the hologram plane d_i is assumed to be constant.

9.1.2 Deterministic Particle Image Intensity

Neglecting the stochastic properties of the recording medium and considering the reconstruction process from a macroscopic point of view, leads to an expression for the reconstructed image intensity I_0 at a fixed point (α_0, β_0) , which is proportional to the exposures E_r and E_σ incident on the holographic plate from the reference wave and the object wave, respectively and also to the square of the hologram aperture area A_t (Goodman, 1967):

$$I_0(\alpha_0, \beta_0) = \left(\frac{\chi^2 (E_r A_t) (E_\sigma A_t)}{\lambda_2^2 d_i^2} \right) I_p, \quad (9.2)$$

with χ being the slope of the t_A - E curve (cf. Section 2.1.3).

For our further discussion it is useful to distinguish two cases by their particle number density when recording the holographic image:

1. First let us assume that the particle distribution in space is not very dense, i.e. a single particle can be viewed as an isolated point source object. Let's further assume that the particles are always smaller than the resolution cell, which is defined by the shape and size of the hologram aperture. Since all light from this cell is collected on the hologram, forming the exposure E_σ , we have diffraction limited imaging. In this case, because the exposure E_σ is independent of the size of the resolution cell, there follows $I_0 \propto A_t^2$. Thus, doubling the aperture size would result in a four times brighter particle image intensity, which is a consequence of the coherent superposition of partial amplitudes. The energy principle is not violated, since the light is now concentrated on a smaller resolution cell due to the increased aperture and the rest of the former has become dark.
2. In the other extreme case the density of particles might be high enough, such that an individual particle could not be fully resolved by the given hologram aperture. According to Goodman (1967) this case could be modelled as a diffusely reflecting surface. Now, the resulting exposure E_σ is proportional to the

area of the cell, which in turn decreases with increasing A_t . Thus, the image intensity goes proportional to the hologram aperture area: $I_0 \propto A_t$. Contrary to the former case, there are no regions that can compensate for the increase in image intensity by getting darker, the energy principle is straight forward.

9.1.3 Signal-to-Noise Ratio of Particle Images and its Dependency on Aperture Size

The signal-to-noise ratio (SNR) of the holographic image of a point source was already introduced in Section 3.2. As can be seen from (3.2) the small-noise treatment, adequately for HPIV, yields a final formula for the SNR:

$$\frac{I_0}{\sigma} = \left[\frac{I_0}{2\langle I_N \rangle} \right]^{1/2}. \quad (9.3)$$

Again let us distinguish the two cases, very low and very high particle number density, from the above (see Section 9.1.2):

1. The deterministic image intensity is proportional to the square of the hologram area, $I_0 \propto A_t^2$. Together with the proportionality from (9.1), $\langle I_N \rangle \propto A_t$ and (9.3), it follows that the SNR is proportional to the square root of the hologram aperture A_t :

$$\frac{I_0}{\sigma} \propto \sqrt{\frac{I_0}{\langle I_N \rangle}} \propto \sqrt{A_t} \propto D, \quad (9.4)$$

where D is the aperture diameter, a parameter which is changed during the experiments described in the following Section.

2. The deterministic image intensity is proportional to the hologram area, $I_0 \propto A_t$. Now, with the proportionality from (9.1), $\langle I_N \rangle \propto A_t$ it follows that the SNR is independent of the hologram aperture A_t :

$$\frac{I_0}{\sigma} \propto \sqrt{\frac{I_0}{\langle I_N \rangle}} = \text{const.} \quad (9.5)$$

With these characteristic dependencies, predicted by the theoretical model from Goodman (1967), an experimental check is given by simply modifying the diameter of a circular reconstructing aperture and determining SNR from the reconstructed particle images.

9.2 Experimental Realisation of the Comparison-Study

The variation of the SNR versus the aperture diameter D is chosen to be a good indicator, whether the theoretical model of the holographic particle imaging process can be applied to describe the imaging properties of HPIV and LiFH-PIV. To this end the deterministic particle image intensity I_0 and the average noise intensity $\langle I_N \rangle$ need to be extracted from the reconstructed and digitised image planes obtained from holograms recorded under well controlled conditions.

For the recording of these particle holograms, both types of set-ups presented in Section 6.1 have been used. The reconstruction was done in both cases with an adapted reconstruction setup, as shown in Section 6.2. Instead of using the full recording aperture, a circular iris was placed as close as possible behind the hologram in a central position. Since in this study no correlation function is calculated from the digitised image planes, the illumination of the holograms by either of the two conjugate waves is only used to check differences in the imaging properties between both multiplexed recordings.

9.2.1 Types of Particle Holograms

Various types of particle holograms have been recorded under different experimental conditions (set-up, density, air or water flow, etc.). Table 9.1 gives an overview of the recordings used for the comparison study. With the exception of "holo11" each group of two holograms forms a set for the direct comparison, with either short or long coherence, resulting in either LiFH-PIV or HPIV recordings, respectively. A further classification can be made by the type of the used recording set-up used and the specific purpose of the holograms:

First comparison: Using the set-up from Figure 6.5, which was discussed in detail in Section 8.1, small DEHS particles ($d_p \approx 1\mu\text{m}$) have been recorded in a large wind-tunnel air-flow at a relatively low number density. It was nearly impossible to get a reliable value for their number density at the moment of the recordings, since the wind-tunnel flow and the open test section had to be continuously seeded. Nevertheless, a rough estimate could be obtained later from the resulting recordings. Most important however, these two holograms differ significantly in their overall exposure due to the fact that the output power of the laser system is generally different when operated in either the long-coherence or short-coherence mode. During the experiments at the wind-tunnel this had not been corrected by use of different neutral density filters. Nevertheless, these recordings already offer a solid basis for a detailed comparison.

Influence of number density: Better conditions to control the exposure and the number density were given in the laboratory. With a set-up according to Figure 6.4 hollow glass spheres (HGS), the so-called Sphericels, have been recorded

Hologram	Type	Medium	Particles	#-density [1/mm³]
dlr13	HPIV	air	DEHS	≈ 12
dlr15	LiFH-PIV	air	DEHS	≈ 12
ndyag32	LiFH-PIV	water	HGS	10,12
ndyag33	HPIV	water	HGS	10,12
ndyag35	LiFH-PIV	water	HGS	17,19
ndyag36	HPIV	water	HGS	17,19
ndyag37	LiFH-PIV	water	HGS	12,35
ndyag38	HPIV	water	HGS	12,35
ndyag39	LiFH-PIV	water	HGS	16,45
ndyag40	HPIV	water	HGS	16,45
ndyag41	LiFH-PIV	water	HGS	8,73
ndyag42	HPIV	water	HGS	8,73
ndyag43	HPIV	PMMA	MR	≈ 45
ndyag44	LiFH-PIV	PMMA	MR	≈ 45
holo11	HPIV	PMMA	MR	≈ 15

Table 9.1: Overview of the holographic recordings used for the performance comparison of HPIV and LiFH-PIV. The holograms are distinguished by their recording principle (HPIV or LiFH-PIV) the carrier medium, the type of particles (which were adapted to the medium) and their number density to model the influence of different noise levels.

dispersed in water. For this a water-cuvette made from planar glass plates was filled with the accordingly diluted dispersion and a fluid flow (vortex) was produced by a magnetic stirrer. A total of five different number densities was produced by diluting down from a stock solution with an extremely high concentration of Sphericels. The later was obtained by mixing clear and filtered water with lots of the dry Sphericels and waiting for the sedimentation process to cease. In that way, only neutrally buoyant particles, $2 - 30 \mu\text{m}$ in size, could be extracted by a careful suction from the middle of the water column with a small tube. The effort undertaken and the remaining problems to quantify the resulting particle number density for each solution is explained in detail in Appendix A.10.

Limiting cases: Model particle fields have been produced from particles embedded in perspex (PMMA for Polymethylmethacrylat), which allows a good control over the particle number density. During the course of these experiments, two recordings from melamine resin (MR) particles, exhibiting an extremely narrow size distribution, have been made using the same set-up as for the water-cuvette holograms. These recordings were made from a model particle field with a higher number density of $n_s = 45 \text{ particles/mm}^3$, which was first considered as the upper limit for successful recording with LiFH. This number has been estimated from the recordings at the wind tunnel (cf. Section 8.3) and the analysis according to Equation (3.4). Another hologram was recorded with the long coherence cw Nd:YAG laser described in Section 6.2.1 from a model particle field holding $n_s = 15 \text{ particles/mm}^3$ with a broader size distribution to judge the influence of the reference beam profile quality. Here, an optimum regarding the homogeneity of the exposure and illumination for reconstruction was realised.

9.2.2 Collection of Aperture-Dependent Data

The reconstruction set-up according to Section 6.2 was placed on a vibration isolated table. An iris (similar to a mechanical shutter) without mechanical connection to the rest of the set-up was operated manually to produce the different aperture sizes right behind the hologram, which in turn was alternately illuminated by the two conjugate waves. Figure 9.1 illustrates the situation and the different positions in which the CCD sensor was placed to digitize the intensity distributions. To image the iris through the hologram, a second CCD camera with objective lens was used. Thus, the aperture diameter used for the reconstruction could be later determined precisely by simple image processing.

For each reconstructed image the exposure time of the CCD was optimised to avoid over-exposure of single pixels and simultaneously use as much of its dynamic range as possible. To examine just the emulsion grain noise experimentally, the CCD sensor was placed next to the area in which particles have been illuminated by the object beam. Here, only the light scattered at the emulsion grains is received by the sensor. The two positions next to the particle field have been used to check reproducibility. In comparing noise data from the two measuring positions, the position farthest away in angle from the illuminating beam yields slightly lower intensity values. This is reason-

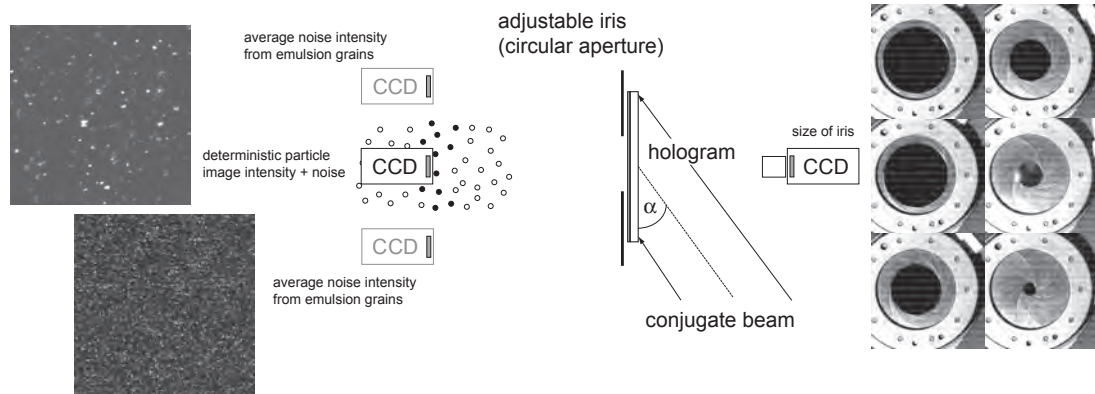


Figure 9.1: Principle diagram of the experimental arrangement to collect aperture-dependent data from long-coherence (HPIV) and short-coherence (LiFH-PIV) recordings. The second CCD camera collects an image of the iris opening, from which the diameter of the aperture is extracted. The CCD in the reconstructed image can be moved outside the holographic image to collect only light scattered by the emulsion grains.

able, because the scattering intensity usually decreases towards higher spatial frequencies as expressed by the Wiener spectrum $\Phi(\nu)$ of the emulsion (cf. Section 3.2.2.1 and Kozma (1968)). The results presented in Section 9.3 have therefore all been accumulated at one position. By placing the CCD directly in the reconstructed particle field, a coherent superposition of scattered and reconstructed light (particle images) is received.

9.3 Evaluation and Results

This Section summarizes the results obtained from the comparison study. The computation of the emulsion grain noise $\langle I_N \rangle$ and the total image intensity is straight forward and shown exemplarily only for the holograms "dlr13 and "dlr15" in Sections 9.3.1 and 9.3.2. Section 9.3.3 then describes the effort undertaken to obtain reliable values for the deterministic particle image intensity I_0 with various methods, the results of which are presented for two methods, a manual and an automated analysis, in the Sections 9.3.4 and 9.3.5, respectively (again exemplarily for the holograms "dlr13 and "dlr15"). Finally, Section 9.3.6 shows the results of an automated analysis of the holograms "ndyag32" to "ndyag42".

9.3.1 Emulsion Grain Noise

Light scattered by the emulsion grains was captured in images obtained with the CCD sensor placed next to the reconstructed particle field. Highest gain without producing overexposure in single pixels was selected manually for every image. The average

emulsion noise $\langle I_E \rangle$ is then calculated from the mean intensity of all pixels normalized by the exposure time of the corresponding recording and plotted versus the aperture diameter D (Figure 9.2).

In the double-logarithmic plot, the linear fit reveals slopes of 1.8 and 2.1 for long and short coherence, respectively. This is a good demonstration of the validity of the random nature of the generating process. The slight deviations from the expected proportionality to the aperture area (slope 2.0) could be due to inhomogeneities of the hologram exposure caused by intensity irregularities in the beam profile of the pulsed high-energy laser. Thus, diffraction efficiency is not constant over the hologram.

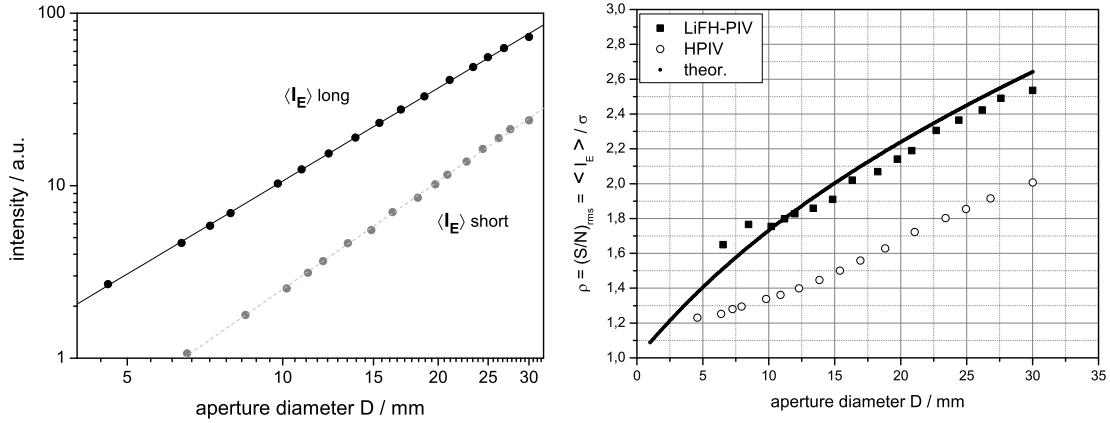


Figure 9.2: Left: average emulsion noise $\langle I_E \rangle$ versus the diameter of the hologram aperture D for the HPIV (long coherence) and LiFH-PIV (short coherence) cases of the air-flow holograms. Right: the ratio $\rho = \langle I_E \rangle / \sigma$ of the same data and its theoretical behaviour predicted according to Goodman (1984).

Another check as to the nature of emulsion noise can be made by calculating the ratio $\rho = \langle I_E \rangle / \sigma$, which according to Goodman (1984) equals the rms signal-to-noise-ratio (reciprocal of the speckle contrast) and the square-root of a parameter \mathcal{M} . For statistically independent random variables, as they are assumed in the speckle-oriented generation process, this ratio should be equal to 1. However, we have to take into account that these data are obtained from spatially integrated samples due to the finite size of the CCD pixels. Since this averaging is more pronounced for small speckle, where σ takes lower values, the ratio ρ is increasing with increasing aperture. The theoretical prediction in the right graph of Figure 9.2 is based on the theoretical speckle size S_c for the given aperture diameter D , the imaging sensor pixel size $S_m = 6.7 \mu\text{m}$ and the resulting number of correlation cells \mathcal{M} , for which according to the same reference it follows $\mathcal{M} \cong \frac{S_m}{S_c}$ for $S_m \gg S_c$. Then, the exact expression for \mathcal{M} can be shown to be

$$\mathcal{M} = \left\{ \sqrt{\frac{S_c}{S_m}} \operatorname{erf} \left(\sqrt{\frac{\pi S_m}{S_c}} \right) - \left(\frac{S_c}{\pi S_m} \left[1 - \exp \left(-\frac{\pi S_m}{S_c} \right) \right] \right) \right\}^{-2}, \quad (9.6)$$

where

$$\operatorname{erf}(x) = \frac{2}{\sqrt{\pi}} \int_0^x e^{-z^2} dz \quad (9.7)$$

is the error function given as twice the integral of a gaussian distribution with zero mean and variance of $1/2$.

Obviously, the data collected from the reconstruction of the LiFH-PIV recording reflects a pure speckle-oriented generation process. It is likely, that these are the result of scattering at emulsion grains. Erroneously recorded reflections are also minimised due to the short coherence recording method. The data from the HPIV recording shows a significantly shallower slope due to larger variance σ .

9.3.2 Average Total Image Intensity

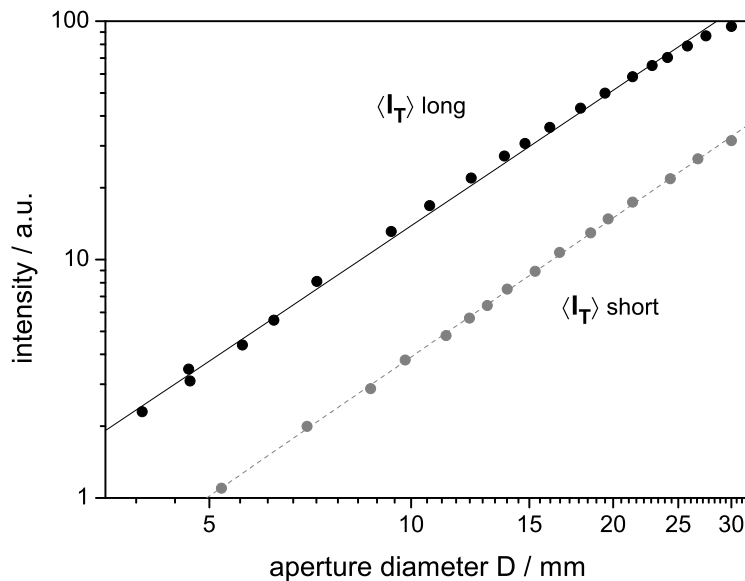


Figure 9.3: Average total image intensity $\langle I_T \rangle$ versus the diameter of the hologram aperture D for the long and short coherence mode, respectively.

The average total image intensity should also increase proportional to the aperture area. Plotting $\langle I_T \rangle$ versus D (see Figure 9.3) reveals a similar behaviour as found for the emulsion grain noise: the slope of the fitted line is in both cases 1.9 and thus close to the expected 2.0. Again, inhomogeneities of the hologram exposure can be made responsible for the deviation from the ideal case.

The difference in the absolute values between the short and long coherence case equals roughly a factor of 5, which expresses that the ordinary holographic images are generally brighter. A matter, however, that does not affect the argument and can easily be compensated for by increasing the exposure times of the CCD accordingly.

9.3.3 Particle Image Detection

To calculate the signal-to-noise ratio according to Equation (9.3), the deterministic particle image intensity I_0 needs to be determined from the experimental results (i.e. the reconstructed and digitised particle images), which is nearly impossible due to the interference of particle images and background. To circumvent this problem all one can do is to replace I_0 by I_i , the mean intensity of all image pixels above a certain threshold. This method implies that every particle image in a digitised plane is at least slightly brighter than the brightest spots of the background. Pixels above this threshold can be grouped and labelled by their size and thus isolated high intensity spots, most likely originating from a bright speckle, can be distinguished from particle images. Another possibility is to identify a certain number of pixels, which most likely belong to a single particle image due to a-priori information and then to compute I_m , the intensity mean value of those pixels. Thus each identified particle image is assigned a SNR.

A variety of methods with varying parameters have been tested as to their capability to successfully identify pixels belonging to particle images. Only those which had a reasonable detection quality (e.g. number of found particle images at a reasonable level) are shortly reported here, although not all of them did produce reasonable SNR results (for further details see Section 9.3.5.1). While the first method explained in the following was chosen to get a quick overview of single image planes, the later were developed and tested to automate the analysis for the exploration of larger data series. Two methods evaluate a global SNR from each reconstructed and digitised image plane, while the two other methods work on single particle images. These can be generally divided into two parts: firstly identifying single particle images and secondly calculating the corresponding SNR from those pixels found to belong to the particle image and those in their direct neighbourhood.

9.3.3.1 Visual Inspection and Manual Thresholding

In a first trial the reconstructed and digitised images have been analysed manually supported by an image processing software. After subtracting the camera offset (i.e. a dark image obtained with the same exposure time), a thresholding procedure was used to identify those pixels which could belong to particle images. The threshold value was selected solely by visual impression, whether a good discrimination between single particle images and the background was achieved or not. For the pixels above the threshold, the mean intensity I_i and the standard deviation were calculated. Furthermore, the standard deviation of all intensities was determined and all values were weighted with the respective exposure time.

9.3.3.2 Histogram-Based Fitting of Probability Density Function for Integrated Speckle

Similar to the contrast-enhancing-methods based on the histogram, the idea of this method is to distinguish pixels most likely belonging to the background from those

most likely belonging to bright particle images by utilisation of the intensity histogram of each digitised image plane. A closer look at the properties of this histogram reveals that it looks similar to the histogram of pure speckle images which have been recorded with a finite measurement aperture (i.e. pixel size in the order of the feature size). As can be seen from the data plotted Figure 9.4, speckles and particle images are similarly and decreasingly resolved when the aperture size is increased. According to Goodman (1984) the form of the probability density function for integrated speckles is approximated by:

$$p_{I_0}(I_0) \cong \frac{\left(\frac{\mathcal{M}}{\langle I_N \rangle}\right)^{\mathcal{M}} I_0^{\mathcal{M}-1} \exp\left(-\mathcal{M} \frac{I_0}{\langle I_N \rangle}\right)}{\Gamma(\mathcal{M})}, \quad (9.8)$$

where the main parameter is again the number of correlation cells \mathcal{M} . Based on this equation a best-fit with the least-square method was realised (solid lines in Figure 9.4).

A general discrepancy is observed especially at higher intensities. These are underestimated by the integrated speckle fit probably due to the contribution of the particle images, which are coherently superimposed to the speckle field. Nevertheless, the fitted curve can be used to estimate a threshold value for the intensity above which the adaptation of the tonal value (see Appendix A.9.3 for details) offers a reasonable reduction of background noise. Typically, a given percentage of the area under the fitted curve was taken to define this threshold value. It was found, that values located between 99 % and 99.9 % of the area of the curve were sufficient to end up with a good choice of potential particle image pixels.

After the tonal value adaptation a segmentation of the particle images from the remaining background was obtained by either simple binarisation or using the Otsu method (Otsu, 1979), a global image thresholding based on a discrimination by the ratio of between-class variance and total variance of grey levels. Both methods result in a b/w-mask, which is then reduced by removing all potential particle images smaller than a certain size (e.g. 3 pixels), since they tend to be contributions from the underlying speckle field. Finally, the mean particle image intensity I_i and the standard deviation of the background were calculated from the original images by either multiplying with the particle identification mask or its inverse mask and a resulting SNR could be derived.

9.3.3.3 Intensity-Based Circular Particle Image Finder

The Particle-Image-Finder-Algorithms are based on the assumption that a meaningful SNR can only be calculated within the immediate neighbourhood of each particle image. Thus two areas need to be defined for every single particle image, belonging either to the particle image itself or to the background. The first Particle-Image-Finder assumes the particle image to be located in a circular region, which is drawn with a radius r_p as obtained by image analysis using auto-correlation. The least-square fit-function describes the experimentally observed dependency of the FWHM of the auto-correlation function obtained from the digitised particle image planes versus their re-

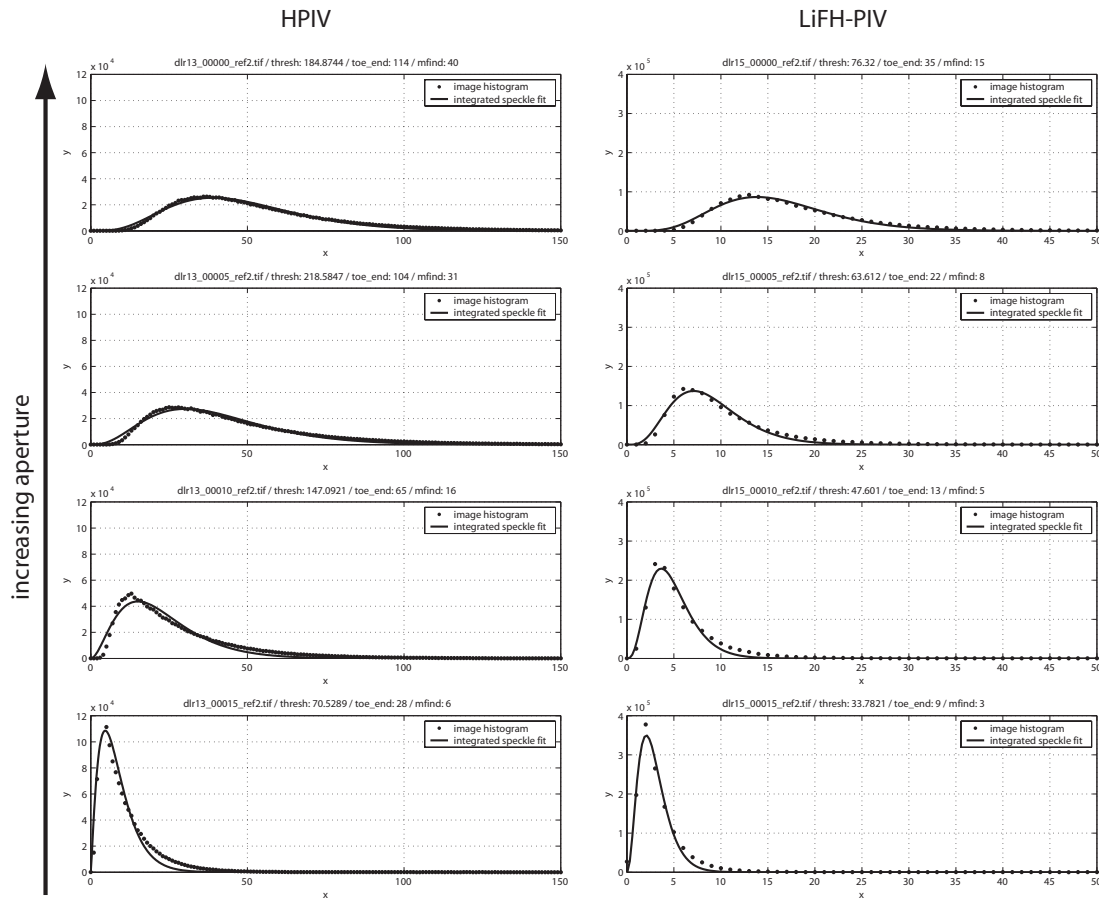


Figure 9.4: Histogram data and integrated speckle fit for both types of reconstructed and digitised particle image planes, the effect of an increasing hologram aperture is found to be similar to those affecting only speckles.

spective aperture diameter (Figure 9.5). Thus for each aperture diameter the respective radius r_p can be calculated. The other area is a ring surrounding the particle image. This region with inner radius $r_i = r_p$ and arbitrarily chosen outer radius $r_p = 3 \times r_i$, is used to calculate the standard deviation of the background intensities. Together with the mean of the pixel intensities I_m from the inner region the SNR for each particle image can be calculated.

To identify single particle images, the original image is first made slightly unsharp using a negative Laplacian filter before the T brightest spots are searched for. The number T can be chosen to equal the expected number of single particle images. The coordinates of those brightest spots are written into a list, a circular neighbourhood is assigned to each of these points and it is checked whether any of the resulting circular areas overlaps with the image border or with another particle image area from the list. This task is carried out considerably fast by first computing the distance of each particle image to the image origin (upper left corner), and then deleting those images from the list with similar distances to one of the others. Although some particle images are removed erroneously and again some high-intensity spots from pure speckles are

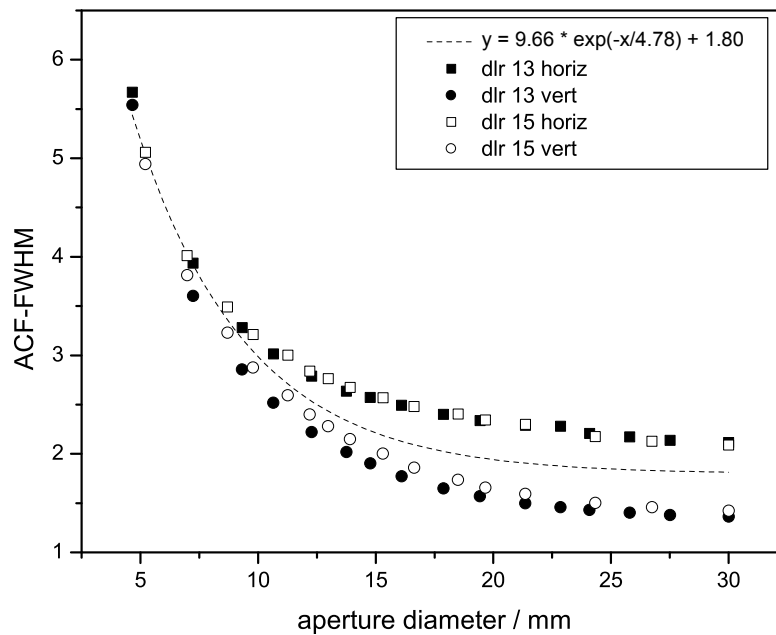


Figure 9.5: FWHM of the autocorrelation signal from the particle images in pixel versus the aperture diameter in mm. The difference between horizontal and vertical size is due to the read-out process of the CCD camera. The fitted function is used as an input to calculate the anticipated particle image radius for a given aperture diameter.

likely to be considered as a particle image, the resulting list of images is large enough to get good statistics from a digitised image plane.

9.3.3.4 Position-Based Particle Image Finder with Edge Detection

The second Particle-Image-Finder-Algorithm incorporates two improvements as compared to that presented above in Section 9.3.3.4. Firstly, a reconstructed and digitised particle image is no longer supposed to be circularly shaped, which accounts for the complex image structures due to Mie-scattering described by Pu and Meng (2004). Secondly, the position of a particle image can be effectively discriminated from positions of bright speckles using a series of reconstructed image planes with varying aperture size. This improvement is based on the basic assumption, that while changing the size of an on-axis aperture, the position of the particle images should not change significantly, but the underlying local speckle pattern intensity is varying strongly. To maintain this experimentally, the aperture was completely decoupled from the reconstruction set-up, which was placed on a vibration-isolated table. Thus the same relative position between CCD and hologram is kept for all aperture settings. By multiplying all reconstructed image planes (Figure 9.6 a- c and e-g) the positions of each single particle image gets clearly visible. This step is followed by a binarisation procedure (Subfigures d and h) and then the coordinates of each particle image are written into a list.

The list of coordinates is further used while processing each reconstructed image, to extract a region of interest surrounding the particle image at each given coordinate.

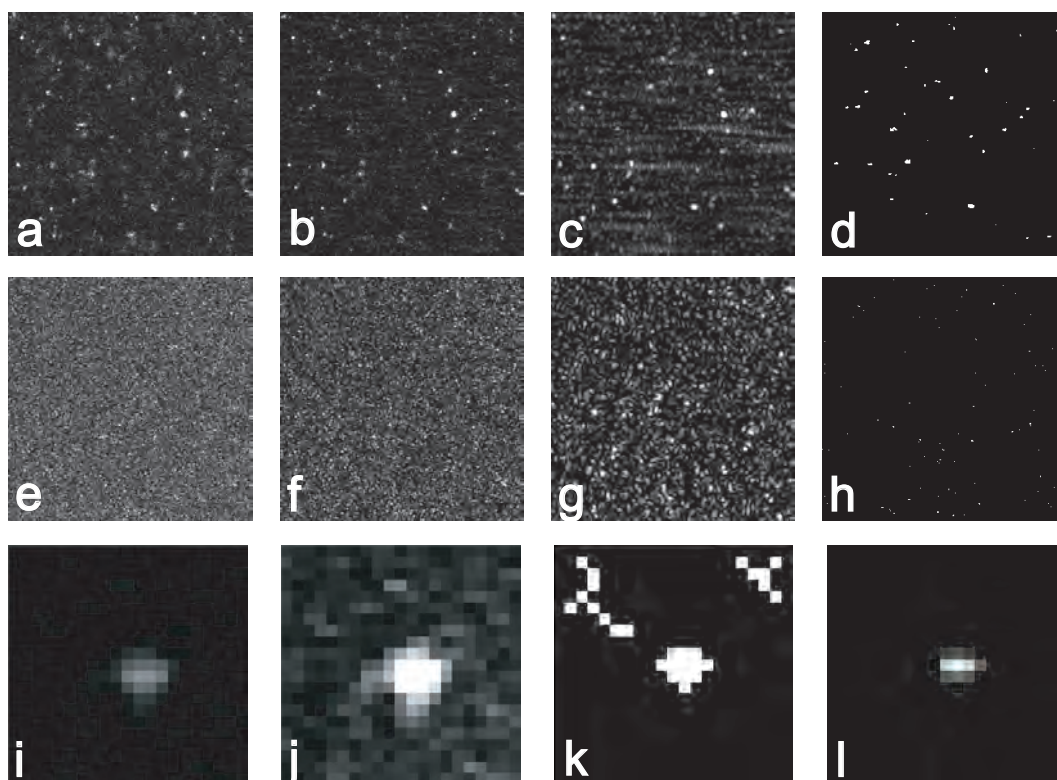


Figure 9.6: Sample data from the position-based particle image finder algorithm: a-c) single particle images from LiFH hologram with decreasing aperture, d) b/w mask obtained from multiplication result, e-g) and h) corresponding data from an ordinary holograms, all fields of view $2 \times 2 \text{ mm}^2$. i) part of the original image around an identified particle coordinate, j) same area but tonal value adapted to increase background intensity, k) result of Canny edge detection with particle area filled, l) contrast enhanced selection of pixels belonging to the found particle image, all fields of view $140 \times 140 \mu\text{m}^2$.

This region is set to ± 10 pixel in each direction. Figure 9.6i shows such a region from an original image, whereas in Figure 9.6j the same data is shown with increased background intensity.

To identify pixels belonging to the particle image, a powerful edge detection algorithm (Canny, 1986) is applied to the selected region. This edge-detection method is part of the Matlab image processing toolbox and differs from the other edge-detection methods in that it uses two different thresholds (to detect strong and weak edges). Thus it includes also the weak edges in the output, but only if they are connected to the stronger edges. This method is therefore less likely to be fooled by noise, and more likely to detect true weak edges. After edge detection, the area around the coordinate pixel is filled within the found edges (Figure 9.6k) and thus forms a closed and connected region. All regions produced by the edge detection are then labelled and describing values (e.g. size of region and center-of-mass) are assigned to each of them, before the biggest region (the area corresponding to the particle image) is extracted. This enables a check,

whether a particle image was found within appropriate borders or a noisy background prevented it. Therefore the results are classified according to the following criteria: a) the detected particle image area is smaller than a given minimal size, b) the particle image position is close to the image border, c) the detected area occupies more than 7% of the region under investigation (this value is found empirically to be the largest area occupied by a single particle image within the region of $11 \times 11 = 121$ pixels), which is probably due to open edges, or d) the detection was fully valid. A single SNR is finally calculated only from the valid detections by division of the mean intensity I_m of the selected pixels by the standard deviation σ of the intensity of the surrounding pixels. Additionally, the mean SNR is calculated for all valid detections and assigned to the whole reconstructed image of particles.

9.3.4 Particle Image Intensity and Resulting SNR from Visual Discrimination Method

In the following, the results of the manual method according to Section 9.3.3.1 applied to the holograms "dlr13" and "dlr15" are analysed. In Figure 9.7 the mean particle image intensity is shown versus the diameter of the hologram aperture on logarithmic scales for the LiFH-PIV (or short) and the HPIV (or long coherence) case. Furthermore, the standard deviation σ of the intensity in all image pixels is also shown for both cases. Due to the low number of particles, there is no significant difference in computing the standard deviation over all pixels instead of computing it over the inverse selection after thresholding the particle images. Roughly, σ and I_i grow with the aperture diameter fairly much like $D^{1.5}$ truly independently of the coherence length. The linear fit (dashed lines) returned exponents 1.47, 1.49, 1.49 and 1.62 from top to bottom.

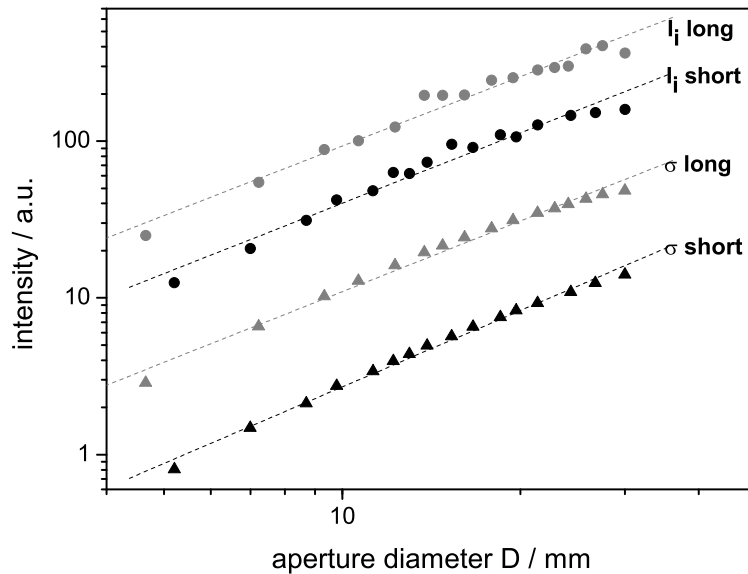


Figure 9.7: Mean particle image intensity I_i and standard deviation σ of the total image intensity versus diameter of the hologram aperture for both coherence cases.

Now it is a straightforward division to get values for the SNR as shown in Figure 9.8. To provide a feeling for the situation, axis-values for the corresponding coherence depth d_c according to Equation (4.15) are introduced for the short coherence case. For the ordinary hologram we find $\text{SNR} \approx 8$ independent of the aperture diameter. For the LiFH case we observe a clearly improved $\text{SNR} \approx 15$ that stays constant up to $D \approx 15$ mm and then drops gradually.

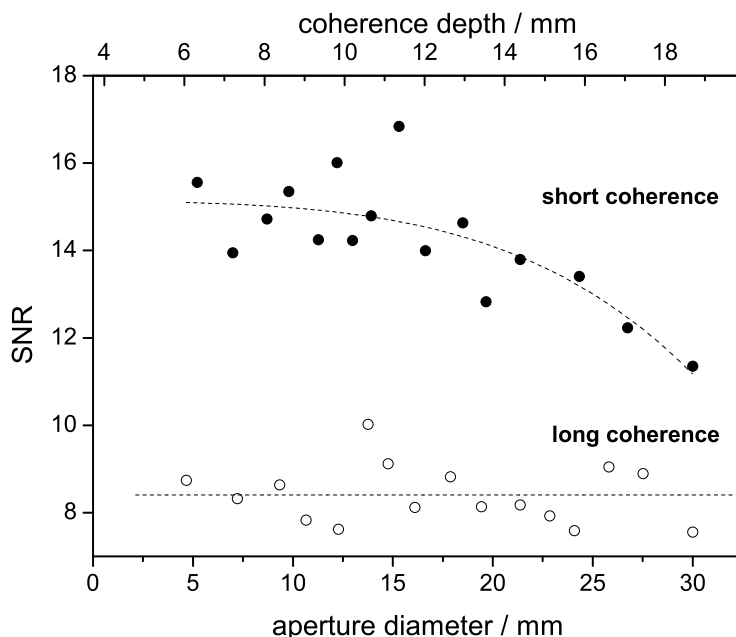


Figure 9.8: Signal-to-noise-ratio in real particle image fields reconstructed from either an ordinary long-coherence or a light-in-flight hologram recorded under nearly the same conditions versus the diameter of the hologram aperture. The axis on top of the graph gives the coherence depth d_c for the respective aperture of the short-coherence case.

The drop can be understood from the special features of light-in-flight holography. The depth location of the CCD sensor has been chosen such, that it coincides with the location for zero-path-length difference between the object and reference light for the central position of the aperture. Thus, only light from within an aperture with a diameter of approximately twice the coherence length contributes to the reconstruction of particle images located at this depth position. For a while, when opening the aperture, additional area on the hologram also adds light to the particle image. When the coherence limit is reached, however, the new aperture area no longer contributes to the image brightness but only increases background noise by reconstructing out-of-focus images and adding scatterers producing the emulsion noise. The real situation is a little more complicated due to the circular aperture, because only the dimension of the aperture parallel to the plane of incidence is affected in this way, while the other direction still carries particle information. Furthermore, coherence does not drop abruptly thus explaining the gradual decrease of SNR.

9.3.5 Particle Image Intensity and Resulting SNR from Automated Discrimination Methods

As mentioned earlier, not all automated methods reported in Section 9.3.3 did produce reasonable results when calculating the SNR. Therefore, the results of disapproved methods are explained only shortly, before the results of the method of choice are shown exemplarily for the reconstructed image planes from the wind tunnel holograms "dlr13" and "dlr15".

9.3.5.1 Disapproved Discrimination Methods

Strong fluctuations of the SNR for neighbouring particle images, as well as fluctuations in the mean SNR of individually reconstructed and digitised image planes have been taken as a criterion to disapprove certain methods. The Histogram-Based-Fitting-Method produced such fluctuating SNR values when processing images with increasing aperture size. Furthermore, a detailed comparison with the thresholds obtained by the manual discrimination method did not show any correlation between the two methods. Obviously, the human interaction in setting the global threshold cannot be reproduced by simple parameters. The Intensity-Based-Circular-Image-Method did recognise potential particle image positions very effectively. But due to the fact, that the ideal model of a round particle image shape does not apply in our case (the image shape is fooled by speckle noise and also affected by the scattering characteristics of the particle itself), the algorithm for calculation of the SNR did often take background pixels as particle pixels and vice versa. As a consequence the mean SNR values of the image planes were also fluctuating, but did usually show a maximum value for the mean SNR at medium aperture sizes. It is assumed that in both methods some of the high intensity speckles from the background have been misinterpreted as particle images, leading to erroneously calculated SNR values.

9.3.5.2 Approved Position-Based-Particle-Finder Discrimination Method

The Position-Based-Particle-Finder-Method has proven to be more robust against misinterpretation of high intensity speckles, which can be easily seen from the results in Figure 9.9a, where we plotted the mean of the single particle image SNRs:

$$\text{SNR}_{\text{mean}} = \sum_{n=1}^{n_v} \frac{I_{mn}}{\sigma_n} / n_v, \quad (9.9)$$

versus the aperture diameter for each image plane reconstructed from the ordinary (H) and short-coherence recordings (LiFH). The number n_v of the single particle images with valid detection is shown in the top graph (a) in grey for each of the reconstructed image planes. For direct comparison, again the corresponding coherence depth is given at the top of both graphs.

Although the absolute SNR values are somewhat lower than in the manual analysis of the same data shown in Figure 9.8, the general tendency of a gradually decrease

of SNR at higher aperture diameters is the same. But now, also the SNR for ordinary holography seems to slightly decrease. The initial increase at small aperture diameters is probably due to a low-pass filtering effect from the larger speckle and feature size, which of course decreases the contrast and hence has an influence on the edge detection and the standard deviation σ .

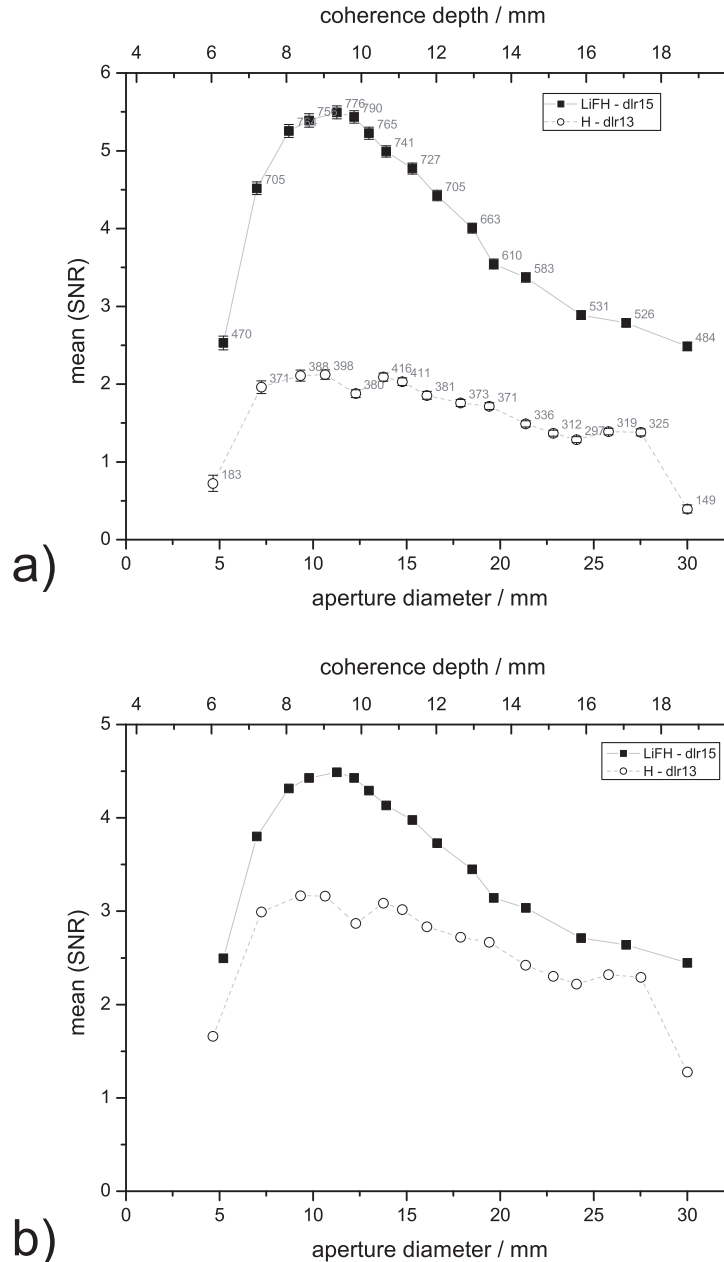


Figure 9.9: Direct results of the automated SNR analysis with the Position-Based-Particle-Image-Finder algorithm using reconstructions of the wind tunnel holograms "dlr13" and "dlr15". Shown is the mean SNR value over the number (given in grey) of single particle images versus the aperture diameter (a) and the corresponding normalised results (expectation values) taking into account the difference in the numbers of found particle images (b).

Already from the exemplary reconstructed images of particles in the Figures 9.1 and 9.6 it can be seen that less particles are visible from the ordinary holographic recordings than from the LiFH recordings. This finding is well confirmed by the difference in the number of valid detections between the two cases. Keeping in mind, that the number density of particles in the wind tunnel air flow was almost the same in both cases, a normalisation of the data is recommended. Due to the multiplication of image planes from reconstructions with different aperture sizes it is likely that also the positions of particle images are found which are not directly visible in a single reconstructed image plane. Consequently we have to assign $\text{SNR} = 1$ to these particle images, since they are completely buried in the background noise. Hence we can define the following expectation value from the calculated mean SNR values:

$$\text{SNR}_{\text{norm}} = \frac{\text{SNR}_{\text{mean}} \cdot n_v + n_f \cdot 1}{(n_v + n_f)}, \quad (9.10)$$

where n_f is the number of those particle images, where the edge detection failed (particle image buried in noise). After normalisation the difference in SNR between the LiFH-PIV and HPIV recordings from the wind tunnel experiment of Chapter 8 is decreased, but still makes a factor of roughly 1.50 using the automated analysis compared to 1.88 from the manual analysis.

9.3.6 Analysis of Particle-Number-Density Series

The imaging performance has been also analysed from the holograms of the water cuvette filled with water and HGS as tracer particles at varying seeding densities ("ndyag32" - "ndyag42") in order to judge their influence on the noise level and to validate the findings of Pu and Meng (2004) reviewed in Section 3.2.

9.3.6.1 Resulting SNR from the Approved Automated Discrimination Method

Due to the huge amount of data (a total of 534 particle images have been reconstructed by varying hologram, aperture size and reference beam) only the automated analysis was feasible. The results of the Position-Based-Particle-Image-Finder algorithm are shown in Figure 9.10 for the holograms "ndyag32" to "ndyag"38" and Figure 9.11 for the holograms "ndyag39" to "ndyag"42". Again as direct results with the number of particles detected as valid in grey (left) and as normalised results (right). It is clearly seen, that the SNR of the LiFH recordings (plotted filled black) is always higher than for the long coherence recordings (open symbols) and that the curves have a behaviour similar to those of the air flow holograms.

For the LiFH-PIV case, a significant difference in the absolute values of the SNR is observed between the reconstructions using either of the two reference beams. A possible explanation is the difference in the orientation of the polarisation vectors between the reference and object beams. However, also the HPIV holograms have been recorded with the same set-up described in Section 6.1.2, where the reference beams from above and below had an inclination angle with the object beam of $\pm \approx 63^\circ$.

Due to the perpendicular polarisation of the beams, only one interference pattern is recorded with parallel polarisations (lower reference beam and object beam), whereas the other, recorded from the upper reference beam has a lower modulation due to the inclined states of polarisation.

9.3.6.2 Dependency of SNR on the Change of Number Density

Regardless of the differences between the results for the two reference beams and the non-normal distributions of SNR values, the results in Table 9.2 show a global mean SNR for each hologram.

Hologram	<i>N</i>	Mean	SD	SEM	MIN	MAX	Range	Number Density [1/mm ³]	Amount of stock-solution
dir15	16	3,59	0,750	0,188	2,45	4,49	2,04	12	
dir13	16	2,56	0,542	0,135	1,28	3,16	1,89	12	
ndyag32	30	6,54	1,962	0,358	2,34	10,05	7,71	10,12	5,95%
ndyag33	30	1,87	0,323	0,059	1,29	2,40	1,11	10,12	5,95%
ndyag35	28	5,22	1,438	0,272	2,54	7,88	5,34	17,19	11,91%
ndyag36	28	1,73	0,142	0,027	1,44	1,95	0,51	17,19	11,91%
ndyag37	32	2,41	0,403	0,071	1,90	3,24	1,34	12,35	23,81%
ndyag38	28	1,58	0,136	0,026	1,39	1,84	0,45	12,35	23,81%
ndyag39	32	2,69	0,359	0,063	1,70	3,15	1,45	16,45	8,93%
ndyag40	32	1,30	0,084	0,015	1,04	1,41	0,37	16,45	8,93%
ndyag41	38	1,34	0,061	0,010	1,18	1,45	0,26	8,73	2,98%
ndyag42	36	1,17	0,048	0,008	1,11	1,28	0,17	8,73	2,98%

Table 9.2: Overview of the Signal-to-noise results from the automated analysis with hologram name, *N* number of normalised mean SNR values per hologram (reconstructions from both reference beams at different aperture sizes), a global mean SNR value per hologram, the standard deviation (SD) and the standard error of the mean (SEM), as well as minimum and maximum values and the range of SNR values. In addition the results of the density measurements are shown for the corresponding water cuvette holograms, the density of particles in the wind tunnel flow could only be roughly estimated.

Plotting this, or the maximum SNR value against the measured seeding densities unfortunately does not show a clear tendency documenting an increasing noise level (see Figure 9.12) for an increasingly measured particle number density. The reasons, which led to this result can only be presumed (see Appendix A.10).

The SNR values in the Figures 9.10 and 9.11 decrease from top to bottom and the holograms are numbered in the sequence of their recording time. When plotting the maximum SNR value against a time axis, a clear dependency is observed for both types of recordings (see Figure 9.13). Exactly the same fluid was used to record each single LiFH-PIV and HPIV pair of holograms and these pairs have been grouped in the figure (dark and light grey columns). Obviously, the calculated SNR values depend on the age of the stock solution, which was diluted down to obtain the fluid filled in the cuvette. Thus, either the measured particle number densities have to be put into question or the used particles (HGS), when immersed in water are not suited for storage over a longer period of time.

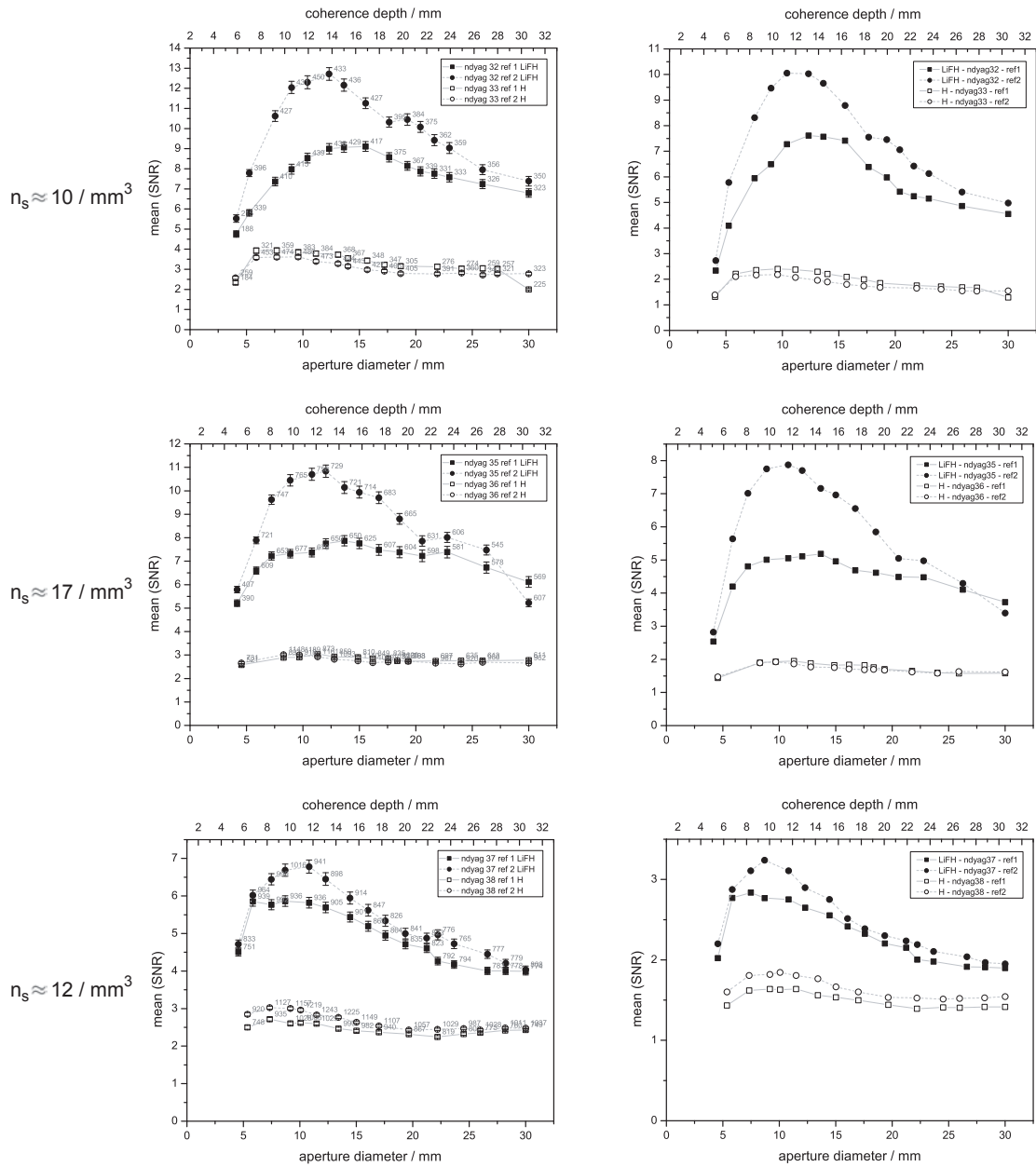


Figure 9.10: Continued in Figure 9.11.

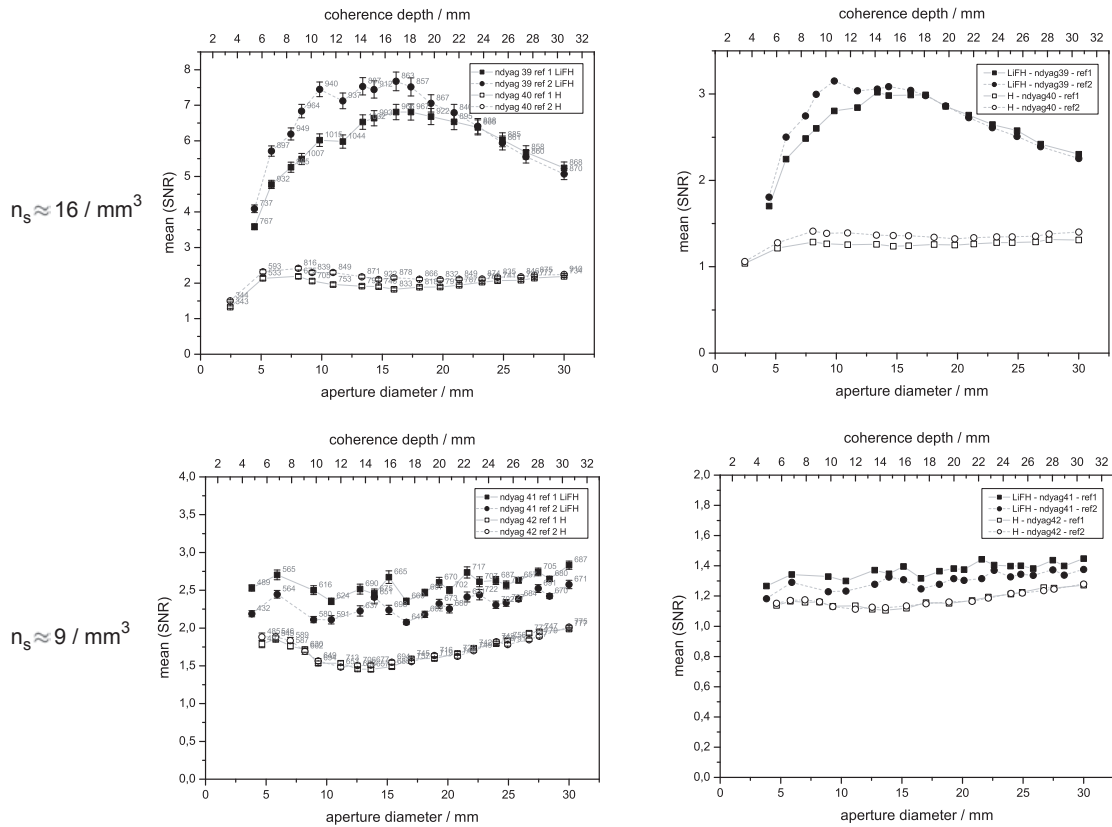


Figure 9.11: Direct Signal-to-noise results of the automated analysis with the Position-Based-Particle-Image-Finder algorithm using reconstructions of the water cuvette holograms "ndyag32" to "ndyag42", shown is the mean SNR value over the number (given in grey) of single particle images versus the aperture diameter (left) and the corresponding normalised results (right).

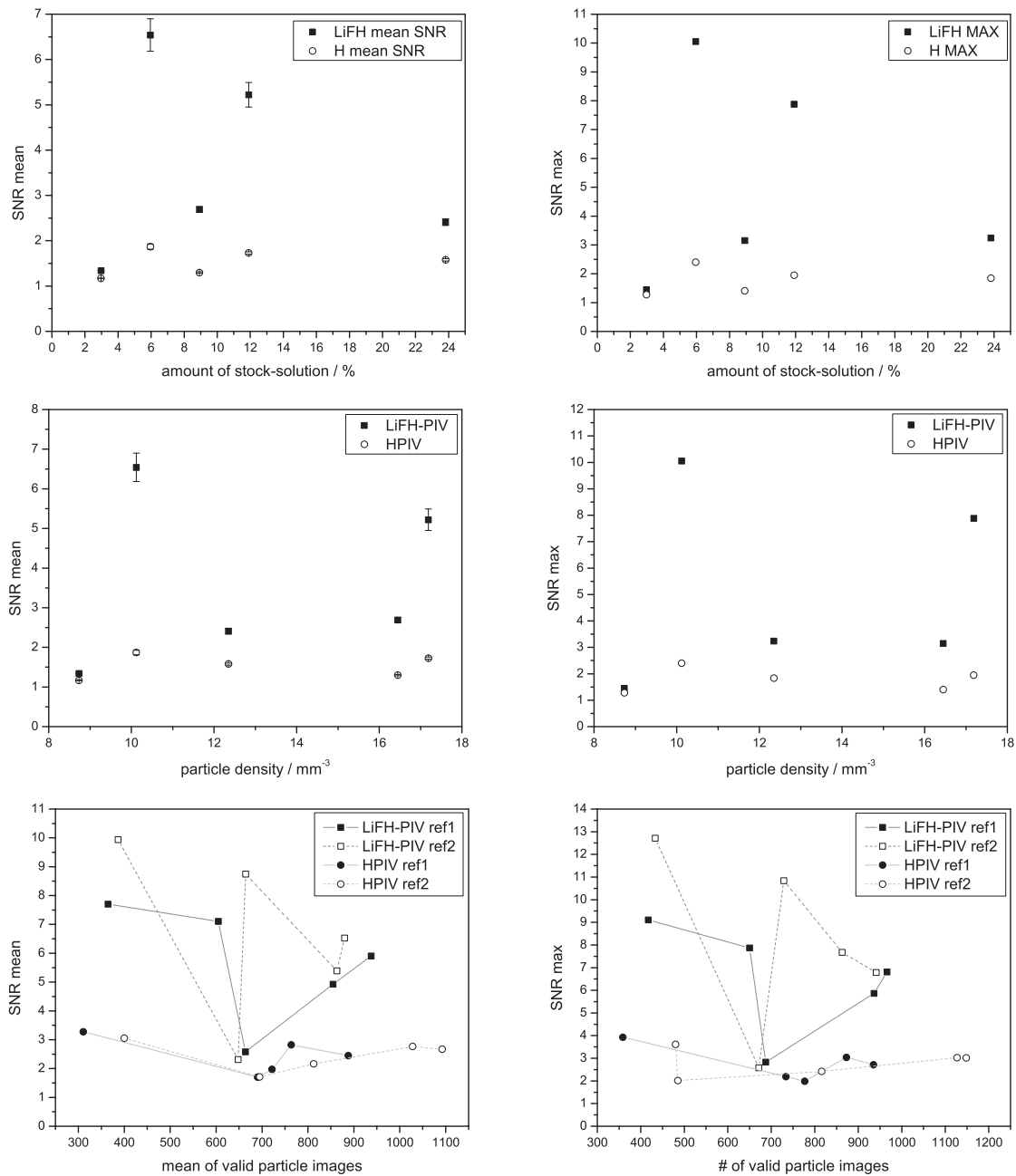


Figure 9.12: Influence of "increasing" particle number densities on the SNR value: Shown is the mean SNR value (left) and the maximum SNR value (right) from the reconstructions of the water cuvette holograms at different aperture sizes versus three parameters describing the particle number density: the amount of stock-solution (top), the measured particle number density (middle) and the mean of all valid detected particle images (bottom). No clear and reasonable correlation between these parameters and the number density is found.

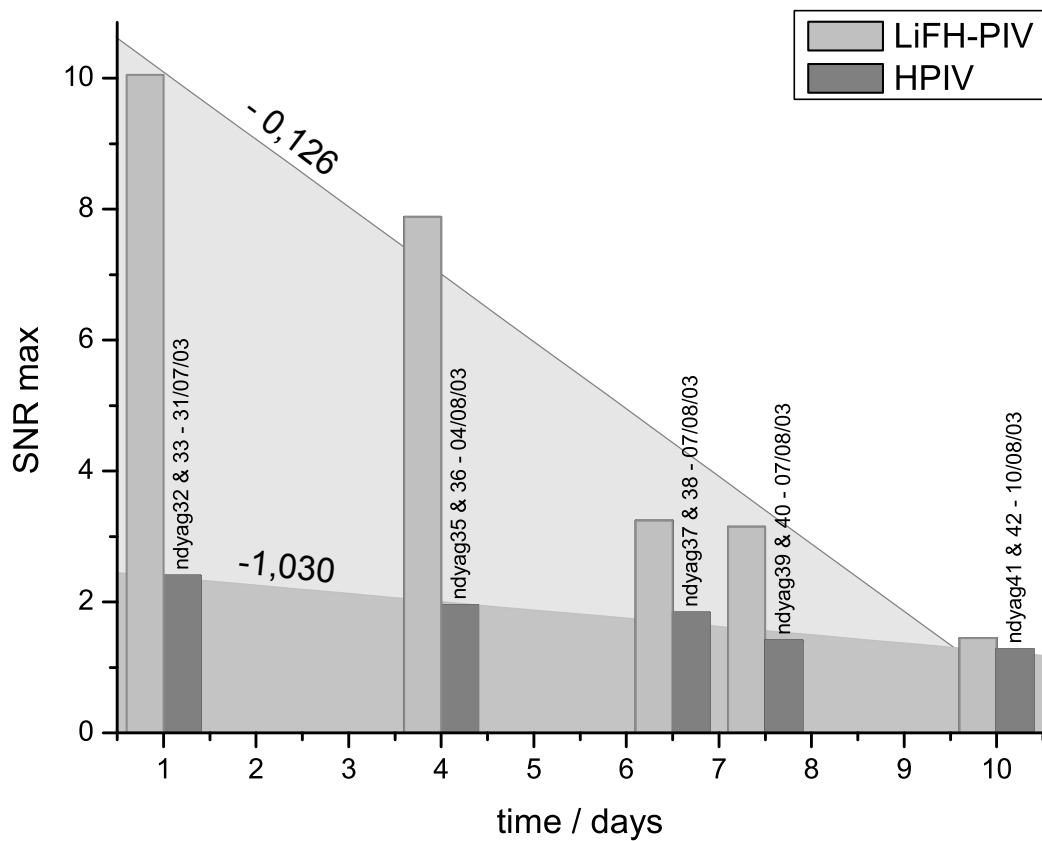


Figure 9.13: Recording-time-dependency of SNR values from water cuvette holograms. The measured SNR correlates with the age of stock-solution or the time of the holographic recording, respectively.

9.4 Discussion

The experiments described in this Chapter have been performed to check ideas on the physical situation responsible for the image quality in particle holography (Hinsch and Herrmann, 2004). The two theoretical cases elaborated in Section 9.1.3 have supported these ideas by establishing that the SNR depends on a simple experimental parameter, the aperture size. The results of the performance comparison are best described by the second case. In this, apparently an ensemble of scattering particles closely packed over a certain depth approaches the case of a diffusely scattering particle cloud and hence the SNR stays constant. This at least holds true for the results from the HPIV holograms, which is in agreement with Goodman (1967) and the consequences derived in Section 9.1.3.

It should be noted however, that the results plotted in Figure 9.7 are not in perfect agreement with the theory mentioned above. Instead of increasing like D^2 for the mean particle image intensity I_i and for the standard deviation of the background intensity σ , only exponents of roughly 1.5 are found. Since the exponents are almost equal, however, this does not influence the SNR result. Three effects could possibly explain the deviation from the theoretically expected exponent 2, none of which can yet be assigned the effect solely:

1. The properties of the laser reference beam may not be sufficiently well controlled to guarantee a phase-conjugate reconstructing wave. The recording was done with a high energy pulsed Nd:YAG laser whose collimated reference beam definitely showed cross-sectional variations (cf. Figure 2.10) in wave intensity. We can assume that there will also be corresponding phase fluctuations. In the reconstruction however, a high-quality cw Nd:YAG laser of fairly constant cross-sectional phase distribution was used. Different sub-areas on the hologram will then contribute with the wrong phase relation and reduce the effects of coherent superposition. To check this assumption, the hologram "holo11", recorded with the cw laser, was reconstructed with varying aperture sizes and the exponents of I_i and σ are found to be 2.12 and 1.94, respectively.
2. Inhomogeneities in the index of refraction and the surface profile of the photographic layer, consequences of the chemical processing, will produce similar effects. While we have not taken any special precautions in this study, in the past much effort has been dedicated to avoiding such effects (Barnhart et al., 1994).
3. Particle scattering is dominated by pronounced angular intensity variations. Different regions on the hologram will thus get quite different amounts of particle light, which is contrary to our assumption that all of the hologram area will be treated equally.

The behaviour of the SNR from LiF holograms is well understood from the increasing depth of the reconstructed particle field when increasing the aperture size. According to (3.4) the SNR is inversely proportional to the particle field depth, calling for a linear decrease in our representation. But an increasing circular aperture used for

the reconstruction of a LiF hologram only contributes with one dimension to an increasing field depth, both dimensions however, have also an effect on the SNR due to the changing image resolution. Furthermore, it is unclear whether the increase of the SNR in the automated analysis data at smaller aperture sizes is a true consequence of the algorithm. In that case the findings from the manual analysis, which are in a good agreement with the theory elaborated in Section 9.1, have to be revised. Anyway, in both cases, ordinary and LiF holography, there is no evidence of a clear increase of the SNR, when increasing the aperture, which is inconsistent with the theory after Pu and Meng (2004) described in Section 3.2. In their theory SNR increases linearly with increasing the half angle aperture Ω and decreases with increasing n_s .

The later findings seem to be valid at least from judging the reconstructed images, but the theoretically predicted behaviour could not be successfully proved, since the results from our density measurements (cf. Appendix A.10) cannot be accepted unquestioningly. A further indication that the SNR value for a given n_s is in the right order, can be obtained from our last set of holograms of this study. The reconstruction of the ordinary hologram "ndyag43" did not show any single particle image but a pure speckle pattern. The LiF hologram "ndyag44" however, still reveals particle images (Figure 9.14) when reconstructed with either of the two reference beams and from these image planes we evaluate the normalised mean SNR ≈ 3.4 and ≈ 2.5 for the first and second reference beam, respectively.

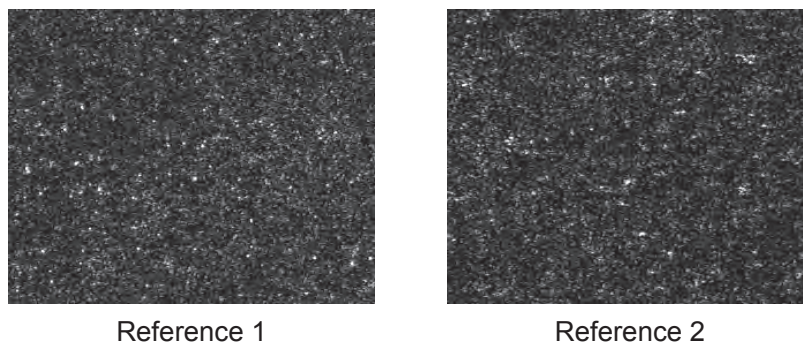


Figure 9.14: Digitised image plane of the reconstruction of a model particle field at a rather high number density of $n_s = 45$ particles/mm³ with either of the two reference beams. Clearly single particle images can be seen and the normalised mean SNR ≈ 3.4 and ≈ 2.5 for the first and second reference beam, respectively.

From the effort undertaken to automate the image quality analysis, it is clear that defining meaningful SNR from a cloud of reconstructed particle images is still difficult. Many experimental parameters seem to have a significant influence on the resulting image. Therefore the experiment with varying particle densities should be repeated with a setup where the direct intensity correlation can be used and instead of analysing the image quality the maximum correlation coefficient can be evaluated. Furthermore, experiments with the model particle fields permit the setting of known displacements and hence validity-rates similar to the corresponding 2D-correlation study of Hinrichs et al. (1998) can be obtained.

10 Summary, Conclusions and Outlook

The following Section 10.1 summarises the contents of the thesis in a compact style and highlights the main achievements from the presented studies. Since the work on LiFH-PIV was carried on, partly by the author himself and followed by extensive work from a successor, conclusions are drawn in Section 10.2 taking into account the state of the work at the end of the year 2003. Finally, Section 10.3 briefly reports from the ongoing research work and gives an outlook to some of the still open questions in LiFH-PIV.

10.1 Summary of the Contents

After motivating the need for three-dimensional flow mapping using holography as a tool, the basics of the classical or analogue variant have been reviewed briefly, including some information on high-resolution recording materials and their wet-chemical processing. Important for measurement purposes is an exact replay of the holographic image, thus the requirements have been explained, before the attention was drawn to the carrier of information in HPIV, the tracer particles and their properties related to holographic imaging.

The particles themselves (those which are not in-focus in a given plane), are the major reason for coherent background noise in HPIV, which partly masks the information to be extracted. Consequently, the different noise contributions have been analysed. From the analysis of the second source of noise, the emulsion grain noise, a novel method for reconstructions of low intensity signals from tiny tracer particles was derived. The method is termed "Particle Holography at the noise limit" and allows to considerably enlarge the flow fields under investigation. It is especially useful, when the amount of the back-scattered light is limited due to either the available laser power or to very tiny particles with less scattering efficiency.

To overcome the background noise from the out-of-focus particles in HPIV, a short-coherence recording method, the so-called Light-in-Flight Holography (LiFH), has been introduced earlier, utilizing a double-pulsed ruby laser. Although in these studies the virtual image reconstruction was chosen for flow analysis, these previous achievements and mainly the fast optical switching from two successive laser pulses for cross-correlation analysis were reviewed. For further elaboration of the method, the basics and the technical requirements of LiFH have been explained and the effect of the limited aperture size was addressed before demonstrating the method with real holographic particle images.

A new double cavity Nd:YAG laser system with amplified and combined beams at

a final wavelength $\lambda = 532$ nm after second harmonic generation was then utilized for HPIV and LiFH-PIV. The system is capable of switching between long and short coherence mode (by either turning a common injection seeder "on" or "off"), where the latter case with a coherence length of $l_c \approx 7$ mm provides a good basis for further LiFH experiments. A special divergence and beam-pointing control assures stable operation for a precise alignment of complex holographic recording set-ups for flow diagnostics. Two types of recording geometries allowing both, ordinary and LiF holography, have been realised at a small test wind-tunnel. Both are using a dedicated reference beam delivery unit to provide for planar reference waves at inclination angles with respect to the holographic plate, which are suited to maintain the increasing optical path along a given direction, which is needed for LiFH. A stabilized continuous-wave Nd:YAG laser with a single longitudinal and a TEM₀₀ mode was then used to build a completely separated and autonomous reconstruction set-up, in which the two recorded holograms are replayed alternately and the whole volume is scanned by means of a CCD sensor mounted on a translation stage.

The evaluation of those huge amounts of digitised image planes from holographic particle replays is a key element of each HPIV system. After reviewing important actual research work on HPIV with respect to the methods used to extract the flow velocities, a straight-forward method (3D intensity correlation) was introduced and implemented in a Matlab environment. Finally, some aspects of computing demands, realisations in a heterogeneous network and constraints arising from special features of LiFH have been discussed.

At a large industrial wind-tunnel the proposed LiFH-PIV system was tested under realistic conditions involving vibrations from the turbines and a global dense seeding. It was proved that the LiFH method is capable to image tiny tracer particles through the "fog" and that holograms recorded with the above mentioned Nd:YAG laser system at the wind tunnel could be analysed later in the laboratory with the separated reconstruction set-up. The main drawback of this system is the small aperture size and thus a resulting reduced depth resolution. A way to overcome this was reported together with the second type of LiFH recording geometry, however this is not compatible with the elaborated 3D intensity correlation method.

Finally the influence of the aperture size in both, LiFH-PIV and HPIV was used to study the particle image quality and noise contributions at varying seeding densities. Quantitatively, a signal-to-noise ratio (SNR) was deduced from a series of holographic recordings with either short or long coherence and a comparison was made between both cases. Based on theoretical assumptions from the speckle model after Goodman (1967) a relationship between aperture size and SNR could be established, showing that for ordinary HPIV the SNR stays constant if a dense particle field is assumed. In fact such a behaviour was observed from the experiments and a significant gain in SNR was found when using LiFH, which however strongly depends on properties of the recorded fields, like the seeding density.

10.2 Conclusions from the Presented Work

Holography once again has proved to be a powerful tool which provides high-resolution and three-dimensional image data from air or fluid flows seeded with small tracer particles. The coherent background noise, a typical problem of methods using ordinary holography for flow diagnostics (e.g. HPIV), has been relaxed with the introduction of the short-coherence recording principle LiFH. This method has been proved to be applicable even in large industrial facilities and opens access to even more detailed flow analyses than commonly used today. However, the reduced aperture needed for the sheet-wise reconstruction of LiF holograms introduces new constraints and needs to be addressed in further refinements of the technique.

A careful analysis based on a given application was carried out to judge between ordinary and LiF holography. In this comparison one parameter, the SNR of the reconstructed and digitized particle images, plays a key role. There is however, no ideal solution to access this parameter solely from the reconstructed images and the presented work can only give an introduction to a theoretical model describing the observed effects. The results of our experiments are in agreement with this model, but also have shown that a good control over the tracer particles and reproducible and stable flows are needed to really link the found SNR from both methods to the actual seeding densities. This was not achieved to full satisfaction yet. A workaround maybe the production of further model particle fields with varying number density and in which particles are embedded in perspex in such a way that the relative index of refraction and their size distribution is comparable to real flow situations.

Although the results with LiFH presented in this thesis are very encouraging in terms of the gain of SNR, the comparison of both methods is not yet completed. A validation of the elaborated algorithms for the evaluation of the particle images is still due and their parameterisation, especially depending on the recording method, needs to be studied in detail. This future task is also linked to the reduced depth resolution when using LiFH, as in this case one can sample the depth coordinate with considerably larger distances between the digitised image planes. From such a detailed study we assume that a trade-off between the depth of a recorded field and an acceptable seeding density will be found for HPIV, which can still confirm the findings of [Pu and Meng \(2003\)](#) and for LiFH a trade-off between acceptable depth resolution and seeding density points the way which method should be preferred for a given application.

Another option for the comparison of both methods are validations rates of the computed velocity vectors. Such an experiment however, requires very stable flows from which the mean velocity is precisely known or again the above mentioned model particle fields which are precisely shifted in known directions. Furthermore, one has to obtain two holographic images which are reconstructed with equal quality over the whole volume to cancel the influence of local changes in the SNR. It should be noted however, that from our experiments using the crossed-polarized beams it was found that the brightness of the two holographic images was considerably different. This is an important drawback, which is already addressed in a further refinement of the LiFH-PIV technique.

10.3 Ongoing Research Work and Outlook

To overcome the above mentioned mismatch in holographic image brightness due to the cross-polarised beams in the set-up of Chapter 6 and the also slightly changing particle image properties from their differing scattering behaviour, a new set-up was realised at the test wind-tunnel. Figure 10.1 shows the different planes of the set-up in green and red, the inter-plane beams are shown in violet. Four times a two-mirror arrangement is mounted in such a way, that the linear state of polarisation of object and reference beams is rotated into a horizontal direction. The front view depicts the remaining mismatch, which is of equal amount for both pulses / recordings and is negligible for the quality of the interference pattern recorded on the holographic plate. Nevertheless, the brightness of the two reconstructed holographic images is still slightly affected by the reciprocity failure of the material and varying pulse intensities. During reconstruction, it is therefore still corrected by the intensity of the reconstructing beam.

To maintain a good overlap of the two reconstructed images, a calibration method using an active reference marker in each holographic recording was developed (Hülsmann, 2005). This method uses the secondary reflections from each wedge plate, which are sufficiently strong to expose the holographic plate from a common exit of an optical fibre. To this end, the reflections are guided to and combined by a beam-splitter in such a way, that they are coupled into the optical fibre after passing a lens arrangement and a half-wave plate to match the polarisation of the reference beams. Each beam-path length, is of course again matched to that of the corresponding reference beam. The end of the optical fibre is placed beneath the test section and emerges a spherical wave illuminating the holographic plate. Opening both shutters in the reconstruction set-up depicted in Figure 6.7, this wave is reconstructed simultaneously from the two holograms and forms an interference pattern, which can be used to match the reconstruction beam angles and remaining divergences to those of the reference beams from the recording set-up.

To handle the huge amount of image data and to further improve the evaluation procedures a tool was developed by Steigerwald (2006), which allows a) to check single correlation cells and their results using different parameterisations, b) to choose the part of the measurement volume to be evaluated and c) to check the results by means of histograms of the velocity components and some cell-related measures, like the maximum of the correlation function or the detectability of the maximum correlation peak (defined as the ratio between the maximum peak value to those of the next highest peak). Furthermore, the detection of the correlation-peak was improved by using a proper weighting function to avoid bias errors and especially adapting it to their larger extend in longitudinal direction.

Figure 10.2 shows an example for a successful flow measurement using the revised set-up. The flow configuration is depicted on the left side. The wind tunnel flow was adjusted to $v = -10$ m/s, hitting the zylinder mounted on top of a plate from the right side. The measured volume extended over 46.23 mm \times 35.90 mm \times 27 mm and was sampled with $54 \times 42 \times 7 = 15,678$ interrogation cells of 128^2 pixels with no overlap.

The total scanning time of the volume, separated in 6×6 depth-wise image series was

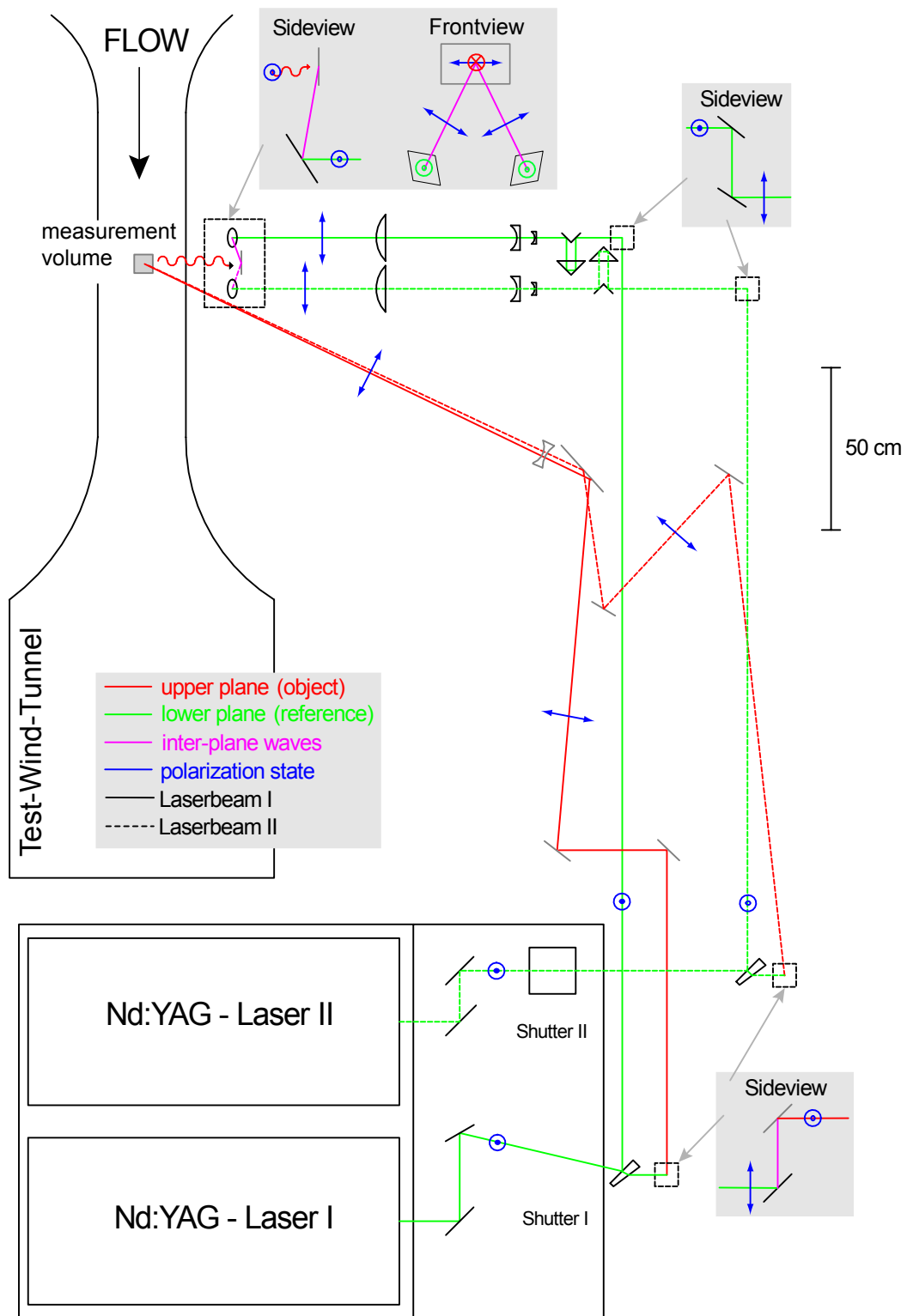


Figure 10.1: Sketch of the revised set-up reducing the holographic-image-brightness problem. The doubled beam guidance for both, the object and reference arm, increases the complexity but is necessary to maintain the same small amount of mismatch in the state of polarisation for the scattered object light and the two reference beams.

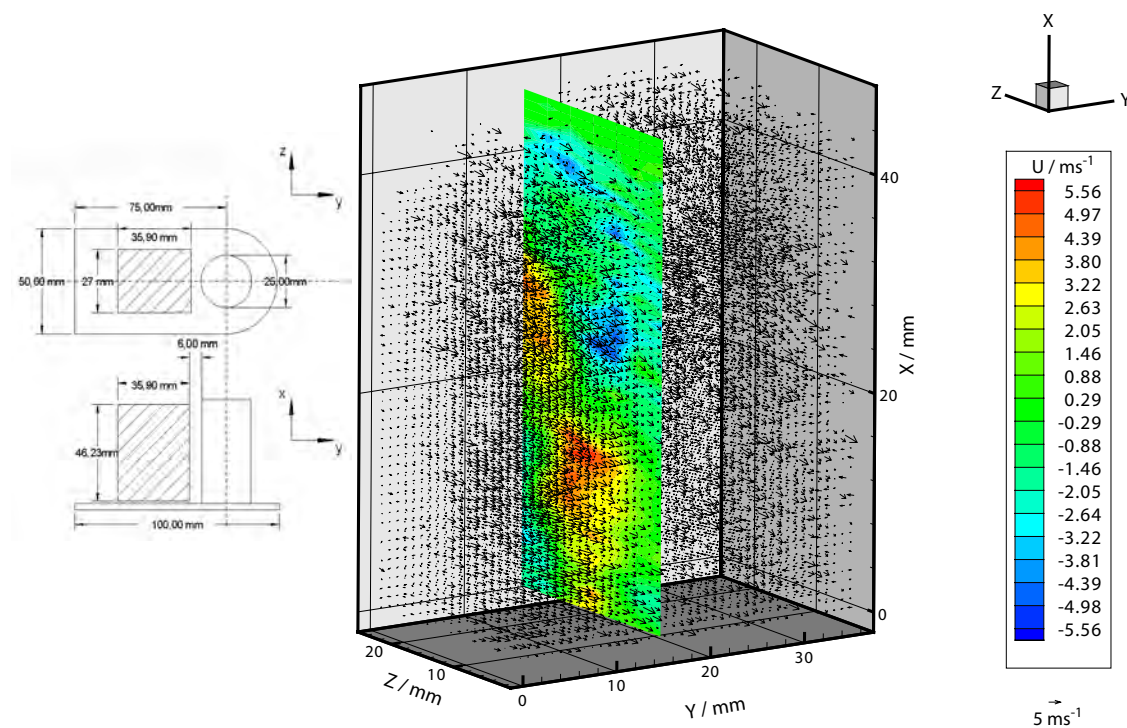


Figure 10.2: Flow configuration (left) and example result of a measurement using the revised LiFH-PIV set-up (right). The wind tunnel flow component $v = -10$ m/s has been subtracted. Shown as contours in one slice is the the u-component of the velocity, illustrating the different areas with a net flow pointing up- or downwards.

about 5 days and the evaluation on a single computer took about 76 hours. The resulting vectors have been filtered by using the histograms of the velocity components. Especially in the upper left corner of the measurement volume erroneous vectors have been removed, which are the result of a missing overlap of the areas formed by the two beams illuminating the particle field. The recorded flow structure is nicely demonstrated by a net flow pointing up- or downwards, as visible from the coloured contour plot in the slice located at $y = 20$ mm.

For future investigations with the revised set-up it is planned to assign each correlation cell some more properties, which are describing the quality of the measurement result. This can be for example a check for the local particle image SNR from each of the two reconstructions and the number of found particle images or a measure describing the background noise. These properties can now be easily calculated by the algorithms presented in Section 9.3.4.

The performance comparison between HPIV and LiFH-PIV can then be repeated, but needs to be additionally based on the results of a detectability study at varying number densities or even on validation criteria's describing the position dependent precision of the velocity results obtained from model particle fields. In that way the knowledge about the influence of speckle noise can still be improved, allowing a much better validation of the models described in the literature. Furthermore, the precision study for both recording methods, HPIV with large aperture and LiFH-PIV with an optimised aperture configuration, is needed to judge the applicability of both methods for future flow measurements in deep and largely cross-sectional sized, densely seeded volumes.

We believe that LiFH has a great advantage in many industrial applications (e.g. aerospace, marine, medicine, automotive) which need detailed information from air or water flows. The work explained in this thesis is thought to represent a major technology mile-stone in the development, evaluation and understanding of practical solutions to the very complex subject of investigating three-dimensional fluid motion phenomena.

A Appendix

A.1 Navier-Stokes Equation

For a complete physical description of fluid mechanical applications the velocity, pressure and density fields are needed. The cumulative expression of these quantities is the generally known Navier-Stokes equation. The i -th component of the velocity field $\mathbf{V}(\mathbf{x}, t)$ of a fluid flow at position \mathbf{x} and at time t is given by the following equation:

$$\frac{\partial}{\partial t} V_i(\mathbf{x}, t) + \mathbf{V} \cdot (\nabla V_i) = \nu \Delta V_i(\mathbf{x}, t) - \frac{1}{\rho} \frac{\partial}{\partial x_i} p(\mathbf{x}, t) + f_i(\mathbf{x}, t). \quad (\text{A.1})$$

An important role for the interpretation of (A.1) plays the so-called Continuity equation, which for incompressible flows ($\rho = \text{const}$) reads:

$$\nabla \cdot \mathbf{V}(\mathbf{x}, t) = 0. \quad (\text{A.2})$$

Equation (A.1) represents the Newtonian motion-equation of a fluid element, where the left-hand side of the equation is the total derivative in time of the elements velocity. The terms on the right-hand side of the equation represent the forces acting on the fluid element. The first, $\nu \Delta V_i(\mathbf{x}, t)$, describes the influence of the inner frictional force. The kinematic viscosity ν is often assumed to be a constant material parameter, which is linked to the dynamical viscosity η by $\eta = \rho\nu$. The pressure forces acting on the element are given by the term $\frac{\partial}{\partial x_i} p(\mathbf{x}, t)$ and $f_i p(\mathbf{x}, t)$ represent the outer forces.

The complex behaviour of a fluid, e.g. turbulent structures, is described by the non-linear relation of the term $\mathbf{V} \cdot (\nabla V_i(\mathbf{x}, t))$, which couples the i -th velocity component to the other two components. Introducing dimensionless variables:

$$\mathbf{W} = \frac{\mathbf{V}}{U}, T = f \frac{U}{L}, \mathbf{X} = \frac{\mathbf{x}}{L}, P = \frac{p}{\rho U^2} \text{ and } F = f \frac{U^2}{L}, \quad (\text{A.3})$$

with U and L arbitrary numbers for the typical velocity and length scale of the experimental configuration, respectively, the Navier-Stokes equation and the Continuity equation now read:

$$\frac{\partial}{\partial t} W_i(\mathbf{X}, T) + \mathbf{W} \cdot (\nabla W_i) = \frac{1}{Re} \Delta W_i - (\nabla P(\mathbf{X}, T))_i + F_i(\mathbf{X}, T) \quad (\text{A.4})$$

and

$$\nabla \cdot \mathbf{W}(\mathbf{X}, T) = 0. \quad (\text{A.5})$$

Two systems having the same dimensionless Reynolds number $Re = \frac{UL}{\nu}$ and similar boundary conditions from the dimensionless variables, typically show the same behaviour regardless of their scaling and material properties.

A.2 Holographic Emulsions

For particle holograms, especially recorded with the LiFH method, a high resolution photosensitive material is needed. Typically, those materials are emulsions based on gelatine (animal renderings) in which silver halide (sometimes referred to as AgH) is suspended. The later consist either of silver chloride (AgCl) or, most commonly and also for the plates used in the experiments of this thesis, of silver bromide (AgBr) or a mixture of the latter with silver iodide (AgI). This material is often spin-coated on glass substrates, which ensures a stable constitution throughout the processing steps and enables us to replace the plates with high precision in an optical setup, for testing purposes sometimes emulsions coated on a plastic (e.g. triacetat) have been used.

Silver halide grains are sensitive to light, so when the plate is exposed, once in a while a photon hits such a silver grain. If this happens a certain number of times, a small site of metallic silver is formed on that grain. Due to the very fine grains in holographic emulsions the chance of a grain to be marked by this site of metallic silver is extremely low, these emulsions are not very sensitive when compared to for example photographic materials. The collection of those marked silver halide grains is referred to as the latent image, an invisible but yet recorded interference pattern in the emulsion.

Since AGFA stopped its production of holographic recording materials only a few solutions could be found for recording with the green light of a Nd:YAG laser. A good overview on commercially available materials, including also those used for the experiments described in this thesis, is given by Bjelkhagen (2002) and shown in Table A.1. Some of them have only been tested once, but did not produce reasonable results. The cause of this, however, was not well understood. It is likely, that an unsuited combination of material and chemistry was used. It turned out that the Slavich VRP-M material produced the best results, in terms of brightness of the particle images and sensitivity to the Nd:YAG laser radiation, which is consistent to the findings of Bjelkhagen.

A.3 Processing of Holographic Recording Materials

Saxby (1988) introduces the fascination of processing holographic materials, which catches almost everyone dealing with conventional holography with a poem from *Alice in Wonderland* from Lewis Carroll:

Beautiful soup, so rich and green,
Waiting in a hot tureen!
Who for such dainties would not stoop?
Soup of the evening, beautiful soup.

Material	Thick- ness [μm]	Spectral sensitivity [nm]	Sensi- tivity [$\mu\text{J}(\text{cm}^{-2})$] at				Resolv. power [lp(mm) ⁻¹]	Grain size [nm]
			442	514	663	694		
SILVER HALIDE EMULSIONS:								
Slavich								
Red PFG-01	7	<700	-	-	80	-	>3000	35-40
Red PFG-03M	7	<700	-	-	1500	-	>5000	10-20
Green VRP-M	7	<550	-	80	-	-	>3000	35-40
Pan PFG-03C	9	400-700	1000	2000	1000	-	>5000	10-20
Coulorholographic								
Red BB-700	7	<700	-	-	50	150	>2500	50-60
Red BB-640	7	<650	-	-	150	-	>4000	20-25
Green BB-520	7	<540	150	150	-	-	>4000	20-25
Blue BB-450	7	<470	150	-	-	-	>4000	20-25
Kodak								
Red 131PX	9	<650	2	-	0.5	-	>1250	70
Red 131CX	9	<650	2	-	0.5	-	>1250	70
Red 120PX	6	<750	60	-	40	40	>2500	58
Red 120CX	6	<750	60	-	40	40	>2500	50
FilmoTec - ORWO								
Red HF 65	10	<650	-	-	1500	-	5000	30
Green HF 53	10	<550	-	700	-	-	5000	30
Ultimate								
Ultimate 15	7	<700	-	150	150	150	>5000	15
Ultimate 08	7	<650	120	200	200	-	>7000	8
DICHROMATED GELATIN EMULSIONS								
Slavich								
Blue PFG-04	16	<515	1×10^5	2.5×10^5	-	-	10000	-
FilmoTec - ORWO								
Blue GF 40	6/20	*	*	-	-	-	-	-
* delivered: non-sensitized								
THERMOPLASTIC MATERIALS								
Tavex America								
Pan TCC-2	-	<800	1	1	1	1	1500	-
PHOTORESIST MATERIALS								
Towne Technologies								
UV-Blue Shipley 1800	1.5-2.4	<450	1.5×10^5	-	-	-	1000	-
Hoya Corporation								
Custom orders only								
BACTERIORHODOPSIN MATERIALS								
MIB GmbH								
BR-WT B-type	30-100	<650	-	80×10^3	-	-	5000	-
BR-D96N M-type	30-100	<650	30×10^3	-	-	-	5000	-

Table A.1: Overview of the commercially available holographic recording materials, after Bjelkhagen (2002). The shaded materials have been used within the experiments described in this thesis.

Consequently, during the experiments a short excursion to chemistry was inevitable to find a good solution for processing the VRP-M material from Slavich exposed by short Nd:YAG pulses. The goal was to obtain comparable results either with long or short coherence recordings. Typically these recording types did show a very different behaviour in most of the tested wet chemical processing schemes. The general processing scheme to produce transmission holograms was always the same, since these show the lowest distortions of the diffraction grating due to wet chemical processing and should thus produce the most precisely reconstructed particle images. After exposure to light the material was developed in a dark room, fixed and bleached as illustrated for the

chemical processes in Figure A.1.

In fact, a detailed step-by-step procedure was used, first keeping the material in a closed box for about half an hour at room temperature to warm up the glass substrate and emulsion (after they have been stored in a refrigerator for a long time). This ensures that no water precipitates at the material and causes swelling of the emulsion. In the meantime the set-up was prepared for recording, starting with a laser warm-up to produce stable pulses (minimum 20 minutes) and starting the fluid flow, as well as controlling the seeding. After exposure with two single pulses from either resonator, the material was replaced in the closed box and transferred to the dark room. Latensification, as typically recommended for pulsed recordings was not used. Some tests have shown a strongly decreased signal-to-noise ratio for particle images. Then, the holographic plates have been soaked carefully in the developer with the emulsion pointing upwards and providing a continuous swivel-motion to the bath. The development time was adapted to the various developers under test. After development, this process was stopped either in a clear water bath or with a weak acetic acid for about two minutes. The fixation was always done with standard from AGFA, the G328 fixer for about 4 minutes. To wash out all remaining silver complexes, the material was rinsed with streaming or recirculating clear water for about ten minutes. Finally, the material was flushed with de-ionized water or a wetting agent and a drying process at 50° with a slight air flow for about half an hour was used to revoke the swelling of the emulsion. To achieve stable reconstructions of the particle images, a drying process at room temperature for about one day is recommended.

AGFA and Kodak D-19 developer produced no useful results with the VRP-M material, for BB520 only the recommended developer based on Metol (upper right recipe in Figure A.2) could produce any useful result with long development times (up to 10 minutes) compared to the other developers. This method, however, could also not produce reasonable results with VRP-M. A developer called SM-6, designed by Bjelkhagen especially for holograms recorded with very short pulses and reducing the reciprocity failure of the material, is recommended for the use with Slavich VRP-M plates and pulsed exposures. It turned out, that a (slight) modification gave the better results in our case for both, the long and short coherence recordings (upper left recipe in Figure A.2).

A.4 Holographic Imaging Equations

The imaging equations for holography have been known for decades and suggest to use an exact replica or its phase conjugate of the reference wave for the reconstruction in order to avoid aberrations (Meier, 1965; Collier et al., 1971; Groh, 1973; Banyasz et al., 1988). They have been obtained with a paraxial approximation describing point sources or point images projected onto the axis of the imaging system. Here an extension to this theory, the nonparaxial imaging equations after Champagne (1967) shall be briefly reviewed to support the understanding of the beam collimation requirements.

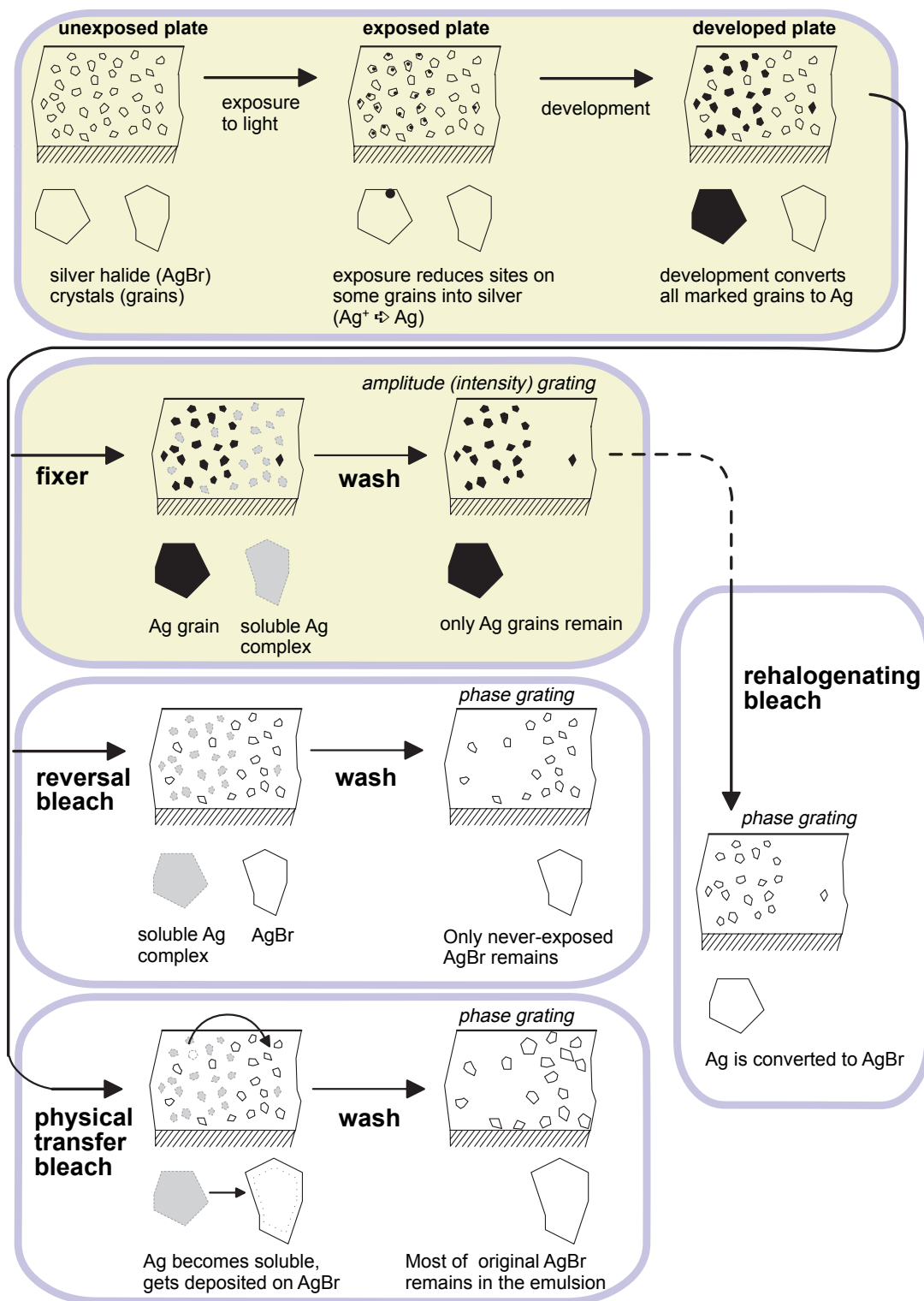


Figure A.1: Overview of the holographic photochemistry processing steps: exposure, development, fixing and bleaching, after Halle (1998). The shaded steps have been used within the experiments described in this thesis.

<p>Phenidon Developer for AGFA, Slavich and Ilford emulsions – fast developer ! 700 ml water (bi-dest), 18g ascorbic acid, 30g Soda (Na₂CO₃), 5g sodium hydroxide (NaOH), 1g Phenidone, water to 1000ml <i>keep under protecting gas !</i> prepared on: _____ by: _____ Usage</p> <table border="1" data-bbox="300 674 762 768"> <tbody> <tr><td>1</td><td>2</td><td>3</td><td>4</td><td>5</td></tr> <tr><td>6</td><td>7</td><td>8</td><td>9</td><td>10</td></tr> <tr><td>11</td><td>12</td><td>13</td><td>14</td><td>15</td></tr> <tr><td>16</td><td>17</td><td>18</td><td>19</td><td>20</td></tr> </tbody> </table>	1	2	3	4	5	6	7	8	9	10	11	12	13	14	15	16	17	18	19	20	<p>HRT Metol Developer for HRT and ORWIS emulsions 700 ml water (bi-dest), 70g sodium carbonate, 15g sodium hydroxide, 4g metol, 25g ascorbic acid, water to 1000ml <i>keep under protecting gas !</i> prepared on: _____ by: _____ Usage</p> <table border="1" data-bbox="858 674 1321 768"> <tbody> <tr><td>1</td><td>2</td><td>3</td><td>4</td><td>5</td></tr> <tr><td>6</td><td>7</td><td>8</td><td>9</td><td>10</td></tr> <tr><td>11</td><td>12</td><td>13</td><td>14</td><td>15</td></tr> <tr><td>16</td><td>17</td><td>18</td><td>19</td><td>20</td></tr> </tbody> </table>	1	2	3	4	5	6	7	8	9	10	11	12	13	14	15	16	17	18	19	20
1	2	3	4	5																																					
6	7	8	9	10																																					
11	12	13	14	15																																					
16	17	18	19	20																																					
1	2	3	4	5																																					
6	7	8	9	10																																					
11	12	13	14	15																																					
16	17	18	19	20																																					
<p>Stop bath for Metol developer for HRT and ORWIS emulsions 1000 ml water (bi-dest), 5g sodium hydrogen sulfate <i>can be used quite often !</i> prepared on: _____ by: _____ Usage</p> <table border="1" data-bbox="300 931 762 1025"> <tbody> <tr><td>1</td><td>2</td><td>3</td><td>4</td><td>5</td></tr> <tr><td>6</td><td>7</td><td>8</td><td>9</td><td>10</td></tr> <tr><td>11</td><td>12</td><td>13</td><td>14</td><td>15</td></tr> <tr><td>16</td><td>17</td><td>18</td><td>19</td><td>20</td></tr> </tbody> </table>	1	2	3	4	5	6	7	8	9	10	11	12	13	14	15	16	17	18	19	20	<p>Simple Bleach for HRT and ??? emulsions 700 ml water (bi-dest), 35g copper sulfate, 100g potassium bromide, 5g sodium hydrogen sulfate, water to 1000ml <i>can be used often – keep some time at air !</i> prepared on: _____ by: _____ Usage</p> <table border="1" data-bbox="858 931 1321 1025"> <tbody> <tr><td>1</td><td>2</td><td>3</td><td>4</td><td>5</td></tr> <tr><td>6</td><td>7</td><td>8</td><td>9</td><td>10</td></tr> <tr><td>11</td><td>12</td><td>13</td><td>14</td><td>15</td></tr> <tr><td>16</td><td>17</td><td>18</td><td>19</td><td>20</td></tr> </tbody> </table>	1	2	3	4	5	6	7	8	9	10	11	12	13	14	15	16	17	18	19	20
1	2	3	4	5																																					
6	7	8	9	10																																					
11	12	13	14	15																																					
16	17	18	19	20																																					
1	2	3	4	5																																					
6	7	8	9	10																																					
11	12	13	14	15																																					
16	17	18	19	20																																					
<p>PBU Bleach for Slavich and AGFA emulsions 700 ml water (bi-dest), 10g potassium persulfate, 50g citric acid, 1g cupric bromide, 20g potassium bromide, 1g amidol (toxic), water to 1000ml <i>very TOXIC !!!</i> prepared on: _____ by: _____ Usage</p> <table border="1" data-bbox="300 1223 762 1305"> <tbody> <tr><td>1</td><td>2</td><td>3</td><td>4</td><td>5</td></tr> <tr><td>6</td><td>7</td><td>8</td><td>9</td><td>10</td></tr> <tr><td>11</td><td>12</td><td>13</td><td>14</td><td>15</td></tr> </tbody> </table>	1	2	3	4	5	6	7	8	9	10	11	12	13	14	15	<p>Kodak D-19 developer for FilmoTec emulsions 500 ml water (bi-dest), 1g metol, 4g hydroquinone, 45g Sodium sulfite (anhydrous), 26.25g Sodium carbonate (anhydrous), 2.5g potassium bromide / 4min at 20° C <i>keep under protecting gas !</i> prepared on: _____ by: _____ Usage</p> <table border="1" data-bbox="858 1223 1321 1305"> <tbody> <tr><td>1</td><td>2</td><td>3</td><td>4</td><td>5</td></tr> <tr><td>6</td><td>7</td><td>8</td><td>9</td><td>10</td></tr> <tr><td>11</td><td>12</td><td>13</td><td>14</td><td>15</td></tr> <tr><td>16</td><td>17</td><td>18</td><td>19</td><td>20</td></tr> </tbody> </table>	1	2	3	4	5	6	7	8	9	10	11	12	13	14	15	16	17	18	19	20					
1	2	3	4	5																																					
6	7	8	9	10																																					
11	12	13	14	15																																					
1	2	3	4	5																																					
6	7	8	9	10																																					
11	12	13	14	15																																					
16	17	18	19	20																																					
<p>NaFe(III) EDTA Bleach for HRT and ??? emulsions 500 ml water (bi-dest), 40g NaFe(III)EDTA, 5g potassium bromide, 1-2ml sulfuric acid / 4-6 min (clearing time + 1min) <i>can be used often – keep some time at air !</i> prepared on: _____ by: _____ Usage</p> <table border="1" data-bbox="300 1469 762 1563"> <tbody> <tr><td>1</td><td>2</td><td>3</td><td>4</td><td>5</td></tr> <tr><td>6</td><td>7</td><td>8</td><td>9</td><td>10</td></tr> <tr><td>11</td><td>12</td><td>13</td><td>14</td><td>15</td></tr> <tr><td>16</td><td>17</td><td>18</td><td>19</td><td>20</td></tr> </tbody> </table>	1	2	3	4	5	6	7	8	9	10	11	12	13	14	15	16	17	18	19	20	<p>MAA-3 Developer Similar to HRT Metol developer 500 ml water (bi-dest), 1,25g metol, 5g ascorbic acid, 27.8g Sodium carbonate (anhydrous), / 4 min at 20°C <i>keep under protecting gas !</i> prepared on: _____ by: _____ Usage</p> <table border="1" data-bbox="858 1469 1321 1563"> <tbody> <tr><td>1</td><td>2</td><td>3</td><td>4</td><td>5</td></tr> <tr><td>6</td><td>7</td><td>8</td><td>9</td><td>10</td></tr> <tr><td>11</td><td>12</td><td>13</td><td>14</td><td>15</td></tr> <tr><td>16</td><td>17</td><td>18</td><td>19</td><td>20</td></tr> </tbody> </table>	1	2	3	4	5	6	7	8	9	10	11	12	13	14	15	16	17	18	19	20
1	2	3	4	5																																					
6	7	8	9	10																																					
11	12	13	14	15																																					
16	17	18	19	20																																					
1	2	3	4	5																																					
6	7	8	9	10																																					
11	12	13	14	15																																					
16	17	18	19	20																																					

Figure A.2: Overview of some of the tested holographic photochemistry receipts, the upper left was used as the standard developer for most of the experiments described in this thesis.

A.4.1 Nonparaxial Holographic Imaging Equations

Consider the situation depicted in Figure A.3a, the hologram of a wave emitted by the subject point source P_s is recorded in the hologram plane (x, y) using the reference wave emitted by the point source P_r . Upon reconstruction with a wave from the point source P_g the real image of the subject point forms a gaussian focus, centered at the image point P_i . In Figure A.3b a dummy subscript q is used to describe the definition of coordinates for the various points.

It follows for the distance r_q of a given point P_q to a selected point $P(x, y)$ in the hologram plane:

$$r_q = \sqrt{(x - x_q)^2 + (y - y_q)^2 + z_q^2} \quad (\text{A.6})$$

and for the distance to the origin:

$$R_q = \sqrt{x_q^2 + y_q^2 + z_q^2}. \quad (\text{A.7})$$

Hence, we can also write:

$$r_q = \sqrt{x^2 + y^2 - 2xx_q - 2yy_q + R_q}. \quad (\text{A.8})$$

A planar reference and the corresponding conjugate illuminating wave are obtained by letting $R_{r,g} \rightarrow \infty$.

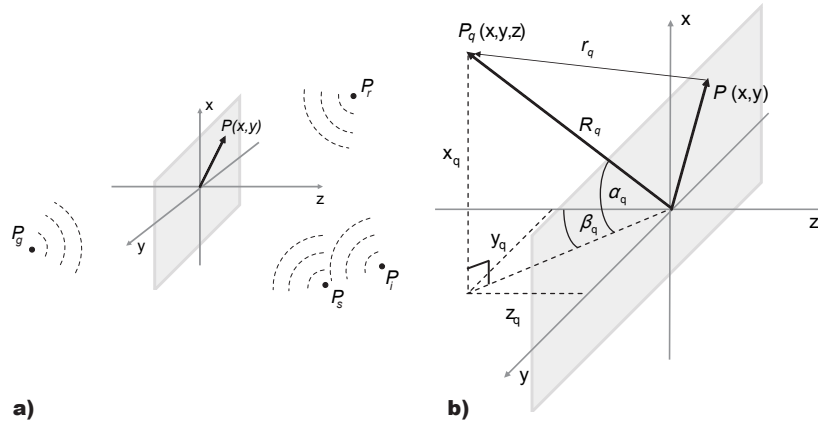


Figure A.3: Arrangement of point sources and point images P_q with dummy index q and indices s for the subject/object point and r for the reference beam during recording as well as g for the beam illuminating the hologram and i for the image point obtained from the reconstruction of the hologram (a). The definition of the coordinate system (b) for all points is used to deduce the holographic imaging equations (after Champagne (1967)).

The spatial variation of the electromagnetic field received from a point source P_q in the hologram plane (x, y) can be written in phasor notation as

$$\mathcal{E}_q = \left(\frac{A_q}{r_q} \right) \exp \left\{ \frac{2\pi i}{\lambda_g} r_q \right\}. \quad (\text{A.9})$$

Neglecting the $1/r$ variation in the fields of the various point sources, that is having a unit amplitude A in the hologram plane, leads to two expressions of the resulting fields

$$\mathcal{E}_1 = A_1 \exp \left\{ \frac{2\pi i}{\lambda_g} r_g \right\} \exp \left\{ \frac{2\pi i}{\lambda_r} (r_s - r_r) \right\} \quad (\text{A.10})$$

and

$$\mathcal{E}_2 = A_2 \exp \left\{ \frac{2\pi i}{\lambda_g} r_g \right\} \exp \left\{ \frac{-2\pi i}{\lambda_r} (r_s - r_r) \right\}, \quad (\text{A.11})$$

which represent a divergent or convergent wave, respectively. Requiring the reconstructed image to be also a point image located at R_i , the equations (A.10) and (A.11) need to be of the form:

$$\mathcal{E}_i = A_i \exp \left\{ \frac{2\pi i}{\lambda_g} r_i \right\}. \quad (\text{A.12})$$

The imaging equations are then obtained by expansion in a binomial series of r_q according to (A.8) about R_q and the comparison of coefficients in (A.10) and (A.11) with (A.12).

For the distance R_i of the gaussian focus the following relation is found from matching the second-order phase terms:

$$\frac{1}{R_i} = \frac{1}{R_g} \pm \left(\frac{\mu}{m^2} \right) \left(\frac{1}{R_s} - \frac{1}{R_r} \right), \quad (\text{A.13})$$

where $\mu = \lambda_g/\lambda_r$ and m is the enlargement of the hologram (cf. Section 2.1.4.3). The \pm -sign corresponds to the above defined cases of a diverging or converging wave, respectively.

Matching the remainder of the second-order phase terms yields:

$$\frac{x_i}{R_i} = \frac{x_g}{R_g} \pm \left(\frac{\mu}{m} \right) \left(\frac{x_s}{R_s} - \frac{x_r}{R_r} \right) \quad (\text{A.14})$$

and

$$\frac{y_i}{R_i} = \frac{y_g}{R_g} \pm \left(\frac{\mu}{m} \right) \left(\frac{y_s}{R_s} - \frac{y_r}{R_r} \right). \quad (\text{A.15})$$

The holographic imaging equations (A.13), (A.14) and (A.15) are of the same form than for the paraxial case, the various R_q , however, replaced the components z_q (Meier, 1965). A significant departure from this case is given by the inequality

$$\left(\frac{x_i}{R_i}\right)^2 + \left(\frac{y_i}{R_i}\right)^2 < 1, \quad (\text{A.16})$$

which has to be satisfied to form an image instead of an evanescent wave \mathcal{E}_i .

A.4.2 Axial Positioning Error of Holographic Particle Images

In the limit of infinitely large radii the reference and conjugate reconstructing wavefronts are planar waves. This ideal situation is never achieved in an experiment, instead the collimation can be made only as good as it can be sensed, for example by a shearing-interferometer as presented in Section 2.1.4.2). The remaining worst case wavefront radius $\pm R_{\text{lim}}$ can be used to estimate a maximum axial positioning error δz of a holographic particle image, which can be expressed as the difference of two radii according to (A.13) with $\mu = m = 1$:

$$\delta z = R_{i1} - R_{i2}. \quad (\text{A.17})$$

Each radius of the reference and reconstructing waves can be affected by this error in both directions, hence:

$$\begin{aligned} R_{g1} &= \pm R_{\text{lim}} \\ R_{r1} &= \mp R_{\text{lim}} \\ R_{g2} &= \mp R_{\text{lim}} \\ R_{r1} &= \pm R_{\text{lim}}. \end{aligned} \quad (\text{A.18})$$

Resolving (A.13) for R_i and introducing (A.18) yields:

$$\begin{aligned} \delta z &= \frac{-R_{\text{lim}}^2 R_s}{-R_{\text{lim}}^2 + 2R_{\text{lim}} R_s} - \frac{-R_{\text{lim}}^2 R_s}{-R_{\text{lim}}^2 - 2R_{\text{lim}} R_s} \\ &= \frac{R_{\text{lim}} R_s}{R_{\text{lim}} - 2R_s} - \frac{R_{\text{lim}} R_s}{R_{\text{lim}} + 2R_s} \\ &= \frac{4R_{\text{lim}} R_s^2}{R_{\text{lim}}^2 - 4R_s^2} = \frac{1}{\frac{R_{\text{lim}}}{4R_s^2} - \frac{1}{R_{\text{lim}}}}. \end{aligned} \quad (\text{A.19})$$

Replacing the radius R_s with the axial distance of the particle to the hologram z_0 then yields with $1/R_{\text{lim}} \rightarrow 0$:

$$\delta z \approx \pm \frac{4z_0^2}{R_{\text{lim}}}. \quad (\text{A.20})$$

A.5 Mie-Scattering Theory

Mie theory solves the wave equation with appropriate boundary conditions for two homogeneous media, one of which is spherical and imbedded in the other. The problem can be reduced to solve a scalar wave equation. For any homogeneous medium this equation is obtained from inserting the description of a planar and harmonic electromagnetic wave into Maxwell's third and fourth equation resulting in:

$$\Delta \mathbf{H} + k^2 \mathbf{H} = 0, \quad (\text{A.21})$$

$$\Delta \mathbf{E} + k^2 \mathbf{E} = 0 \quad (\text{A.22})$$

with $k^2 = \omega^2 \epsilon \mu$.

Hence, the scalar wave equation is:

$$\Delta \psi + k^2 \psi = 0 \quad (\text{A.23})$$

and one can find after transformation to polar coordinates and a separation into radial and angular components:

$$\psi(r, \theta, \phi) = R(r)\Theta(\theta)\Phi(\phi) \quad (\text{A.24})$$

linearly independent solutions of A.23 from the corresponding radial function:

$$\rho \frac{d}{d\rho} \left(\frac{dZ}{d\rho} \right) + (\rho^2 - (n + 1/2)^2) Z = 0, \quad (\text{A.25})$$

with the dimensionless variable $\rho = kr$ and the function $Z = R\sqrt{\rho}$, which is solved by linear combinations of Bessel functions. These solutions are the Hankel functions or spherical Bessel functions of the third type:

$$h_n^{(1)} = j_n(\rho) + iy_n(\rho) \quad (\text{A.26})$$

$$h_n^{(2)} = j_n(\rho) - iy_n(\rho), \quad (\text{A.27})$$

with the spherical Bessel functions of the first (J_ν) and second (Y_ν) type:

$$j_n(\rho) = \sqrt{\frac{\pi}{2\rho}} J_\nu(\rho) \quad (\text{A.28})$$

$$y_n(\rho) = \sqrt{\frac{\pi}{2\rho}} Y_\nu(\rho), \quad (\text{A.29})$$

with $\nu = n + 1/2$.

The equations solving (A.23) are then:

$$\psi_e(r, \theta, \phi) = \cos(m\phi) P_n^m(\cos \theta) z_n(\rho) \quad (\text{A.30})$$

$$\psi_o(r, \theta, \phi) = \sin(m\phi) P_n^m(\cos \theta) z_n(\rho), \quad (\text{A.31})$$

with $P_n^m(\cos \theta)$ the associated Legendre functions of the first type, m an ordinal number, $n = m, m + 1, \dots$ the number of modes and $z_n(\rho)$ one of the functions (A.26) and (A.27).

Multiplying (A.30) and (A.31) with the vector \mathbf{r} , which equals the particle radius, leads to four solutions for the vectorial wave functions, two for each of the equations (A.21) and (A.22). These solutions are called spherical surface functions which are used to determine the electrical and magnetic field of the incident, the scattered and the internal wave. For a proper solution of the problem, these functions need to be orthogonal. Furthermore, the radial symmetry of the particle requires a $\pi/2$ -phaseshift of the scattered field when its polarization is perpendicular to the incident wave. Together with the boundary condition:

$$(\mathbf{E}_{\text{inc}} + \mathbf{E}_{\text{sca}} - \mathbf{E}_{\text{int}}) \times \hat{\mathbf{n}}_r = (\mathbf{H}_{\text{inc}} + \mathbf{H}_{\text{sca}} - \mathbf{H}_{\text{int}}) \times \hat{\mathbf{n}}_r = 0, \quad (\text{A.32})$$

which quotes that for the reason of energy conservation the tangential components of both fields need to be steady, for each incident wave an expression of the internal and the scattered field can be found by choosing the appropriate Bessel functions.

Solving the above equations is usually done with the aid of a computer by determining the elements S_1 and S_2 of the Jones scattering matrix:

$$\begin{pmatrix} E_{\text{sca},\parallel} \\ E_{\text{sca},\perp} \end{pmatrix} = \frac{\exp(ik(r-z))}{-ikr} \begin{pmatrix} S_2 & 0 \\ 0 & S_1 \end{pmatrix} \begin{pmatrix} E_{i,\parallel} \\ E_{i,\perp} \end{pmatrix}. \quad (\text{A.33})$$

These are expressed by a series expansion of a linear combination from the two normal modes of a spherical particle (vector spherical harmonics). These modes are identified as those spherical surface functions, which show a zero radial component of either the electrical or magnetic field vector and hence:

$$S_1 = \sum_n^{\infty} \frac{2n+1}{n(n+1)} \left(a_n \frac{P_n^1}{\sin \theta} + b_n \frac{dP_n^1}{d\theta} \right) \quad (\text{A.34})$$

and:

$$S_2 = \sum_n^{\infty} \frac{2n+1}{n(n+1)} \left(a_n \frac{dP_n^1}{d\theta} + b_n \frac{P_n^1}{\sin \theta} \right). \quad (\text{A.35})$$

In the equations (A.34) and (A.35) the weighing coefficients a_n and b_n for the external field are determined by:

$$a_n = \frac{m\psi_n(mx)\psi'_n(x) - \psi_n(x)\psi'_n(mx)}{m\psi_n(mx)\zeta'_n(x) - \zeta_n(x)\psi'_n(mx)} \quad (\text{A.36})$$

and:

$$b_n = \frac{\psi_n(mx)\psi'_n(x) - m\psi_n(x)\psi'_n(mx)}{\psi_n(mx)\zeta'_n(x) - m\zeta_n(x)\psi'_n(mx)}, \quad (\text{A.37})$$

where $\psi_n(\rho) = \rho j_n(\rho)$ and $\zeta_n(\rho) = \rho h_n^{(1)}(\rho)$ are Ricatti-Bessel functions to simplify the recursive computations, $m = n_{\text{particle}}/n_{\text{medium}}$ is the relative index of refraction and:

$$x = kr = \frac{2\pi n_{\text{medium}} r}{\lambda} \quad (\text{A.38})$$

is a modified size parameter (cf. size parameter a in Section 2.3) including the complex index of refraction in the surrounding of the particle.

Summarizing, in a first step the amount contributing to the scattered wave is determined for each partial wave before the amplitude of the scattered field is determined from the incident amplitude.

For calculations according to Mie's theory, the Matlab Mie functions by Barnett (1996) or a fortran code according to Bohren and Huffman (1983) have been used throughout this thesis. Both requiring an input and giving the output with the corresponding Stoke's vector $\mathbf{I} = (I, Q, U, V)$ for polarized light, coupled by the Mueller matrix formalism (Walker, 1954):

$$\mathbf{I}_{\text{sca}} = \underline{\underline{\mathbf{M}}} \mathbf{I}_{\text{inc}} = \begin{pmatrix} S_{11} & S_{12} & 0 & 0 \\ S_{21} & S_{22} & 0 & 0 \\ 0 & 0 & S_{33} & S_{34} \\ 0 & 0 & S_{43} & S_{44} \end{pmatrix} \mathbf{I}_{\text{inc}}, \quad (\text{A.39})$$

with:

$$S_{21} = S_{12} \quad (\text{A.40})$$

$$S_{22} = S_{11} \quad (\text{A.41})$$

$$S_{44} = S_{33} \quad (\text{A.42})$$

$$S_{43} = S_{34} \quad (\text{A.43})$$

and:

$$S_{11} = [(S_2 S_2^*) + (S_1 S_1^*)] / 2 \quad (\text{A.44})$$

$$S_{11} = [(S_2 S_2^*) - (S_1 S_1^*)] / 2 \quad (\text{A.45})$$

$$S_{11} = [(S_1 S_2^*) + (S_2 S_1^*)] / 2 \quad (\text{A.46})$$

$$S_{11} = i [(S_1 S_2^*) - (S_2 S_1^*)] / 2. \quad (\text{A.47})$$

A.6 Line-width, Coherence Time or Length and Spectrum of Radiation

It can be shown that the coherence length l_c is inversely related to the spectral width, or linewidth $\Delta\nu$ by using the Wiener-Khintchine-Theorem (Wiener, 1930; Khintchine, 1934), which states that the power spectral density $W(\nu)$ is the Fourier transform of the self coherence function $\Gamma(\tau)$:

$$W(\nu) = \int_{-\infty}^{+\infty} \Gamma(\tau) \exp(-i2\pi\nu\tau) d\tau.$$

Assuming $W(\nu)$ to be gaussian shaped, also $\Gamma(\tau)$ has a gaussian shape. By substituting $\tau = \Delta l/c$ it then follows:

$$\Gamma(\Delta l) = \exp \left[- \left(\frac{\pi \Delta\nu}{2\sqrt{\ln(2)}} \frac{\Delta l}{c} \right)^2 \right].$$

Defining the coherence length l_c as the length Δl at which the amount of the self coherence function has decreased to $1/e$ of it's initial value:

$$\Gamma(\Delta l) = \frac{\Gamma(0)}{e}$$

we find:

$$l_c = 2 \cdot \frac{2\sqrt{\ln(2)}}{\pi} \frac{\lambda_0^2}{\Delta\lambda} \approx \frac{\lambda_0^2}{\Delta\lambda}.$$

Using the relation

$$\Delta\nu = \frac{c\Delta\lambda}{\lambda_0^2} \text{ for } \Delta\lambda \ll \lambda_0$$

we finally have for the coherence length or time, respectively:

$$l_c \approx \frac{c}{\Delta\nu} \text{ or } \tau_c \approx \frac{1}{\Delta\nu}.$$

A.7 Specifications for Nd:YAG Laser System

Version for ordering laser system for the University of Oldenburg (3 pages)

(18.10.2001)

S.F. Herrmann, K.D. Hinsch

General

A frequency doubled Nd:YAG laser system consisting of two unstable oscillators (gaussian front mirror) with amplifiers and an injection seeder for SLM operation is required, which allows to deliver two light pulses (approximately 1.4 J output energy per pulse at $\lambda = 532$ nm) with an adjustable time delay (0 ns to 10 ms) and a maximum repetition rate of 10 Hz. Beam quality, pulse energy, coherence length and other properties of the laser must be suited to perform Holographic PIV (standard and Light-in-Flight) with small tracer particles (diameter $1 \mu\text{m}$) in the environment of an industrial wind tunnel at large illumination and recording distances (up to 8 m) as well as in laboratory environment with short distances. The laser system must be compact, robust, reliable, easy to handle, flexible and transportable. The laser system must be mounted on a single board (1.25 m maximum width) and must be extendable with a second similar laser system later on. The laser system has to be delivered to the University of Oldenburg, Germany, for testing and system integration.

Laser description

All specifications for the laser system are made with respect to a wavelength of $\lambda = 532$ nm and a repetition rate of 10 Hz of the two pulses, unless otherwise stated.

The Nd:YAG laser shall consist of two oscillators (approximately 1.4 J output energy in accordance to the valid data sheet) and two second harmonic generators. The polarization state of the output beams must be orthogonal to each other in standard configuration and parallel after a few system modifications. The necessary modifications as well as all required alignments must be possible with reasonable effort by the user and under constraints of the system specifications (pulse energy, spatial intensity, divergence, co-linearity ...).

Both oscillators of the laser system must be seeded from the same injection seeder. Changing the coherence length of the emitted light must be easily possible by switching the injection seeder "on". The seeder must be protected from possible distortions due to light coming from the other oscillators. The output beams from the oscillators must be perfectly superimposed and co-linear in standard configuration (see specifications). Furthermore it must be possible that the beams emerge from the laser head at different ports if required (user modification).

The laser system must have two externally triggerable (TTL) shutters such that just two pulses emerge from the laser housing while the laser is running in 10 Hz mode for the specific needs of holographic recording. In addition, a mechanical shutter which prevents laser pulses leaving the laser head as long as the shutter has not been released,

is required. The shutter release must be possible by a small hand-held button (safety reasons).

The system must have double pulse capabilities (i.e. two pulses out of one oscillator within a limited time range and at reduced pulse energy).

The whole set-up must be insensitive to dust and must be stable with respect to vibrations and changes of temperature. Misalignments of the system during the running time of the experiments in the wind tunnel or after having transported the system to another facility are not tolerated.

It must be possible to combine two of such laser systems (i.e. 2 x 2 oscillators) in order to have a 4 pulse configuration or two pulses with twice the output energy for more sophisticated applications.

The system must have a calibrated photodiode for energy control with an output signal for monitoring the pulse sequence and allowing to measure the time delay between the pulses.

Synchronization

The system must accept an external TTL trigger signal with a repetition rate of 10 Hz. This signal starts each pulse sequence of the laser. The different pulses, required for the system can be generated externally or internally. If generated internally, all pulses must be accessible externally and the time delay between the light pulses must also be easily adjustable externally. The time delay must be very precise and constant. If generated internally, the control and generation of single sequences of light pulses must be possible due to an external ARM signal (by continuously firing the flash lamps and arming / disarming the Pockels cells).

The system must have an interface to external trigger electronics and a computer interface for selecting the time delay between pulses and triggering the flash-lamps (additional to manual setting).

Certifications

Data, which have been certified, will be verified in presence of representatives of the manufacturer and the University of Oldenburg after the installation. Power drift measurements and determination of the beam quality according to the following table of specifications are done by representatives of the University of Oldenburg. The variation with time of the main parameters, determining the performance of the system for application at PIV, as pulse energy, stability of energy etc. has to be specified. A pre-delivery check will be performed at the manufacturer's site together with a representative from the University of Oldenburg.

Specifications

According to the above description the following specifications (Table A.3) are defined: The laser system and all specifications are made with respect to a wavelength of $\lambda = 532$ nm and a repetition rate of 10 Hz of the two pulses, unless otherwise stated. The specifications are given for a laser operated in a standard laboratory environment. **Generally it is more important that the optical properties of both oscillators are nearly identical than to achieve the optimum for each single oscillator.**

Repetition rate of each laser	10 Hz (and integral fractions of 10)
Pulse energy for each of two pulses	1.2 J
Polarization in standard configuration	Orthogonal
Linewidth	$\leq 1.4 \text{ cm}^{-1}$ (at $\lambda = 1064 \text{ nm}$)
Linewidth with injection seeder	$\leq 0.003 \text{ cm}^{-1}$ (at $\lambda = 1064 \text{ nm}$)
Power drift over 8 hours, without readjustment of phase-matching for $\pm 3^\circ\text{C}$	$\leq \pm 5\%$
energy stability - pulse to pulse, peak to peak, 99% of pulses	$\leq \pm 3\%$
Beam pointing stability (rms, on 200 alternating pulses at the focal plane of a 2 m lens) for combined beams	$\leq \pm 100 \mu\text{rad}$ without and $\leq \pm 50 \mu\text{rad}$ with Beam-Lok
Divergence (full angle on 200 pulses at $1/e^2$ of the peak, 85% of total energy)	$\leq 0.5 \text{ mrad}$ full angle same direction for both laser beams: both beams converging or both beams diverging
Roundness measured at specific distance from laser output (ratio between two perpendicular axis: major axis and minor axis)	$\geq 90\%$ @ 1m, $\geq 85\%$ @ 3m
Spatial intensity modulation (beam profile) at 1 m, 3m and 8 m from laser output	$(I_{max} - I_{min}) / (I_{max} + I_{min}) \leq 0.25$ (Full width half maximum pulse width) 1)
Beam quality (with half beam diameter ω estimated at $1/e^2$ and half opening angle Θ) on a pulse-to-pulse basis (e.g. within 200 pulses)	$\Theta\omega \approx \text{const}$ according to: $(\Theta_1\omega_1 - \Theta_2\omega_2) / (\Theta_1\omega_1 + \Theta_2\omega_2) \leq \pm 5\%$
Temporal separation between pulses	from 0 ns to 100 ms
Timing jitter between following laser pulses of each oscillator	$\leq 0.5 \text{ ns}$ (internal jitter)
Timing jitter between following pulses of different oscillators	$\leq 0.5 \text{ ns}$ (internal jitter)
umbilical length between laser head and power supply	5 m
umbilical mount	easily detachable
working temperatures ²⁾	$15^\circ\text{C} - 35^\circ\text{C}$
power requirements	1 x 220 - 240 V, 50 Hz, 25 A
safety rules to be satisfied	CE

¹⁾ Variation from mean of 200 pulses within the given range and NOT fit to gaussian curve! ²⁾ Range within the system can be operated to fulfil all given specifications provided the over-day variations in temperature are within $\pm 3^\circ\text{C}$.

Table A.3: Overview of the specifications agreed with the manufacturer of the Nd:YAG laser system.

A.8 Distributed Correlation

To speed up the correlation of thousands of sub-volumes, an optimised evaluation routine was developed under Matlab. It comprises two parts. The first part is building several matrices, most of which are describing the measurement volume after reading the description file produced by the scanning software. This part of the routine can be parameterised with the interrogation cell size and their overlap, as well as by a decision over the computation method (local on the server or distributed using mDICE clients).

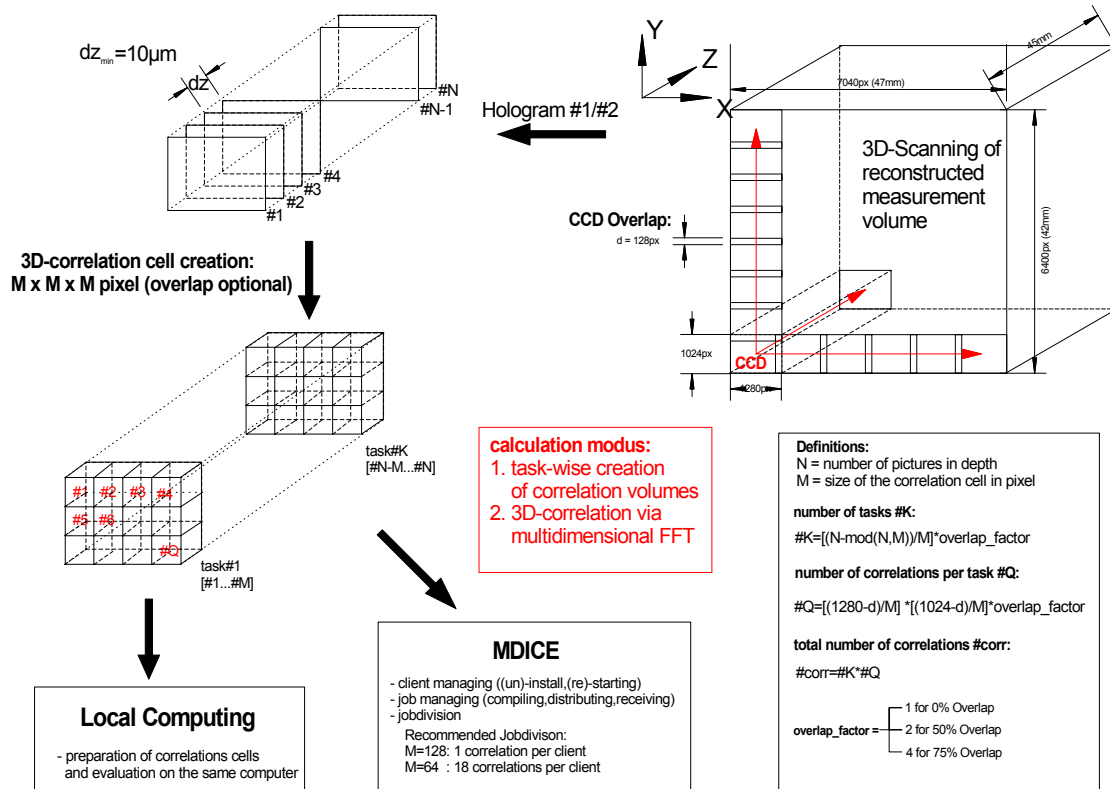


Figure A.4: Principal of task-wise correlation and distributed computing: The two reconstructed particle images have been scanned in a predefined volume, alternately and plane-by-plane. Each series of depth-wise adjacent digitised image planes from both reconstructions is then made up of N planes, which are subdivided into K tasks, each made up of Q interrogation cells. After data preparation for a given task, the calculation is directed to either the local computer or the distributed network computers and all tasks are processed sequentially.

Each of these matrices corresponds to a single interrogation cell (IC) and is assigned a unique ID. The routine also gives pointers to the relevant pixels (in different digitized images) holding the reconstructed image intensities. Additionally, the matrices holding the final measurement results are instantiated and filled either with their coordinates in the scanned volume (X, Y, Z - corresponding to the middle of each correlation cell) or with a Not-a-Number (NaN) value for those later holding the velocity components or the correlation coefficient (U, V, W and C). Finally a matrix describing the different

computation tasks, to be carried out step by step is build.

Figure A.4 illustrates the second part, which handles each task contained in the last matrix in the following way: Firstly, initialising memory for Matlab and under Windows, reading the corresponding image data plane by plane and creating the ICs of the given task (this is typically done in such a way, that each digitized image has to be opened only once). Secondly, correlating each pair of cells, either locally for the whole task or distributed on several computers by dividing the task in different jobs. Thirdly, writing the results to the matrices U , V , W and C and deleting the data from the actual task before repeating the steps one to three with the next task.

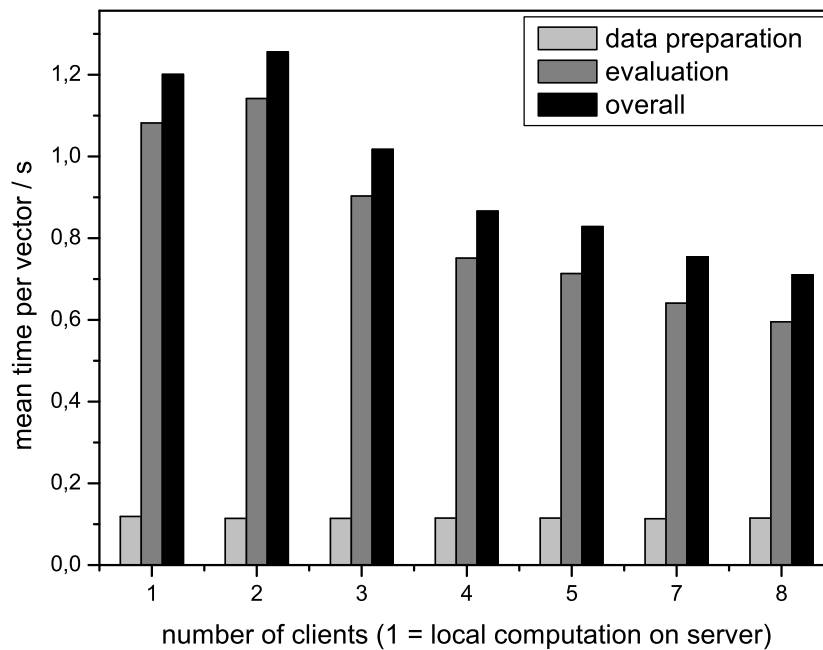


Figure A.5: Mean times per vector for data preparation and evaluation by cross-correlation and peak-finding when using distributed computation over several computers for a total of 45,360 interrogation cells, each 64^3 pixels in size.

Although the resulting gain in performance is strongly dependent on the actual load of the network and the machines used as client, a general idea of the decrease in mean computation time per vector can be obtained from Figure A.5, where for each given number of computers a total of 45,360 vectors has been computed at a IC-size of 64^3 pixel. It can be seen, that to realize a speed-up of factor 2 roughly 10 clients are needed. For further improvements a high-performance network is thus recommended.

A.9 Image Enhancements

This Appendix briefly documents image processing methods frequently used for the evaluation of particle images.

A.9.1 Thresholding and Binarisation

Simple thresholding can be used to suppress low intensity speckle noise. When using thresholding on noisy particle images, the particle contributions are supposed to be significantly brighter than the background. All pixels with intensity values below the threshold are set to zero. Those pixels above the threshold either remain unchanged in their grey value or they are set to the maximum value. The second case is commonly known as binarisation, often used to produce valid / non-valid masks.

A.9.2 Contrast Enhancements

A variety of methods to enhance the contrast in digital images is known from image processing software. Often only the dynamic range of images is maximised by mapping the original grey values to the full dynamic range, e.g. $[0, 255]$ for 8bit images. The image processing software Adobe Phtoshop offers automatic and manually parameterised methods, for enhancements. Another, more complex enhancement method is the so-called histogram equalisation. Given a desired histogram H , the histogram equalization algorithm chooses the grayscale transformation T to minimize $|c_1(T(k)) - c_0(k)|$, where c_0 is the cumulative histogram of the input image a , c_1 is the cumulative sum of H for all intensities k . This minimization is subject to the constraints that T must be monotonic and $c_1(T(a))$ cannot overshoot $c_0(a)$ by more than half the distance between the histogram counts at a . The algorithm uses this transformation to map the grey levels in X to their new values (see Matlab help for `histeq`). In Figure A.6 the above mentioned methods are compared by plotting the resulting histogram data from a reconstructed particle image of the ndyag39 hologram at a medium aperture size.

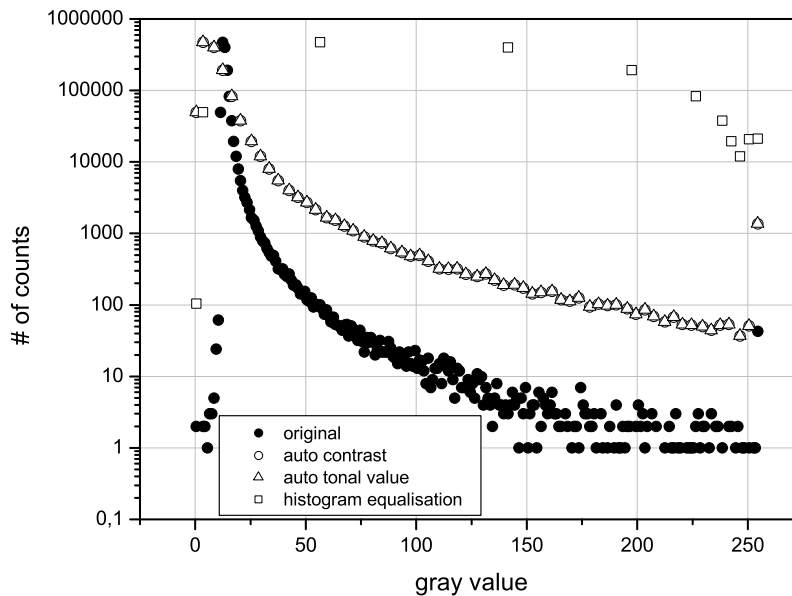


Figure A.6: Comparison of two contrast enhancement methods from Adobe Photoshop.

A.9.3 Noise Reduction

During the course of the experiments a noise reduction algorithm was developed which can be used for either LiFH-PIV or ordinary HPIV particle images. The algorithm uses an adaptive threshold value calculated from the particle image histograms. For this, a least-square fit is used to approximate the probability density function of an integrated speckle pattern Goodman (1984). Lower intensity values belong more likely to the underlying speckle pattern, whereas most of the high intensity contributions in the image belong to the in-focus particle images.

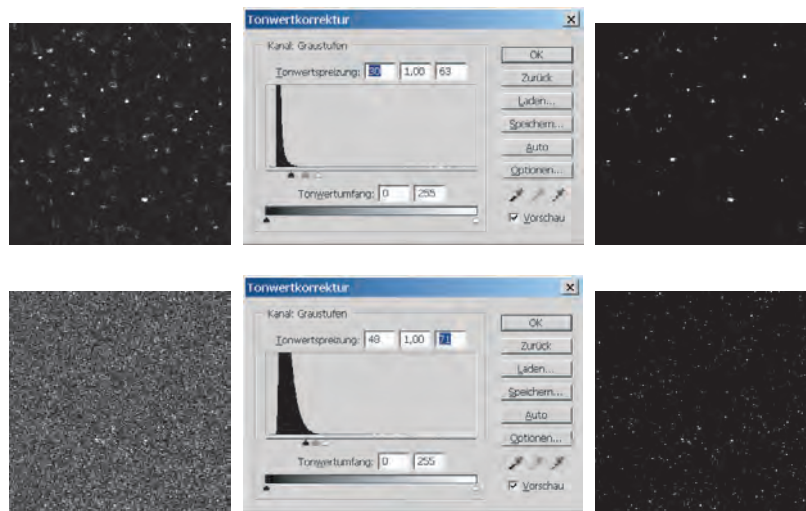


Figure A.7: Tonal value adaptation as an example on reconstructed images from the holograms ndyag39 (LiFH) and ndyag40 (H) where a dispersion of hollow glass spheres in water was recorded. All images are additionally contrast enhanced for the purpose of optimum reproduction when printed.

By using a common image processing method, the tonal value adaptation, the background can effectively be suppressed (Figure A.7). The high-intensity contributions from the speckle field are often slightly smaller in size than the particle images themselves, thus they can be found after a suited binarisation step and removed after labelling of connected components and sorting according to their size.

A.10 Determining Dispersed Particle Densities in Water

The experiments with varying seeding density in water have been performed with hollow glass spheres (HGS) as tracer particles. For the purpose of seeding water flows, one product, the so-called "Sphericels 110P8", have drawn special attention (Figure A.9). They offer considerable high reflection, are chemically insensitive and most of the spheres stay in the water column for a long time. However, their size distribution is rather broad. The experimental study tried to take advantage of these neutral buoyancy particles, since a dilution series had to be produced and the different dispersion

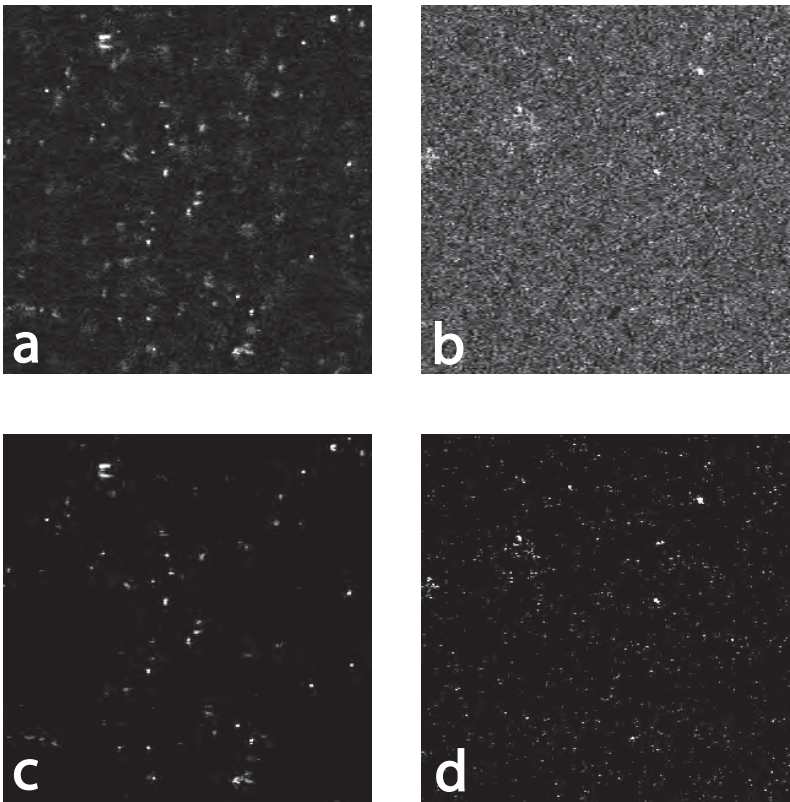


Figure A.8: Noise reduction by adaptation of the tonal value to suppress low intensity contributions.

have to be used after long term intervals for setting up the experimental apparatus and processing the holograms. Each dispersion was used twice to record the long and short coherence hologram. In the meantime, evaporation of the ultra-clean water was suppressed by covering the cuvette. Furthermore, from each dispersion two samples have been drawn for later analysis of the seeding density.

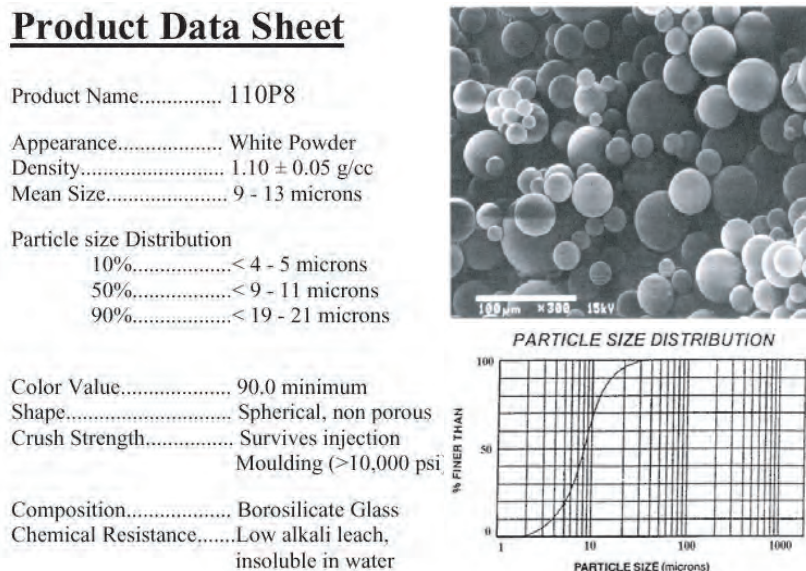


Figure A.9: Data from the Sphericel product sheet (left), REM image showing the perfect spherical form of the hollow glass spheres (upper right) and measured size distribution of a typical batch (lower right).

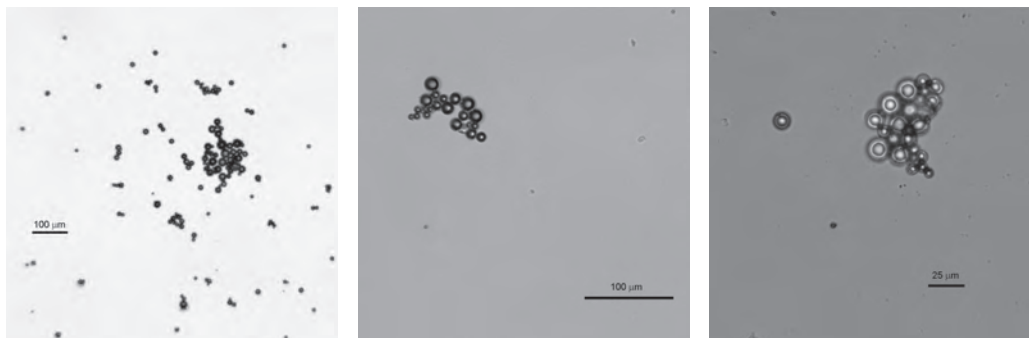


Figure A.10: Microscopic images of hollow glass spheres (Sphericels 110P8) intended to be used for the determination of particle density in a precise pipetted volume.

First, a microscopic analysis was envisaged, but it turned out to be very difficult to handle the small and precise pipetted fractions of the dispersion on the probe glass. Without any cover, the water evaporated fast and the Sphericels turned into a dry state, in which they are easily blown away from the slightest airflow. Using a cover, many Sphericels were broken by the adhesive forces. Only a few images could be taken uncovered (see Figure A.10), the fluid flow due to the evaporation was strong and clustering took place. It was impossible to get reliable data on the number density of the particles.

The second approach to measure the number density, uses a principle similar to the Coulter-Counter. During suction of the fluid through a small capillar (precise bore in a rubin) the electrical resistance is measured against an internal probe-electrolyte. Whenever a particle of a given volume suppresses the volume of the fluid in the capillar, the measured resistance-signal forms a pulse. While in the Coulter-Counter only the maximum amplitude of this signal is evaluated, the system used for this study (Model Casy1 from Schärfe System GmbH (1997)) evaluates the pulse form with more than 100 supporting points and draws conclusions about the volume of the particle from the area under this pulse. Exemplarily one measured size distribution is shown on the left in Figure A.11. Three times a volume of 200 μl was measured and the resulting mean value needs to be subtracted by a calibration value from a clean water measurement of 20 particles resulting to particle density of 22.8 p/mm^3 in the measured sample. It must be noted however, that the system is only able to register particles larger than 3 μm . Comparing with the Sphericel size distribution in Figure A.9 we have to assume that a small fraction of particles ($\approx 5\%$) is not measured.

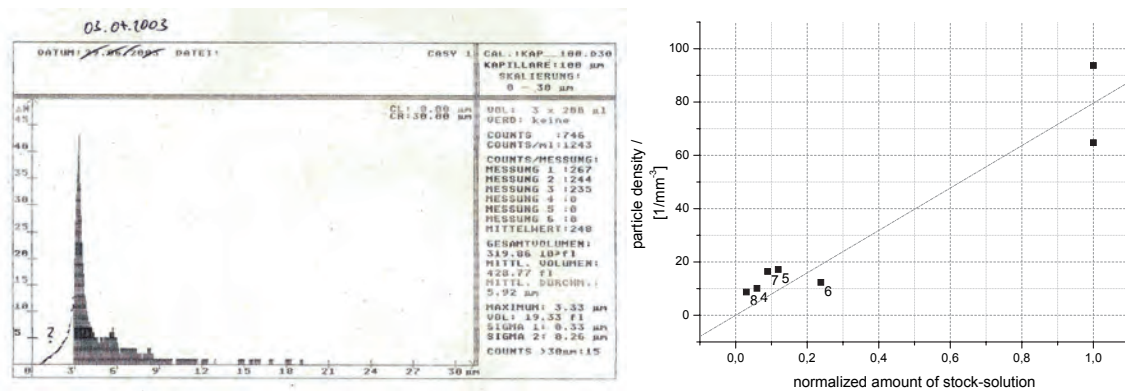


Figure A.11: Results of the Casy measurements: repeated (3x) measurement result from one sample dispersion with size distribution and single and mean count value (left), overview of the results from all samples plotted versus the normalized amount of stock solution used to be diluted by clear water (right).

An overview of the Casy measurements is shown on the right side of Figure A.11, where the particle density is plotted versus the normalized amount of stock solution. Differences in the measurement of two basically equal samples of the stock solution leads to the conclusion, that either the stock-solution was not homogeneous or that even inside the well-mixed samples a sedimentation process takes place within the minutes of the measurement. The reason might be also an unexplainable effect that leads to a malfunction of the system when HGS are used. The system, initially designed for counting biological cells, might not have been tested yet with such a type of particles. The later thesis is supported by the questionable results of the SNR dependency on the measured particle number density as explained in Section 9.3.6.2.

References

- Abramson, N. H. (1972). The holo-diagram VI: Practical device in coherent optics. *Appl. Opt.* 11, 2562–2571. 53
- Abramson, N. H. (1978). Light-in-Flight Recording by Holography. *Opt. Lett.* 3(4), 121–123. 53, 55
- Abramson, N. H. (1983, January). Light-in-flight recording: high speed holographic motion pictures of ultrafast phenomena. *Appl. Opt.* 22(2), 215–232. 53, 54
- Abramson, N. H. (1984a, May). Light-in-flight recording II: Compensation for the limited speed of the light used for observation. *Appl. Opt.* 23(10), 1481. 55
- Abramson, N. H. (1984b, November). Light-in-flight recording III: Compensation for optical relativistic effects. *Appl. Opt.* 23(22), 4007. 55
- Abramson, N. H. (1985, October). Light-in-flight recording IV: Visualizing optical relativistic phenomena. *Appl. Opt.* 24(20), 3323. 55
- Abramson, N. H. (1987, November). Optical fibre tested using light-in-flight recording by holography. *Appl. Opt.* 26(21), 4657. 55
- Abramson, N. H., S.-G. Pettersson, and H. Bergstrom (1989, February). Light-in-flight recording V: Theory of slowing down the faster-than-light motion of the light shutter. *Appl. Opt.* 28(4), 759. 55
- Abramson, N. H. and K. G. Spears (1989). Single pulse light-in-flight recording by holography. *Appl. Opt.* 28(10), 1834–1841. 55
- Adrian, R. J., C. D. Meinhart, D. H. Barnhart, and G. C. Papen (1993). An HPIV System for Turbulence Research. In E. P. Rood (Ed.), *Holographic Particle Image Velocimetry*, Volume FED-Vol. 148, pp. 17–22. ASME. 13, 97
- Andrés, N., P. M. Arroyo, H. Hinrichs, and M. Quintanilla (1999). Digital speckle pattern interferometry as full field velocimetry technique. *Opt. Lett.* 24, 6997–7007. 37
- Arroyo, M. P., N. Andrés, and M. Quintanilla (2000). The development of full field interferometric methods for fluid velocimetry. *Opt. Laser Technol.* 32, 535–542. 37

- Arroyo, M. P. and C. A. Greated (1991). Stereoscopic particle image velocimetry. *Meas. Sci. Technol.* 2(11), 1181–1186. 97
- Austin, M. (1984). The dependence of the image quality of holographic real images on the reconstruction geometry. *J. Phys. D: Appl. Phys.* 17, 1953–1959. 29
- Banyasz, I., G. Kiss, and P. Varga (1988). Holographic image of a point source in the presence of misalignment. *Appl. Opt.* 27, 1293–1297. 158
- Barnett, D. (1996). Matlab Mie functions from <http://www.lboro.ac.uk/departments/el/research/photonics/matmie/mfiles.html>. Internet source as .m-files. 31, 33, 166
- Barnhart, D. H., R. J. Adrian, and G. C. Papen (1994). Phase-conjugate holographic system for high-resolution particle image velocimetry. *Appl. Opt.* 33(30), 7159–7170. 5, 24, 67, 97, 145
- Barnhart, D. H., N. Hampp, N. A. Halliwell, and J. M. Coupland (2002). Digital holographic velocimetry with bacteriorhodopsin (BR) for real-time recording and numeric reconstruction. In R. J. Adrian, D. F. G. Durão, M. V. Heitor, M. Maeda, C. Tropea, and J. H. Whitelaw (Eds.), *Laser Techniques for Fluid Mechanics*, pp. 2.6. 19
- Barnhart, D. H., W. D. Koek, T. Juchem, N. Hampp, J. M. Coupland, and N. A. Halliwell (2004). Bacteriorhodopsin as a high-resolution, high-capacity buffer for digital holographic measurements. *Meas. Sci. Technol.* 15, 639–646. 19
- Barnhart, D. H., G. C. Papen, and R. J. Adrian (1993). Phase Conjugate Image Reconstruction for HPIV Systems. In E. P. Rood (Ed.), *Holographic Particle Image Velocimetry*, Volume FED-Vol. 148, pp. 13–16. ASME. 97
- Bass, M., P. A. Franken, J. F. Ward, and G. Weinreich (1962). Optical rectification. *Phys. Rev. Lett.* 9(11), 446–448. 77
- Belz, R. A. and F. M. Shofner (1990). *Selected Papers on Holographic Particle Diagnostics*, Volume MS 21 of *Milestone Series*, Chapter Characteristics and measurements of an aperture-limited in-line hologram image, pp. 351–358. Bellingham, Washington: SPIE Optical Engineering Press. 33
- Bjelkhagen, H. I. (2002, December). An update on commercial recording materials. SPIE's International Technical Group Newsletter. Holography 13.2. 156, 157
- Bohren, C. and D. Huffman (1983). *Absorption and scattering of light by small particles*, Chapter Modified BHMIE function by B.T. Draine, Princeton University, pp. 477–482. New York: John Wiley & Sons, Inc. 33, 166
- Bohren, C. and D. Huffman (1998). *Absorption and scattering of light by small particles*. New York: John Wiley & Sons, Inc. 31

- Booth, B. L., S. M. Jarrett, and G. C. Barker (1970, January). Holograms made with pulsed Argon-Ion lasers operating in various transverse modes. *Appl. Opt.* 9(1), 107–111. 59
- Born, M. and E. Wolf (1980). *Principles of Optics* (sixth edition ed.). Cambridge University Press. 28, 31
- Burckhardt, C. B. (1966). Diffraction of a plane wave at a sinusoidally stratified dielectric grating. *J. Opt. Soc. Am.* 56, 1502. 42
- Canny, J. (1986). A Computational Approach to Edge Detection. *IEEE Transactions on Pattern Analysis and Machine Intelligence PAMI-8*(6), 679–698. 134
- Cha, S. S., K. J. Huang, and J. S. Slepicka (1993). Double-Reference-Beam Off-Axis Holographic Particle Image Velocimetry. *Am. Soc. Mech. Eng. FED-148*, 23–26. 13
- Champagne, E. B. (1967). Nonparaxial imaging, magnification and aberration properties in holography. *J. Opt. Soc. Am.* 57, 51–55. 24, 29, 158, 161
- Chan, K. T., R. M. C. So, W. O. Wong, and Y. J. Li (2000, August). Particle image aberrations in off-axis holography. In G. M. Carlomagno and I. Grant (Eds.), *CD Rom Proc. 9th Int. Symp. on Flow Visualization*, Edinburgh, UK. ISBN: 0 953399117. 29
- Chan, V. S. S., W. D. Koek, D. H. Barnhart, N. Bhattacharya, J. J. M. Braat, and J. Westerweel (2004). Application of holography to fluid flow measurements using bacteriorhodopsin (bR). *Meas. Sci. Technol.* 15, 647–655. 19
- Collier, R. J., C. B. Burckhardt, and L. H. Lin (1971). *Optical Holography*. Orlando: Academic Press, Inc. 11, 12, 16, 17, 23, 158
- Cooley, J. W. and J. W. Tukey (1965). An algorithm for the machine calculation of complex Fourier series. *Math. Comput.* 19, 297–301. 102
- Coupland, J. (Ed.) (2003). *Proceedings of the International Workshop on Holographic Metrology in Fluid Dynamics*, Loughborough, Leics, LE11 3TU, UK. Loughborough University. 5
- Debye, P. (1909a). Das Verhalten von Lichtwellen in der Nähe eines Brennpunktes oder einer Brennlinie. *Ann. d. Physik* 4(30), 755. 28
- Debye, P. (1909b). Der Lichtdruck auf Kugeln von beliebigen Material. *Ann. d. Physik* 30(IV), 57. 32
- Dudderar, T. D. and P. G. Simpkins (1982). The development of scattered light metrology. *Opt. Eng.* 21(3), 396–399. 37
- Forbes, S. J. and T. H. Kuehn (1990). In-Line Particle Holography Using Photographic Threshold Technique. *Am. Soc. Mech. Eng* 95, 45–47. 28

- Foucaut, J. M., B. Miliat, N. Perenne, and M. Stanislas (2004). *Particle Image Velocimetry: Recent Improvements*, Chapter Characterization of Different PIV Algorithms using the ERUOPIV Synthetic Image Generator and Real Images from Turbulent Boundary Layer, pp. 163–184. Berlin: Springer. ISBN: 3-540-21423-2. 101
- Fourney, M. E., J. H. Markin, and A. P. Waggoner (1969). Aerosol Size and Velocity Determination via Holography. *The Review of Scientific Instruments* 40(4), 205–213. 4
- Friesem, A. A., A. Kozma, and G. Adams (1967). Recording parameters of spatial modulated coherent wavefronts. *Appl. Opt.* 6(5), 851–856. 42
- Gabor, D. (1948). A New Microscopic Principle. *Nature* 161, 777–778. 9
- Gabor, D. (1949). Microscopy by reconstructed wavefronts. *Proc. Roy. Soc. A197*(454). 15, 24
- Gabor, D. (1971). *Nobel Lectures, Physics 1971-1980*, Chapter Holography, 1948-1971. Singapore: World Scientific Publishing Co. 15
- Gauss, C. F. (1866). Nachlass: Theoria interpolationis methodo nova tractata. In *Werke Band 3*. Königliche Gesellschaft der Wissenschaften, Göttingen. 103
- Geiger, M., S. F. Herrmann, K. D. Hinsch, and J. Peinke (2000). Analysis of free jet turbulence with cross-correlation Light-in-Flight holography (LiFH). In M. Trinite, B. Lecordier, and C. Letailleur (Eds.), *Proc. Euromech 411*, Rouen, France. CORIA UMR 6614. 66, 67
- Gharib, M., D. Kremers, M. M. Koochesfahani, and M. Kemp (2002). Leonardo's vision of flow visualization. *Exp. in Fluids* 33, 219–223. 1
- Goodman, J. W. (1967). Film grain noise in wavefront-reconstruction imaging. *Appl. Opt.* 57(4), 493–502. 39, 121, 122, 123, 145, 148
- Goodman, J. W. (1984). *Laser speckle and related phenomena*, Chapter Statistical properties of laser speckle patterns, pp. 9–75. Berlin: Springer Verlag. 29, 40, 128, 131, 174
- Gouesbet, G. and G. Grehan (1999). Generalized Lorenz-Mie theory for assemblies of spheres and aggregates. *J. Opt. A: Pure Appl. Opt* 1, 706–712. 32
- Grant, I. (Ed.) (1994). *Selected papers on Particle Image Velocimetry*. SPIE Milestone Series MS99. Bellingham, Washington: SPIE Optical Engineering Press. 3
- Gray, J., P. Thomas, and X. D. Zhu (2001). Laser pointing stability measured by an oblique-incidence optical transmittance difference technique. *Rev. Sci. Inst.* 72(9), 3714–3717. 81
- Groh, G. (1973). *Holographie, Physikalische Grundlagen und Anwendungen*. Stuttgart: Verlag Berliner Union GmbH. 23, 158

- Gui, L. and S. T. Wereley (2002). A correlation-based continuous window-shift technique to reduce the peak locking effect in digital PIV image evaluation. *Exp. in Fluids* 32(4), 506–517. 101
- Halle, M. (1998, October). Holographic photochemistry, a summary. Internet Source. MAS 450/854. 159
- Herrmann, S. F., M. Geiger, K. D. Hinsch, and J. Peinke (2002). *Laser techniques for fluid mechanics*, Chapter Light-in-flight holography with switched reference beams for cross-correlation in deep volume PIV, pp. 3–23. Lisbon conference series. Springer. 65
- Herrmann, S. F., H. Hinrichs, K. D. Hinsch, and C. Surmann (2000). Coherence concepts in holographic particle image velocimetry. *Exp. Fluids* 29(S1), S108–S116. 63
- Herrmann, S. F. and K. D. Hinsch (2001). Particle holography and the noise limit. In J. Kompenhans (Ed.), *4th Int. Symp. on PIV*, Volume DLR Mitteilung 2001-03, Goettingen, pp. paper no. 1021. 37
- Herrmann, S. F. and K. D. Hinsch (Eds.) (2004a). *Holographic Metrology in Fluid Dynamics*. Bristol, UK: Institute of Physics Ltd. Institute of Physics Ltd. 5, 119
- Herrmann, S. F. and K. D. Hinsch (2004b). Light-in-flight holographic particle image velocimetry for wind-tunnel applications. *Meas. Sci. Technol.* 15, 613–621. 68
- Hinrichs, H., K. D. Hinsch, J. Kickstein, and M. Böhmer (1997). Light-in-flight holography for visualization and velocimetry in three-dimensional flows. *Opt. Lett.* 22, 828–830. 65
- Hinrichs, H., K. D. Hinsch, J. Kickstein, and M. Böhmer (1998). Deep field noise in holographic particle image velocimetry (HPIV): numerical and experimental particle image field modelling. *Exp. Fluids* 24, 333–339. 64, 146
- Hinrichs, H., K. D. Hinsch, R. Netter, and C. Surmann (1998). Light-in-flight particle holography for velocimetry in a wind tunnel. In G. M. Carlomagno and I. Grant (Eds.), *Proceedings of 8th International Symposium on Flow Visualization*, pp. 19.1–19.5. ISBN: 0953399109. 65
- Hinsch, K. D. (1993). *Speckle Metrology*, Chapter Particle Image Velocimetry, pp. 235–322. New York: Marcel Dekker. 3
- Hinsch, K. D. (1995). Three-dimensional Particle Velocimetry. *Meas. Sci. Technol.* 6, 742–753. 3
- Hinsch, K. D. and S. F. Herrmann (2004). Signal quality improvements by short-coherence holographic particle image velocimetry. *Meas. Sci. Technol.* 15, 622–630. 68, 145

- Hinsch, K. D., H. Hinrichs, G. Kufahl, and P. Meinschmidt (1990). Holography with controlled coherence for 3-D particle image velocimetry. In T. Tschudi (Ed.), *Proc. Holographics*, pp. 51–57. 60
- Hinsch, K. D., H. Hinrichs, A. Roshop, and F. Dreesen (1993). Holographic and stereoscopic advances in 3-D PIV. In E. P. Rood (Ed.), *Holographic particle image velocimetry*, Volume ASME FED-Vol. 148 of *ASME*, New York, pp. 33–36. American Society of Mechanical Engineers. 60
- Hobson, P. R. and J. Watson (1999). Accurate three-dimensional metrology of underwater objects using replayed real images from in-line and off-axis holograms. *Meas. Sci. Technol.* 10, 1153–1161. 24
- Hülsmann, C. (2005, October). Entwicklung von Justierverfahren zur Erhöhung der Genauigkeit holografischer Strömungsmessung. Diploma thesis. 21, 150
- International Organization for Standardization (1999). Lasers and Laser-Related Equipment, Test Methods for Laser Beam Parameters, Beam Positional Stability. ISO 11670. 81
- Keane, R. D. and R. J. Adrian (1990). Optimization of particle image velocimeters. Part I: Double pulsed systems. *Meas. Sci. Technol.* 1, 1202–1215. 47, 48, 49, 65
- Keane, R. D. and R. J. Adrian (1991). Optimization of particle image velocimeters. Part II: Multiple pulsed systems. *Meas. Sci. Technol.* 2, 963–974. 65
- Keane, R. D. and R. J. Adrian (1992). Theory of cross-correlation analysis of PIV images. *Appl. Sci. Res.* 49. 65, 101, 106
- Keane, R. D., R. J. Adrian, and Y. Zhang (1995). Super-resolution particle imaging velocimetry. *Meas. Sci. Technol.* 6, 754–768. 101
- Khintchine, A. (1934). *Math. Ann.* 109, 604. 58, 167
- Kilpatrick, J. M. and J. Watson (1994). Precision replay of underwater holograms. *Meas. Sci. Technol.* 5, 716–725. 24
- Kneubühl, F. K. and M. W. Sigrist (1995). *Laser*. Stuttgart: Teubner Verlag. 55, 58
- Koehler, W. (1999). *Solid-state laser engineering* (5th rev. and updated ed. ed.). Berlin: Springer. ISBN 3-540-65064-4. 58, 76, 77, 80
- Kompenhans, J. (2003). PivNet2 - A European collaboration on development, quality assessment, and standardization of Particle Image Velocimetry for industrial applications. EC grant number: G4RT-CT-2002-05081. 4
- Konrath, R., W. Schröder, and W. Limberg (2002). Holographic particle image velocimetry applied to the flow within the cylinder of a four-valve internal combustion engine. *Exp. Fluids* 33, 781–793. 24, 26, 88

- Kozma, A. (1968). Effects of film-grain noise in holography. *J. Opt. Soc. Am.* 58, 436–438. 42, 127
- Kähler, C. J., B. Sammler, and J. Kompenhans (2002). Generation and control of tracer particles for optical flow investigations in air. *Exp. in Fluids* 33, 736–742. 119
- Lauterborn, W., T. Kurz, and M. Wiesenfeldt (1995). *Coherent Optics* (1st edition, 2nd printing 1999 ed.). Berlin: Springer. ISBN: 3-540-58372-6. 56
- Lecordier, B., J. C. Lecordier, and M. Trinté (1999). Iterative sub-pixel algorithm for the cross-correlation PIV measurement. In *Proceedings of the 3rd International Workshop on PIV*, Santa Barbara. University of California. 101
- Leith, E. N. and J. Upatnieks (1962). Reconstructed Wavefronts and Communication Theory. *J. Opt. Soc. Am.* 52, 1123–1130. 9, 13
- Lommel, E. (1885). *Abh. Bayer. Akad. Abth.* 2, 233. 28
- Lorenz, L. (1898). Oeuvres scientifiques de L. Lorenz, revues et annotées par H. Valentinier. *Librairie Lehman et Stage, Copenhagen.* 32
- Lozano, A., J. Kostas, and J. Soria (1999). Use of holography in particle image velocimetry measurements of a swirling flow. *Exp. Fluids* 27, 251–261. 34, 68
- Mantravadi, M. V. (1992). *Lateral Shearing Interferometers* (2nd ed.), Chapter 4, pp. 124–168. John Wiley & Sons, Inc. 21
- Meier, R. W. (1965, August). Magnification and Third-Order Aberrations in Holography. *Fluid Dynamics Research* 55(8), 987–992. 23, 158, 163
- Meng, H., W. L. Anderson, F. Hussain, and D. D. Liu (1993). Intrinsic speckle noise in in-line particle holography. *J. Opt. Soc. Am.* 10(9), 2046–2058. 13
- Meng, H. and F. Hussain (1991). Holographic particle velocimetry: a 3D measurement technique for vortex interactions, coherent structures and turbulence. *Fluid Dynamics Research* 8(1-4), 33–52. 13
- Meng, H. and F. Hussain (1993). Holographic Particle Velocimetry: Prospects and Limitations. *Am. Soc. Mech. Eng. FED-148*, 1–11. 13
- Meng, H. and F. Hussain (1995). In-line recording and off-axis viewing technique for holographic particle velocimetry. *Appl. Opt.* 34, 1827–1840. 42
- Meng, H., G. Pan, Y. Pu, and S. H. Woodward (2004). Holographic particle image velocimetry: from film to digital recording. *Meas. Sci. Technol.* 15, 673–685. 19, 99
- Mie, G. (1908). Beiträge zur Optik trüber Medien, speziell kolloidaler Metallösungen. *Ann. d. Physik* 4(25), 377–442. 31

- Murty, M. V. R. K. (1964, April). The Use of a Single Plane Parallel Plate as a Lateral Shearing Interferometer with a Visible Gas Laser Source. *Appl. Opt.* 3(4), 531–534. 21
- Nogueira, J., A. Lecuona, A. Acosta, and P. A. Rodríguez (2004). *Particle Image Velocimetry: Recent Improvements*, Chapter The Local Field Correction Advanced PIV Algorithm, pp. 85–96. Berlin: Springer. ISBN: 3-540-21423-2. 101
- Nogueira, J., A. Lecuona, and P. A. Rodríguez (2001). Local field correction PIV implemented by means of simple algorithms and multigrid versions. *Meas. Sci. Technol.* 12(11), 1911–1921. 101
- Otsu, N. (1979). A threshold selection method from grey-level histograms. *IEEE Trans. on systems, Man, and Cybernetics SMC-8*(1), 62–66. 131
- Park, Y. K., G. Giuliani, and R. L. Byer (1980). Stable Single-Axial-Mode operation of an UNstable-Resonator Nd:YAG Oscillator by Injection Locking. *Opt. Lett.* 5, 96. 79
- Pettersson, S.-G., H. Bergstrom, and N. H. Abramson (1989, February). Light-in-flight recording VI: Experiment with view-time expansion using a skew reference wave. *Appl. Opt.* 28(4), 766. 55
- Pfarrhofer, R., P. Bachhiesl, M. Kelz, H. Stögner, and A. Uhl (2003). MDICE - a Matlab Toolbox for Efficient Cluster Computing. Internal report - unpublished. 106
- Poppen, C. (2003). Aspekte zur Auswertung rekonstruierter reeller Bilder in der holografischen PIV. Diploma thesis. 30, 34
- Prasad, A. K. and R. J. Adrian (1993). Stereoscopic Particle Image Velocimetry applied to Liquid Flows. *Exp. in Fluids* 15, 49–60. 97
- Pu, Y. (2002). *Holographic particle image velocimetry: from theory to practice*. Ph. D. thesis, Buffalo. 99
- Pu, Y., L. Cao, and H. Meng (2002). Fundamental issues and latest development in holographic particle image velocimetry. In *Proc. of the Int. Mech. Eng. Congr. Exhib.*, Number Paper 33171, New Orleans. ASME. 40, 119
- Pu, Y. and H. Meng (2000a). An advanced off-axis holographic particle image velocimetry (HPIV) system. *Exp. Fluids* 29, 184–197. 34, 68, 99, 105
- Pu, Y. and H. Meng (2000b, January). Particle Image Velocimetry Apparatus and Methods. Patent Cooperation Treaty, PCT/US99/15449. International Publication Number: WO 00/03308. 99
- Pu, Y. and H. Meng (2003, October). Intrinsic aberrations due to Mie scattering in particle holography. *J. Opt. Soc. Am. A* 20(10), 1920–1932. 34, 36, 99, 149
- Pu, Y. and H. Meng (2004, July). Intrinsic speckle noise in off-axis particle holography. *J. Opt. Soc. Am. A* 21(7), 1221–1233. 40, 41, 99, 133, 139, 146

- Pu, Y., X. Song, and H. Meng (2000). Off-axis holographic particule image velocimetry for diagnosing particulate flows. *Exp. Fluids [Suppl.]*, S117–S128. 99
- Raffel, M., C. E. Willert, and J. Kompenhans (1998). *Particle Image Velocimetry*. Berlin: Springer. 2, 3, 101, 104
- Rahn, L. A. (1985). Feedback stabilization of an injection-seeded Nd:YAG laser. *Appl. Opt.* 24(7), 940–942. 79
- Rimmer, M. P. (1974). Method for Evaluating Lateral Shearing Interferograms. *Appl. Opt.* 13(3), 623–629. 21
- Roth, G. I. and J. Katz (2001). Five techniques for increasing the speed and accuracy of PIV interrogation. *Meas. Sci. Technol.* 12, 238–245. 99, 101
- Royer, H. (1997). Holography and particle image velocimetry. *Meas. Sci. Technol.* 8, 1562–1572. 28
- Saxby, G. (1988). *Practical Holography*. Prentice Hall. 156
- Scarano, F. (2002). Iterative image deformation methods in PIV. *Meas. Sci. Technol.* 13, R1–R19. 101
- Scarano, F. and M. L. Riethmuller (2000). Iterative image deformation methods in PIV. *Exp. in Fluids* 29(7), S51–S60. 101
- Schnars, U. and W. Jüptner (1994). Direct recording of holograms by a CCD-target and numerical reconstruction. *Appl. Opt.* 33, 179–181. 34
- Schnars, U. and W. P. O. Jüptner (2002). Digital recording and numerical reconstruction of holograms. *Meas. Sci. Technol.* 33, R85–R101. 34
- Schärfe System GmbH (1997). *Casy Cell Counter and Analyser System*. Krämerstraße 22, D-72764 Reutlingen: Schärfe System GmbH. www.casy-technology.com. 177
- Sheng, J., E. Malkiel, and J. Katz (2003, January). Single Beam Two-Views Holographic Particle Image Velocimetry. *Appl. Opt.* 42(2), 235–250. 98
- Sholes, K. and P. V. Farrell (2000, November). Optical alignment-induced errors in holographic particle image velocimetry. *Appl. Opt.* 39(31), 5685–5693. 20, 22
- Slavich, I. W. (2001, January). Emulsions for holography - technical product specifications and sales information brochure. www.slavich.com. 16
- Stanislas, M., J. Kompenhans, and J. Westerweel (Eds.) (2000). *Particle Image Velocimetry - Progress towards industrial application*. Dordrecht / Boston / London: Kluwer Academic Publishers. ISBN 0-7923-6160-1. 4
- Stanislas, M., J. Kompenhans, and J. Westerweel (Eds.) (2004). *Particle Image Velocimetry: Recent Improvements*. Springer. ISBN: 3-540-21423-2. 4

- Staselko, D. I., Y. N. Denisyuk, and A. G. Smirnow (1969). Holographic recording of the time-coherence pattern of a wave train from a pulsed laser source. *Opt. Spectrosc.* 26, 413. 55
- Steigerwald, C. (2005-2006). Matlab GUI for evaluation of LiFH-PIV data. private communication. 150
- Tao, B. (2000). *Development of holographic image velocimetry and its application in three-dimensional velocity measurement and modeling of high Reynolds numbers turbulent flows*. Ph. D. thesis, Baltimore. 99
- Thompson, B. J. (1964). Diffraction by opaque and transparent particles. *SPIE Journal* 2, 43–46. 4
- Thompson, B. J. and J. H. Ward (1966). Particle sizing - the first direct use of holography. *Scientific Research* 1(10), 37–40. 4
- Trollinger, J. D., W. M. Farmer, and R. A. Belz (1968). Multiple exposure holography of time varying three-dimensional fields. *Appl. Opt.* 7(8), 140–1641. 4
- van de Hulst, H. C. (1981). *Light scattering by small particles*. New York: Dover Publications, Inc. 31
- Vikram, C. S. (1972). Holographic recording of moving objects. *Nouv. Rev. Optique appliquée* 3(6), 305–308. 25
- Walker, M. J. (1954). Matrix Calculus and the Stokes Parameters of Polarized Radiation. *Am. J. Phys.* 22, 179. 166
- Weber, H. and G. Herziger (1972). *Laser - Grundlagen und Anwendungen* (1. Auflage ed.). Weinheim: Physik Verlag. 59
- Westerweel, J. (1993). *Digital particle image velocimetry - Theory and application*. Ph. D. thesis, TU Delft. 3, 102
- Westerweel, J. (1997). Fundamentals of digital particle image velocimetry. *Meas. Sci. Technol.* 8, 1379–1392. 101
- Westerweel, J., D. Dabiri, and M. Gharib (1997). The effect of a discrete window offset on the accuracy of cross-correlation analysis of digital PIV recordings. *Exp in Fluids* 23, 20–28. 106
- Wiener, N. (1930). *Acta Math.* 55, 117. 58, 167
- Willert, C. E. and M. Gharib (1991). Digital Particle Image Velocimetry. *Exp. in Fluids* 10, 181–193. 102
- Zernike, F. (1938). *Physica* 5, 785. 56
- Zhang, J., B. Tao, and J. Katz (1997). Turbulent flow measurement in a square duct with hybrid holographic PIV. *Exp. Fluids* 23, 373–381. 68, 98, 99

Acknowledgements

It is my pleasure that I list some of the persons by name, who have been involved in this work.

First of all, my deep thank goes to Klaus Hinsch for five and a half years of fruitful collaboration, and some more for also being my doctoral adviser including a thorough review of the first version of this thesis. This PhD would not have been possible without his foresight, ongoing supervisory and scientific guidance with simultaneous freedom to organise and develop my own research activities.

For the necessary corrections concerning the English grammar and vocabulary I am deeply grateful to Peter Sharp, who finally got over this document twice.

In addition, I wish to acknowledge Heinz Helmers for many interesting discussions and his often short-termed assistance in the lab, as well as for his support in finding a way to analyse the SNR of single particle images using Matlab.

Furthermore, I am indebted to many of the other (former) members of the research group in Oldenburg. I am owing thanks to Rolf Harms for his craftsmanship and technical support, Gerd Gülker for the ever-motivating words, Karin Wolff and Holger Joost for the entertainment during tea-time, Carsten Poppen, Hendrik Sroka & Marco Ohm for assisting me during the time of their diploma thesis and lab practice, respectively and to Markus Schellenberg for his continuous help. Last, but not least the two months together with my successor Christian Steigerwald and the new diploma candidate Christian Hülsmann are greatly acknowledged. They continued the experiments with the same tenor and ensured the survival of LiFH-PIV until today.

For the excellent communication concerning HPIV, I wish to thank the following persons, who always had a quick answer and also supported my work by letting me visit their labs: Ye Pu and Hui Meng, Donald Barnhart, Jeremy Coupland and Neil Halliwell (many thanks for the great experience when organising and holding the HPIV workshop in Loughborough!), Pilar Arroyo and Nieves Andres as well as Jerry Westerveel. The helpful discussions with Bo Tao, Joseph Katz and Julio Soria are also acknowledged.

The research at the University of Oldenburg was supported by a grant from the European Community within the EUROPIV 2 project, which started in April 2000 and ended in June 2003. On behalf of the consortium my thanks for three years of fruitful and encouraging discussions and meetings go for Michel Stanislas. Support for the wind-tunnel measurements from the team at DLR in Göttingen, Germany is gratefully acknowledged. The author would like to thank Janos Agocs, Holger Frahnert, Jürgen

Kompenhans, Bernd Sammler and Andreas Schröder personally for their help during the campaign.

EUROPIV2 (a joint programme to improve PIV performance for industry and research) is a collaboration between LML URA CNRS 1441, DASSAULT, AVIATION, DASA, ITAP, CIRA, DLR, ISL, NLR, ONERA and the universities of Delft, Madrid, Oldenburg, Rome, Rouen (CORIA URA CNRS 230), St Etienne (TSI URA CNRS 842) and Zaragoza. The project is managed by LML URA CNRS 1441 and is funded by the European Community within the 5th Framework (Contract No. G4RDCT-2000-00190).

Finally, I wish to thank my family for the support throughout the time of my PhD work. Special thank goes to my wife, Katja Herrmann, for her love and patience. Her sacrifices in supporting the writing of this thesis as well as those numerous days, weekends and late nights which, otherwise I would have spent with her, are greatly acknowledged.

Curriculum Vitae

Person

Name: Sven Frieder Herrmann
Academic grade: Graduate physicist (Diplomphysiker)
Date of birth: September, 15th 1972
Place of birth: Bremen
Citizenship: German
Marital status: married



School

1979 - 1983 Primary school: Grundschule Walle, Bremen
1983 Primary school: Grundschule Erichshof, Weyhe
1983 - 1992 High school: Orientierungsstufe und Gymnasialzweig der KGS Weyhe
1992 Graduation: Abitur

Civilian Service

1992 - 1993 DRK Rettungsdienst e.V. Syke

Studies

1993 - 1995 Undergraduate studies, University of Oldenburg
1995 Vordiplom
1995 - 1998 Graduate studies, University of Oldenburg
1998 - 1999 Diploma thesis: "Strömungsmessung mit Light-in-Flight Holographie: Optische Schalter zur Auswertung durch Kreuzkorrelation"
1999 Diploma
1999 - 2004 Doctoral candidate, University of Oldenburg

Employments

1999 - 2004 Scientific co-worker, University of Oldenburg
2005 - 2006 Development Engineer at the Corporate Sector of Research and Advance Engineering, Robert Bosch GmbH, Schwieberdingen / Germany

Scientific activities

Feb. - May 1997 Practice at the "Minerva center for high T_c superconductivity" at the Technion in Haifa / Israel.
Aug. - Sep. 1997 Summer student program at the "Deutsches Elektronen-Synchrotron (DESY)" in Hamburg / Germany.
May 2003 Organisation and part of realisation of the "International Workshop on Holographic Metrology in Fluid Dynamics" in Loughborough / UK.
April 2004 Guest Editor for the special feature on "Holographic Particle Image Velocimetry" of Meas.Sci.Technol. 15(4)

Statement

Erklärung gemäß § 10 Absatz 2 b) der Promotionsordnung vom 11.12.2003

Hiermit versichere ich, dass ich diese Arbeit selbstständig verfasst und keine anderen als die angegebenen Quellen und Hilfsmittel verwendet habe. Einzelne Passagen der Arbeit sind bereits in ähnlicher Form in den von mir zitierten eigenen Publikationen enthalten.

Schwieberdingen, den 30. Mai 2006

(Sven Herrmann)

